Modelling the role of polarity and geometry in cell-fate dynamics of mammary organoids

Joshua W. Moore

School of Mathematics

Cardiff University

A thesis submitted for the degree of

Doctor of Philosophy

June 2023

For Lucy. My sunshine, inspiration, and love.

Acknowledgements

Firstly, I wish to thank Thomas. Following a simple email as a second-year undergraduate, you provided me with countless opportunities and guidance over the last five years. Not only are you a wonderful academic mentor but you have made working on this project a pleasure with your endless enthusiasm and empathy. I also wish to express my gratitude to Trevor. Your biological mentorship, support and advice have been fundamental to the progression of this thesis and my career. It has been a privilege to have you both as my supervisors.

Of course, I would like to thank Dr Bethan Lloyd-Lewis, Dr Mairian Thomas, Dr Victoria Marsh Durban and everyone in the Dale lab for your insightful discussions, patience with me in the lab, and for providing me with the data used in this study. I would like to thank KESS2 and my industrial partner Cellesce Ltd for providing their support to make this project possible.

A special thanks go to Tim, Michela, Lizzie, Matthew, Mike, Layla, and the rest of the PGR cohort (Figure 0 - sorry everyone wasn't there for the photo) for making the last three and half years so enjoyable with our tea-induced nonsense, even through a pandemic. In particular, the Procrastination Squad (you know who you are) who are to blame for my recent absences from the pub in order to finish this thesis.

Sincerely, thank you Lucy. Without your constant encouragement and support, I would never have considered pursuing a PhD, let alone finishing one! This has been a journey for both of us and I cannot overstate how influential your passion and perseverance has been on me. Oh and how can I forget, the progress of this thesis was significantly hindered by Apollo and all his attention-seeking performances.

Figure 0: The culprits. Thank you.

Abstract

Mammary organoids are three-dimensional structures that are derived from mammary gland cells and can recapitulate the complex architecture and functionality of the mammary gland *in vitro*. Mammary organoids hold great promise for advancing our understanding of mammary gland biology, breast cancer, and precision medicine. However, phenotypic and genetic instabilities observed in long-term expansion limit their applications to prolonged experiments and large-scale production.

A proposed factor driving this organoid-wise heterogeneity is plasticity within mammary epithelial cells, the phenotypic switching of cells. Therefore, we examine the dynamics of key intracellular pathways that govern cell-fate commitment in mammary organoids. Specifically, we explore the influence of local tissue geometry and polarity in cell-cell signalling in stabilising cell-fate determinants using a combination of analytic and numerical multiscale modelling approaches.

We introduce interconnected dynamical systems, graph-coupled dynamical systems with input-output representations to describe intercellular signal flow between cells. Exploiting structural properties of the bilayer graphs describing mammary tissue architecture, we derive low-dimensional forms of these models enabling the analytic examination of the interplay of structure and polarity on cell-fate patterning, extending existing methods to include pathway crosstalk and providing rigorous links between low-dimensional and their associated large-scale representations.

Supporting the analytic investigations of static spatial domains with cell-based modelling, we provide evidence that sufficiently strong cell-cell signal polarity has the capacity to generate and sustain bilayer laminar patterns of Notch1, a critical cell-fate determinant and inducer of plasticity in mammary epithelial cells. Furthermore, we demonstrate how local tissue curvature can relax the constraints of polarity supporting healthy tissue growth and supporting branching morphologies. Fundamentally, this study highlights the significance of cell signalling polarity as a control mechanism of cell-fate commitment. Thus, the establishment and maintenance of epithelial polarity should be considered in long-term mammary organoid expansion protocol development.

Relevant publications

[1] Joshua W. Moore, Trevor C. Dale, and Thomas E. Woolley. Polarity driven laminar pattern formation by lateral-inhibition in 2D and 3D bilayer geometries. *IMA Journal of Applied Mathematics* (2022). [Chapter 2]

Additional comments: This manuscript was selected as a finalist for the IMA Lighthill-Thwaites ECR prize. In Chapter 2, we extend the section on laminar patterns in stochastic spatial domains using overlapping sphere models to consider stochastic growing bilayer domains using vertex models. The original stochastic spatial domains section in this paper is given in Appendix A.

[2] Joshua W. Moore, Trevor C. Dale, and Thomas E. Woolley. Modelling polarity-driven laminar patterns in bilayer tissues with mixed signalling mechanisms. *SIAM Journal of Applied Dynamical Systems* (2023). [Chapter 4]

Additional comments: In Chapter 4, we extend the main results on quotient and large-scale laminar pattern convergence presented in this publication to consider a larger class of generic inhibition, induction and mixed induction-inhibition kinetics. We now also provide formal links between quotient and large-scale graphs with spectral control. In addition, novel low-dimensional pattern stability conditions for MIMO systems are now presented.

Statement of Originality

I confirm to the best of my knowledge that the content of this thesis is my own and that this thesis has not been submitted for any other degree or purposes. No primary data was produced in this work and therefore sources of data have been clearly stated in-text where relevant. Confocal images of mammary organoids analysed in Chapter 3 were kindly provided by the Lloyd-Lewis Lab (University of Bristol) and Cellesce Ltd with permission for publication. All analysis conducted on these data is novel and conducted by myself unless stated otherwise. In addition, I co-supervised three undergraduate projects relating to the content of this thesis. I can confirm that any of the content produced from these projects used in this thesis is clearly stated within the text.

Contents

Chapter 1

Introduction

This thesis explores the interplay of tissue geometry and cell signalling polarity in the patterning of cell-fate determinants in developing mammary organoids. Before stating the explicit motives driving the aims and objectives of this work, we first introduce the relevant biological background. Thereafter, we briefly review a range of mathematical approaches taken to study similar phenomena at different characteristic spatial scales in developmental biology. Lastly, we present an outline of the structure and results of the thesis.

1.1 A brief introduction to mammary organoids

The mammary gland is an organ found in female mammals, which is highly specialised for the primary function of milk production and secretion, as a nutrient source for their offspring. This glandular tissue is located in the breasts and undergoes substantial remodelling after birth, specifically during puberty and pregnancy [1]. The sensitivity of mammary glands to their environment which promotes these developmental changes indicates the presence of complex autoregulatory mechanisms present to sustain healthy organ growth [2].

Nevertheless, high environmental sensitivity yields increased susceptibility to disease initiation and progression. Critically, dysregulation of hormone-dependent homeostatic mechanisms is a fundamental characteristic of breast cancer progression [3]. Breast cancer is currently the most common form of cancer diagnosed among women in the UK, with over 55,000 diagnoses a year and leading to approximately one in four fatal cases [4]. Though research in healthy and disease mammary biology is a growing and highly active field, the fundamental processes governing mammary gland development are still unknown due to the spatial and biochemical complexity of this highly adaptive organ [5, 6].

1.1.1 The structure and function of the mammary gland

During the embryonic stages of mammalian development, ductal structures composed of epithelial cells grow outward from the nipple generating tree-like branched structures (figures 1.1a and 1.1b) within the breast tissue [1]. These branching structures establish a core architecture of the organ for later development during puberty and pregnancy, namely, ductal extension for the production and transport of milk at lactation in response to hormonal cues.

The ductal sections of the organ consist of a distinct bilayer structure of epithelial cells that is typical in glandular tissue. In the mammary gland, these ducts are comprised of an outer layer of basal cells and an inner layer of luminal cells which surround a hollow region known as a lumen, as shown in Figure 1.1a. These contrasting layers of cells present both functional and morphological differences. Luminal cells occupy the largest volume of the duct, presenting cuboidal cellular shapes with the function of milk synthesis and release into the lumen [1]. The majority of the basal cell population consists of myoepithelial cells which are elongated along the outer surface of the duct. The myoepithelial cells are responsible for physically promoting milk secretion using contractive mechanisms in response to hormone stimulation [7]. It is reported that the mammary stem cell population are located within the basal layer [8], facilitating the renewal and regeneration of the duct.

These distinct cell populations are typically identified using their differential expression of Keratin subtypes, a protein found on the membrane of epithelial cells [1]. Luminal cells express the Keratin 8, 11 and 18 subtypes (K8, K11 and K18) whereas basal cells are identified by the 5 and 14 subtypes (K5 and K14). In addition, basal cells can be phenotypically isolated by their expression of smooth-muscle actin (SMA). Figure 1.1c shows the differential expression of the Keratin subtypes within a mammary duct, highlighting the bilayer epithelial architecture.

The mammary ducts are embedded within fatty tissue in the breast. Namely, surrounding the ducts is the stroma, which is composed of various connective tissue cells, including fibroblasts, adipocytes, and immune cells, as well as extracellular matrix proteins. The stroma supports the healthy development of the mammary gland by providing a structural framework for glandular growth as well as epithelial mediation by the secretion of growth factors [11].

Between the stroma and basal population lies the basement membrane. The basement membrane is a sheet-like network of protein fibres that regulates the interactions between the stroma and the basal cells and is also responsible for orientating the mammary epithelia for functional ductal growth [12].

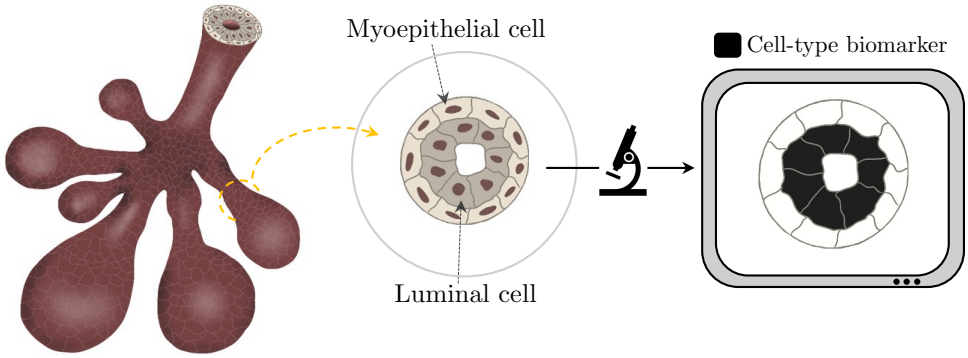

(a) Representative mammary duct epithelial structure.

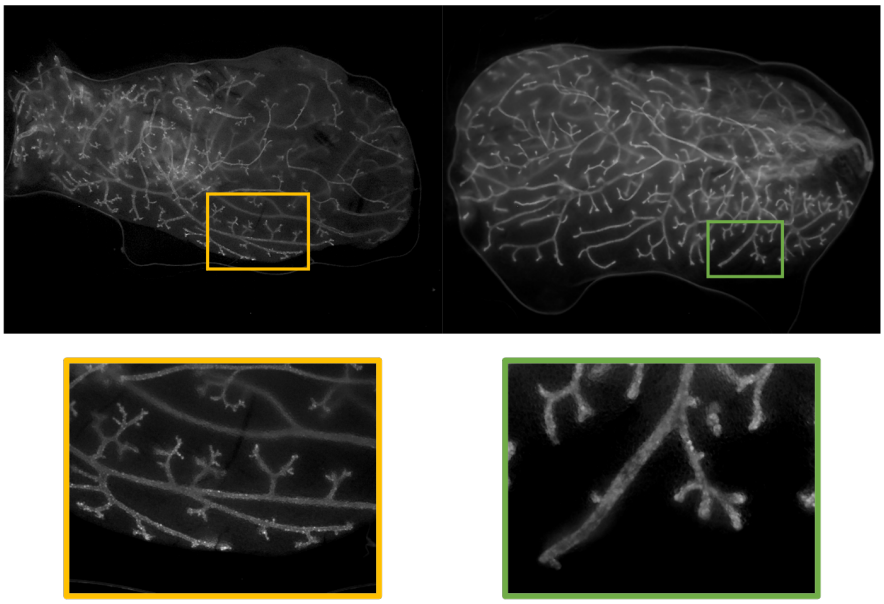

(b) Branching tree-like structure of the mammary gland.

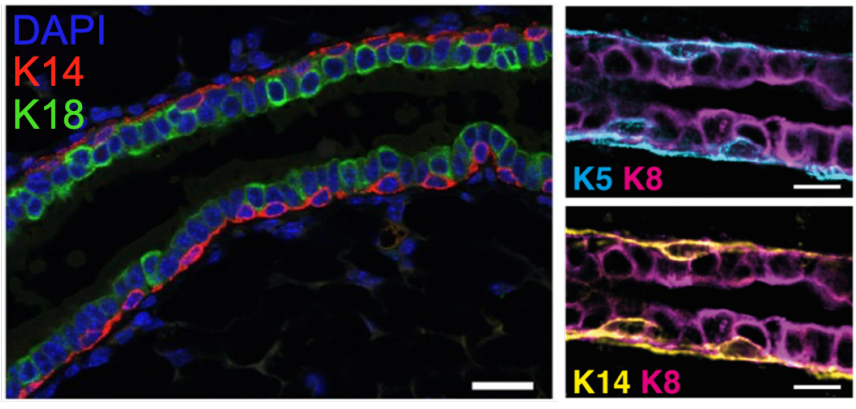

(c) Bilayer epithelial ductual structure.

Figure 1.1: The epithelial and tissue structure of the mammary gland. (a) A schematic of the bilayer epithelial structure within mammary ducts and their identification using immunofluorescence microscopy. (b) Adult mouse mammary ducts show the branching architecture of the mammary gland. The epithelial cells are tagged with membrane reporters to highlight global tissue structure. Insets show local mammary gland branches. Images provided by Dr Bethan Lloyd-Lewis.

Figure 1.1: (Continued.) (c) Differential Keratin expression in mammary ducts. Mammary epithelial cells within ducts are stained using immunofluorescence Keratin targets and imaged using confocal microscopy. The left-most image is additionally stained with DAPI, a nucleic identifier, scale bar 20μm. The right-most images highlight the simultaneous Keratin activation of K14 and K5 in the basal population, scale bar 10μm. Images reprinted from [9] and [10], respectively.

1.1.2 Mammary organoids

In vitro culture systems refer to those performed outside a living organism, whereas *in vivo* relates to processes performed within a living organism. In addition, culture systems that use cells directly isolated from the source animal in a laboratory environment are called *ex vivo* [13]. *In vitro* and biological models of organs are important tools for the control, scalability and simplification in experimental design and allow researchers to isolate key mechanisms relating, but not limited to, tissue growth, self-organisation and disease control [14]. Subsequently, generating culture systems that most accurately represent *in vivo* biological conditions is fundamentally important to the study of healthy and disease developmental biology. Over the past decade, significant advances in culture technologies have focused on the development of 3D suspension techniques to avoid physical contact with the plastic well or dish, which would otherwise induce artificial cellular behaviour [15].

Organoids are tissues grown *in vitro* that closely recapture both the structure and functions of an organ *in vivo*, and therefore are also referred to as 'mini-organs' [15]. Specifically, an organoid is a collection of cells derived from a specific tissue and grown in a 3D culture system that is designed to recapitulate the natural tissue as simply as possible. Organoid cultures differ from existing 3D culture systems due to their regenerative capacity following a sustained stem cell population, which is supported by continuous growth media supplementation [16]. Critically, these organoid cultures containing stem cells demonstrate a complete set of differentiated cell types found in the original tissue, which are arranged in an architecture specific to the organ and communicate through physiologically relevant signalling mechanisms. Moreover, these culture systems enable long-term cultures which can be expanded to generate more organoids, facilitating high-throughput analysis from a small amount of starting material. Furthermore, using these organoid technologies in *ex vivo* contexts generates highly relevant physiological behaviours derived from the source organ which is both reproducible and experimentally controllable, a more accurate and reliable description of of the biology underpinning the organ compared to *in vitro* cultures [17]. However, the resources required to isolate primary cells and sustain *ex vivo* organoid cultures

are significantly greater than *in vivo* systems [18]. The benefits of organoid culture systems have led to their applications in drug screening, as well as personalised and regenerative medicine [14].

Mammary organoids are organoids generated from stem-cell rich mammary epithelial fragments and have the capacity to form the bilayer epithelial ductal structures that are observed in mammary glands from simple spherical clusters (Figure 1.2). Building upon culture protocols developed for intestinal organoids [19], the Dale lab developed the long-term culture protocols for mammary organoids [16, 20], specifically focusing on hormone supplementation for stem cell conservation. Since the establishment of sustainable mammary organoids, extensions to these protocols have been designed to investigate specific features of mammary biology, accelerating our understanding of the epithelial processes driving cell-fate decisions [21], branching morphogenesis [22], lactation [23], and cancer initiation and progression [24].

In contrast to the *in vivo* mammary gland, mammary organoids present as an unconstrained *in vitro* model of mammary biology driven purely by the mammary epithelial cells (MECs) and their interaction with an extracellular matrix (ECM) termed matrigel. The ECM may recapitulate features of the previously described basement membrane. However, the active role of fibroblasts is removed from organoid cultures. This feature of mammary organoids allows the investigation of epithelial-driven collective MEC behaviour at high-resolution, particularly during the early stages of glandular development and breast cancer [25]. For example, mammary organoid technology was used to decipher suitable microenvironmental conditions generated by local MECs for the existence of spatial clusters for mammary stem cell (MaSC) renewal, known as a stem cell niche [16].

However, the dissociation of fibroblasts and MECs generates atypical environmental conditions for mammary organoid growth with the loss of physical and biochemical cues provided to the MECs [26]. Consequently, organoid culture is difficult and expensive to maintain for high-throughput experimental studies due to the existence of genetic instabilities and phenotypic defects [20]. Therefore, this thesis aims to understand the processes involved in sustaining healthy mammary organoid development, specifically through the lens of cell-cell communication and cell-type commitment. Thereby providing novel insights for high-throughput mammary organoid culture development.

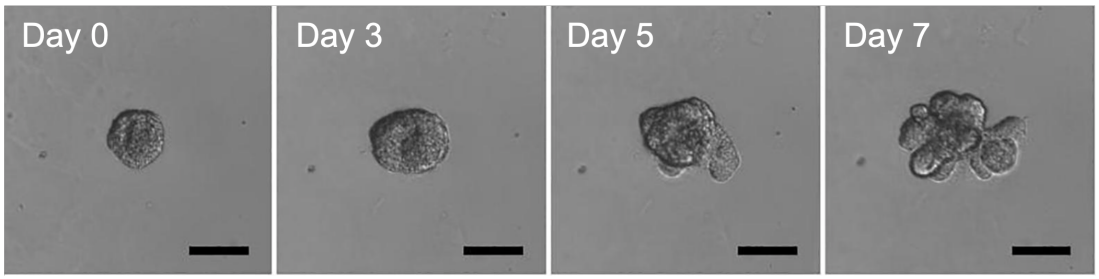

Figure 1.2: Mammary organoids from simple spheroids to branching structures. Timelapse brightfield images of a mammary organoid from the initial day of epithelial fragment seeding depicting branching morphogenesis under FGF2 supplementation. Scale bar 100μm. Images reprinted from [23].

1.2 Cellular communication in mammary epithelial cells

To facilitate the self-organisation of MECs to form functional glands, precise and coordinated exchange of signals between cells are employed to allow each cell to communicate and respond to changes in their environment, a process called cell signalling. Cell signalling involves a variety of mechanisms, including the release of chemical messengers called signalling molecules, the activation of receptor proteins on the surface of cells, and the transmission of signals through intracellular signalling pathways, as illustrated in Figure 1.3. These processes enable cells to interpret and respond to a wide range of environmental cues, such as changes in the concentration of nutrients, growth factors, and hormones. In particular, cell-cell signalling coordinates local cell-type determination and proliferation in developing tissues [27].

1.2.1 Mechanisms of cell signalling in mammary epithelia

Local cell-cell signalling mechanisms in epithelial cells can be categorised into three distinct processes; paracrine, autocrine, and juxtacrine signalling [27]. Paracrine signalling is a long-range signalling process, where signal molecules are secreted by a cell which then binds to specific signal receptors on the surface of near cells, typically transported by extracellular diffusion. However, paracrine signalling has been observed to exhibit additional mechanisms of long range signal molecule transport such as planar transcytosis and cytonemes [28]. Namely, in planar transcytosis the signal molecule binds to a receptor on a cell and then is transported through the cell to be expressed at a different location on the surface where this process is repeated in an adjacent cell [29]. Subsequently, paracrine signalling has the largest scale length of those discussed in this section, with the

capacity to secrete signals up to a distance of 100μm (approximately 5 MEC diameters) of the signal sending cell [30].

Autocrine signalling is the mechanism where signalling molecules secreted from a cell bind to receptors on the surface of the same cell. The autocrine mechanism serves as a self-regulatory process, initiating a feedback loop that can activate an intracellular cascade, thereby controlling the behaviour of the cell. For example, autrocrine signalling of the growth factors epidermal growth factor (EGF) and transforming growth factor-beta (TGF-β) is essential for proliferation and branching morphogenesis in the mammary gland [16, 31].

Juxtacrine signalling is a contact-dependent signalling mechanism whereby membrane-bound signal activators on the surface of signal sending cells bind to membrane-bound receptors on adjacent cells, initiating the activation of downstream pathways. This signalling process accounts for the most local intercellular communication and is commonly observed in cell-type coordination in developing tissues [27]. Critically, this method of cell-cell communication is not only dependent on the concentration of available activators and receptors on the surface of the cell, but also the geometry of cell for surface contact regions [32]. That is, cellular behaviours influenced by juxtacrine-dependent signalling factors are highly susceptible to local and global tissue morphological deformations which are common during organ development.

A summary of the epithelial signalling mechanisms is given in Figure 1.3. MECs simultaneously employ each of the signalling mechanisms during mammary organoid growth, coordinating proliferation, apoptosis, motility and cell-type changes. Before discussing specific pathways that employ these mechanisms regulating the development of mammary organoid, we first introduce one of the main themes of this thesis, polarity in cell signalling.

1.2.2 Polarity in cell signalling

In a broad sense, cell polarity is the asymmetry of the shape and/or molecular distribution in a cell. Cell polarity is a crucial mechanism for epithelial cell function specialisation and self-organisation during tissue growth, for example, the localisation of adhesion molecules for lateral tissue strength in epithelial sheets [33]. The two most common types of polarity observed in epithelial cells are apical-basal polarity (ABP) and planar cell polarity (PCP) [34], representing local and global contributions of cellular directionality, respectively. ABP refers to the asymmetric distribution of cellular components along the apical-basal axis of a cell. PCP refers to the coordinated alignment of cells within an epithelial tissue and is typically directed orthogonal to the apical-basal axis. Both polarity mechanisms are controlled by a host of intercellular signalling pathways and

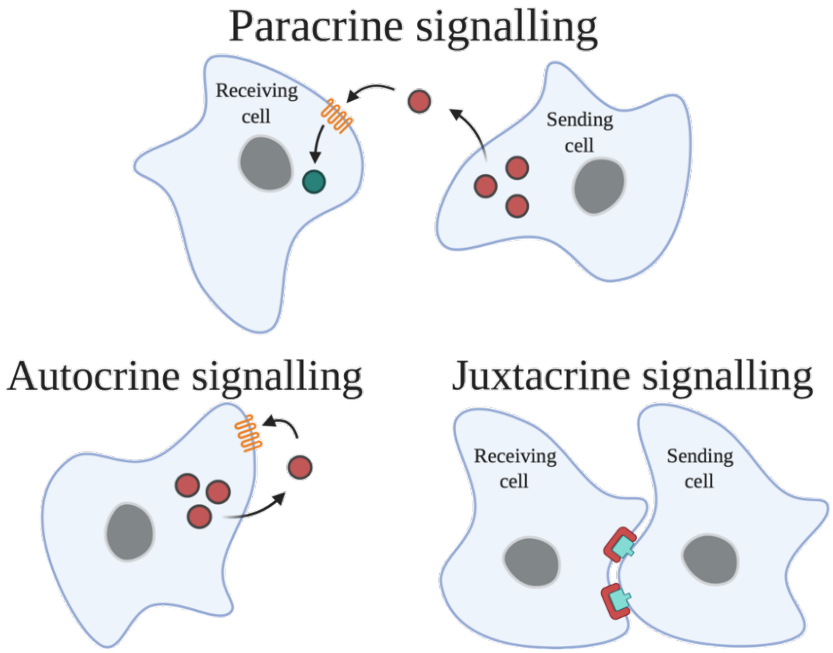

Figure 1.3: A summary of the signalling mechanisms employed by MECs for cell-cell communication.

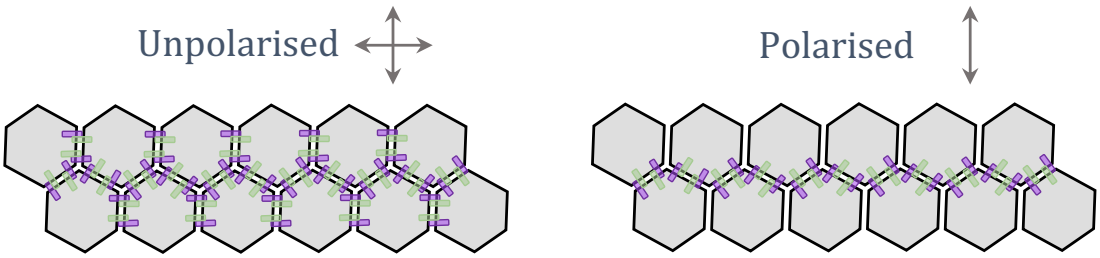

Figure 1.4: Schematic of cell signalling polarity in a bilayer tissue using a juxtacrine signalling mechanism. Signal activators and receptors are represented using purple and green rectangles.

cues from the cellular environment, common examples include the Par and Wnt pathways for ABP and PCP, respectively [35].

Critically, both ABP and PCP can induce asymmetries in cell signalling proteins, causing anisotropic communication flow between cells and specifying a niche of adjacent interacting cells. This process is defined as cell signalling polarity [36]. Figure 1.4 highlights this property with ABP. Polarity in cell signalling can amplify signals within cells, leading to more efficient and precise signalling for robust cell-cell coordination during morphogenesis, specifically regulating cell migration, cell division and differentiation [33].

MECs are highly polarised cells, adapted and specialised for milk production and secretion into the lumen. In particular, luminal cells exhibit apical-basal polarity through localised expression of cell-cell adhesion mediator E-cadherin near the apical surface (facing the lumen), binding luminal cells together for

lumen formation and preservation [37]. In addition, lumen-supporting tight junctions form at the apical surface of luminal cells, driven by zonal occludens-1 (ZO1) which generate a membrane surface barrier of intercellular proteins [38], allowing only small solutes to permeate through to the basal domain from the lumen. Furthermore, it has been demonstrated that myoepithelial cells are coordinators of polarity in luminal cells through their expression of laminin-1 [39].

Cellular polarity is a dynamic feature of cells and is altered during substantial physiological changes to tissues, such as injury [40] and pregnancy [41]. The reactive nature of polarity in cells is responsible for the restoration and maintenance of tissue integrity through processes of cell migration, apoptosis, formation of tight junctions, differentiation and dedifferentiation [42]. In addition to these homeostatic properties, in the mammary gland, ABP is also regarded as a gatekeeper against breast tumour development and metastasis [43], namely, the aberrant reaction of such cellular processes following mutation or cues from the local environment. Specifically, the mechanisms stablising ABP inhibit epithelial-mesenchymal transition (EMT) programs in mammary organoids. EMT is the process where epithelial cells increase mobility through the loss of cell-cell adhesion and remodelling of the cytoskeleton, a common characteristic of aggressive cancer spread [44]. Moreover, loss of polarity in mammary tissue can also initiate breast cancer. Deletion of the ABP regulator Scribble in MECs inhibits apoptosis in damaged cells, disrupting ductal morphogenesis through dysplasia, resulting in the loss of lumen [45].

Critically, polarity is a core control mechanism employed by MECs for healthy tissue development, specifically in mediating the phenotypic traits of MECs. The ability of cells to alter phenotype without genetic mutation is known as plasticity. Though plasticity is required for homeostasis in the presence of substantial and abrupt changes to the tissue, plasticity is also a common driver of breast cancer progression and mammary organoid growth instability following abnormal activity of these polarity-guided cell-fate alterations [20]. Therefore, we explore polarity on establishing and sustaining functional MEC cell-types in mammary organoids, specifically with the perspective of improving culture conditions. In the following section, we review the structure and regulators of the mammary lineage hierarchy and evidence of plasticity therein.

1.3 Cell-fate determination in MECs

To form specialised tissues, cells differentiate to form phenotypically different cells such as myoepithelial and luminal cells in the mammary gland. During the initial stages of morphogenesis, cells can start at an undifferentiated state with

a generic shape and function, and then must decide their future type through a process known as cell-fate determination. In the mammary gland, epithelial fates are tightly regulated by the microenvironment and cell-cell signalling for the autonomous coordination of bilayer tissue architectures [2].

1.3.1 Mammary cell lineage and plasticity

The hierarchy of mammary cell lineage is composed of two branches, see Figure 1.5a. At the head of the tree are the bipotent MaSCs, representing the undifferentiated cell population that undergoes renewal for tissue growth and regeneration [46]. Given the appropriate cues from the microenvironment, MaSCs differentiate into an intermediate lineage-restricted stem-like state known as a progenitor for each of the luminal or basal branches. The primary function of progenitor cells is to proliferate, therefore repopulating and sustaining the downstream lineage. Upon further differentation, cells transform into their highly specialised states, i.e., the myoepithelial and luminal cells. Luminal cells can be further classified by their responsiveness to estrogen (ER), that is, ER positive (ER+) and ER negative (ER-), where luminal ER- cells are associated with milk production in the mammary gland [47]. Furthermore, luminal ER- cells can later differentiate into ER+ state following ductal migration [20]. A summary of the MECs lineage structure is given in Figure 1.5a.

Due to the intense mechanical and biochemical stress imposed on MECs during organoid expansion, frequent plasticity events have been observed in mammary organoids, disrupting the canonical model of the MEC lineage hierarchy [20]. In particular, organoids seeded with epithelial fragments of purely luminal populations (ER- and ER+) under high R-spondin1/Wnt media conditions were able to reconstitute both lineage branches with typical bilayer tissue structure, evidencing luminal to MaSC plasticity. In support, elevated and sustained Notch1 conditions, a determinant of luminal fate, have been demonstrated to induce basal progenitor (K5+ cells) to luminal plasticity events in mammary organoids [21], and will be discussed in further detail in the following section.

Taken together, the hierarchical models of MEC lineage in mammary organoids cannot be viewed as unidirectional, as shown in Figure 1.5b. The sensitivity of the MEC phenotypes observed in mammary organoid models reflects the control underlying mechanisms governing robust morphologies of the highly dynamic organ. However, the details of such mechanisms at the intracellular resolution are widely unknown [20].

The reduced lineage restriction observed in mammary organoids may indicate the realisation of the functional plasticity that likely underlie epithelial responses

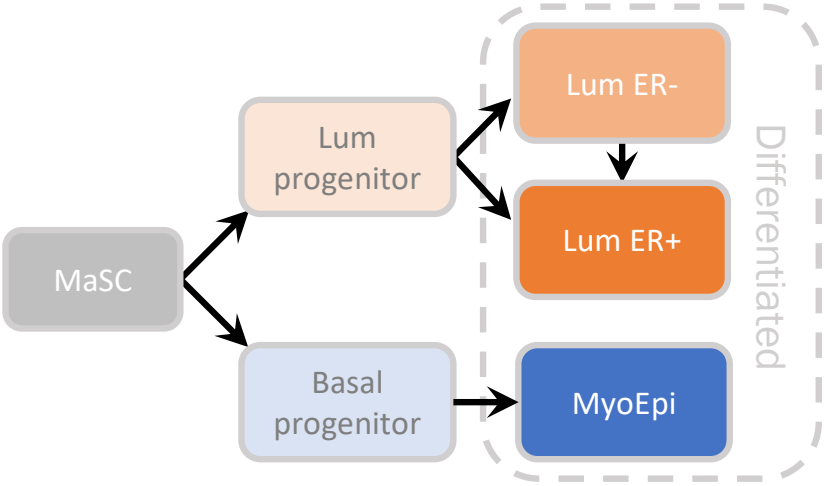

(a) Traditional MECs hierarchy in the mammary gland.

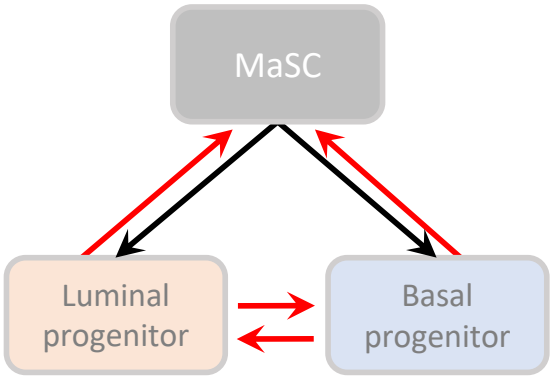

(b) Simplified plastic behaviour observed *in vitro* MECs.

Figure 1.5: Cellular differentiation hierarchy of the mammary gland. (a) A hierarchical model of cell differentiation derived from *in vivo* and *in vitro* lineage tracing experiments within the mammary gland. An initial bipotent MaSC population forms either luminal (Lum) or basally restricted stem cells known as progenitors which each serve to repopulate their respective differentiated lineages. Image adapted from [20]. (b) A simplified model of the MEC hierarchy with red arrows signifying the presence of plasticity during the initial stages of mammary organoid development as experimentally observed in [20], and induced by aberrant Notch1 activity [21].

in vivo that have not yet been studied (e.g. wound repair, infection, cellular stress etc.). In other words, the lineages presented in Figure 1.5a may represent the most frequent developmental trajectories that occur during normal mammary morphogenesis. By contrast, the simplified organoid environment may allow for a wider range of developmental responses to generate niche signals as a consequence of the reduced environmental constraints.

1.3.2 Pathways for cell-fate determination and function in MECs

To explore how the distinct bilayer tissue geometries and MEC polarity controls cell-fate determination, we review some key intracellular pathways that are well-established biomarkers for cell state predictions. Specifically, this thesis focuses on Notch pathway dynamics during mammary organoid development as it is strongly evidenced as a critical cell-fate determinant in MECs [48, 49], is highly susceptible to local tissue geometry [50, 51], is known to be influenced by polarity [52], and is an inducer of plasticity in MECs [21, 49]. However, the processes that govern the precise cell-fate coordination are complex such that these pathways do not act in isolation. Therefore, we also briefly discuss other notable pathways that should be considered when investigating MEC fate decisions and plasticity.

1.3.2.1 The canonical Notch pathway

The canonical Notch pathway is a highly-conserved juxtacrine signalling mechanism that plays an essential role in cell fate determination and morphological bifurcations in developmental systems [21, 53–55]. The Notch pathway describes a lateral-inhibition mechanism between neighbouring cells. The activation of the Notch receptor via membrane-anchored Delta ligands on adjacent cells leads to the accumulation of Notch-intracellular-domain (NICD) within the cytosol. The build-up of NICD leads to the transcription of members of the Hair-Enhancer of Split (HES) superfamily, which acts as an inhibitor of the target genes that promote the downstream production of Delta ligands and lineage-specific gene repressor [48]. That is, the activation of Notch leads to the inactivation of Delta within the same cell as illustrated in Figure 1.6. Mammals exhibit four paralogues of the Notch receptor, Notch1 to Notch4, each with associated Delta-like ligands (Dll) that each observes the autoregulation mechanism outlined by the canonical pathway [48]. Further details on the canonical Notch pathway be found in [56].

Notch1 signalling is a critical determinant of luminal cell differentiation in MaSCs [48, 49]. Critically, the intracellular depletion of the Notch1 promotor

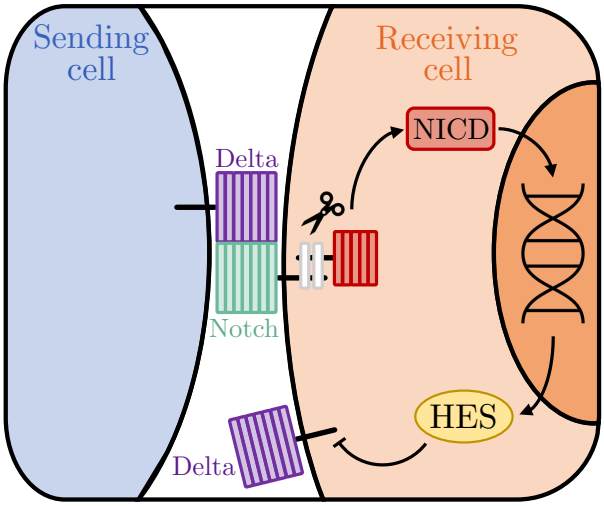

Figure 1.6: A simple diagram of the canonical Notch-Delta kinetics. Membrane-bound Delta ligands (purple rectangles) on a signal-sending cell bind to membrane-bound Notch receptors (green rectangles) on a receiving cell. The activation of Notch receptors initiates the cleavage of Notch into the cytosol of the receiving cell known as NICD. The NICD then translocates to the nucleus where it promotes the transcription of HES, an inhibitor of Delta ligand targets.

Cbf-1 generated MaSC-enriched populations highlighting that Notch1 facilitates differentiation in MECs. Furthermore, cells expressing the Notch1 gene are primarily located within the luminal population. In contrast, the basal population exhibits reduced Notch1 expression and increased Delta1 expression (Figure 1.7a), providing strong evidence that the canonical Notch kinetics govern MEC fate decisions. In addition, sustained activation of Notch1 is required for luminal progenitor renewal [49], and that Notch1-driven fate choices are made during embryonic development [21], before the establishment of differentiated MECs and functional tissue architecture. Critically, as a result of the differential expression of Notch1 in the basal and luminal populations, layer-wise laminar patterns of Notch1 are observed both in mammary organoids and their *in vivo* counterparts (Figure 1.7b).

Critical to both organoid development and tumour progression, Notch1 has the ability to reprogram lineage committed MECs [21, 58]. Namely, artificial sustained Notch1 activation in lineage-committed pubertal MECs for over 72 hours, triggers the loss of basal identity in myoepithelial progenitors, expressing MaSC signatures before transferring down the luminal committed lineage. Similarly, the same lineage switching dynamics have also been observed using the Notch1 antagonistic ΔNp63, where luminally committed cells switched to basal phenotypes [59], providing further support for the core role of Notch1 in cell fate stability.

Owing to the highly conserved nature of this pathway, evidence of Notch

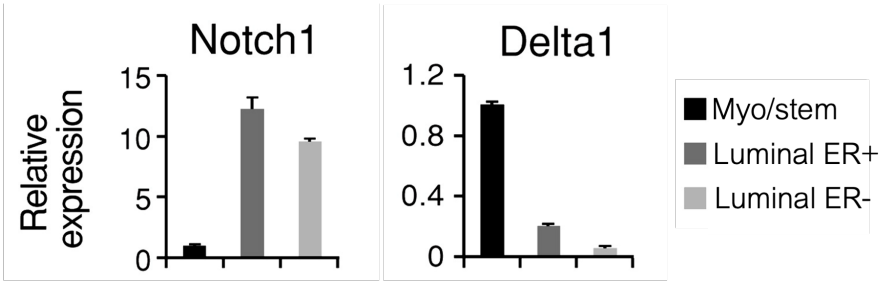

(a) Differential Notch-Delta expression in MECs.

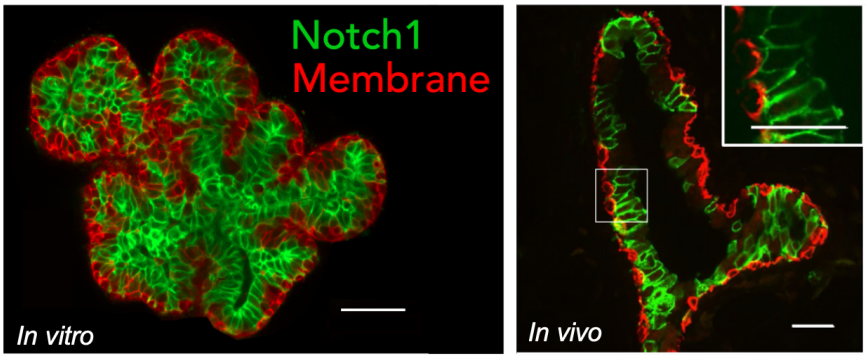

(b) Spatial patterning of Notch1 in bilayer epithelial structure.

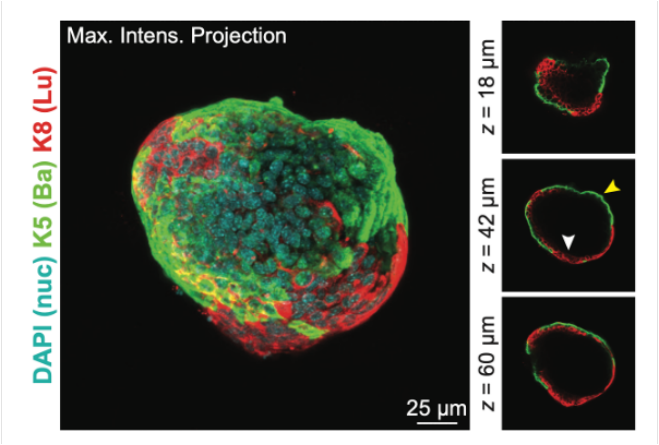

(c) Irregular phenotypic structure in a mammary organoid.

Figure 1.7: Notch-Delta activity and MECs structure. (a) *In vivo* Notch1 and Delta1 gene expression in mammary epithelial cells of an adult virgin mouse. Figure reprinted from [49]. (b) Spatial distribution of Notch1 activity is shown *in vitro* (left) and *in vivo* using transgenic Notch1-mTmG reporters. (left) Mammary organoid derived from an adult mouse mammary gland and imaged at day 7 after initial seeding. Image provided by Dr Bethan Lloyd-Lewis, scale bar 50μm. (right) Mouse mammary ducts fixed and imaged six-weeks after birth. Image reprinted from [21], scale bar 20μm (inset 10μm). (c) Immunofluorescence staining of mouse mammary organoid displaying an irregular epithelial bilayer after 10 days in culture. Image reprinted from [57].

driven plasticity events have also been observed in the brain, lung and lymphoid tissue [60–62]. Fundamentally, these results suggest that MEC phenotypes are dynamic and that dysregulation of Notch1 in mammary organoids can induce substantial structural defects, as is observed during prolonged mammary organoid expansion (Figure 1.7c).

As previously discussed, Notch kinetics are sensitive to both polarity and tissue geometry as a consequence of contact-based intercellular communication [51, 52]. Critically, both the bilayer geometries and highly polarised epithelial cells are key features of glandular organs, yet their influence on Notch-dependent phenotypic stability remains unexplored.

1.3.2.2 Other notable pathways for MEC lineage commitment

The Wnt pathway plays a critical role in various biological processes, including cell growth and differentiation, embryonic development, tissue homeostasis, and regeneration. The pathway is named after a family of secreted proteins called Wnts that bind to cell surface receptors and activate downstream signaling events. When a Wnt ligand binds to its receptor, it activates a cascade of intracellular signaling events that ultimately lead to the stabilization and nuclear translocation of β-catenin, a transcriptional co-activator that regulates the expression of Wnt target genes [63].

In the mammary gland, the Wnt pathway is essential for the maintenance of mammary stem cells and their progeny. Activation of this pathway promotes the proliferation and self-renewal of these cells, which are responsible for the development and maintenance of the mammary gland during puberty and pregnancy. Targeting this pathway for organoid culture optimisation has been studied in [16, 20], demonstrating the 'just right' conditions sufficient for MaSC renewal for long-term culture. Moreover, evidence of antagonistic crosstalk between the Notch and Wnt pathways through β-catenin and Hes1 coupling components has been suggested to support the dichotomous cell lineage commitment in the mammary gland [64].

During mammary gland development, Fibroblast Growth Factor (FGF) signaling is involved in the regulation of cell proliferation and differentiation, as well as branching morphogenesis [65]. FGF signaling is activated by paracrine or autocrine secretion of FGF ligands from surrounding stromal cells or other epithelial cells. The binding of FGFs to FGF receptors on mammary epithelial cells leads to the activation of downstream signaling pathways, including the MAPK/ERK and PI3K/Akt pathways. Activation of these pathways can stimulate the expression of transcription factors and other molecules involved in mammary epithelial cell differentiation, such as E-cadherin and β-casein [66].

1.3.3 Motivating biological problem summary

There is increasing evidence across various biological systems, indicating that polarity not only serves as a spatial coordinator for cell-fate specification but also facilitates physical feedback loops to maintain local cell types crucial for the proper functioning of healthy tissues [36]. While existing literature suggests the existence of polarised Notch interactions supports tissue homeostasis [67–69], direct evidence of this in MECs is yet to be observed. In addition, it is well-established that tissue geometries affect mammary ductal growth [31], however, the qualitative understanding of geometric influences on cell-fate dynamics in MECs have yet to be studied both theoretically and experimentally.

Mathematical modelling of cellular processes is a powerful tool for elucidation and prediction of underlying mechanisms within the complexity of the biological system, aiding and accelerating experimental design [70]. Subsequently, we seek to understand the viability of a polarity-guided cell-fate determination and commitment mechanism in mammary organoids using mathematical models of intracellular dynamics in collective tissues. Using spatiotemporal models of mammary cell fate dynamics, we combine aim to combine two characteristic features of the mammary gland, epithelial polarity and bilayer epithelial geometries, neither of which have been previously considered in mathematical models of MEC dynamics, as reviewed in the following section. Critically, these models enable the exploration of the interplay of polarity and tissue geometry and their influence on cell-fate dynamics in developing mammary organoids from the perspective of plasticity control. Fundamentally, this study aims to isolate the role of polarity as a homeostatic plasticity control mechanism within mammary organoids for consideration in future culture innovation for improved stability in organoid maintenance.

1.4 Approaches to modelling cell-fate dynamics in developing systems

Cell-fate modelling is a well-established and highly active area of mathematical biology [71], presenting as a powerful tool for understanding and predicting the complex processes that govern cell-fate decisions, and as an important complement to experimental design. In the 1940s, Waddington's descriptions of the cell-fate choice as an epigenetic landscape of hills and branching valleys representing stable and unstable cell states, respectively [72], acted as a catalyst for mathematical descriptions of the phenomena. Modelling approaches are still evolving today as novel sources and forms of experimental data arise.

In this section, we briefly review common approaches taken when modelling cell-fate decisions at different spatial resolutions, and their applicability to mammary organoid development, as summarised in Figure 1.8. Further details on modelling MEC cell-fate determinants are provided during the introductions of the proceeding chapters in this thesis.

1.4.1 Investigations of intracellular behaviour

As indicated in Section 1.3.2, the internal processes involved in cell-fate determination are complex. Comprehensively describing the regulatory interactions of cell-fate often involves hundreds of molecules, proteins and complexes coupled in temporal cascades [73]. Therefore, to isolate key motifs of cellular behavior from these regulatory networks, simplified modelling formalisms are often employed, as reviewed in [74].

A highly constructive approach to modelling intracellular pathway dynamics is the conversion of chemical reaction networks describing protein interactions into systems of differential equations [70]. A chemical reaction network is a set of transformations involving one, or more, chemical species, where reactants are transformed into products at a specified kinetic rate. The Law of Mass Action can then be used to construct a system of ordinary differential equations (ODEs) for each chemical species [70]. Using known or proposed pathway interactions, a time-dependent ODE model be used to both quantitatively and/or qualitatively analyse intracellular behaviour to predict response to external stimuli. In particular, the dynamics of cell-fate determinants within the pathway. For example, the construction of a Notch-Wnt pathway crosstalk ODE system using mass action approaches was used to predict the existence of a MaSC niche and local cell control of MaSC fate decisions following the linear stability and bifurcation analysis [75], specifically highlighting the dominant role of Delta (Notch receptor activator) in MaSC differentiation.

However, the introduction of detailed pathway interactions increases both the number of species and parameters in the ODE models. Large dynamical systems are often inaccessible to explore using analytic methods, instead relying on numerical methods which can inhibit our understanding of the core components and features of the model that determine the observed behaviour [74]. Furthermore, quantitative analysis of ODE models of intracellular dynamics requires subcellular temporal protein dynamics data for model calibration, which is often unavailable or contains substantial amounts of noise [76, 77]. Parameter estimation can be employed through a variety of methods, such as Approximate Bayesian Computation [78], although large numbers of unknown parameters may

induce high parameter uncertainty, resulting in the loss of the predictive power of the ODE model [79, 80].

In addition to protein dynamics, intracellular pathways may involve the activation of genes, which are both discrete and inherently stochastic [81]. Derived from Molecule Collision Theory, the introduction of stochastic and discrete events into ODE descriptions of intracellular pathways is often performed using a Gillespie-type algorithm [82]. Though stochastic simulations provide a more accurate representation of the underlying biology, parameterisation and large system analysis still limit applications, specifically in the scalability of stochastic simulations [74].

A commonly used alternative approach to modelling intracellular behaviour with a large number of species is describing protein interactions through Boolean networks. The system is modelled as a network of nodes or components, where each node represents a pathway component and each edge represents positive (activation) or negative (inhibition) interactions between nodes. In a Boolean network, the activation or inactivation of a pathway component is described by a binary variable that is either on or off. Boolean networks present as one of the most qualitative frameworks for modelling intracellular dynamics as they only require information on component interaction structure for their analysis, yet can still describe phenomena such as oscillations, multi-stationary events, long-range correlations, switch-like behaviour stability and hysteresis as in their continuous counterparts [83]. For example, the effects of genetic mutations during EMT were analysed using a Boolean network in MECs, isolating that the activity of the genes *Zeb* and *Snail* as significant promoters of EMT during breast cancer metastasis [84].

Standard Boolean approaches neglect temporal discrepancies in interactions and the precise protein dynamics, such as degradation rates and synthesis delays, limiting physiologically relevant predictions. Subsequently, this modelling approach generates fewer parameters requiring calibration from experimental data when compared to the ODE methods. Therefore Boolean networks are often employed and analysed to supplement more detailed modelling approaches by first locating core pathway components [85], or extending through hybrid continuous-discrete methods [86].

1.4.2 Cell-fate dynamics in coupled cell systems

Though comprehensive descriptions of intracellular dynamics are useful to elucidate key pathway motifs in cell-fate decisions and plasticity, neglecting the dynamics of the local microenvironment limits applications in developmental biology where cellular communication is critical for functional coordination. The

introduction of spatial components to models of signalling pathways often comes with the loss of the complexity within the intracellular dynamics when conducting analytic investigations, producing simpler descriptions repeated in a collection of coupled cells [70].

When expanding intracellular pathway ordinary differential equation (ODE) models to encompass small cellular systems consisting of two or three cells, it is common to employ the strategy of redescribing complex systems biology models using simpler kinetics. Namely, coupling intracellular ODEs of cells that are communicating to produce a larger global system of ODEs to be analysed as a first approach to incorporating spatial dynamics within the model. These spatially reduced ODE models are particularly useful when investigating the influence of spatial connectivity on the emergence of dynamics symmetry breaking required for patterning, as analytic approaches for exploring intercellular behaviour are still viable in low-dimensional systems.

In 1996, Collier and co-authors employed and examined this spatially reduced method of intercellular dynamics to investigate Notch-Delta dynamics for cell differentiation [87]. This was the first general ODE system representing intercellular lateral-inhibition feedback and was used to highlight the divergent cell state amplification effect of lateral-inhibition. Using a two-cell coupled system of cells, the authors predicted the emergence of fine-grained patterns of Notch activation under sufficiently strong feedback, demonstrating the spatial implications of a purely temporal model using standard techniques in linear stability analysis. The predicted fine-grained patterns of Notch activation were later confirmed through numerical simulations, evidencing their robustness to boundary conditions. The simplicity and experimental agreement of this model has led to it forming the foundation of many studies examining contact-dependent lateral-inhibition dynamics (as reviewed in [88]), including this thesis, and subsequently is discussed in further detail in Chapter 2.

More recently, the pseudo-spatial methods of coupling two-cell intracellular ODE systems have been used to demonstrate the role of Hes1 as a Wnt-Notch coupling point in stem cell-fate decisions [89]. The authors demonstrate the oscillatory dynamics of Hes1, which is an indicator of stemness, are only transient in the presence of extrinsic noise. This indicates the emergence of diverging cell states in developing tissue and that the lateral-inhibition kinetics dominate local cell-fate decisions. Moreover, the activation of the Wnt pathway, namely, the accumulation of β-catenin was highlighted to prolong oscillatory periods before coupled cell divergence [89], further evidencing the leading role of Notch signalling in cell-type specification using simple coupled cell models.

A significant limitation of the coupled cell ODE representations of intracellular determinants of cell-fate is the absence of space, i.e., cell positions and geometry, which are essential factors in contact-based signalling. To fully explore the effect of spatial features in coupled cell systems and symmetry breaking, phase-field models can be used to simultaneously describe physical properties and intracellular protein distributions.

Phase-field models are commonly used to represent dynamic interfaces (cell membranes) within domains and are modelled using a continuous scalar field function which determines the phase (inside or outside the cell) at any given location in the domain, providing a smooth transition between phases [90]. The transition between phases represents the cell membranes which can be dynamically modified using partial differential equations (PDEs). The PDEs cause the phase-field to evolve over time, replacing standard fixed boundary conditions in cytosolic dynamics. Moreover, the geometries of multiple cells can be simultaneously modelled using multi-phase-field functions, enabling spatially heterogenous intercellular signalling [50].

When combining phase-fields for heterogeneous and dynamic membrane geometries with spatiotemporal Notch-Delta kinetics extended from [87], Lee demonstrated that the size of the cell plays a significant role in cell-fate decisions [50]. In particular, the variations in the contact surface area of two coupled cells induced by differences in cell volume and circularity is sufficient to promote asymmetries in cell-fate determinant, Notch, under the canonical lateral-inhibition kinetics. Critically, these results support that the geometry asymmetries which are typically a consequence of asymmetric stem cell division, promote diverging cells types. Namely, initial cell-fate decisions can be instigated at the initial stages of development. Critically, these size-dependent cell-fate decision predicted in [50] were further examined in [91], where the authors confirm the existence of size-dependent (contact area) Notch-Delta dynamics using an independent model and experimental data. However, as these phase-field descriptions of cellular geometries and intercellular signalling rely on solving systems of nested PDEs, the computational cost of these models is high when compared to the pseudo-space type ODE coupled models [92].

1.4.3 Tissue-scale cell-fate patterning

At the tissue scale, one of the most common frameworks to model autonomous patterning of cell-fate determinants involving paracrine-type signalling is reaction-diffusion (RD) equations. Introduced by Turing in 1952 in the context of pattern formation in developmental biology, the RD equations are a system of parabolic PDEs that describe the interaction and diffusion of chemicals (or

morphogens or cell-fate determinants) over a region in the tissue [93]. RD equations can be used to explore diffusion-driven bifurcations that generate spatial heterogeneity under the assumption of stable reaction kinetics. Such dynamics provide a theoretical basis for the molecular pre-patterning required in morphogenesis, for example in hair follicle formation [94], embryonic limb growth [95], and animal coat patterns [96], each driven by cell-fate choices. The theory of diffusion-driven patterning is diverse and actively growing as novel applications, computational methods and analytic approaches arise, as reviewed in [97].

As conceptualised by Wolpert in the 1960s, thresholding cell-fate determinant gradients produced by RD systems can be used to describe divergent cell-types within a tissue [95]. This is commonly referred to as the French flag model for cell type differentiation. For example, a RD system describing antagonistic protein interactions in human pluripotent stem cell colonies were used to predict differentiation from the spatial location [98]. Namely, increasing the fixed values of the Dirichlet boundaries and colony size facilitated the emergence of spotted regions of differentiated cell clusters, in agreement with the observed experimental data. These results suggest that cell-fate determination during gastrulation may be governed by intrinsic RD dynamics.

However, the diffusive formulation of RD systems is not consistent with the discrete nature of juxtacrine signalling such that there exists no direct spatial continuum extension to the lateral-inhibition kinetics for fine-grained patterning. O'Dea and King have produced approximate continuum presentations of the discrete spatial operator in lateral-inhibition feedback models for grid and hexagonal cellular domains by employing methods of multiple scales and sufficient coordinate transformations [99, 100]. Thereby facilitating the use of classical Turing analysis within discrete structures for isolating pattern modes and feedback-strength-induced heterogeneity. However, this approximate continuum formulation does not generalise to irregular cellular domains.

More recently, representing juxtacrine signal feedback through local convolutions within a continuous spatial domain has been used formalise the lateral-inhibition fine-grain patterning in the context of preserving cellular structure within the tissue, demonstrating an equivalence between discrete and continuous domains [101]. Similar to the phase-field models of cellular geometries, kernals defining cellular shapes are introduced into lateral-inhibition kinetics via convolution shift operators, extending their ODE descriptions to PDEs. In doing so, the equivalence between discrete non-uniform lattice cellular geometries and continuous domains extends the work of O'Dea and King, again facilitating classical approaches to pattern analysis such as Fourier series expansion in linear stability analysis.

1.4.4 Multiscale methods for cell-fate patterning

Multiscale modelling is used to examine the complex processes involved in the development of organisms at different levels of organisation. It integrates information from various scales, ranging from molecular and cellular interactions to tissue-level dynamics. Combining these different resolutions of interactions within a singular model is a powerful tool for investigating how microscale processes have a collective macroscale effect.

Cell-based models computationally simulate autonomous individual cells that interact within a larger tissue, each with internal processes that determine cellular behaviours such as motility, division, death, and adhesion, which can be influenced by local and global cues [102]. Cell-based modelling provides an alternative to the homogenisation approach of continuum models, allowing for cell-to-cell heterogeneity within the population and seamless coupling of physical and biochemical properties of cells. Subsequently, cell-based models have been used to investigate the subcellular processes and local intercellular interactions in a wide variety of phenomena in developmental biology [103], and in particular, breast cancer metastasis [104], lumen formation [105], and branching morphogenesis [106].

Collective cell-fate patterning during morphogenesis has also been studied using cell-based models. That is, spatially dynamic cellular properties such as proliferation, death and migration are typically excluded from tissue-scale cell-fate patterning studies of lateral-inhibition kinetics, however, neighbourhood remodelling plays a significant role in contact-dependent dynamics [102]. For example, a cell-based model with cell-fate dynamics governed by stochastic lateral-inhibition kinetics in inner mass cells showed that cell-type clusters can form from the asymmetric division of cells [107], a critical feature in the initial stages of embryogenesis. Furthermore, Thalhiem and co-authors demonstrate that coupling Wnt-Notch crosstalk kinetics with local tissue geometry, proliferation, and differentiation, initiates and sustains a stem cell niche within crypts of intestinal organoids [108]. Both demonstrate the critical role of auxiliary developmental processes in cell-fate patterning.

Cell-based modelling facilitates the study of complex emergent tissue scale behaviour from a range of physiologically relevant cellular processes at different spatial resolutions. However, these models require parameter values for cell behaviors, interactions, and environmental factors. Obtaining accurate parameter values from experimental data can be challenging, and the choice of parameters can significantly impact outcomes [102]. Additionally, parameter values obtained from one experimental system may not be directly applicable to another,

leading to uncertainties in model predictions. In addition, simulating large cell populations is computationally demanding. Though there have been recent efforts to reduce computational cost through parallelisation [109, 110], the inherently coupled intercellular interactions prevent total parallelisation, which may render methods of multi-parameter estimation impractical.

Similar to the coupled cell systems, graph-coupled dynamical systems provide an alternative approach for multiscale cell-fate modelling with large populations whilst preserving cellular identity [111]. A graph is a collection of vertices that are connected by edges, such that a cell can be represented as a vertex and if two cells are signalling to each other, an edge is drawn between them. A large-scale dynamical system can then be constructed by coupling the intracellular ODEs of cell-fate determinants using the graph edges. These systems present as a discretised PDE description of space and have been used in applications of mathematical biology for over 50 years to understand how local interactions have global effects [111].

A significant advantage of graph-coupled dynamical systems is the topological representation of space, and therefore are independent of spatial dimension allowing for immediate transitions and comparison between 2D and 3D tissue geometries that would otherwise be cumbersome using PDE descriptions. Subsequently, the edge structure of the spatial graphs plays a substantial role in manipulating intracellular dynamics. In the early in 2000s, Steward, Golubitsky and co-authors highlighted this feature by exploiting symmetries structures within graphs to isolate core dynamical motifs from nonlinear kinetics [112–114]. Critically, they showed how graph structure alone can induce chaotic, periodic and convergent non-periodic global dynamics from identical kinetics.

At a similar time, Angeli and Sontag presented how recasting intracellular kinetics as input-output (IO) systems can reduce the dimension of the dynamical systems and enable control theoretic approaches for analysing convergent cell-wise behaviour [115, 116]. We will introduce input-output systems in Chapter 2, but briefly, viewing cells within a tissue as transformers within an electric circuit, intercellular signalling is presented as information flow over the system which can be summarised using transfer functions. A system of coupled IO models is denoted as an interconnected IO system within the fields of control and electrical engineering. The authors highlight properties of the transfer functions, such as monotonicity, can be exploited to yield analytically accessible cell state stability criteria in systems with a large number of cells.

A decade later, Arcak demonstrated that intercellular lateral-inhibiton kinetics are indeed a monotone interconnected dynamical system [117]. Thereby generalising previous lattice-constrained analysis to derive dichotomous pattern

existence and stability criteria by isolating spatial and intracelullar kinetics, independent of physical geometry and number of cells within the tissue. These results were later extended to isolate specific patterns within the graph structures by deriving patterning templating methods using existing symmetry methods [118]. Critically, these interconnected representations of the cell-fate kinetics allow for the direct analytic study of spatial structure on a specific patterning observed within developing tissue due to these dimension-reducing transformations. In addition, by only requiring characteristic information for intracellular dynamics using transfer function, qualitative analysis is accessible with minimal subcellular spatiotemporal experimental data. We review these methods in detail in Chapter 2.

1.4.5 A summary of modelling approaches to cell-fate dynamics over different spatial scales

The methods of modelling individual and collective cellular behaviour discussed in this section are by no means exhaustive. However, we highlight that appreciating the spatial scale and access to appropriate data on the motivating biological process should fundamentally guide the modelling approach. Consequently, we seek to understand how tissue structure, local cell interactions, and subcellular kinetics, influence cell-fate commitment, a multiscale problem. Yet, mammary organoids are a relatively new biological system and therefore high-resolution spatiotemporal data on epithelial structure and cell-fate determinants is limited. Adopting the topological IO model formalism to study polarity-driven cell-fate patterning and stability provides spatial flexibility, which is necessary for developing tissues and enables general analytic investigations on the impact of tissue deformations on intracellular dynamics. However, current spatial representations using graphs in interconnected IO systems are static. Therefore, we supplement our analysis of polarity-guided cell-fate patterning using cell-based modelling, using the Chaste library [119] for model development. A summary of the modelling approaches discussed in this section is provided in Figure 1.8.

1.5 Thesis aims and outline

This thesis aims to qualitatively analyse the interplay of tissue architecture and cell signalling polarity in robust control of stratified cell-fate determinants in mammary organoids. We specifically aim to construct a general framework for analysing fine-grain pattern formation using low-dimensional representations of the kinetics that govern cell-fate commitment in mammary epithelial cells, independent of physical dimension, the precise intracellular kinetics and their

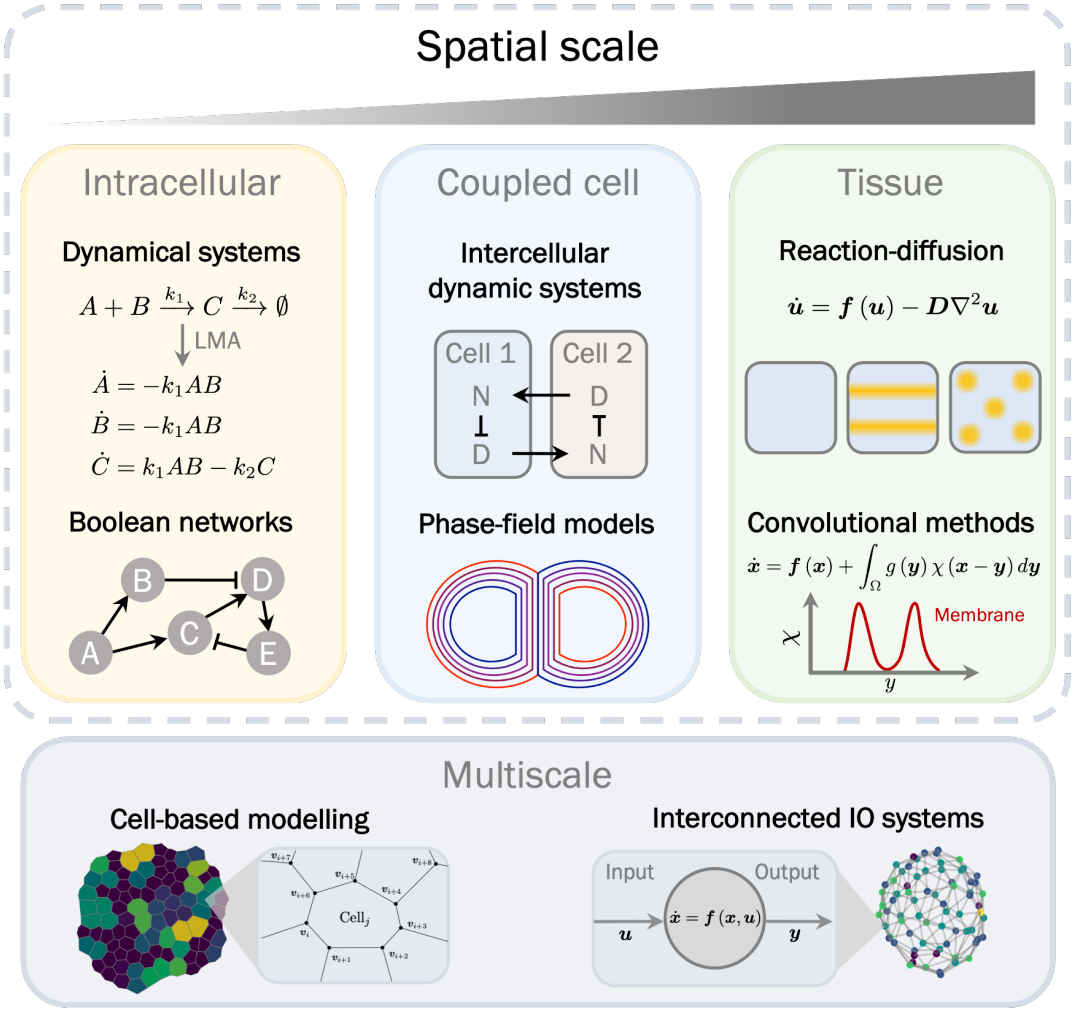

Figure 1.8: A summary of potential approaches to modelling cell-fate dynamics at different spatial scales in developmental biology.

parameterisation therein. The flexibility of the topological representation of space used in this study allows for the direct interrogation of tissue structure and signal anisotropy on intracellular dynamics which are particularly applicable to biological systems with limited access to primary data at multiple resolutions. Each chapter in this thesis builds upon the complexity of the spatial structures analysed, starting with symmetric graphs, then semi-symmetric graphs and finally multilayer semi-symmetric graphs. Though we present our results in generality, each spatial iteration sheds new light on the viability of polarity-driven cell-fate control within mammary organoids.

In Chapter 2, we introduce the fine-grain pattern templating methods as derived in [118] that generate low-dimensional representative dynamical systems by using symmetries within the spatial structure of the tissue. We extend these methods to include signal polarity by employing edge-weighted graphs to represent anisotropic cell-cell signalling in simple bilayer tissues akin to those found in mammary organoids. Using these low-dimension representations of

the intercellular dynamics, we derive necessary and sufficient conditions on the tissue structure and signalling polarity to generate laminar patterns using general lateral-inhibition kinetics. We demonstrate how to recast classical juxtacrine dynamical system models into interconnected input-output systems using the Notch-Delta lateral-inhibition model formulated in [87], thereby applying our analytic conditions to highlight the pattern generating potential of polarity in mammary bilayers for cell-fate commitment. Extending our analysis to growing bilayer domains using agent-based modelling, we highlight that our analytic bounds on the sufficient polarity required for laminar pattern stability are also sufficient to stabilise cell-fate determinants in dynamic domains.

In Chapter 3, we explore how the local geometry of the tissue affects the intracellular dynamics in mammary organoids. That is, we design and employ a curvature-connectivity image analysis pipeline to extract local cell-type dependent edge-weighted signalling graphs from confocal multiplex images of mammary organoids. Using a combination of primary and synthetic curvature and connectivity data, we generate characteristic edge topology regimes within various morphological regions of mammary organoids. To analyse the polarity-driven laminar pattern formation of cell-fate determinants in these local regions, we extend our weighted pattern templating methods to include layer-wise semi-regular bilayer graphs. We then explore the links between cross-layer connectivity asymmetries and laminar pattern stability, independent of the precise lateral-inhibition kinetics. Revisiting the Notch-Delta model from Chapter 2, we demonstrate that polarity-assisted plasticity events are more likely in highly convex regions of mammary organoids, in agreement with the underlying processes driving branching morphogenesis.

In Chapter 4, we focus on extending the polarity-driven laminar pattern analysis framework detailed in chapters 2 and 3 to include multiple spatially dependent intracellular components, broadening the scope of our methods to include pathway crosstalk and multiple signalling mechanisms. We introduce the multilayer graphical representation of polarised cell signalling for interconnected IO systems in bilayer geometries. We then provide accessible conditions for the polarity-driven cell-fate symmetry breaking with the large-scale systems. Moreover, we extend the pattern templating methods to multiple-input-multiple-output interconnected systems. Thereby, providing explicit polarity conditions for the convergence of laminar patterns in the multilayer quotient representative graphs for general induction, inhibition and mixed intracellular kinetics. We explore the links between quotient and large-scale IO system dynamics, proving the convergence of laminar patterns in the associated large-scale IO systems under sufficient polarity-connectivity conditions in generality. Finally, we extend the

control theoretic methods used to assess pattern stability in Chapter 2 to include multiple signalling mechanisms, highlighting that the effect of each signalling graph on laminar pattern stability can be assessed independently, generating no additional computational complexity when compared to single-input-single-output systems. An example of a juxtacrine and paracrine signal crosstalk system is provided throughout the chapter.

Chapter 5 includes our general conclusions, biological interpretations, and immediate and long-term directions for future research. Namely, we discuss how this study provides additional support for the core role of epithelial polarity in mammary organoid homeostasis and subsequent polarity-mediated culture innovations for stable organoid expansion.

Chapter 2

Graphical approaches to cell-fate determination by lateral-inhibition in mammary bilayers

Lateral-inhibition is considered to be a fundamental driving process for the emergence of fine-grained patterns in developing tissues [27]. At the cellular resolution, lateral-inhibition is the mechanism in which the signalling of a cell is inhibited by the increased activity in neighbouring cells. This interaction prevents the neighbouring cells from converging to the same activity state [27], producing fine-grained patterns at the tissue scale (Figure 2.1). These fine-grained patterns are critical in the development of many multicellular biological systems such as *Drosophila* eye formation [120], murine hair organisation in auditory epithelial cells [121], establishing blood vessels during human embryogenesis [122], and critically, tubulogenesis in mammary glands [48], as discussed in Section 1.1.1.

Lateral-inhibition is mediated by juxtacrine signalling, a signalling mechanism which relies on membrane-bound signal proteins on a sender cell binding to surface anchored receptors on a receiving cell, imposing a contact-dependence for cell-cell communication [27]. Critically, cells can only use juxtacrine signalling to communicate with their direct neighbours in the absence of activator/receptor extensions [123], as highlighted in Figure 2.1.

Juxtacrine signalling-dependent pattern formation has been extensively studied over the last two decades [123–127], commonly focusing on lateral-inhibition mechanisms. An overarching conclusion from the family of studies focused on juxtacrine pattern analysis of lateral-inhibition models is that linear analysis techniques in isolation are insufficient to determine precise conditions for patterning, and are only able to predict the existence of patterning [124]. In light of this, there has been a reliance on numerical simulations to elucidate parameter

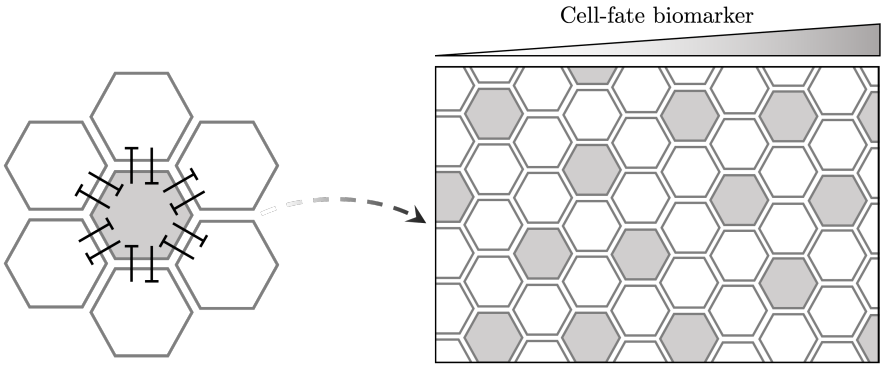

Figure 2.1: Isotropic lateral-inhibition induces 'salt and pepper' type fine-grained patterns such that the local neighbourhood of any cell is composed of an opposing biochemical state.

regimes in which patterns occur.

Intracellular kinetics are not the only factor influencing the emergence of patterns. The geometry of the cellular domain on which the juxtacrine model is being applied has a large impact on the obtainable patterning due to the cellular contact dependence of juxtacrine signalling. This was highlighted in [126] where hexagonal and four-point grid 2D domains were compared, showing considerable differences in parameter regimes required to achieve similar patterns in different domain types. Extending the numerical analysis to include irregular cellular domains, heterogeneous intracellular protein distributions, and inductive signalling, the authors present the existence of staggered travelling waves which later evolve into 'salt and pepper' patterns, as observed in *Drosophila* neuronal differentiation and wing hair formation [126]. Furthermore, when coupling a mechanism for cellular protrusions with a lateral-inhibition spatially discrete ODE system, a large family of distinct patterns is observed over a regular 2D honeycomb spatial domain. Specifically, the generation of stripes, spots and labyrinthine patterns from lateral-inhibition mechanisms, akin to those observed in Reaction-Diffusion description equipped with a continuous domain [123], evidencing the fundamental role of cellular connectivity in cell-fate determination mechanisms.

The striped patterns, referred to as laminar patterns herein, driven by lateral-inhibition mechanisms have been observed in various biological systems such as in the mammary gland and zebrafish skin pigments [21, 128]. Though to achieve laminar patterns using the lateral-inhibition model, it was demonstrated that cellular protrusions must be preferentially directed perpendicular to the active row of cells, to ensure contact with the inactivated cells and maintain their activity [123]. Critically, mammary epithelial cells (MECs) do not possess such a membrane protrusion mechanism but yet are highly polarised in their functional

differentiated states with respect to adhesions affinities [129] and proliferation [130]. These results suggest the existence of a ABP/PCP cell signalling polarity mechanism of cell-cell receptors and/or activators to generate laminar patterns using a lateral-inhibition mechanism for cell-fate determination.

As introduced in Section 1.4.4, an alternative approach to pattern formation analysis in lateral-inhibition models was introduced in [117], where cells are represented as vertices on a connected graph that interact using dynamic input-output systems, known as interconnected dynamical systems. Namely, interconnected dynamical systems are constructed from coupling ODE subsystems using networks, whereby the internal kinetics are embedded within each node. This approach generates analytic conditions for the existence and stability of 'salt and pepper' patterning in cyclic domains, independent of the size of the tissue, thus, extending the analysis conducted in [87, 124], restricted to only a few coupled cells due to the nonlinearity of the systems studied.

Moreover, the graph-theoretic approach to juxtacrine systems was later refined when graph partitioning was applied to represent patterning within collections of cells [118], generalising the previous results of [117], which developed a framework to analyse the existence and stability of a family of patterns within periodic domains with spatial symmetries. These studies emphasise the relationship between how cells are connected and the obtainable patterns, and specifically generated topological methods to study the existence of a prescribed pattern within the tissue. Nonetheless, these conditions were derived using static domains and were heavily dependent on several assumptions regarding the graph's topology (reviewed in Section 2.1.3). These assumptions cannot always be adhered to when investigating patterning on an evolving biological system, although they may be true in certain quasi-steady stages of its development where static cellular geometries may be applicable.

Mammary organoids are highly dynamic biological systems with respect to spatial movement and biochemical interactions in the early stages of development [16, 131]. During the early stages of development, MECs are capable of self-organising to form a bilayer of cells surrounding a hollow lumen presenting layer-wise contrasting Notch1 (and Dll1) expression, as discussed in Section 1.3.2.1 [49, 132]. The canonical intracellular interactions between Notch (Notch1) and Delta (Dll1) for cell-fate determination are classically used as an example of lateral-inhibition kinetics [133] and presently, it is unclear whether this spatial patterning of Notch is a consequence or cause of the morphology of developing mammary glands. There is evidence to suggest that the laminar patterning of the bilayer of cell-fate biomarkers are robust to morphological variations. Namely, the observed laminar patterning of Notch expression in the mammary gland cannot be achieved

by the canonical intracellular lateral-inhibition mechanism in isolation [49, 123], providing further evidence of an intercellular intervention in signal transfer during cell-fate determination.

Conditions defining laminar pattern formation in bilayer geometries using a simple mathematical lateral-inhibition model describing activator anisotropy have yet to be derived. Here, we apply the general interconnected systems framework to a previously developed ODE model of Notch-Delta [115] and obtain conditions on Delta cell-cell transmission that are sufficient for the bilayer laminar patterns to form in agreement with experimental observations. Specifically, we induce activator polarity within each cell by introducing layer-wise dependent edge weights to the graph representing cellular connectivity, thus describing the signal anisotropy within the network of cells. Using the layer-dependent connectivity framework, we analyse the interplay of cellular neighbourhood composition and activator polarity, independent of precise intracellular kinetics and physical dimension, for the instability of the homogeneous steady state of the large-scale dynamical system. Following properties of monotone dynamical systems, the instability of the homogeneous steady state ensures the existence of pattern formation for the given bilayer template. We then demonstrate the applicability and limitations of the analytic activator ligand polarity conditions for static domains to developing dynamic cellular networks, highlighting the requirement of adaptive control mechanisms for pattern stabilisation in evolving connectivity graphs.

This chapter is structured as follows. In Section 2.1.1 we start with a classical ODE system used to study intercellular Notch Delta interactions and demonstrate how to recast such kinetics as an interconnected dynamical system using regular connected graphs in Section 2.1.2. In Section 2.1.3 we describe methods of graph partitioning for large-scale system reduction that preserve global connectivity properties. Next, in Section 2.1.4, we review the literature from interconnected dynamical systems that we apply in this study, particularly outlining the results that allow us to derive analytic conditions on cell-type dependent weightings of Delta cell-cell transmission. In Section 2.2 we predict the existence and stability of laminar patterns in regular bilayer structures by exploiting existing results in graph theory, monotone systems and control theory [117, 118]. We apply the analytic conditions to mammary organoids in Section 2.3.2 using a Notch-Delta model (NDM), thereby employing a family of fixed regular 2D and 3D structures to investigate the role of local neighbourhood composition on laminar pattern formation. Finally, in Section 2.3.3, we use cell-based modelling to explore the role the polarity in establishing and preserving laminar pattern formation in growing bilayer domains. Critically, we show that polarity is a sufficient laminar pattern

stabilisation mechanism in quorum sensing and non-quorum sensing regimes, however, the loss of bilayer connectivity can cause pattern degradation.

2.1 Interconnected ODE systems for multicellular pattern formation by lateral-inhibition

In this section we introduce a framework to investigate the interplay of domain geometry and cellular signalling polarity in laminar pattern formation. To elucidate the dependence of cell-type transmission of Delta in bilayer structures, we consider the original lateral-inhibition ODE model constructed in [87]. By adapting the spatial averaging term to include cell-type dependent weightings on Delta transmission to represent cellular polarity, we impose signal transfer anisotropy within the cellular system to promote bilayer laminar pattern formation of Notch-Delta that are experimentally observed (figures 1.7a and 1.7b).

In addition, we introduce the graphical representation of cellular connectivity and a framework for cellular coupling. We later review the properties of the interconnected ODE system and its associated graph that are used in pattern analysis for lateral-inhibition mechanisms.

2.1.1 A Notch-Delta model of intercellular lateral-inhibition dynamics

The spatially discrete NDM developed by Collier et al. (1996) was the first explicit lateral-inhibition model that was used to investigate fine-grained patterns that are observed in a variety of biological systems [87]. The intracellular kinetics contains only two components, Notch (N) and Delta (D) activation, simplifying the underlying biochemical processes describing the cannocial cascade as discussed in Section 1.3.2.1. When studying the dynamics of Notch-Delta in the mammary organoid, we will consider N to be the NICD active protein concentration within the cytosol and D to be the amount of available membrane-bound Delta ligands on the surface of the cell, as depicted in Figure 1.6. The inverse relationship between intracellular Notch and Delta is the key feature of the spatially discrete ODE model, which is described by the negative feedback loop depicted in Figure 2.2 and thus is characterised by the following assumptions:

(i) Cells interact through Delta-Notch signalling only with cells with which they are in direct contact, that is, adhering to the juxtacrine mechanism.

(ii) The rate of production of Notch activity is an increasing function of the level of Delta activity in neighbouring cells.

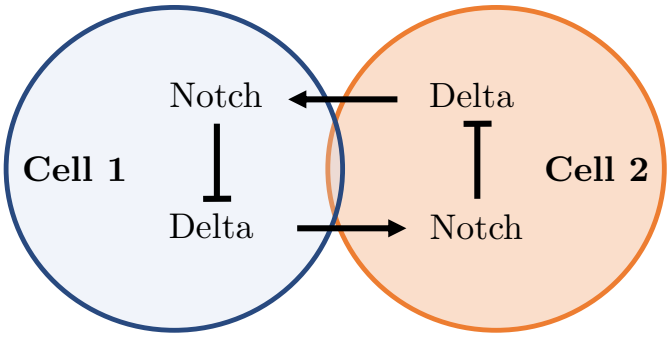

Figure 2.2: A schematic of the reduced intercellular Notch-Delta kinetics describing a generic lateral-inhibition mechanism as proposed in [87].

(iii) The rate of production of Delta activity is a decreasing function of the level of activated Notch in the same cell.

(iv) Production of Notch and Delta activity is balanced by decay, described by a simple exponential decay with fixed-rate constants.

(v) The activity of Notch and Delta are uniformly distributed throughout the cell.

(vi) There is the instantaneous transcription of downstream Notch targets, such that the model assumes no delay in Notch and Delta interactions.

These assumptions outline the Notch-Delta lateral-inhibition model, which can be formalised mathematically as

$$\dot{N}_i = \underbrace{f\left(\langle D_i \rangle\right)}_{\substack{\text{NICD activation via} \\ \text{Delta binding from} \\ \text{adjacent cells}}} - \underbrace{\mu_1 N_i}_{\substack{\text{NICD} \\ \text{degradation}}}, \tag{2.1}$$

$$\dot{D}_i = \underbrace{g\left(N_i\right)}_{\substack{\text{Delta inhibition} \\ \text{by NICD}}} - \underbrace{\mu_2 D_i}_{\substack{\text{Delta} \\ \text{degradation}}}, \tag{2.2}$$

where f and g are bounded increasing and decreasing functions respectively. These functions have the form,

$$f(x) = \frac{x^r}{\alpha + x^r} \quad \text{and} \quad g(x) = \frac{1}{1 + \beta x^s}, \tag{2.3}$$

where parameters $\alpha, \beta, \mu_1, \mu_2 > 0$ and Hill coefficients $r, s \geq 1$. The subscript i corresponds to cell identity within the system and the definition of the local spatial mechanism, $\langle D_i \rangle$, will be discussed in Section 2.1.2 to embed the NDM (2.1-2.2) system into a network of cells.

2.1.2 A graphical approach to cellular connectivity with signal anisotropy

As an initial approach to investigating the interplay of polarity and cell-cell connectivity on cell-fate determination, we consider only undirected and regular graphs representing spatial connectivity. Specifically, the undirected property follows from the symmetry of contact-dependent signalling such that all cells in contact have equal capacity to communicate. In addition, a graph is regular if all vertices have the same number of edges emanating from them, and is denoted by d-regular for d edges. This initial restriction to study regular graphs allows for the exploitation of the edge-wise symmetries present within graphs to generate quotient representations, which will later be discussed in Section 2.1.3.

To recast the NDM (2.1-2.2) as an interconnected dynamical system we represent the cell-cell communication as an undirected connected N_c-regular graph $\mathcal{G} = \mathcal{G}(V, E)$, where vertices $v \in V$ represent cells and edges $e \in E$ correspond to cellular connections, as in Figure 2.3. For any vertices v_i and v_j representing cells i and j, an edge, $e_{i,j}$, is drawn which connects v_i and v_j if these cells are signalling to each other. In the context of juxtacrine signalling, we say that $e_{i,j} \neq \emptyset$ if the cell membranes of cell i and j are in contact.

To represent the cell-type stratified bilayer structures of the mammary gland, we consider two layers of vertices separated layers of the tissue as seen in Figure 1.7. Subsequently, we represent signalling polarity by filtering the signal strength of cellular connectivity between cells i and j using nonnegative layer-wise dependent weighting coefficients $w_{i,j}$. That is, $w_{i,j} = 0$ if cells i and j are not connected. If cells i and j are connected and within the same layer then, $w_{i,j} = w_1$, and if cells i and j are connected and are in different layers then $w_{i,j} = w_2$, as highlighted in Figure 2.3. Formally,

$$w_{i,j} = \begin{cases} w_1 & \text{if } e_{i,j} \neq \emptyset \text{ and } \tau_i = \tau_j, \\ w_2 & \text{if } e_{i,j} \neq \emptyset \text{ and } \tau_i \neq \tau_j, \\ 0 & \text{if } e_{i,j} = \emptyset, \end{cases} \tag{2.4}$$

where $w_1, w_2 \in \mathbb{R}_{>0}$ and layer location of cell i is denoted by τ_i. The structure of the bilayer edge weighting is shown in Figure 2.3.

The graph $\mathcal{G}$ is considered an undirected graph such that $w_{i,j} = w_{j,i}$, due to the symmetry of the contact-dependent signalling between any two cells. The coefficients $w_{i,j}$ can be used to mediate Delta transmission between adjacent cells dependent on cell-type inducing a membrane activator anisotropy within the cellular connectivity graph and thus $w_{i,j}$ will be the focus of our study.

We introduce graph cellular connectivity to the NDM (2.1-2.2) using the associated weighted adjacency matrix of $\mathcal{G}$. We consider a system of $\mathcal{N}$ cells

such that $\mathcal{N} \in \{2n : n \in \mathbb{N}\}$ to account for bilayer regular structures, i.e., there are n cells in each layer. Then the weighted adjacency matrix of $\mathcal{G}$ is defined by $[w_{i,j}] = \boldsymbol{W} \in \mathbb{R}_{\geq 0}^{\mathcal{N}\times\mathcal{N}}$ as in [117, 118], where we have extended their formulation to include cell-type dependent edge weights.

As $\mathcal{G}$ is an undirected connected N_c-regular graph, we are assuming the lattice structures representing cellular connectivity are symmetric with respect to each layer and have periodic boundaries in 2D and 3D. Critically, both of these properties are induced by the regularity of the graph, that is, each vertex is equipped with the same number of edges and associated weights. Following from the bilayer structure of the graph $\mathcal{G}$, the associated weighted adjacency matrix $\boldsymbol{W}$ can be constructed from the matrices $\boldsymbol{W}_1, \boldsymbol{W}_2 \in \mathbb{R}_{\geq 0}^{(\mathcal{N}/2)\times(\mathcal{N}/2)}$. Namely, $\boldsymbol{W}$ has the following form,

$$\boldsymbol{W} = \begin{bmatrix} \boldsymbol{W}_1 & \boldsymbol{W}_2 \\ \boldsymbol{W}_2 & \boldsymbol{W}_1 \end{bmatrix}. \tag{2.5}$$

Here row i of $\boldsymbol{W}_1$ represents the cellular connections of cell i to adjacent cells in the same layer and the rows of $\boldsymbol{W}_2$ correspond to the cellular connections to cells of within the opposing layer, where cells indexed 1 to $\mathcal{N}/2$ in the can be considered as luminal cells and $\mathcal{N}/2 + 1$ to $\mathcal{N}$ as basal cells. For example, the standard orthogonal template for a bilayer of cells given in Figure 2.3, has connectivity matrices,

$$\boldsymbol{W}_1 = w_1 \begin{bmatrix} 0 & 1 & 0 & 0 & \cdots & 0 & 1 \\ 1 & 0 & 1 & 0 & \cdots & 0 & 0 \\ 0 & 1 & 0 & 1 & 0 & \cdots & 0 \\ \vdots & \ddots & \ddots & \ddots & \ddots & \ddots & \vdots \\ 0 & \cdots & 0 & 1 & 0 & 1 & 0 \\ 0 & 0 & \cdots & 0 & 1 & 0 & 1 \\ 1 & 0 & \cdots & 0 & 0 & 1 & 0 \end{bmatrix} \quad \text{and} \quad \boldsymbol{W}_2 = w_2 \boldsymbol{I}_{\mathcal{N}/2}, \tag{2.6}$$

where $\boldsymbol{I}_{\mathcal{N}/2}$ is the $(\mathcal{N}/2) \times (\mathcal{N}/2)$ identity matrix.

The network representation of cellular connectivity is introduced to the NDM (2.1-2.2) via the averaging operator $\langle\cdot\rangle$. Explicitly, layer-wise (or cell-type) dependent Delta transmission between adjacent cells in static geometries is described by

$$\langle \boldsymbol{D}(t) \rangle = \frac{1}{n_1 w_1 + n_2 w_2} \boldsymbol{W} \boldsymbol{D}(t), \tag{2.7}$$

where $\boldsymbol{D}(t)$ represents a vector of Delta concentrations for each cell in the system, $\boldsymbol{D}(t) = [D_1(t), ..., D_N(t)]^T$. The value n_1 corresponds to the number of cells in the same layer which is adjacent to cell i, whereas n_2 is the number of cells adjacent in the opposing layer, such that $N_c = n_1 + n_2$, for example, $n_1 = 2$ and $n_2 = 1$ in Figure 2.3. In addition, we introduce notation for the total scale weighting for each cell, $N_w = n_1 w_1 + n_2 w_2$, for brevity. The inclusion of the scaling term

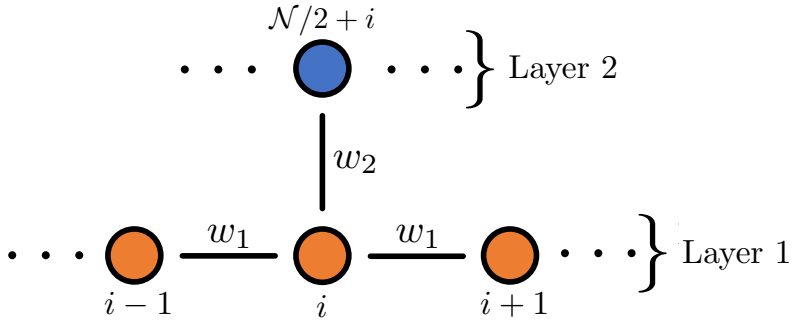

Figure 2.3: An illustrative connectivity template for cell-type dependent weighted graph structure of a bilayer $\mathcal{N}$ cells. We consider the edge structure from the perspective of cell i within a bilayer graph, where layer 1 and layer 2 vertices are coloured orange and blue, respectively. The edge weights w_1 and w_2 determine the strength of connectivity between cells in the same layer and different layers, respectively.

preserves the averaging process that is assumed for the spatially well-mixed NDM (2.1-2.2) (assumption (v)) [87], and also enables the direct comparison of cellular connectivity to a probability transition matrix of a reversible Markov chain, such that in each row $(1/N_w)\sum_j w_{i,j} = 1$ for all i, as previously discussed in [117]. Each node within the network is now equipped with the lateral-inhibition dynamics, which defines a large-scale dynamical system composed of topologically connected subsystems, thus, the establishment of equation (2.7) recasts the NDM (2.1-2.2) as an interconnected dynamical system.

By representing cells as vertices in the connected graph $\mathcal{G}$, we can now manipulate the topology of the graph to investigate parameter regimes of w_1 and w_2 producing an edge weight anisotropy, such that we obtain the desired cell-fate patterning. In this chapter, we explore a variety of regular periodic (cyclic) fixed lattices 2D and 3D to generate graphs that are shown in Figure 2.5. We assume that $e_{i,j} \neq \emptyset$ if cell j lies within a circle (or sphere) of radius ρ_c drawn around cell i where the rest length of the lattice is unitary. The circle (or sphere) can be viewed as the cell membrane to which the Notch receptors and Delta ligands are anchored. In addition, we introduce notation for the cell-type ratio for each cell, which is defined as,

$$R_\tau = \frac{\#\text{ of adjacent cells of the same cell-type}}{\#\text{ of adjacent cells of a different cell-type}} = \frac{n_1}{n_2}, \tag{2.8}$$

due to the symmetry of the domains (regular undirected graphs), R_τ is homogeneous for all cells in the system for the given connectivity graph $\mathcal{G}$. We chose three representative lattice structures in this study: (1) grid, (2) triangulated and (3) overlapped grid, to characterise the quasi-steady cellular configurations that may occur during the development of mammary organoids.

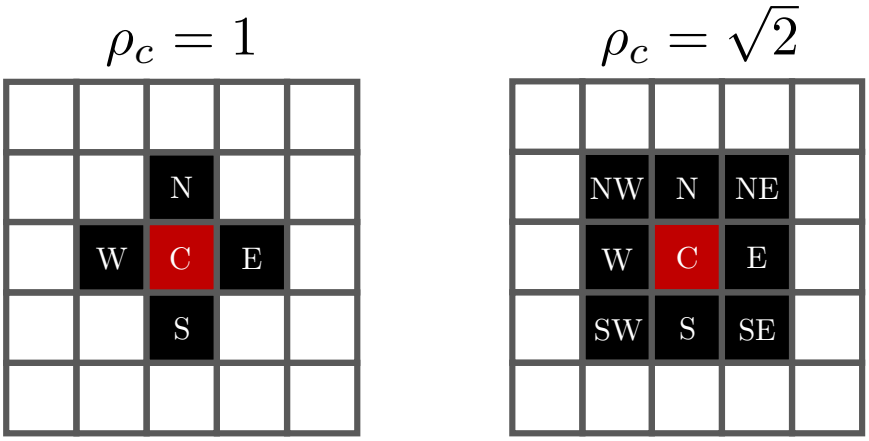

(a) VN connectivity. (b) Moore connectivity.

Figure 2.4: A diagram of the cellular neighbourhoods defined by (a) Von Neumann and (b) Moore on an unitary static grid lattice.

We then increase the connectivity radius, ρ_c, to obtain different neighbourhoods around each cell.

For example, when considering a unitary grid lattice, we examine two common cellular neighbourhoods used within the field of Cellular Automata [134]. That is, taking $\rho_c = 1$ yields a Von Neumann neighbourhood, which is defined by a central node, surrounded by 4 other nodes in the north, east, south and west directions (Figure 2.4a) [135]. Whereas increasing the connectivity spheres radius such that $\rho_c = \sqrt{2}$, we obtain a Moore neighbourhood, that includes the diagonal nodes missing from the Von Neumann neighbourhood (Figure 2.4b) [135].

Illustrations of the various 2D and 3D bilayer geometries explored in both analytical and numerical investigations for laminar pattern formation in mammary organoids are given in Figure 2.5 with a summary of the graph properties given in Table 2.1.

In this section, we recast the classical NDM (2.1-2.2) into an interconnected dynamical system using layer-wise dependent weighted graphs and outlined the specific edge structures we consider in our computations. This enables the analysis of cellular connectivity structure coupled to the intracellular kinetics in large-scale systems, providing a general approach to intercellular interactions. In the following section, we discuss methods of reducing the dimensionality of large-scale systems, whilst preserving the connectivity structure and thus the behaviour of the dynamical systems.

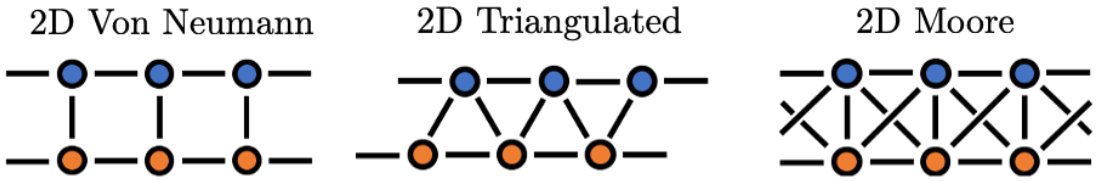

(a) Example bilayer graphs for 2D geometries.

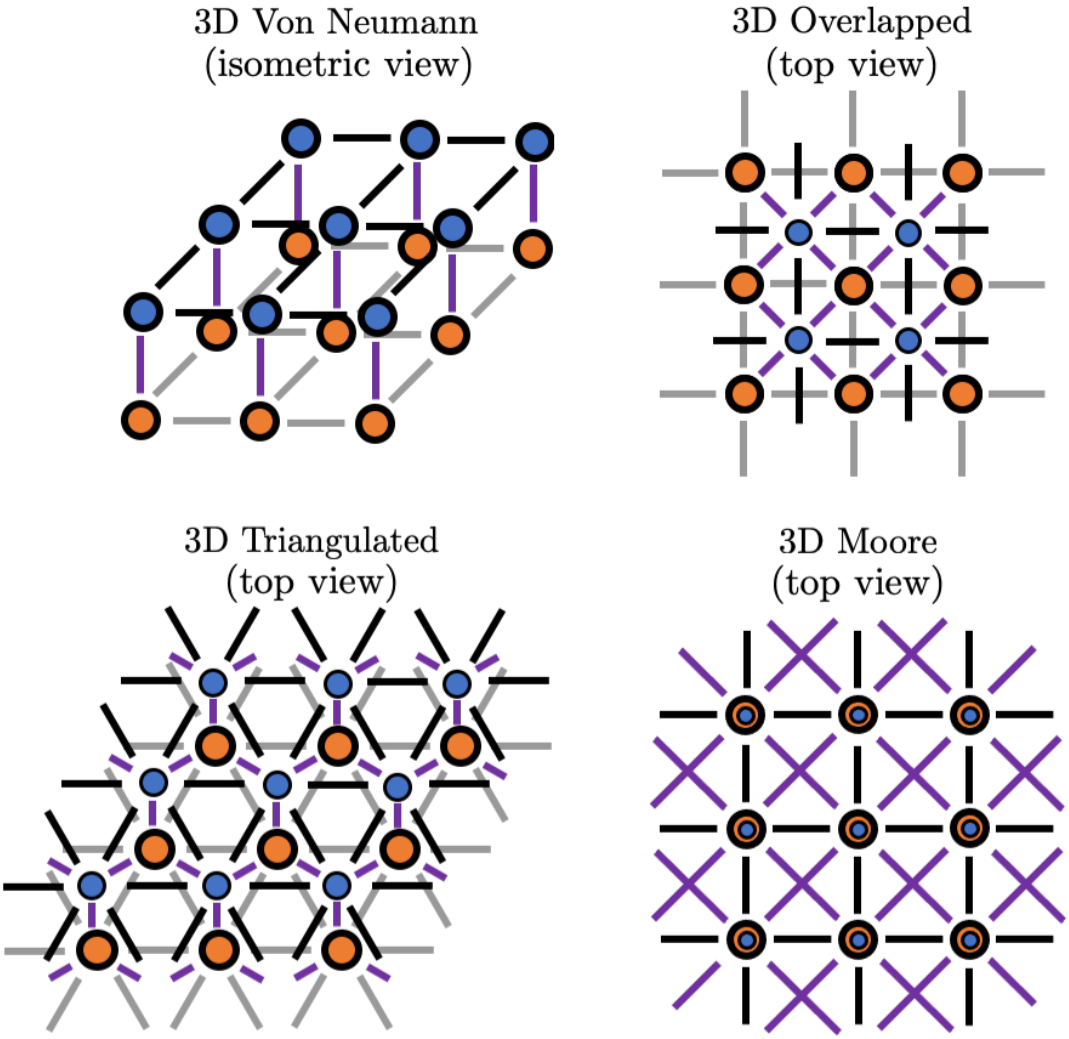

(b) Example bilayer graphs for 3D geometries.

Figure 2.5: Connectivity diagrams of the bilayer mammary organoid. Layer 1 cells are shaded orange and layer 2 cells are shaded blue. (a) Representative diagrams of 2D geometries studied, solid black lines correspond to cellular connections. (b) Schematics of 3D lattices, grey lines correspond to connections between layer 1 cells, black lines are connections between layer 2 cells and purple lines represent connections between the layers.

Lattice type	Connectivity radius, ρ_c	Cellular connectivity, N_c	Layer-wise ratio, R_τ
2D Von Neumann (2DVN)	1	3	2
2D Triangulated (2DT)	1	4	1
2D Moore (2DM)	$\sqrt{2}$	5	2/3
3D Von Neumann (3DVM)	1	5	4
3D Overlapped (3DO1)	1	8	1
3D Triangulated (3DT)	1	9	2
3D Overlapped (3DO2)	$\sqrt{2}$	12	2
3D Moore (3DM)	$\sqrt{2}$	13	8/5

Table 2.1: A summary of the lattice geometries in 2D and 3D that can be found in Figure 2.5 outlining the cellular neighbourhoods.

2.1.3 Graph partitioning for large-scale system dimension reduction

This study applies the pattern analysis framework of Ferreira and Arcak to edge weight anisotropic bilayer graphs. Specifically, the symmetries of the cellular connectivity graph $\mathcal{G} = \mathcal{G}(V, E)$ were used to develop analytical conditions for the existence and stability of inhomogeneous steady states in lateral-inhibition ODE models independent of the precise tissue geometry [118]. These methods were employed by considering contrasting pattern states of cells as partitions of the graph which can be viewed as a prescribed pattern template. A graph partition π is the grouping of vertices $v \in V$ into the sets $P_i \subseteq V$ such that the subsets P_i are disjoint [136]. For example, each cell in $\mathcal{G}$, represented by a vertex $v \in V$, can be collected into a set that converges to the same biochemical state, thus producing subsets of V defining the graph partition π (Figure 2.6a). Using graph partitions, we define two additional properties that are key for the analysis conducted in [117, 118] for pattern analysis in large-scale interconnected systems.

Equitable partitions are those that preserve the underlying structure of a graph $\mathcal{G}$ by using the regularity (symmetries) of the edge structure such that all vertices $v_j \in P_i$ have the same number of edges with identical weights. Thereby selecting representative cells from each subset P_i we generate a quotient graph that has the potential to reduce the number of vertices in the graph whilst retaining the topology of the original connectivity. Figure 2.6a illustrates the reduction of a cell-type stratified bilayer regular graph to a quotient graph of only two representative vertices.

Definition 2.1.1 (Equitable partitions and quotient graphs [137])**.** *Let $\mathcal{G} = \mathcal{G}(V, E)$ be a graph with adjacency matrix $\boldsymbol{W}$. Consider a partition of π of $\mathcal{G}$ that allocates each vertex $v \in V$ into one of the sets $P_1, ..., P_k$. The partition π is*

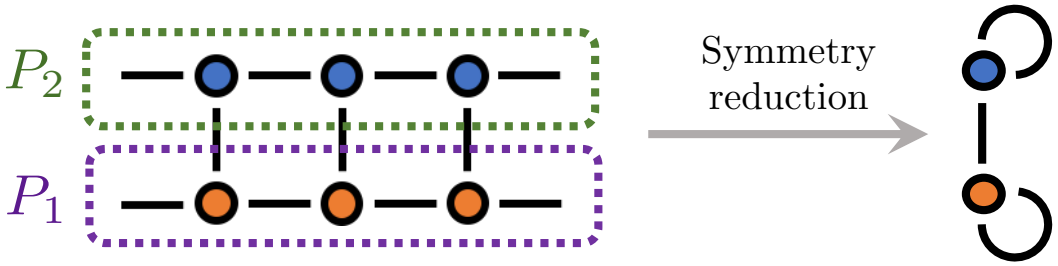

(a) Generating quotient graphs from equitable partitions.

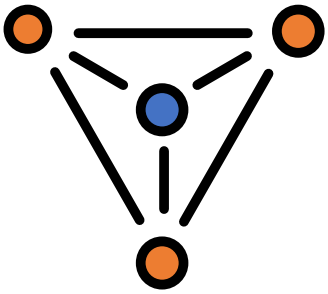

(b) An equitable graph.

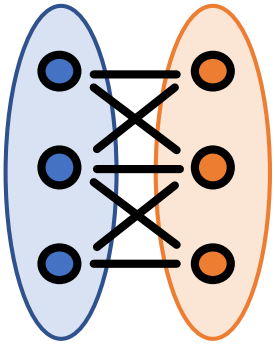

(c) A bipartite graph.

Figure 2.6: Graph partitioning, symmetry reduction and example graphs. (a) A diagram representing the partitioning and symmetry reduction process for a bilayer structure of two subpopulations representing a mammary organoid, see Section 2.1.2. The graph defining the bilayer is partitioned into layers, such that layer 1 cells lie in the partition P_1 and layer 2 cells lie in the partition P_2. By exploiting the symmetries of edge connectivity, a reduction of vertices is made to consider only representative cells from each partition, P_1 and P_1, generating a quotient graph. (b) An example graph with the equitable partitions property. The partitions are highlighted using colours, the diagram highlights that the blue node always has three connected orange nodes, and any orange node has only one blue node connected. (c) An example graph with the bipartite property. The full graph consisting of both blue and orange nodes can be decomposed into two disjoint sets of vertices highlighted by the shaded regions.

said to be equitable if there exists $\overline{w}_{ij}$ *for all* $i, j \in \{1, ..., k\}$ *such that*

$$\sum_{v \in P_j} w_{uv} = \overline{w}_{ij} \quad \forall u \in P_i, \tag{2.9}$$

where w_{ij} *are the elements of* $\boldsymbol{W}$*. Moreover, the graph of a single representative vertex from each partition* $P_1, ..., P_k$ *constructed from the reduced adjacency matrix* $[\overline{w}_{ij}] = \overline{\boldsymbol{W}}$ *is called the quotient graph and is denoted by* $\mathcal{G}/\pi = \mathcal{G}_\pi$*.*

Intuitively if π is an equitable partition of $\mathcal{G}$, then the edge structure, namely, the number of edges and associated edge weights are identical, independent of the choice of vertices in the same set P_i. An example of an equitable partition π with

two vertex sets P_1 and P_2 is given in Figure 2.6b. Furthermore, we introduce an additional graph property that is required for monotone system transformations that are discussed in the following section.

Definition 2.1.2 (Bipartite graphs [136])**.** *A graph $\mathcal{G}$ is said to be bipartite if $\mathcal{G}$ can be constructed by the union of two disjoint sets of vertices such that no vertices within the same set are connected.*

Figure 2.6c depicts an example of a bipartite graph. The bipartite property of a graph $\mathcal{G}$ need not induce the regular structure as is the case of an equitable partition however it can limit the types of connectivity possible, which may detract from the biological relevance of the connectivity graphs in large-scale systems as discussed in [117]. Although, it has been shown that the bipartite property of the quotient graph is not a restriction in the case of two distinct subpopulations [118].

To apply the results of [118] to the bilayer tissue geometries that we consider in this study, we make the following assumptions on the connectivity graphs:

(A1) There exists an equitable partition π_2 of the graph $\mathcal{G}$ that groups the vertices into two sets P_1 and P_2;

(A2) The quotient graph $\mathcal{G}_{\pi_2}$ is bipartite omitting self-loops.

The 2D and 3D bilayer structures outlined in Section 2.1.2 conform to (A1) and (A2) as we assume each layer of the N_c-regular graph is constructed from cells of the same type, for example, see Figures 2.5 and 2.6a. Critically, Ferreira et al. (2013) use (A1) and (A2) to develop methods of pattern templating, namely, using quotient graphs to generate a pre-defined pattern structure for contrasting states of representative cells [118]. Specifically, the dimension reduction from the equitable partition π acts on the scaled weighted adjacency matrix $\boldsymbol{W}_0 = (1/N_w)\boldsymbol{W}$ as constructed in Section 2.1.2 such that for two representative cells in the bilayer system, the scaled reduced adjacency matrix has the form

$$\overline{\boldsymbol{W}}_0 = \begin{bmatrix} \frac{n_1 w_1}{n_1 w_1 + n_2 w_2} & \frac{n_2 w_2}{n_1 w_1 + n_2 w_2} \\ \frac{n_2 w_2}{n_1 w_1 + n_2 w_2} & \frac{n_1 w_1}{n_1 w_1 + n_2 w_2} \end{bmatrix}, \tag{2.10}$$

following from the connectivity symmetry of $\mathcal{G}$ induced from the regular edge structure.

Informally, the reduced scaled adjacency matrix (2.10) represents the connectivity of the partitions as proportional values between representative cells from each partition, where we consider each partition to contain a single cell type (Figure 2.6a). Substituting the quotient graph for cellular connectivity into the interconnected dynamical system constructed in sections 2.1.1 and 2.1.2 generates

a quotient dynamical system, which is more amenable to deriving analytic bounds on signal polarity for laminar pattern formation. The links between the dynamics of quotient and large-scale dynamical systems are discussed in detail in Chapter 4.

We have shown that the large-scale interconnected ODE systems can be reduced to smaller, analytically tractable quotient systems for bilayer regular structures of two distinct subpopulations. In the following section, we further discuss interconnected systems in generality and existing results that leverage properties of intracellular kinetics and their associated connectivity graphs to isolate the spatial and temporal influence on pattern convergence.

2.1.4 Monotone interconnected dynamical systems

The interconnected lateral-inhibition model constructed in sections 2.1.1 and 2.1.2 can be generalised to form a single-input-single-output system (SISO), a common representation of interconnected ODEs in control theory with a single state variable connecting the respective subsystems [116]. Formally, the SISO of a lateral feedback model has the form,

$$\dot{\boldsymbol{x}}_i = \boldsymbol{f}\left(\boldsymbol{x}_i, u_i\right), \tag{2.11}$$

$$y_i = h\left(\boldsymbol{x}_i\right), \tag{2.12}$$

for each cell $i \in \{1, ..., \mathcal{N}\}$, where $\boldsymbol{x}_i \in X$ is a vector of reactants (e.g. Notch and Delta), $u_i \in U$ is the input value to each cell, determined by the discrete spatial operator $\langle\cdot\rangle$, as defined in equation (2.7). The signal output is given by $y_i \in Y$. Namely, for $\boldsymbol{u} = [u_1, ..., u_{\mathcal{N}}]^T$ and $\boldsymbol{y} = [y_1, ..., y_{\mathcal{N}}]^T$, we have that $\boldsymbol{u} = \boldsymbol{W}_0\boldsymbol{y}$. The function $\boldsymbol{f} : X \times U \to X$ defines the nonlinear dynamics of the feedback model, and $h : X \to Y$ is the function defining the relationship between the intracellular kinetics and the output signals of the cell. It is assumed that both $\boldsymbol{f}$ and h are continuously differentiable. A diagram of cell-cell lateral-inhibition interactions from the perspective of a SISO system is given in Figure 2.7.

For example, for the lateral-inhibition model defined by the NDM (2.1-2.2), we have that $\boldsymbol{x}_i = [N_i, D_i]^T$, where the internal kinetics are of the form,

$$\boldsymbol{f}\left(\left[N_i, D_i\right]^T, u_i\right) = \begin{bmatrix} f\left(u_i\right) - \mu_1 N_i \\ g\left(N_i\right) - \mu_2 D_i, \end{bmatrix} \tag{2.13}$$

for $f\left(\cdot\right)$ and $g\left(\cdot\right)$ the increasing and decreasing functions as defined in Section 2.1.1. The output signal of each cell is the current Delta value $y_i = h\left(\left[N_i, D_i\right]^T\right) = D_i$, and thus the input signal of cell i is determined by the connectivity structure of $\mathcal{G}$ such that $u_i = \left(\boldsymbol{W}_0\boldsymbol{D}\right)_i$. As we consider the input signals u_i to be composed of only a linear combination of output signals y_j from

other cells, the interconnected system defined by the NDM (2.1-2.2) is closed-loop with no external stimuli.

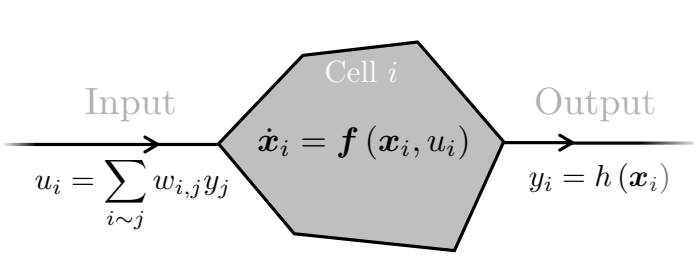

Figure 2.7: A signal flow diagram for a single cell in a SISO interconnected lateral-inhibition system. The scalar input signal u_i is determined by the output signals of the connected cells to cell i via the connectivity graph $\mathcal{G}$, namely, $i \sim j$ if cell i and cell j are in contact, where each output signal strength y_j is mediated by the edge weight $w_{i,j}$. The input signal u_i then stimulates a response from cell i which is determined by the intracellular dynamical system $\dot{\boldsymbol{x}}_i = \boldsymbol{f}(\boldsymbol{x}, u_i)$. The resultant changes to the state variables $\boldsymbol{x}_i$ update the output signals of the cell y_i thereby influencing the behaviour of those cells connected to cell i.

To summarise the internal dynamics of each cell, we introduce the characteristic transfer function $T : U \to Y$, which defines the input-to-output signal transfer of the dynamical system for each cell,

$$T(\cdot) := h(\boldsymbol{S}(\cdot)), \tag{2.14}$$

where $\boldsymbol{S} : U \to X$ maps the information from connected cells to the intracellular dynamical system (2.11). Namely, the function $\boldsymbol{S}(\cdot)$ is the solution to the intracellular dynamical system (2.11) for input signal $u \in U$. As we consider the transfer function to emulate the cellular response to receptor activation, it is assumed that $T(u_i)$ is positive and bounded, and characteristically, $T(u_i)$ is a decreasing function for lateral-inhibition and increasing for lateral-induction [117]. For the nonlinear dynamics required to produce patterning via lateral-inhibition mechanisms [138], the characteristic transfer function, $T(u_i)$, is generally algebraically intractable as it is constructed by the composition of nonlinear functions that define the intracellular kinetics [117].

Although directly intractable, we can use the standard method of linearisation to gain insights into the behaviour of the transfer function (2.14). We do not present the derivation here (see [117] for details) but it can be shown that the derivative of the transfer function (2.14) can be linearly approximated by

$$T'(u) = -\left(\frac{\partial h}{\partial \boldsymbol{x}}\right)\left(\frac{\partial \boldsymbol{f}}{\partial \boldsymbol{x}}\right)^{-1}\left(\frac{\partial \boldsymbol{f}}{\partial u}\right)\Bigg|_{\boldsymbol{x}=\boldsymbol{S}(u)} = -\boldsymbol{C}\boldsymbol{A}^{-1}\boldsymbol{B}. \tag{2.15}$$

Namely, the components $\boldsymbol{A}$, $\boldsymbol{B}$ and $\boldsymbol{C}$ form the linearised SISO system

$$\dot{\boldsymbol{x}}_i = \boldsymbol{A}\boldsymbol{x}_i + \boldsymbol{B}u_i, \tag{2.16}$$

$$y_i = \boldsymbol{C}\boldsymbol{x}_i, \tag{2.17}$$

near steady states in the input, output and internal spaces U, Y and $\boldsymbol{X}$ respectively such that the linearised components are evaluated with respect to a given input u_s by

$$\boldsymbol{A} = \left(\frac{\partial \boldsymbol{f}}{\partial \boldsymbol{x}}\right)\Big|_{\boldsymbol{x}=\boldsymbol{S}(u_s)} \quad \boldsymbol{B} = \left(\frac{\partial \boldsymbol{f}}{\partial u}\right)\Big|_{\boldsymbol{x}=\boldsymbol{S}(u_s)} \quad \boldsymbol{C} = \left(\frac{\partial h}{\partial \boldsymbol{x}}\right)\Big|_{\boldsymbol{x}=\boldsymbol{S}(u_s)}. \tag{2.18}$$

A key property of SISO lateral-inhibition models is the monotonicity of the transfer function $T(u_i)$. Monotone interconnected systems preserve the order of trajectories within respective nonempty subsets of Banach spaces [115]. Namely, if $\boldsymbol{\phi}(\boldsymbol{x^*}, t) = \boldsymbol{\phi}_t(\boldsymbol{x}^*)$, is a solution to a monotone dynamical system with initial condition $\boldsymbol{x}^*$, then $\boldsymbol{\phi}_t(\boldsymbol{x}_1) \leq \boldsymbol{\phi}_t(\boldsymbol{x}_2)$ for all $\boldsymbol{x}_1 \leq \boldsymbol{x}_2$ and $t \in (0, \infty]$, where $\leq$ is considered element-wise. However, to formally define the ordering of solutions for interconnected systems, we first need to introduce the spaces that the input, output and internal kinetics lie in, denoted as trajectory spaces [115].

The trajectory spaces, $K \subset \mathbb{R}^n$, we consider are extended orthants in Euclidean space which have the following properties:

1. K is a cone, that is, $\alpha k \in K$ for all $\alpha \in \mathbb{R}_{\geq 0}$ and $k \in K$.

2. K is convex, for any $\alpha, \beta \in \mathbb{R}_{\geq 0}$ and $k_1, k_2 \in K$ then $\alpha k_1 + \beta k_2 \in K$.

3. K is pointed, namely, $\{0\} \in K$.

An example of the above properties of the trajectory space is shown in Figure 2.8. The systems we consider represent intracellular protein activation and thus always lie in the positive orthant (i.e. $\boldsymbol{x}_i, u_i, y_i \geq 0$) which conforms to the properties of the pointed, convex cone, K. However, the positivity of these cones may alter following a coordinate transformation thus requiring the general definition stated above. Given a cone K, we define partial ordering such that $\boldsymbol{x}, \hat{\boldsymbol{x}} \in K$, then $\boldsymbol{x} \leq \hat{\boldsymbol{x}}$ means that $\hat{\boldsymbol{x}} - \boldsymbol{x} \in K$ [117]. The trajectory spaces of the interconnected system (2.11-2.12) $\boldsymbol{X}, U$ and Y, can be defined as cones K^X, K^U and K^Y as they are closed and bounded vector spaces of $\mathbb{R}^n$ [115]. The formal definition of monotonicity of SISO systems (2.11-2.12) is given as follows.

Definition 2.1.3 (Monotone SISO interconnected systems [115])**.** *Given the cones K^U, K^Y, K^X for the input, output and state spaces, respectively, the I0 system $\dot{\boldsymbol{x}}_i = \boldsymbol{f}(\boldsymbol{x}, u_i)$, $y_i = h(\boldsymbol{x}_i)$ is said to be monotone if for all $i \in \{1, ..., \mathcal{N}\}$*

we have $\boldsymbol{x}_i(0) \leq \hat{\boldsymbol{x}}_i(0)$ *and* $u_i(t) \leq \hat{u}_i(t)$ *implies that the resulting solutions satisfy* $\boldsymbol{x}_i(t) \leq \hat{\boldsymbol{x}}_i(t)$ *for all* $t \geq 0$*, and the output map is such that* $\boldsymbol{x}_i \leq \hat{\boldsymbol{x}}_i$ *implies* $h(\boldsymbol{x}_i) \leq h(\hat{\boldsymbol{x}}_i)$*.*

It has previously been shown that the interconnected system defined by the NDM (2.1-2.2) is monotone with respect to the cones $K^U = \mathbb{R}_{\geq 0}$, $K^Y = \mathbb{R}_{\leq 0}$ and $K^{\boldsymbol{X}} = \{\boldsymbol{x} \in \mathbb{R}^2 : x_1 \geq 0, x_2 \leq 0\}$ [117]. These cones outline the characteristic behaviour of the lateral-inhibition mechanism such that if the input signals of Delta from adjacent cells are monotonically increasing, we expect the output signal of Delta in the receiving cell to be monotonically decreasing.

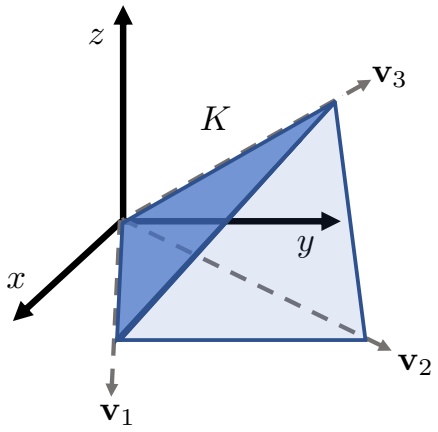

Figure 2.8: An example of a pointed, convex cone K in Euclidean space, where $K = \{\boldsymbol{x} \in \mathbb{R}^3 : \boldsymbol{x} = a_1\mathbf{v}_1 + a_2\mathbf{v}_2 + a_3\mathbf{v}_3 \ \forall a_i \in \mathbb{R}_{\geq 0}\}$.

The monotonicity of SISO systems (2.11-2.12) has previously been used to investigate the stability of component-wise steady states in biological contexts [115, 117, 118]. Namely, monotone interconnected systems yield predictable behaviour via the trajectory cones and thus the geometry of the cellular domain can be manipulated using the connectivity graph $\mathcal{G}$ to achieve the desired states for the cells.

In control theory, the stability of SISO systems (2.11-2.12) can be assessed by analysing the transition of inputs and output between components of the connected system. A particular measure of a connected system is the $\mathcal{L}_2$-gain, which is a nonnegative quantity that describes the response of a system to an input. We first provide a general definition of a $\mathcal{L}_p$-gain.

Definition 2.1.4 ($\mathcal{L}_p$-gain of a SISO system [139])**.** *The* $\mathcal{L}_p$*-gain,* $\gamma_{i,p} > 0$*, of a SISO system (2.11-2.12) is defined by*

$$\gamma_{i,p} = \sup_{t \leq \tilde{t}} \left(\frac{||y_i(t)||_p}{||u_i(t)||_p} \right) \tag{2.19}$$

for all y_i *and* $u_i \neq 0$ *for* $i = 1, ..., N$, *and* $\tilde{t} > 0$ *denotes the truncation of the Hilbert spaces for the input and outputs of the system,* $\mathcal{L}_p(U)$ *and* $\mathcal{L}_p(Y)$, *respectively.*

The $\mathcal{L}_p$-gain, $\gamma_{i,p}$, is the maximal ratio of output to input over a specified region of time for the output and input domains defined generally over Hilbert spaces. In the biological systems we consider, all functions are smooth, continuous and differentiable and thus satisfy these general conditions. However, the $\mathcal{L}_p$-gains of an interconnected system require analytic forms of inputs, $u_i(t)$, and outputs, $y_i(t)$ for each cell which are not obtainable in large-scale nonlinear systems. Although, for monotone systems such that the output map $h(\boldsymbol{x}) \geq 0$ for all $\boldsymbol{x} \in X$, we have that the $\mathcal{L}_2$-gains of a nonlinear SISO system can be approximated by

$$\gamma_{i,2} = |-\boldsymbol{C}\boldsymbol{A}^{-1}\boldsymbol{B}| = |T'(u_i^*)| \tag{2.20}$$

for the linearisation of the SISO system about the steady input state, u_i^*, as derived previously (see [140] for derivation), these properties will be discussed in further detail in Chapter 4. Critically, the output signals we consider in the biological systems represent protein activation and thus are nonnegative, i.e. we have that $h(\boldsymbol{x}) \geq 0$ for all $\boldsymbol{x} \in X$ is always satisfied. Therefore, by demonstrating a nonlinear SISO system is monotone, we have a convenient procedure to compute the $\mathcal{L}_2$-gains for each cell to measure the output signal response to input perturbations, providing a control measure of cell state stability. For the remainder of the study, we consider only the $\mathcal{L}_2$-gains for each cell as this is the standard norm for the Euclidean vector spaces, therefore we set $\gamma_{i,2} = \gamma_i$.

The $\mathcal{L}_2$-gains of interconnected SISO systems are particularly useful for understanding the stability of the feedback between the connected components. The Small Gain theorem yields a sufficient bound on two interconnected components for the global stability of feedback.

Theorem 2.1.1 (Small Gain theorem [139])**.** *For all bounded inputs, a SISO system (2.11-2.12) of two interconnected cells* c_1 *and* c_2, *in a closed-loop are locally asymptotically stable if* c_1 *and* c_2 *are independently stable and*

$$\gamma_1\gamma_2 < 1, \tag{2.21}$$

where γ_1 *and* γ_2 *are the* $\mathcal{L}_2$*-gains of* c_1 *and* c_2, *respectively.*

In terms of multicellular systems we consider, Theorem 2.1.1 states that given intracellular kinetics that are not self-exciting in isolation, i.e. $\boldsymbol{A}$ is asymptotically stable, then the interconnection of these two cells remain globally stable provided their respective gains (transfer function dynamics, $T'(u_i)$) are suitably bounded.

The application of an equitable partition π to generate a quotient graph $\mathcal{G}_\pi$ consisting of only two representative cells allows for the use of Theorem 2.1.1 in the quotient interconnected systems representing cell-type stratified bilayer geometries that we consider in this study.

We now present the results previously derived in [118] that generate and maintain binary patterns in large-scale interconnected SISO systems using the monotonicity of the lateral-inhibition mechanisms and regularity of the cellular connectivity structures via equitable partitions. The first result we consider provides a simple condition for the instability of the homogeneous steady state of the quotient interconnected SISO system. Critically, provided the SISO system (2.11-2.12) is monotone with a bounded transfer function, the instability of the homogeneous steady state yields the convergence to contrasting fixed states for each representative cell.

Theorem 2.1.2 ([118])**.** *Let π be an equitable partition of $\mathcal{G}$ such that (A2) is satisfied. Let $\overline{\lambda}_r$ the smallest eigenvalue of reduced quotient matrix associated with $\mathcal{G}_\pi$. If the input-output characteristic function, $T(u_i)$, is positive, bounded and decreasing, and if for the homogeneous input steady state, u^*, we have*

$$|T'(u^*)|\overline{\lambda}_r < -1, \tag{2.22}$$

then there exists heterogeneous steady states in the representative vertices of $\mathcal{G}_\pi$.

The second result derived in [118] that we consider defines conditions for the stability of heterogeneous steady states via $\mathcal{L}_2$-gains of the representative cells within the quotient system. By exploiting the regularity of the large-scale connectivity graph, and therefore assuming each cell within the same partition behaves identically, the $\mathcal{L}_2$-gains for those cells will also be identical. Let $\overline{\boldsymbol{\Gamma}} = \text{diag}\{\gamma_1, ..., \gamma_k\}$ represent the $\mathcal{L}_2$-gains from each representative cell in each patterning partition $P_1, ..., P_k$. In addition, if $\boldsymbol{A}$ is a square matrix with the set of eigenvalues $\sigma(\boldsymbol{A})$, then the spectral radius of $\boldsymbol{A}$ is defined by

$$\rho(\boldsymbol{A}) = \max\{|\lambda| : \lambda \in \sigma(\boldsymbol{A})\}. \tag{2.23}$$

Using the spectral properties of the connected graph defined by the cellular domain, the stability criterion for the heterogeneous steady states is stated as follows.

Theorem 2.1.3 ([118])**.** *Consider the quotient system as defined in Theorem 2.1.2. The steady state pattern defined by heterogeneous steady states is locally asymptotically stable if*

$$\rho\left(\overline{\boldsymbol{M}}\,\overline{\boldsymbol{\Gamma}}\right) < 1, \tag{2.24}$$

where $\overline{\boldsymbol{M}}$ *is a reduced quotient adjacency matrix that satisfies (A1) and (A2), and* $\rho(\cdot)$ *represents the spectral radius.*

The application of Theorem 2.1.2 and Theorem 2.1.3 to the signal anisotropic bilayer geometries defined in sections 2.1.2 and 2.1.3 allow us to derive conditions for the amount of signal polarisation for a given connectivity structure that required to generate and maintain laminar patterns using lateral-inhibition kinetics.

2.2 Existence and stability of laminar pattern formation in quotient SISO systems

In this section, we derive conditions on the cell-type signal weights w_1 and w_2 of the connectivity graphs constructed in sections 2.1.2 and 2.1.3 that yield the existence and stability of heterogeneous states in quotient bilayer systems. Specifically, by leveraging the monotone properties of the quotient SISO systems, we significantly reduce the complexity involved in juxtacrine pattern analysis in multicellular systems to investigate the role of anisotropic cellular connectivity in cell state stratification.

2.2.1 Conditions on cell-type signal strength for the existence of bilayer laminar patterns

We apply Theorem 2.1.2 to the reduced geometry of a bilayer periodic lattice described in Section 2.1.3. The following result yields a distinct monotonic relationship between same-layer and cross-layer signal weights when we consider the vertex sets P_1 and P_2 of $\mathcal{G}$ to contain layer 1 and layer 2 cells, respectively, as shown in Figure 2.6a.

Theorem 2.2.1. *Let* $\mathcal{G}$ *be an undirected, connected graph that satisfies (A1) and (A2) where the quotient graph* $\mathcal{G}_\pi$ *has the associated reduced scaled adjacency matrix as defined in (2.10). Consider* $T(\cdot)$ *the input-output transfer function of a lateral-inhibition SISO system (2.11-2.12) such that* $T(\cdot)$ *is positive, bounded and decreasing. Then there exists heterogeneous steady states between partitions* P_1 *and* P_2 *if*

$$w_1 < \left(\frac{|T'(u^*)| - 1}{|T'(u^*)| + 1}\right) \frac{w_2}{R_\tau}, \tag{2.25}$$

provided that $n_1 w_1 < n_2 w_2$.

Proof. The result follows directly from the application of Theorem 2.1.2 to the regular bilayer structures with layer stratified cells-types that define the

sets P_1 and P_2. Specifically, we consider the general quotient reduced matrix $\overline{\boldsymbol{W}}_0$ as defined in equation (2.10) and seek the smallest eigenvalue. By direct computation, we have that

$$\sigma\left(\overline{\boldsymbol{W}}_0\right) = \left\{\lambda_1 = 1, \lambda_2 = \frac{n_1 w_1 - n_2 w_2}{n_1 w_1 + n_2 w_2}\right\}. \tag{2.26}$$

As $\lambda_2 < \lambda_1$ independent of the bilayer geometry, and, we have $\lambda_2 < 0$ from the assumption that $n_1 w_1 < n_2 w_2$ then $\lambda_2 = \overline{\lambda}_r$ in Theorem 2.1.2. Applying Theorem 2.1.2 to the bilayer geometry, we substitute λ_2 into inequality (2.22) as follows

$$|T'(u^*)| \left(\frac{n_1 w_1 - n_2 w_2}{n_1 w_1 + n_2 w_2}\right) < -1, \tag{2.27}$$

which can be rearranged to yield inequality (2.25). □

Inequality (2.25) bounds the cell-type dependent signal strength and highlights the influence of cellular connectivity on pattern formation by R_τ, the cell-type ratio in the neighbourhood of any given cell. For example, as we increase the number of connected cells within the same partition (n_1) then we require greater amounts of signal polarisation (edge weight anisotropy) directed towards those cells within the other partition to induce laminar patterns, i.e. w_1 must decrease. Critically, as

$$0 < \frac{|T'(u^*)| - 1}{|T'(u^*)| + 1} < 1 \tag{2.28}$$

for all $|T'(u^*)| > 1$, then Theorem 2.2.1 indicates that $w_1 < w_2$ in all physiologically relevant spatial domains (appropriate values of R_τ) for the existence of polarity-driven laminar pattern formation. That is, preferential cross-layer signalling is required for laminar pattern existence in bilayer geometries with lateral-inhibition kinetics.

2.2.2 Conditions on cell-type signal strength for the stability of bilayer laminar patterns

Applying Theorem 2.1.3 to the geometry of the general quotient representation of the bilayer of cells (2.10) yields the following restriction on the signal polarity strength parameters, w_1 and w_2, for the stability of the heterogeneous states that are produced by Theorem 2.2.1. Namely, the following statement provides sufficient signal polarisation conditions for the maintenance of laminar pattern formation between static cells in each partition P_1 and P_2.

Theorem 2.2.2. *Let $\mathcal{G}$ be an undirected, connected graph that satisfies (A1) and (A2) where the quotient graph $\mathcal{G}_\pi$ has the associated reduced scaled adjacency matrix as defined in (2.10). Consider the $\mathcal{L}_2$-gains of the representative cells, γ_1*

and γ_2 from the partitions P_1 and P_2 associated with the heterogeneous steady states $\boldsymbol{x}_1$ and $\boldsymbol{x}_2$, respectively. Then if any of the following gain relations hold:

(i) $\gamma_1 + \gamma_2 \leq 2$

(ii) $\gamma_1 + \gamma_2 > 2 \quad \textit{and} \quad w_1 < \left(\frac{2}{\gamma_1+\gamma_2-2}\right) \frac{w_2}{R_\tau}$

then the local asymptotic stability of the heterogeneous steady states $\boldsymbol{x}_1$ and $\boldsymbol{x}_2$ is guaranteed if

$$\frac{n_1 w_1}{n_1 w_1 + n_2 w_2} \left(\gamma_1 + \gamma_2 - 2\gamma_1\gamma_2\right) < 1 - \gamma_1\gamma_2 \tag{2.29}$$

is satisfied. Moreover, if $\gamma_1 > 1$ and $\gamma_2 < 1$, or vice versa, then the laminar pattern stability criterion (2.29) has the form

$$w_1 < \left(\frac{1 - \gamma_1\gamma_2}{\gamma_1 + \gamma_2 - \gamma_1\gamma_2 - 1}\right) \frac{w_2}{R_\tau}. \tag{2.30}$$

Proof. Consider the reduced scaled weighted adjacency matrix $\overline{\boldsymbol{W}}_0$ (2.10) associated with the cell-type partitioned quotient graph $\mathcal{G}_\pi$. Let $a = n_1 w_1 / N_w$ and $b = n_2 w_2 / N_w$ and therefore we have,

$$\overline{\boldsymbol{W}}_0 \, \overline{\boldsymbol{\Gamma}} = \begin{bmatrix} a\gamma_1 & (1-a)\gamma_2 \\ (1-a)\gamma_1 & a\gamma_2 \end{bmatrix}, \tag{2.31}$$

where $b = (1 - a)$ due to the row stochastic property of the reduced adjacency matrix $\overline{\boldsymbol{W}}_0$. The matrix $\overline{\boldsymbol{W}}_0 \, \overline{\boldsymbol{\Gamma}}$ is nonnegative and irreducible as each entry is a product of positive values. By the Perron–Frobenius theorem [141], $\rho\left(\overline{\boldsymbol{W}}_0 \, \overline{\boldsymbol{\Gamma}}\right)$ is a real eigenvalue of $\overline{\boldsymbol{W}}_0 \, \overline{\boldsymbol{\Gamma}}$. Solving for the eigenvalues of $\overline{\boldsymbol{W}}_0 \, \overline{\boldsymbol{\Gamma}}$ yields

$$\rho\left(\overline{\boldsymbol{W}}_0 \, \overline{\boldsymbol{\Gamma}}\right) = \frac{a\left(\gamma_1 + \gamma_2\right)}{2} + \frac{\sqrt{a^2\left(\gamma_1 - \gamma_2\right)^2 + 4\left(1 - 2a\right)\gamma_1\gamma_2}}{2}, \tag{2.32}$$

and so by applying Theorem 2.1.3 to the spectral radius (2.32), we ensure the local asymptotic stability of the heterogeneous states associated with γ_1 and γ_2. If the necessary conditions (i) or (ii) for pattern stability are satisfied, then we have that

$$\sqrt{a^2\left(\gamma_1 - \gamma_2\right)^2 + 4(1-a)^2\gamma_1\gamma_2} < 2 - a\left(\gamma_1 + \gamma_2\right) \tag{2.33}$$

is well-defined as the leftmost term of inequality (2.33) must be real and positive by the Perron–Frobenius theorem. Namely, Theorem 2.1.3 can only be satisfied provided the conditions (i) or (ii) hold. Subsequently, both sides of inequality (2.33) are positive and therefore squaring both sides preserve the inequality, which can be expanded and rearranged as follows

$$\gamma_1\gamma_2\left((1-a)^2 - a^2\right) + a\left(\gamma_1 + \gamma_2\right) < 1 \tag{2.34}$$

which yields inequality (2.29) from further rearrangement.

In the case where $\gamma_1 > 1$ and $\gamma_2 < 1$ (or $\gamma_1 < 1$ and $\gamma_2 > 1$), then $(\gamma_1 - 1)(\gamma_2 - 1) < 0$. Moreover, this implies that

$$\gamma_1 + \gamma_2 > 1 + \gamma_1\gamma_2, \tag{2.35}$$

after expansion. In addition, inequality (2.34) can be rearranged to the following form

$$n_1 w_1 (\gamma_1 + \gamma_2 - \gamma_1\gamma_2 - 1) < (1 - \gamma_1\gamma_2)\, n_2 w_2. \tag{2.36}$$

Therefore by inequality (2.35) the left-most terms of inequality (2.36) are positive and so the division of inequality (2.36) by $(\gamma_1 + \gamma_2 - \gamma_1\gamma_2 - 1)$ preserves direction of the inequality, producing the pattern stability criterion explicitly in terms of signal weights w_1 and w_2. □

Corollary 2.2.1. *If the homogeneous steady state u^* of a monotone SISO system (2.11-2.12) yields $|T'(u^*)| \geq 3$, then the gain relation (ii) in Theorem 2.2.2 is always satisfied.*

Proof. Without loss of generality, we have that $\gamma_2 < |T'(u^*)| < \gamma_1$ as the contrasting input states u_1 and u_2 will diverge from u^* in opposing directions by the monotonicity of the SISO reduced system [118]. From inequality (2.25) we know that $1 < \gamma_1$ must hold as $w_1 \in \mathbb{R}_{\geq 0}$, that is $|T'(u^*)| > 1$ is required for the existence of laminar patterns. Therefore, if we assume that the homogeneous steady state of the monotone SISO system (2.11-2.12) is unstable, producing contrasting states in the representative cells, then inequality (2.25) is satisfied. Comparing the pattern existence inequality (2.25) and the necessary condition (ii) for pattern stability, we have that inequality (ii) holds when

$$\frac{1}{\gamma_1 - 1} < \frac{2}{\gamma_1 + \gamma_2 - 2} < \frac{|T'(u^*)| - 1}{|T'(u^*)| + 1}, \tag{2.37}$$

where the left-most term follows from $\gamma_2 < \gamma_1$. Rearranging inequality (2.37) yields

$$\frac{2|T'(u^*)|}{|T'(u^*)| - 1} < \gamma_1, \tag{2.38}$$

then applying our assumption $|T'(u^*)| < \gamma_1$, inequality (2.38) can be satisfied by solving the more restrictive bound

$$\frac{2|T'(u^*)|}{|T'(u^*)| - 1} < |T'(u^*)|, \tag{2.39}$$

which has the minimum of $|T'(u^*)| = 3$. Moreover, this implies that $\gamma_1 > 3$ which immediately satisfies $\gamma_1 + \gamma_2 > 2$, and therefore condition (ii) holds. □

Inequality (2.29) outlines the relationship between cellular connectivity (n_1, n_2) and signal protein feedback (w_1, w_2) that is required to be balanced to ensure the maintenance of pattern formation in bilayer static geometries. However, we note that the $\mathcal{L}_2$-gains are dependent on the geometry, as they are a function of the input value defined by the discrete spatial operator $\langle\cdot\rangle$, see Definition 2.1.4. Thus, inequality (2.29) cannot determine explicit conditions for the relationship between geometry and feedback model, as in the existence inequality (2.25). However, provided the $\mathcal{L}_2$-gains of the representative cells satisfy the appropriate conditions outlined in Theorem 2.2.2, inequalities (2.25) and (2.30) are in a directly comparable form with respect to signal transfer dynamics.

In addition, inequality (2.34) and therefore inequality (2.30) describes a relaxation of the Small Gain theorem for closed-loop systems, commonly used in control theory applications [142]. To demonstrate this relaxation of the Small Gain theorem, w.l.o.g. assume that $\gamma_2 < \gamma_1$, as we expect the partitions P_1 and P_2 of $\mathcal{G}$ to obtain contrasting solution states. In this case, inequality (2.34) is bounded from above by setting $\gamma_2 = \gamma_1$,

$$\gamma_1\gamma_2\left(1-2a\right)+a\left(\gamma_1+\gamma_2\right)<\gamma_1\left(\left(1-2a\right)\gamma_1+2a\right), \tag{2.40}$$

where $a = n_1 w_1 / N_w$ as in Theorem 2.2.2 and noting that $(1-2a) > 0$ from Theorem 2.2.1. Therefore if

$$\gamma_1\left(\left(1-2a\right)\gamma_1+2a\right)<1 \tag{2.41}$$

holds, then inequality (2.34) must also be satisfied. The positive parabola defined by inequality (2.41) has roots $\gamma_{1,+} = 1$ and $\gamma_{1,-} = 2a - 1 < 0$. Namely, if $\gamma_1 < 1$ then the dynamical system is locally asymptotically stable. Moreover, if $\gamma_1 < 1$ then $\gamma_1\gamma_2 < 1$, thus satisfying the Small Gain theorem (Theorem 2.1.1). As a special case of Theorem 2.2.2, if each cell in the cellular domain has no adjacent cell within the same pattern partition, namely $n_1 = 0$, then inequality (2.34) is equivalent to the Small Gain theorem, as demonstrated previously for checkerboard patterns using lateral-inhibition models (Figure 2.1) [118], highlighting the applicability of the general form of cellular connectivity defined in Section 2.1.3 to control mechanisms of lateral-inhibition systems.

2.3 Notch-Delta laminar pattern formation in mammary organoids

To illustrate the results of Section 2.2, we use the Notch-Delta lateral-inhibition model outlined in Section 2.1.1 that was recast as an interconnected dynamical

system in sections 2.1.2 and 2.1.4. Namely, we seek cell-cell signal polarity conditions between luminal and basal cells in the mammary organoid to achieve the experimentally observed laminar pattern formation of Notch in a bilayer of cells (Figure 1.7). Specifically, we use the laminar pattern existence and stability signal strength bounds derived in Section 2.2 to isolate regions of w_1 and w_2 that facilitate the aforementioned Notch patterns in quotient systems representing the family of static regular graphs described in Section 2.1.2. Furthermore, we validate the analytic regions of w_1 and w_2 using fixed lattice large-scale simulations for each graph. Furthermore, we then investigate the applicability of our static domain analytical results to dynamic cellular domains using cell-based modelling in 2D in Section 2.3.3 and in 3D in Appendix A.

2.3.1 Static lattice simulations

The 2D fixed lattice geometries were considered as a 100 cell system, split equally as luminal and basal cells as demonstrated in Figure 2.5a. This cyclic geometry generates a dynamical system of 200 state variables that were coupled via the scaled adjacency matrix $(1/N_w)\boldsymbol{W}$ as previously discussed in Section 2.1.2. Similarly, for the 3D fixed geometries in Figure 2.5b, the interconnected dynamical systems were constructed with 120 cells, producing a dynamical system with 240 state variables. For both 2D and 3D geometries, the ODE systems were solved numerically using the `ode15s` function in Matlab 2019b. The simulations were solved for 100-time units. If all solutions varied less than 1×10^{-4} over four consecutive iterations, then we assume that the system was considered to have converged to a steady state. We note that all simulations presented in this study satisfied the convergence criteria.

To determine if the system has converged to laminar patterns of Notch-Delta expression, the mean value of Delta expression was taken from each layer of cells. Explicitly, let d_j denote the mean final Delta values in each layer of cells ($j = 1, 2$). The difference $\Delta d = |d_1 - d_2|$ indicates the existence of laminar bilayer pattern formation. We considered the system to have achieved a laminar bilayer pattern if Δd was greater than a prescribed tolerance, $\delta > 0$.

The static simulation parameter sweeps for w_1 and w_2 were conducted over a discretised 150×150 regular grid lattice for $w_1 \in (0, 0.25]$ and $w_2 \in (0, 1]$, resulting in 22500 simulations per static geometry. In all static lattice simulations, we choose $\alpha = 0.01$, $\beta = 100$, $\mu_N = \mu_D = 1$, $s = 1$ and $r = 2$ as parameter values for the NDM (2.1-2.2), as previously defined [87].

2.3.2 Cell-type dependent signal anisotropy regions using a Notch-Delta lateral-inhibition model in static bilayer domains

We consider the bilayer cellular domain described by the regular graph $\mathcal{G}$ to be partitioned by layer. Namely, let π be an equitable partition of $\mathcal{G}$ such that all luminal cells are allocated in P_1 and basal cells allocated in P_2 as in Figure 2.6a. To apply both Theorem 2.2.1 and Theorem 2.2.2 to locate signal strength parameter regimes for laminar patterning, we first explicitly recast the spatially discrete ODE (2.1-2.2) in the form of a quotient SISO system (2.11-2.12). Let $\boldsymbol{x}_i = [N_i, D_i]^T$ denote the vector of state variables of the system, where i designates cellular identity. Then the input to each cell is the local spatial information received via the $\langle\cdot\rangle$ operator, such that $u_i = \langle D_i \rangle = \overline{\boldsymbol{W}}_0 \boldsymbol{D}$. Similarly, the output of each cell is the Delta expression $y_i = D_i$. To apply Theorem 2.2.1 to our biological model, we need to determine the following: (i) the derivative of the transfer function, T, of the SISO system and (ii) the homogeneous steady state, $\boldsymbol{x}^*$, of the dynamical system.

(i) The derivative of the transfer function can be derived by taking the partial derivative of the SISO system w.r.t. the input, output and state variables, as shown in equation (2.15). Thus, for NDM (2.1-2.2) as presented as an interconnected system in Section 2.1.4,

$$\frac{\partial h}{\partial \boldsymbol{x}_i} = \begin{bmatrix} 0 & 1 \end{bmatrix}, \quad \frac{\partial \boldsymbol{f}}{\partial \boldsymbol{x}_i} = \begin{bmatrix} -\mu_N & 0 \\ -\frac{\beta s N_i^{s-1}}{\left(1+\beta N_i^s\right)^2} & -\mu_D \end{bmatrix} \quad \text{and} \quad \frac{\partial \boldsymbol{f}}{\partial u_i} = \begin{bmatrix} \frac{\alpha r u_i^{r-1}}{\left(\alpha+u_i^r\right)^2} \\ 0 \end{bmatrix}. \tag{2.42}$$

Therefore, multiplying the matrices in equation (2.42) and making the substitution $N_i = f(u_i)/\mu_N$ at steady state, yields the following,

$$\begin{aligned} T'(u_i) &= -\begin{bmatrix} 0 & 1 \end{bmatrix} \begin{bmatrix} -\mu_N & 0 \\ -\frac{\beta s N_i^{s-1}}{\left(1+\beta N_i^s\right)^2} & -\mu_D \end{bmatrix}^{-1} \begin{bmatrix} \frac{\alpha r u_i^{r-1}}{\left(\alpha+u_i^r\right)^2} \\ 0 \end{bmatrix}, \\ &= -\frac{\alpha\beta r s \mu_N^s \left(\alpha+u_i^r\right)^{s-1} u_i^{rs-1}}{\mu_D \left(\mu_N^s \left(\alpha+u_i^r\right) + \beta u_i^{rs}\right)^2}. \end{aligned} \tag{2.43}$$

(ii) We now solve the NDM (2.1-2.2) for the homogeneous steady state. This problem is reduced to solving $\boldsymbol{f}(\boldsymbol{x}^*, D^*) = 0$ as $u_i^* = D_i^* = D^*$ for all $i = 1, ..., N$ in the case of a system of identical cells. Solving the system (2.1-2.2) for homogeneous steady states leads to the following polynomial for D^*,

$$\beta\mu_D \left(D^*\right)^{rs+1} + \mu_N^s \left(\mu_D D^* - 1\right)\left(\alpha + \left(D^*\right)^r\right)^s = 0. \tag{2.44}$$

To apply Theorem 2.2.1, we require that $|T'(u^*)| > 1$ as $w_1 > 0$ by definition. This condition is equivalent to the requirement derived by direct linear analysis

of a single cell as in [87], where the authors demonstrate that the existence of the homogeneous steady state instability can only occur when

$$f'(u^*)g'(N^*) < -1. \tag{2.45}$$

It can be shown that $T'(u^*) = f'(u^*)g'\left(f\left(u^*\right)/\mu_N\right)/(\mu_N\mu_D)$ for a closed-loop system of two cells [117], then applying the same parameter groupings and values for μ_N and μ_D as in [87] yields the equivalent condition. Moreover, $|T'\left(u^*\right)|$ is a monotone increasing function with respect to r (Figure 2.9), hence increasing the nonlinearity of the ODE system relaxes the restrictions on w_1 for the existence of pattern emergence imposed by Theorem 2.2.1, emphasising the relationship between the connectivity of the cells and the characteristics of the intracellular ODE system.

Solving the cubic polynomial (2.44) when $r = 2$ yields a homogeneous steady state $D^* = 0.049$, and subsequently, we have both (i) and (ii). Applying Theorem 2.2.1 to the NDM system (2.1-2.2) using equation (2.43) and D^* yields the following bound on signal strength parameters,

$$w_1 < p_{ex}\frac{w_2}{R_\tau}, \tag{2.46}$$

for $p_{ex} = \left(|T'\left(u^*\right)| - 1\right)/\left(|T'\left(u^*\right)| + 1\right) = 0.21$. Specifically, inequality (2.46) defines a strict (w_1, w_2) parameter space for the emergence of laminar patterning between layers (region below the black line in Figure 2.10b), highlighting the requirement of substantial cross-layer signal anisotropy for a polarity-driven HSS instability given the Collier NDM kinetics.

As we have found the necessary bound on w_1 for laminar pattern formation, we now seek to use Theorem 2.2.2 to impose a sufficient bound on w_1 to ensure laminar pattern stability. To apply Theorem 2.2.2, we require the $\mathcal{L}_2$-gains for each representative cell at steady state γ_1 and γ_2 from P_1 and P_2, respectively. By the monotonicity of the NDM system (2.1-2.2) with respect to the cones $K^U = \mathbb{R}_{\geq 0}$, $K^Y = -K^U$ and $K^{\boldsymbol{X}} = \{\boldsymbol{x} \in \mathbb{R}^2 | x_1 \geq 0, x_2 \leq 0\}$ [117], we are able to use the steady state relation (2.20) to compute the gains of the pattern states. To determine the $\mathcal{L}_2$-gains, we solve for the heterogeneous steady states $\boldsymbol{x}_1$ and $\boldsymbol{x}_2$, with associated input steady states

$$u_1 = \frac{n_1 w_1 D_1 + n_2 w_2 D_2}{N_w} \quad \text{and} \quad u_2 = \frac{n_1 w_1 D_2 + n_2 w_2 D_1}{N_w}, \tag{2.47}$$

then using equation (2.43), $\gamma_1 = |T'\left(u_1\right)|$ and $\gamma_2 = |T'\left(u_2\right)|$. For each static geometry outlined in Table 2.1, a parameter sweep of the signal strength parameter space (w_1, w_2) was conducted to highlight regions that satisfy the conditions (i) or (ii) and inequality (2.29) from Theorem 2.2.2, where the

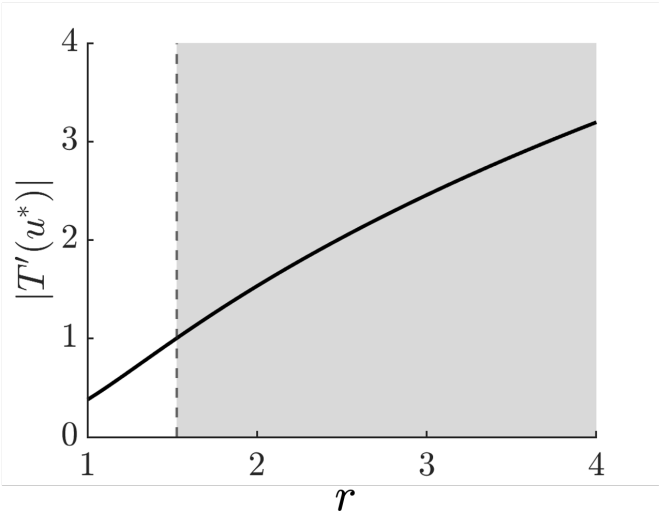

Figure 2.9: Monotonicity $|T'(u^*)|$ with respect to r. Parameter values were chosen as parameter values $\alpha = 0.01$, $\beta = 100$, $\mu_N = \mu_D = 1$ and $s = 1$. For each r, the homogeneous steady state was solved using equationEquation 2.44. The shaded region represents the values of r that satisfies $|T'(u^*)| > 1$, which is required for the instability of the homogeneous steady state in Theorem 2.2.1, highlighting a lower bound of $r_{\min} = 1.5$.

heterogeneous steady states of the representative cells $\boldsymbol{x}_1$ and $\boldsymbol{x}_2$ were numerically solved. The resulting stability regions in the (w_1, w_2)-space (red shaded regions in Figure 2.10b) have the same linear form as the analytical existence bound inequality (2.46). Therefore, assuming the same form of relationship between w_1, w_2 and R_τ, a ubiquitous gradient parameter β was extracted from each static lattice parameter sweep. That is, to ensure the local asymptotic stability of the laminar bilayer patterns (Figure 2.10a) in both 2D and 3D,

$$w_1 < p_{stab} \frac{w_2}{R_\tau} \tag{2.48}$$

must be satisfied, for $p_{stab} = 0.04$ determined using linear regression ($R^2 = 0.99$). We have provided a refinement on inequality (2.46) from necessary to sufficient for laminar pattern formation using the NDM system (2.1-2.2). Nevertheless, this defines a highly restrictive parameter bound on w_1 for the given intracellular kinetics parameters, implying that almost all cell-cell signals must be directed towards cells in the opposing later emphasising the requirement of luminal-basal layer contact.

Finally, using static lattice simulations for each of the 2D and 3D geometries described in Table 2.1 (see Section 2.3.1), we conduct a parameter sweep over the (w_1, w_2)-space to verify the necessary bound of inequality (Equation 2.46) and the sufficient bound of inequality (2.48.) Namely, the NDM system (2.1-2.2) were numerically solved for each of the connectivity graphs and allowed to converge to steady state, thereby the difference in Delta activation was measured between the

layers of cells to verify the existence of laminar patterns. The parameter regions that exhibited the layered patterning using a pattern tolerance of $\delta = 0.1$ (see Section 2.3.1) were consistent with the analytical inequalities (2.46) and (2.48) as shown in Figure 2.10 by the blue-shaded regions. Furthermore, the regions defining the observed patterns from numerical simulations had the same linear upper bound for w_1 as a function of w_2 for all 2D and 3D geometries. Therefore, as conducted for the stability inequality (2.48), we extracted a ubiquitous gradient parameter p_{obs}. Namely, laminar patterning in a bilayer of cells can be observed if w_1 satisfies,

$$w_1 < p_{obs}\frac{w_2}{R_\tau} \tag{2.49}$$

where $p_{obs} = 0.11$ is lifted from our numerical data ($R^2 = 0.99$). Note that due to the symmetry of the system, that is, each cell has identical internal kinetics that are spatially coupled by a regular and undirected graph, then to achieve the laminar patterning in the correct direction, the system required a small perturbation using initial conditions. Moreover, as the pattern tolerance $\delta \to 0$ (see Appendix 2.3.1) then $p_{obs} \to p_{ex}$, due to the contrast between the layers becoming weaker, as in Figure 2.10c. Thus the arbitrary choice of δ defines what is considered acceptable patterning, though we note that the necessary bound provided by 2.2.1 is always satisfied.

As the observed pattern regions lie within the existence bound regions ($p_{obs} < p_{ex}$) and the sufficient stability bound regions are a subset of the observed pattern regions ($p_{stab} < p_{obs}$) in (w_1, w_2)-space (Figure 2.10b), we numerically verify the analytical conditions imposed on the signal strength parameters w_1 and w_2 by Theorem 2.2.1 and Theorem 2.2.2 using the NDM system (2.1-2.2). In each case, for existence, stability and numerical observation, there exists a consistent form for the upper bound of the cell-type dependent signal strength parameter w_1, which relates cellular connectivity to signal strength polarisation, via R_τ, independent of lattice dimension.

2.3.2.1 Implications of the NDM static domain laminar pattern analysis

In summary, from the analytic and empirical upper bounds on the homotypic signal strength, w_1, outlined above reveal that the lattice geometries with the low R_τ values require less active polarisation to generate and maintain laminar patterns. For example, the 2DM lattice (see Table 2.1) has lowest neighbourhood cell-type ratio with $R_\tau = 2/3$, and therefore has the largest regions in (w_1, w_2)-space for existence, stability and observed laminar patterns (Figures 2.10b and 2.10c). In contrast, the 3DVN lattice has the largest R_τ value, thus producing

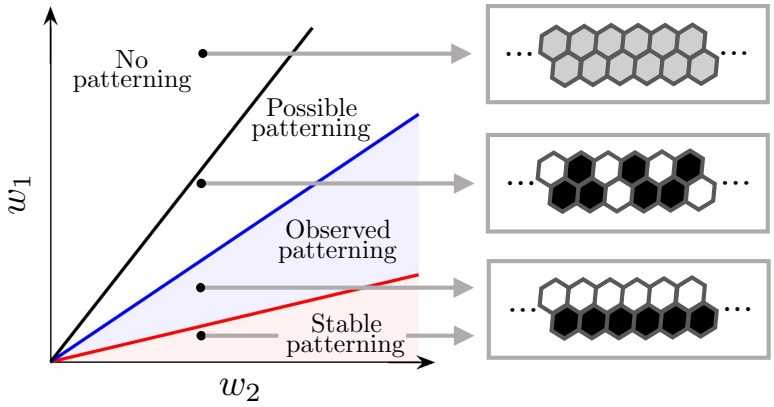

(a) Laminar pattern signal polarity regimes diagram.

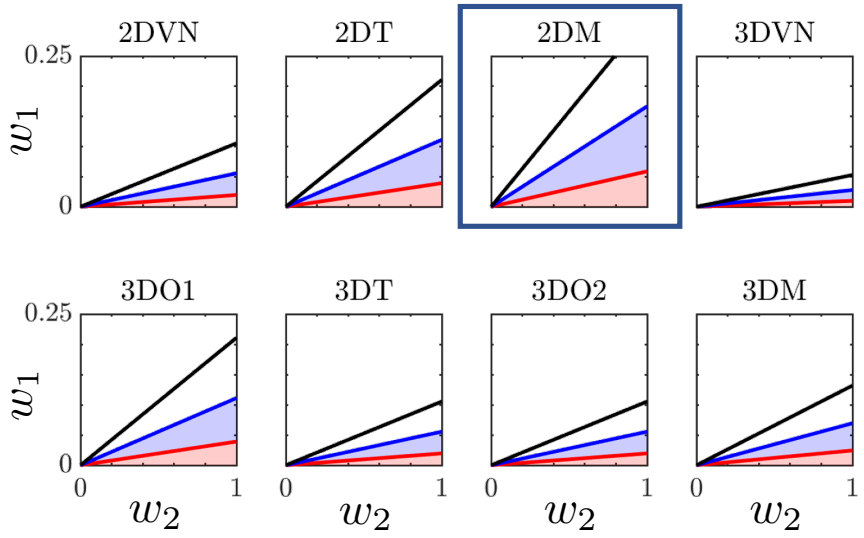

(b) Existence, stability and observed pattern regimes in 2D and 3D geometries.

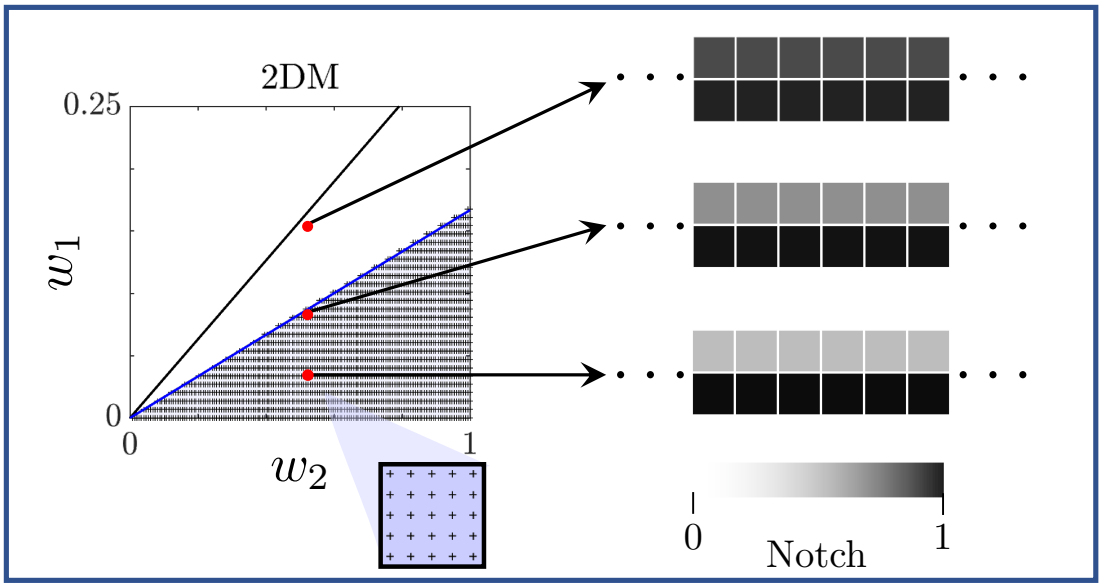

(c) Example laminar patterns for the 2DM geometry.

Figure 2.10: Cell-type dependent signal strength polarisation regions for laminar pattern formation in static bilayer geometries. (Continued on the following page.)

Figure 2.10: (Continued.) (a) The left diagram represents the (w_1, w_2) parameter space that yields conditions for bilayer laminar patterning. The region above the black line corresponds to the stability of the steady state, where the black line is the upper bound of w_1 provided by inequality (2.25) in Theorem 2.2.1. The blue line is the upper bound of w_1 determined from numerical simulations of the ODE system and the red line is the upper bound for analytical stability of the heterogeneous steady states provided by inequality (2.29) in Theorem 2.2.2. Representative patterns are embedded into the 2D Triangulated lattice. (b) (w_1, w_2) parameter space highlighting laminar pattern regions shown in (a) for each static geometry outlined in Table 2.1 with example simulation results shown in (c) using the 2DM lattice (highlighted). The magnified region of (w_1, w_2)-space demonstrates the high density of parameter values with the capacity to produce laminar patterning, denoted by +, which defines the blue observed regions in all static lattice simulations. Red points represent the parameter values used in the example simulations on the right. For further details on static simulations, see Section 2.3.1.

the smallest patterning regions and therefore a large amount of polarisation is needed to produce laminar patterns (Figure 2.10b). These findings highlight that laminar pattern formation using a lateral-inhibition mechanism is highly sensitive to neighbourhood composition of the bilayer structure, suggesting that the contrasting phenotypes of the basal and luminal cells (elongated and cuboidal shapes, respectively) may play a significant role in pattern maintenance during mammary development. Though the cell-type composition is an important factor, we found that all 2D and 3D geometries we considered required signal polarisation to achieve laminar patterning, such that $w_1 < w_2$ (Figure 2.10b), indicating the existence of a polarity mechanism within the intracellular system.

The graph partitioning methods applied here highlight the flexibility of the cellular domain in pattern formation analysis. Specifically, the only information required is the cell-type neighbourhood composition for any given cell, independent of the physical dimension. Therefore, we propose such a neighbourhood composition sensing mechanism could be used by cells to maintain the observed pattern formation in developing systems where connectivity graphs are not regular and independent of time. That is, our simplified modelling framework indicates the existence of a mechanism in which activator ligands adaptively localised to specified regions on the cell surface dependent on the cell-type composition of adjacent cells.

2.3.3 Adaptive signal anisotropy mechanisms using a Notch-Delta lateral-inhibition model in growing bilayer domains

In Section 2.3.2, analytical and numerical bounds on the polarity ratio, w_1/w_2, were derived for the existence and stability of Notch-Delta polarisation in static bilayer cell domains. Motivated by the consistency of the laminar patterning of Notch in a healthy developing mammary gland [21, 49], we explore if these static bounds can produce and maintain laminar patterns in growing bilayer domains[1]. In addition, we investigate the role of quorum sensing in polarity modulation. Quorum sensing is the process of changing the behaviour of a cell dependent on its current microenvironment using both chemical signals and mechanical cues and has been observed in mammary epithelia to influence proliferation and differentiation rates of MaSCs from local tissue densities [144]. Subsequently, we study the use of adaptive signalling polarity dependent on local cellular neighbourhood compositions as a stabilisation and energy optimisation mechanism for cell-fate determination.

2.3.3.1 Simulating growing bilayers

As an initial approach to modelling growing bilayers to explore the role of polarity in Notch pattern formation, we consider a growing monolayer of epithelial cells in 2D representing a cross-section of a mammary organoid. Namely, we simulate growing bilayer domains using a cell-based approach by implementing the vertex model (VM) framework within the Chaste (Cancer, Heart And Soft Tissue Environment) library [119, 145] as these models are able to generate heterogeneous cellular and tissue morphologies have been designed to investigate mechanochemical interactions which include short-range cell signalling [102]. Alternative cell-based modelling frameworks are also applicable to model juxtracrine signalling in spatially dynamics tissues such as the Overlapping Spheres or Voronoi Tessellation frameworks [119]. However both frameworks approximate cellular morphology which would fail to capture the contrasting phenotypes in a mammary bilayer. For a detailed review on the applicability of alternative cell-based modelling frameworks, see [102].

Cells are represented by polygons with dynamic vertices, $\boldsymbol{v}_i$, that are dependent on space and time as shown in Figure 2.11. The position of each

[1]This section of the chapter differs from the reference paper [143] as here we focus polarity-driven pattern formation on growing bilayers. For the original section which explored stochastic connectivity graphs using cell-based modelling, see Appendix A.

vertex, $\boldsymbol{v}_i$, is denoted by $\boldsymbol{r}_i$ and evolves according to first-order dynamics

$$\eta \frac{d\boldsymbol{r}_i}{dt} = \boldsymbol{F}_{i,tot}, \tag{2.50}$$

where $\boldsymbol{F}_{i,tot}$ is the total force acting on vertex i and η is the drag coefficient. We employ the Nagai-Honda (NH) energy potential model [146] for vertex forces which are composed of three parts: (1) deformation energy, (2) membrane surface tension energy, and (3) cell-cell adhesion energy, and has the form

$$\boldsymbol{F}_{i,NH} = -\nabla_i \sum_{k \in \mathcal{N}_i} \left(a \left(A_k - A_{0_k,} \right)^2 + c \left(C_k - 2\sqrt{\pi A_{0_k}} \right)^2 + \sum_{j=0}^{n_k - 1} b_{k,j} d_{k,j} \right). \tag{2.51}$$

$\mathcal{N}_i$ denotes the set of polygon indices assigned to $\boldsymbol{v}_i$. The values A_k and A_{0_k} are the current and target cell area of the polygon associated with $\boldsymbol{v}_i$. Whereas C_k is the current cell perimeter and it is assumed that the cell aims to conserve cell membrane length resulting in a circular shape. The positive coefficients a and c define the contribution of cell deformation and surface membrane tension in vertex dynamics, respectively. The final term in equation (2.51) represents differential adhesion between neighbouring cells dependent on cell-type, where n_k is the number of vertices associated with polygon k, $b_{k,j}$ is a positive constant dependent on cell-types and $d_{k,j}$ is the distance between the vertices $\boldsymbol{v}_j$ and $\boldsymbol{v}_{j+1}$ ordered anticlockwise from polygon k (Figure 2.11).

We note that the NH energy potential model is designed to describe apical cellular dynamics, specifically for tissues with constant geometry in the apical-basal axis [146]. Therefore, to employ the NH model to describe the cellular dynamics of a cross-section of a mammary organoid, that is, the apical-basal axis of the basal-luminal bilayer, we relax the model constraint for minimising energies near circular cellular geometries by increasing the deformation energy coefficient, a, see Table 2.2. Alternative energy-based models have been proposed to model apical-basal dynamics using the VM framework [147]. Namely, the authors include an additional outward normal force term to minimise the local curvature of the tissue, specifically to investigate tissue buckling from internal stress. As similar mechanical processes has been suggested to aid mammary branch initiation and lumen maintenance [131, 148], it would be interesting to incorporate this addition term into the NH model in future studies. However, we note that the apical-basal energy model proposed in [147] still considers only the apical surface of a cellular monolayer and therefore is not directly applicable here.

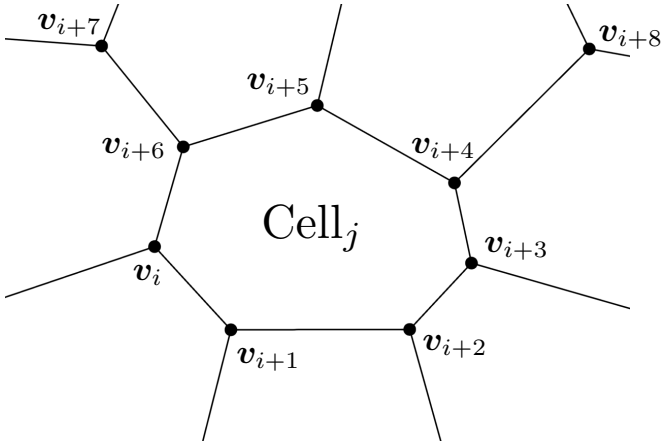

Figure 2.11: A representative cell in a VM. Each vertex is equipped with a unique identifying index and each polygon representing the cells are defined by an ordered list of vertices, for example, cell_j is given by $[v_i, ..., v_{i+6}]$. Edges are drawn between vertices that are assigned to the same polygon and are adjacent in the ordered list.

It has been demonstrated that lumen pressure is present in developing mammary organoids and that internal pressure is a factor in lumen preservation [149, 150]. Subsequently, we introduce an additional outward pressure force on each vertex which is emanating from the centre of the tissue. The lumen pressure force is assumed to decay exponentially from the centre of the tissue and therefore is given by

$$\boldsymbol{F}_{i,LP} = p_1 \frac{\boldsymbol{r}_i - \boldsymbol{c}}{||\boldsymbol{r}_i - \boldsymbol{c}||} \exp\left(-p_2 ||\boldsymbol{r}_i - \boldsymbol{c}||\right), \tag{2.52}$$

where p_1 and p_2 represent pressure force magnitude and decay, respectively, and $\boldsymbol{c}(t)$ is the position of the centre of the tissue at time t. For simplicity, we allow the pressure force (2.52) to act on all vertices to encourage outward growth away from the lumen. By selecting low values of p_1, we ensure that this force is weak relative to the active mechanical forces acting on each vertex. Similarly, choosing p_2 appropriately ensures the force acts dominantly on the interior interior vertices. We note that this force should act only on the interior vertices as this represents the initial internal fluidic pressure produced from the apoptosis of inner most luminal cells [105]. Furthermore, imposing an explicit pressure term at the interior vertices and incorporating the curvature penalisation force terms introduced in [147] may more accurately describe bilayer dynamics determined by the tight adhesion junctions formed at the apical surface of the mammary organoid, which generate the irregular MEC morphologies. As we are concerned only with Notch-Delta patterning on dynamics bilayer domains, we suggest these implementations for future studies.

In addition, we also impose stochastic movement of cells to encourage the dynamic cellular neighbourhood compositions and is implemented by the random

force

$$\boldsymbol{F}_{i,rnd} = \sqrt{\frac{2\xi}{\Delta t}}\boldsymbol{\nu}, \tag{2.53}$$

for ξ a constant defining the size of the random perturbation, Δt the simulation timestep and $\boldsymbol{\nu}$ a sample for a standard multivariate normal distribution, as previously defined in [102]. Therefore, we define the total force acting on each vertex by

$$\boldsymbol{F}_{i,tot} = \boldsymbol{F}_{i,NH} + \boldsymbol{F}_{i,LP} + \boldsymbol{F}_{i,rnd}, \tag{2.54}$$

where the mechanical dynamics governed by equation (2.50) are solved using the forward Euler method with timestep Δt [151].

To simulate growing bilayers that resemble developing mammary glands, we consider three generic cell-types: (1) boundary cells, (2) interior cells, and (3) ghost cells. The boundary cells are located on the outer ring and are equivalent to myoepithelial cells. The interior cells are located inside the boundary cells to simulate the luminal population, and the ghost cells represent the hollow lumen as shown in Figure 2.12. Mammary lumen formation is driven by an apoptotic mechanism from sustained contact with luminal cells in the absence of basal contact [105, 152] and therefore we define simple local neighbourhood rules for cell-type specification:

- Cells on the tissue boundary are boundary-type;
- Cells not on the tissue boundary are interior-type;
- Cells neighbouring six interior-type cells for over 3 time-units are ghost-type.

Ghost-type specification is terminal to represent cell death whilst maintaining lumen structure, whereas we allow for plasticity between boundary and interior types.

Boundary and interior cells are assumed to proliferate where the total cell cycle length, (T_{cycle}), is determined at the birth of the cell. The duration of the cycles for boundary and interior cells are sampled from a Gamma distribution with parameters determined by observed cycle lengths in basal and luminal subpopulations in the mammary gland [153], see Table 2.2 for cell-type dependent distribution parameters. Ghost cells are non-proliferative as they represent the lumen.

An additional measure to promote and maintain growing bilayer domains is the introduction of directed proliferation. Namely, the apical-basal polarity of the mitotic spindle in proliferating cells is critical in the development of bilayer tissues and lumen formation [105, 148, 154] such that cells divide along the tissue

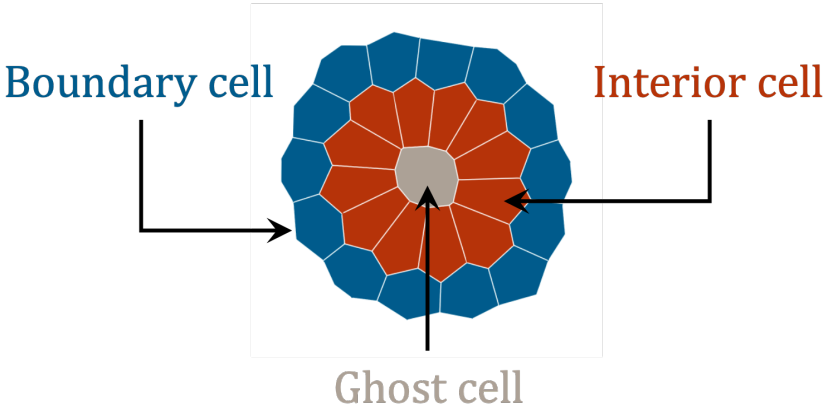

Figure 2.12: An example of the cell-type architecture during the VM growing bilayer simulations. Boundary cells representing myoepithelial/basal cells are coloured blue, interior cells representing luminal cells are coloured orange and ghost cells representing the lumen are coloured grey.

surface to prevent protrusions and lumen filling, and to encourage mechanical buckling of the tissue for branching morphologies. Therefore, upon cell division of a boundary or interior cell, the axis of division is determined by a new edge placed through the centroid of the cell which passes through the arithmetic mean of the centroids of the neighbouring cells of a different type, see Figure 2.13. Two new vertices are placed at the intersection of the division plane and the dividing cell to produce a daughter cell along the surface of the tissue.

All simulations are initialised with cells in the bilayer ring as shown in figures 2.12 and 2.14, and fixed seeds were used to generate pseudo-random numbers for stochastic spatial domains. Parameter values of the mechanical system dynamics can be found in Table 2.2.

2.3.3.2 Emergence and stability of Notch laminar patterning with fixed and adaptive polarity

Each cell in the VM is equipped with the NDM (2.1-2.2) as implemented in [102]. The method for coupling the NDM and the cell-based dynamics are as follows. At each mechanical timestep, after cell positions have been updated, the input signal Delta, u_i, is calculated using the cell-type dependent edge weighted adjacency graph defined by the tissue mesh. Then over the short time interval between the next mechanical timestep, $[n\Delta t, (n+1)\,\Delta t]$, the input signal Delta is assumed to be constant and the NDM (2.1-2.2) is updated using an adaptive Runge-Kutta scheme. This implementation scheme for coupling signalling dynamics and cell mechanics is fully contained within the Chaste software [119] and further details, see [102].

Parameter	Description	Value	Dimensions	Reference
η	Drag coefficient	1	Time (Length)$^{-1}$	[145]
a	Deformation energy coefficient	30	Force (Length)$^{-3}$	-
A_{0_b}	Target boundary cell area	0.8	(Length)^2	[155]
A_{0_i}	Target interior cell area	1	(Length)^2	[155]
A_{0_g}	Target ghost cell area	1	(Length)^2	-
c	Membrane surface energy coefficient	50	Force (Length)$^{-1}$	[102]
$b_{b,b}$	Boundary-boundary cell energy coefficient	1	Force	-
$b_{g,g}$	Ghost-ghost cell energy coefficient	1	Force	-
$b_{i,i}$	Interior-Interior cell energy coefficient	1	Force	-
$b_{i,b}$	Interior-boundary cell energy coefficient	1	Force	-
$b_{i,g}$	Interior-Ghost cell energy coefficient	1	Force	-
$b_{b,g}$	Boundary-ghost cell energy coefficient	0	Force	-
p_1	Lumen pressure magnitude coefficient	0.2	Force (Length)$^{-1}$	-
p_2	Lumen pressure decay coefficient	0.05	Non-dimensional	-
ξ	Random force coefficient	0.003	(Time)$^{-1}$(Length)^2	-
$T_{\text{cycle,b}}$	Boundary cell cycle length	$\Gamma(13.2, 1.2)$	Time	[153]
$T_{\text{cycle,i}}$	Interior cell cycle length	$\Gamma(15, 2)$	Time	[153]
Δt	Simulation timestep	0.005	Time	[102]

Table 2.2: Parameter values used in VM simulations of growing bilayers. Parameters referenced by - were selected for bilayer maintenance.

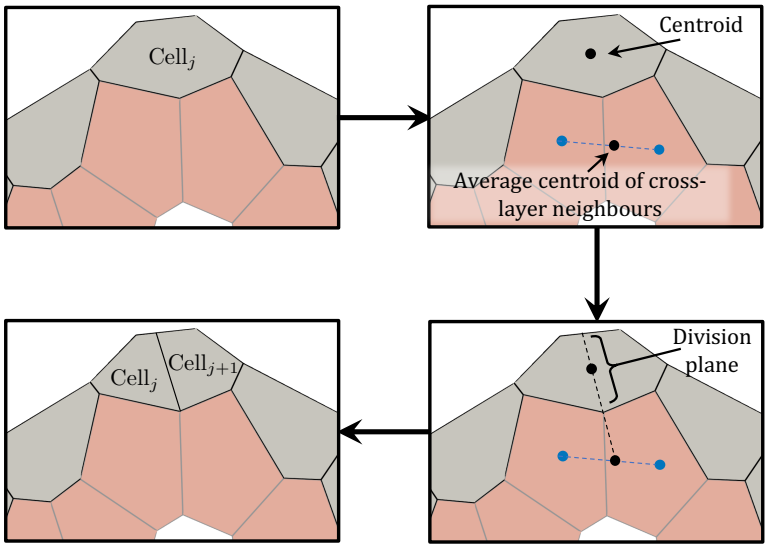

Figure 2.13: A schematic of the steps involved in the apical-basal division with respect to a dividing boundary cell. Boundary cells are coloured grey and interior cells are coloured red.

When transitioning to dynamic spatial domains, we cannot assume the preservation of layer-wise edge symmetry in the connectivity graphs during bilayer growth and consequently, we cannot apply the equitable partition theory to analyse laminar pattern formation. Instead, we use the static domain inequalities (2.48-2.49) to gain an intuition for ligand activator polarisation conditions in dynamic geometries to generate and maintain laminar patterns. In particular, we focus on how a cell responds to the microenvironment via two polarisation mechanisms: (i) globally fixed values of the polarity ratio w_1/w_2 and (ii) a locally adaptive polarity ratio w_1/w_2. By investigating these two types of signal strength mechanisms in the dynamic cellular domains, we can measure the influence of varying cellular connections on pattern stability as the system evolves.

The fixed polarity mechanism (i) is used to represent high inertia of cellular adaptability to the local environment of the cell, that is, layer-wise signal transmission strengths are defined at birth. Here, the w_1/w_2 is set to agree with the observable pattern inequality (2.49) for $R_\tau = 1$. In contrast, the adaptive (ii) polarity mechanism is used to represent low inertia of cellular response to the microenvironment. For each cell, the layer-wise polarity ratio w_1/w_2 is updated at each timestep to satisfy the observed static inequality (2.49) by determining $R_{\tau,i}$, i.e., the cell-type composition of the neighbourhood cell i.

Cell-based NDM simulations were initiated from a small bilayer structure on a hexagonal lattice and performed for 100 time units as shown in Figure 2.14. Due to the stochasticity of cell cycle lengths and imposed forces, the simulations were repeated for ten prescribed seeds of pseudo-random number generation. For each

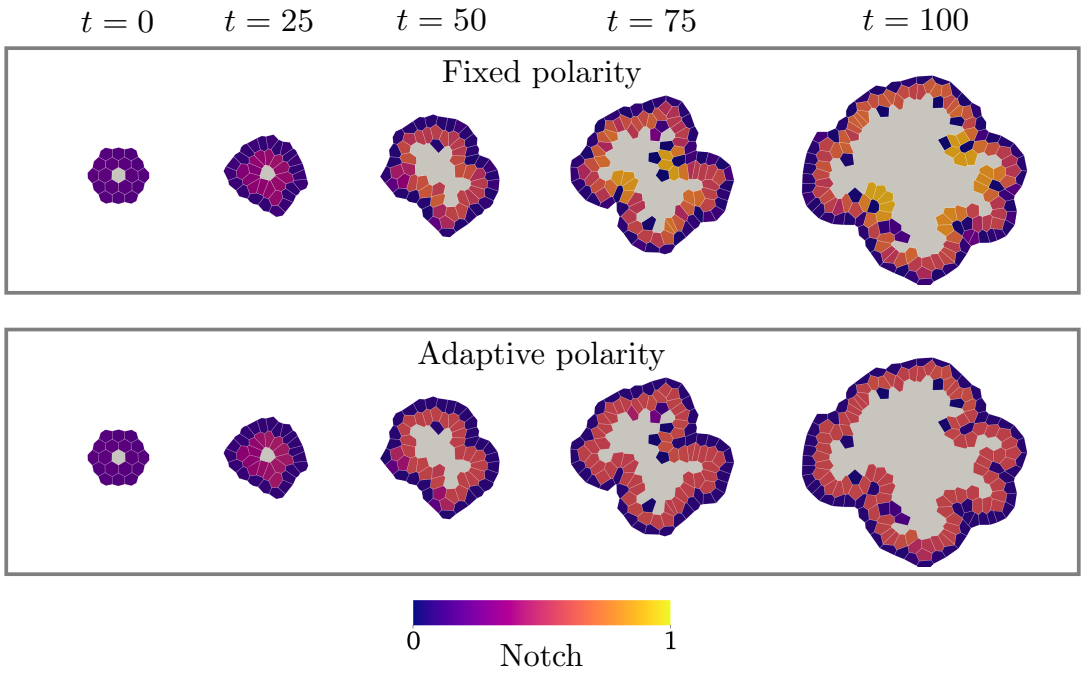

Figure 2.14: Example simulations of Notch laminar pattern formation in a growing bilayer domain with fixed and adaptive polarity mechanisms. Simulations are performed for a period of 100 time units with a fixed pseudo-random number generation seed to reproduce the spatial domains for polarity mechanism comparisons. Cells are coloured by Notch values and the grey regions represent the hollow lumen.

different growing domain geometry, the NDM (2.1-2.2) was solved using the fixed and adaptive polarity mechanism, initialised Notch and Delta values perturbed about the homogeneous steady state as in the static domain analysis in Section 2.3.2. An example of a growing bilayer domain is in Figure 2.14.

In all of the growing bilayer simulations, the polarity induced by the observable laminar pattern inequality (2.49) derived on static domains is sufficient to produce and maintain laminar patterns of Notch, independent of the polarity mechanism. This is evidenced in Figure 2.15 as the interior cells expressed a median 9-fold and 8.6-fold increase in Notch expression over the boundary cells for the fixed and adaptive mechanisms, respectively, at $t = 100$. These relative differences in Notch are comparable to those observed in mammary epithelial cells where a 9.8 to 12.3-fold increase in *Notch1* gene expression was found in luminal populations when compared to stem cell enriched basal population [49], demonstrating that Notch activator polarity is able to reproduce the same order of magnitude in differential Notch expression using a simple lateral-inhibition model. This suggests that either polarity mechanism is a potential cell-fate regulator for lateral-inhibition kinetics in mammary development.

Adaptive polarity produces homogeneous pattern states of Notch between

boundary and interior cells throughout the growth of the tissue as shown in Figure 2.14. Namely, for $t \geq 50$ there is low variance in the Notch distributions centred about the laminar pattern states, specifically in the boundary cells where neighbourhood compositions always consist of both boundary and interior cells (Figure 2.15). However, the loss of opposing cell-type connectivity in the interior subpopulation introduces Notch expression irregularities and slight variance in the Notch distributions for the interior cells, indicating that an adaptive polarity mechanism still allows for marginal subpopulation heterogeneity in Notch dynamics. In contrast, the Notch variance in the tissues using the fixed polarity is significantly greater in both the boundary and interior cells for $t \geq 50$ (Figure 2.15). In particular, tissue regions where boundary cells were highly connected to interior cells, typically located near the buckling positions, produced exaggerated Notch expression niches as shown in (Figure 2.15), suggesting that cells with a fixed layer-wise polarity mechanism are highly influenced by the local geometry of the tissue. Alternatively, the adaptive polarity mechanism presents as geometry invariant when forming laminar patterns of Notch.

When examining the polarity ratios from the adaptive mechanism simulation, Figure 2.16 highlights that overall less polarity is required to initiate and maintain laminar patterns when cells are able to actively sense their cell-type neighbourhood compositions or density and adjust their signalling accordingly than when compared to the fixed polarity simulations. Subsequently, the relaxation of the activator localisation may minimise the energy required to maintain bilayer structures whilst reducing the heterogeneity in Notch within the subpopulations, mitigating plastic behaviour during development. Furthermore, Figure 2.16 revealed that stricter polarity ratios are required in boundary cell populations to maintain patterning reflecting that boundary cells have more on average cross-layer connections than interior cells by the significant decrease in the polarity ratio, w_1/w_2. Namely, the boundary cells become elongated along the surface of the tissue due to the internal outward forces from proliferation and lumen pressure, which increases connections to the interior cells, whilst simultaneously decreasing the number of connections between interior cells to boundary cells the volume of the cell is preserved. Thus, this process may indicate that because of the wider audience, it is the boundary cells that are driving the polarisation process and therefore the laminar patterns, whilst the interior cells are reactive to their behaviour.

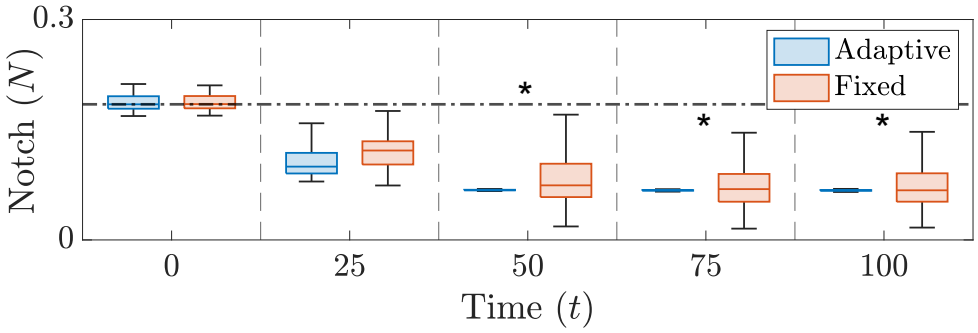

(a) Boundary cell Notch expression over time.

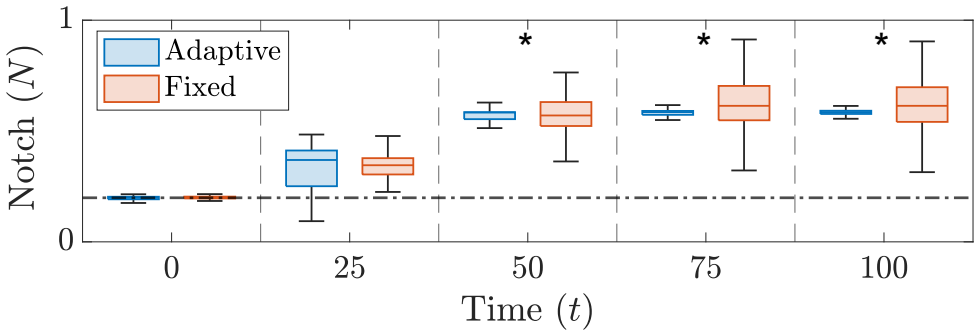

(b) Interior cell Notch expression over time.

Figure 2.15: Summary Notch values in boundary and interior cells over time using the fixed and polarity mechanisms. Box plots represent the aggregate Notch values of each (a) boundary and (b) interior cells over all growing bilayer simulations at times 0, 25, 50, 75 and 100. The horizontal dashed line represents the homogeneous steady state value of Notch, N^*. The asterisks (*) denote a significant difference in variance of Notch distributions for $p < 0.01$ using the Ansari-Bradley test.

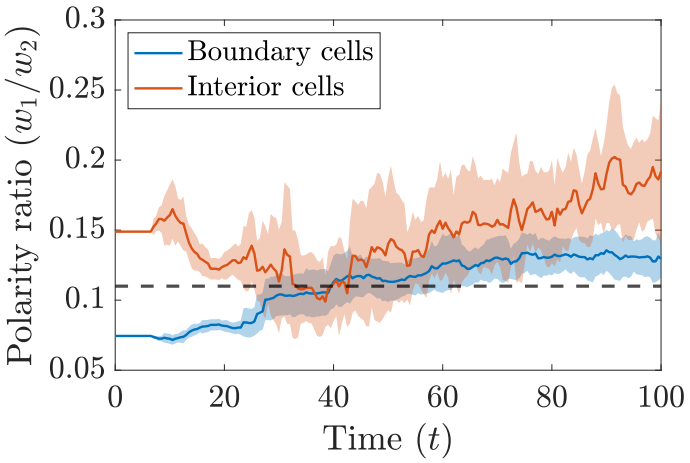

Figure 2.16: Polarity ratio values in the adaptive polarity mechanism growing bilayer VM simulations. Solid lines represent the average polarity ratio for each of the cells in all adaptive polarity simulations. Shaded regions correspond to a standard deviation about the mean and the dashed line is the polarity ratio set for all fixed polarity mechanism simulations. The dashed line represented the fixed value of the polarity ratio used in all fixed polarity simulations $w_1/w_2 = 1$.

2.4 Discussion

We have generated general conditions for exploring layer-wise dependent juxtacrine signal strength polarisation conditions for the emergence and stability of laminar patterning in symmetric bilayer structures via lateral-inhibition. Leveraging previous results of graph partitioning on monolayers, we show how the geometry of the cellular domain has a large impact on the capacity of the system to produce heterogeneity. Moreover, using this framework, we replace the algebraically demanding process of linear analysis of large multicellular systems with an exploitation of the spectral properties of the quotient graphs, therefore addressing the complexity issue discussed in previous juxtacrine pattern analysis studies [138].

In Section 2.2, we provided necessary and sufficient conditions for the existence of laminar patterns in a bilayer of cells. Both existence and stability inequalities (2.25) and (2.29) highlight that increasing connectivity with opposing cell-types allows for larger existence and stability regions in signal strength (w_1, w_2)-space. In the context of mammary organoids with fixed, as global concavity of the structure increases, luminal cells have a greater probability to connect with more basal cells, thereby relaxing the existence and stability conditions imposed by Theorem 2.2.1 and Theorem 2.2.2 by decreasing R_τ, the cell-type ratio composition in the adjacent cells. However, this would violate the symmetry between partitions required to apply both Theorem 2.2.1 and Theorem 2.2.2,

hence we propose investigating asymmetric connections between layers of cells may allow for a relationship between global curvature of the cellular structure and pattern stability.

Allowing the global connectivity graph to be semi-regular such that each of the basal and luminal subpopulations retain regular edge structure, though these structures may differ between the partitions. Subsequently, the semi-regular structures conform with the equitable partition requirement, thus enabling the analytical study of laminar pattern formation with more authentic cell-cell interactions, i.e. preserving phenotypes and subpopulation sizes, however, how connectivity changes with respect to variation in tissue morphology are yet to be investigated.

By studying a family of 2D and 3D static cellular domains of varying connectivity, we gain insight into the emergence and stability of concentric layer pattern formation in dynamic domains. Namely, by employing the bounds on w_1 derived from the static simulations, we were able to generate and maintain laminar patterns in growing bilayer domains using a classical later-inhibition model NDM (2.1-2.2). Critically, we demonstrate that applying a fixed global polarity ratio (w_1/w_2) derived by the static domain investigations is able to produce and preserve laminar patterns of Notch with rapid neighbourhood changes, highlighting the viability of polarity as a cell-fate stabilisation mechanism during the early stages of mammary organoid development. Furthermore, introducing quorum sensing for adaptive polarity further stabilises the patterning between the layers, providing homogeneous Notch activation in each respective layer. These results demonstrate the applicability of using static graph theoretic methods to explore intracellular behaviour in spatial dynamic systems. We expect the 2D dynamic domain pattern formation results presented in this chapter to agree in 3D bilayer morphologies following the topological description of cellular connectivity in the pattern templating analysis.

In this chapter, we assume that the laminar pattern formation is driven purely by signal strength polarisation between the layers, thus neglecting the effect of the external environment on the biological system. That is, we neglect the influence of stroma or extracellular matrix and the importance of the lumen to the luminal cells in supporting the high contrast of Notch expression *in vivo* and *in vitro*, respectively [48]. Thus, applying supplementary boundary conditions in dynamic domains in addition to signal polarisation may achieve laminar patterning, invariant to morphological perturbations.

Furthermore, we note that the model framework and parameters chosen for the cell-based simulations were selected to preserve a bilayer structure in a growing domain whilst encouraging the morphological differences in luminal and basal

cells. Consequently, in Appendix A, using the Overlapping Spheres cell-based model in 2D and 3D, we highlight the sensitivity of our pattern analysis methods to the requirement of bilayer connectivity, specifically in the instance of a bilayer disconnect resulting in sudden dissipation of laminar patterns (figures A.2 - A.3). As it is common for luminal cells not to be in contact with basal cells during the early stages of mammary organoid development (see Section 1.1.1), pattern stabilisation during bilayer disconnection should be explored to determine if the signal polarity is a dominant mechanism in cell-fate preservation. To explore the role of loss of basal contact during mammary organoid development using the interconnected methods applied in this chapter, an immediate extension is to consider a more general pattern template for the inclusion of only luminal-luminal contacts, generating three representative pattern cells in the quotient graphs. Specifically, this luminal extension could be used to isolate the viability of a polarity-guided lateral-inhibition mechanism for cell-fate commitment during the initial stages of organoid growth.

Applying the analytical polarisation conditions of Theorem 2.2.1 and Theorem 2.2.2 to the context of a mammary organoid using the Collier et al. (1996) NDM we revealed that if patterns are to be experimentally observed then we require almost no juxtacrine communication between cells within the same layer. A plausible process to address the polarisation of Notch activators may involve Cadherins [156], which are transmembrane proteins that mediate cell-cell adhesions. Differential expression of Cadherins (E-cadherins are associated with luminal cells and P-cadherins are associated with the basal cells) are suggested to promote self-organisation to form bilayer structures in the mammary gland via cellular affinity to homophilic interactions [156]. Increasing evidence observes an exclusionary spatial relationship between Notch1 and E-cadherins on the cell surface in a variety of organs, and specifically in the mammary gland [157–159]. In addition, it has been verified that E-cadherins located between luminal cells promote lumen formation during mammary organoid development [160]. Therefore, we propose that there exists a Cadherin adhesion-dependent Delta inhibition mechanism that promotes the localisation of Delta ligands on the luminal-basal interface (Figure 2.17)[2].

[2]Since our initial proposal of an agonistic interaction between Cadherins (Ecad) and Delta (Dll1) in [143] interaction, direct evidence of Dll1-Ecad exclusion has been found in neural progenitor cells [161].

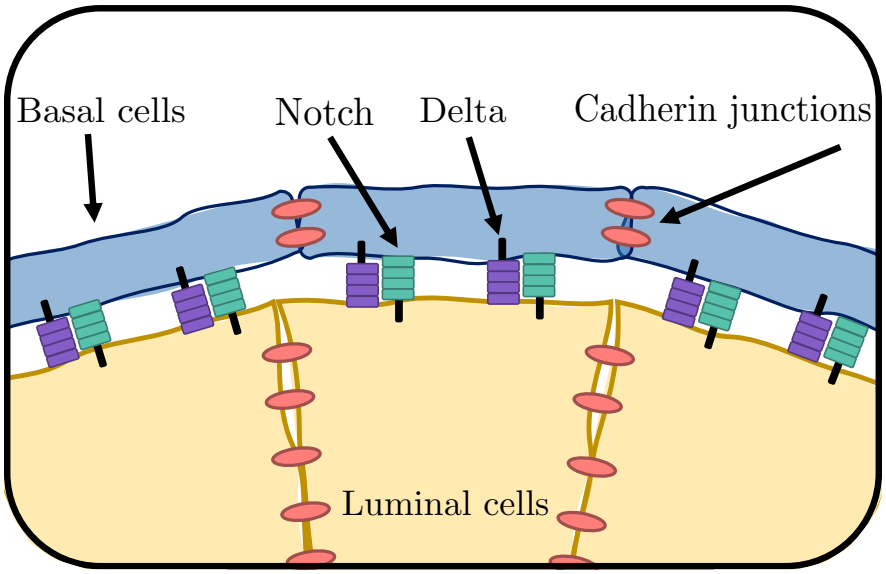

Figure 2.17: Proposed spatial distribution of Notch, Delta and Cadherin junctions within a developing mammary organoid. Due to the adhesion required to maintain the bilayer structure with a hollow lumen, tight junctions form, inhibiting the function of the membrane-bound Notch receptors and Delta ligands between cells in the same layers.

Chapter 3

Investigating the effect of local tissue structure on cell-fate commitment

The morphology of mammary organoids is highly dynamic throughout development, changing in response to hormonal and environmental cues [16, 22]. Subsequently, mammary organoids have the capacity to produce a range of complex branch-like morphologies from simple spheroid structures, whilst preserving the functional cell-type bilayer architecture (Figure 3.1). At the cellular level, these substantial changes in organoid shape are driven by the migration and proliferation of mammary epithelial cells (MECs) to generate a network of ductal structures for the primary function of the host organ, the production and secretion of lactate [23, 131]. Thus, the complex morphologies of mammary organoids reflect the intricate interplay between different cell types and signalling pathways that regulate the development and function of the organ.

Yet the geometry of the tissue plays a crucial role in regulating cell signalling processes; variations in cellular spatial organisation affect local cellular neighbourhood compositions, access to nutrients from external sources and axis of polarity for proliferation, migration and signalling receptors [162, 163]. In diffusive paracrine signalling processes (described using reaction-diffusion dynamics), it is well-established that variation in the geometry of the cellular domain influences the convergent steady state patterning of the protein species [164, 165], and that selection of boundary conditions (access to external growth dependent nutrients) affects the susceptibility of geometry to generate pattern bifurcations [166]. This phenomenon has been shown to give rise to a morphology-biochemical feedback mechanism for branched architecture in mammary glands [31]. In particular, it has been observed both experimentally and numerically that the local tissue curvature dictates branching locations by altering the local abundance of TGF-β, a cytokine that is actively diffused by MECs and inhibits

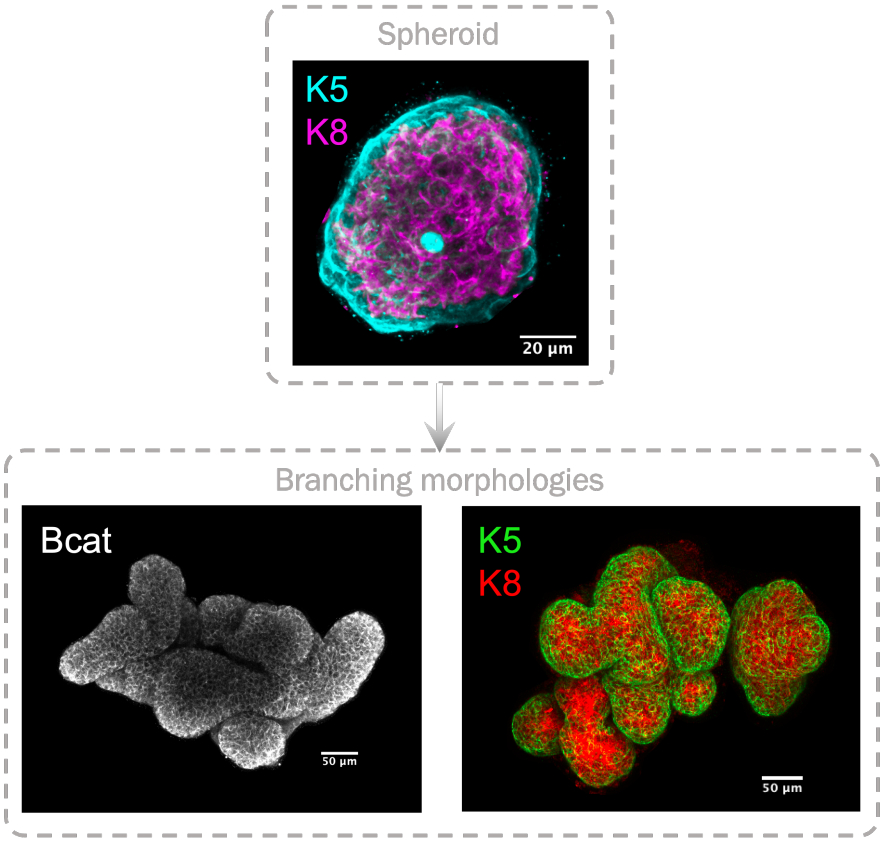

Figure 3.1: Evolving morphologies of mammary organoids. Maximum intensity z-projections are shown for spheroid and branching mammary organoids during development. The top and right organoids are stained with basal and luminal cell-type markers, Keratin5 (K5) and Keratin8 (K8), respectively. The leftmost organoid is stained for β-catenin (Bcat), indicating proliferative and stem-like activity. Images are provided by Dr Bethan Lloyd-Lewis where detailed descriptions of materials and methods for image acquisition can be found in [16].

proliferation by inducing apoptosis, such that growth is promoted in the most convex regions of the tissue.

These morphological effects on spatial patterning are amplified in developmental processes that employ juxtacrine signalling, i.e., contact-dependent communication. Tissue morphogenesis is driven by cellular growth, division and death, which fundamentally induces change to local cellular neighbourhood compositions [167], and consequently, induces local change into juxtacrine-dependent intracellular behaviour [51]. The deep links between cellular connectivity topology and fine-grained juxtacrine patterning were first explored at the global tissue scale by Webb and Owens in 2004 [126], where the authors highlight that changing the cellular domain from square to hexagonal lattice structures requires increased lateral-inhibition to generate consistent checkerboard patterns. On a more local scale, stochastic heterogeneity in cellular shape producing irregular cellular domains has been shown to yield local

clusters of intracellular activity in lateral-inhibition processes [125], indicating the existence of geometry-induced niche formation in developing systems.

Since these initial studies, the influence of cellular geometry on fine-grained pattern formation by lateral-inhibition has been explored using a range of methods such as intracellular phase-field models [50], agent-based models [168, 169], spatially discrete dynamical systems [117, 118] and continuum descriptions [99–101]. Each of these studies demonstrates that geometric features of the cellular domain have the capacity to induce the instability of the homogeneous states in small systems of cells. Specifically, variations in cell volume and surface area have been identified as geometric cell-fate promoters. Namely, contact-area dependence of signal activator-receptor binding suggests that smaller cells are more likely to signal senders, thus adopting the lineage trajectory associated with low Notch high Delta [50, 169]. Critically, differences in cell shape are commonly observed in early mammary gland development due to asymmetric division of stem cells [170], suggesting a geometric influence on cell-fate symmetry breaking in mammary organoids. Yet, the relationship between cell shape, cell-cell connectivity and local tissue morphology is overlooked using these modelling approaches.

Mammary organoids present as an unconstrained biological model of the mammary gland due to the absence of fibroblasts that provide essential signals for the function and maintenance of the tissue throughout development. Therefore, organoids enable investigations of purely epithelial processes [15, 171]. Consequently, MECs within mammary organoids have an increased sensitivity to plastic cell-fate behaviour [16, 20], and in particular, it has been shown that artificial activation of Notch1 leads to phenotypic basal-luminal switching [21]. In agreement with the mammary (EpH4) curvature-dependent branching study [31], rapid phenotypic changes for branch elongation via migration and proliferation has been observed in mammary organoids [131]. Critically, morphological regions with increased positive curvature contain increased stem-like cells, that transition to a reduced dynamic state within the ductal regions. As phenotypic reprogramming is often correlated with disease development and metastasis [172], understanding the mechanisms that control cell-fate commitment is critical for the preservation of healthy and functional tissue.

In Chapter 2 we demonstrated that signaling polarity has the capacity to generate and stabilise bilayer laminar patterns of Notch, with a clear dependence on cell-cell connectivity structure. Thus, motivated by the curvature-dependent proliferation in MECs [31], in this chapter, we examine the efficacy of cell signal polarisation in cell-fate control within different morphological regions of mammary organoids. To address this statement, we first introduce an

image analysis pipeline for the extraction of cell-type dependent connectivity graphs and morphometric features of mammary organoids. We combine deep learning methods for membrane detection with bespoke algorithms for cell-type identification and vertex-curvature association to classify the connectivity topology in local regions of organoids. Extending the local connectivity analysis from imaging data, we use agent-based modelling to mimic experimental stamping studies for tissue shape control to generate a morphology dependent cell-cell connectivity regimes for developing mammary organoids.

As the input-output (IO) signalling framework introduced in Section 2.1 enjoys spatial flexibility from the topological description of cell-cell connectivity, we employ this model framework to analyse the influence of local tissue geometry on the sufficient signal polarity required to initiate and stabilise laminar patterns of cell-fate determinants in MECs. We extend our existing theoretic insights for regular bilayer connectivity structures derived in Chapter 2 to allow for layer-wise semi-regular graphs, and highlight the existence of connectivity asymmetries for the stability of laminar patterns with lateral-inhibition kinetics in generality. Critically, by combining our image and synthetic connectivity data with our IO analysis, we provide evidence for a polarity-driven cell-fate control mechanism in developing mammary organoids in agreement with existing experimental studies for MEC plasticity and branch elongation [31, 131].

The structure of this chapter is as follows. In Section 3.2 we describe and employ an image workflow used to extract contact-based cell-cell connectivities and local tissue curvature from confocal multiplex images of mammary organoids. In Section 3.3, we supplement our initial insights from primary image data with synthetic data from agent-based models to propose a characteristic relationship between local tissue geometry and cell-cell connectivities. In Section 3.4, we outline a general lateral-inhibition input-output (IO) model spatially coupled using bilayer semi-regular graphs, whereby we analyse the influence of cross-layer connectivity on the existence and stability of laminar pattern formation. Then in Section 3.5, we revisit the canonical Notch-Delta kinetics from Chapter 2 to apply our semi-regular pattern analysis methods to developing mammary organoids with characteristic graphs identified by image and synthetic data analysis.

3.1 Development of an image analysis pipeline for curvature-connectivity analysis

To investigate the effect of local tissue deformations on cell-fate dynamics in mammary organoids, we design an image analysis pipeline to extract and couple tissue curvature and local cell-type dependent signalling graphs from multiplex

confocal images of mammary organoids. We combine a recently developed deep learning package for membrane segmentation, PlantSeg [173], with additional algorithms for cell-type classification, cell-cell connectivity weighted graph construction and local boundary curvature estimation. The details of each component of the pipeline are provided below with a pipeline summary presented in Section 3.1.5.

3.1.1 CNN membrane prediction for confocal microscopy

Convolutional Neural Networks (CNN) are powerful and versatile tools for semantic boundary detection [173, 174]. In particular, the U-net CNN is designed to address the challenge of accurately segmenting objects in images by providing a robust framework for both localization and segmentation [175]. It has a U-shaped architecture consisting of a contracting path (encoder) an expansive path (decoder). The contracting path captures the contextual information and extracts high-level features from the input image through a series of convolutional and pooling layers. This process gradually reduces the spatial dimensions of the input. The expansive path, which is symmetric to the contracting path, aims to upsample the encoded features to the original input resolution.

U-nets were initially designed for edge detection in low-resolution for 2D brightfield and DIC images [175] has since been adapted to analyse 2D and 3D multiplex confocal organoid images with improved accuracy compared to existing intensity thresholding methods [176, 177]. PlantSeg employs a CNN with the U-net architecture which is trained on a range of membrane-stained plant tissues over different length scales in 2D and 3D. Recently, the trained CNNs in PlantSeg have been shown to retain high accuracy for membrane detection in confocal images of mammalian tissues with no additional retraining [178], demonstrating applicability to organoid segmentation.

Before applying the CNN for membrane boundary prediction, we first remove all background fluorescence noise by cropping around the tissue of interest. In addition, we flatten all membrane markers into a single greyscale image to provide the most complete coverage of each cell membrane in the tissue. Finally, the images are then rescaled to match the training dataset.

The output of the CNN is a probability map of cell membranes masked over the input image. These boundary probabilities are then used to guide cell segmentation for semantic to instance object acquisition, i.e., assigning each cell with a unique ID and associated properties. An example of the CNN output is given in the pipeline summary Figure 3.5.

3.1.2 Watershed and graph partitioning methods for cell segmentation

Following boundary detection, PlantSeg also contains a variety of methods for boundary-guided cell segmentation in 2D and 3D. For our application of segmenting relatively noisy MECs from mammary organoids, we employ a combination of watershed and hierarchical graph clustering methods. Namely, a distance transform is applied to the boundary probability map that yields potential cell centroids at the local maxima. These local maxima are then used as initial seed locations for a watershed algorithm [179]. That is, boundary probability map is viewed as a topographic surface where the intensity values represent the elevation. Then filling the surface with water from the basins of the map (initial seeds), pixels with the filled water regions as assigned to the same instance object. Filling stops when large regions merge, i.e., the peaks of the surface are submerged.

The watershed algorithms are calibrated to over-segment by allowing for shallow minima through thresholding, potentially producing multiple instances for the same cell. These instances will be later refined using boundary-guided graph clustering methods. Critically, the watershed over-segmentation ensures no cell is lost during the semantic-to-instance transformation process and has been evidenced to provide increased accuracy when combined with graph-based linkage filters [173].

The boundary-guided cell clustering of the watershed objects is performed using the generalized framework for agglomerative clustering of signed graphs procedure (GASP) [180]. Namely, watershed objects of the image are presented using vertices and edges are drawn between adjacent components producing a graph. The vertices are then clustered into the regions contained by the boundaries of the cell membrane. Specifically, superpixellation is performed on the watershed segmented objects to reduce the number of vertices of the region graph such that any two adjacent watershed objects are connected with an edge. Each edge is weighted by the mean boundary probability w_e along the common boundary of the two adjacent watershed objects.

The vertex pairs are then clustered based on the linkage criterion for edge weights. That is, positive linkage is associated with vertex attraction and thus are clustered, whereas negative linkage represents vertex repulsion. We apply the averaged linkage criterion (denoted by HCC-avg in [180])

$$\mathcal{W} = \frac{1}{2|E_{i,j}|} \sum_{e \in E_{i,j}} (2w_e - 1), \tag{3.1}$$

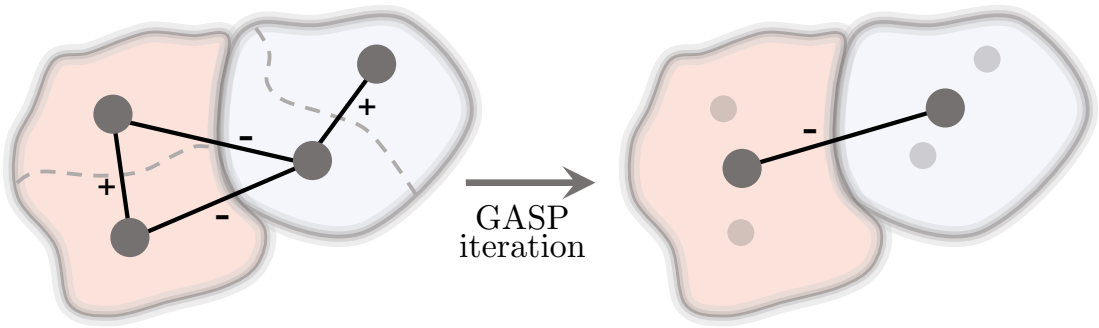

Figure 3.2: A schematic of a GASP vertex clustering iteration using the average linkage weight criterion. Dashed lines presented instance regions produced by over-segmented watershed methods. Gradient grey solid lines represent the boundary probability map given by CNN output. Vertices correspond to each region and edges are drawn between vertices if region boundaries are shared. If the common boundary is aligned with the boundary probabilities, then edge weights are negative, and are positive otherwise. Positively weighted connections are combined into a single vertex, and then the process is repeated until only negative weights are found.

where $E_{i,j}$ is the set of edges between the vertex clusters S_i and S_j. Intuitively, if the boundary between two superpixellated objected lines on a membrane boundary detected by the CNN, then the linkage between those objects will be negative. After each pairwise clustering, linkage is recalculated and the process is repeated until all clusters have a negative linkage. Figure 3.2 describes the GASP clustering process and for further details on the GASP implementation, see [180].

3.1.3 Identifying cell-types and constructing cell-cell signalling graphs

In addition to direct membrane markers, if cells are stained with fluorescence markers for basal or luminal phenotypes, an intensity thresholding method is applied to classify the type of segmented cells. In the datasets used in this study, basal and luminal cells are Keratin5 (K5) and Kertain8 (K8) active as in Figure 3.1. Therefore to delineate these cell types, the normalised sum of the fluorescence markers is taken over each segmented cell and compared. To account for different staining methods that produce plasma membrane-bound or cytosolic fluorophores, the normalised sum can be globally scaled for each image stack.

Formally, let Ω_{c_i} be the region of the image defined by the segmented cell, C_i. Define the cell-type marker intensity function $I_{mkr}(x, y)$ which provides the pixel value of the marker within the image, where the subscript mkr denotes the Keratin biomarker. The locally normalised cell-type identifier is then given by

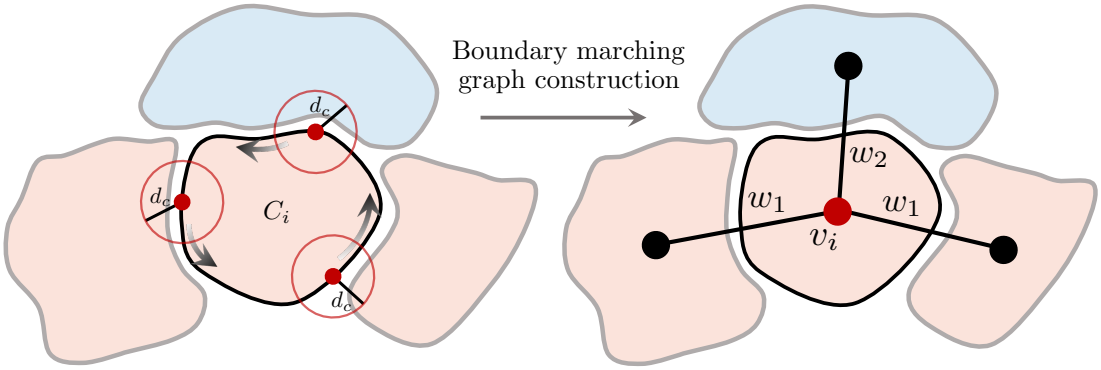

Figure 3.3: A digram outlining the marching boundary approach for cell-type dependent signalling graph construction. Luminal and basal cells are coloured orange and blue, respectively.

$$\mathcal{I}^i_{mkr} = \epsilon_{mkr} \int_{\Omega_{c_i}} \frac{I_{mkr}(x,y)}{\max\limits_{\boldsymbol{x}\in\Omega_{c_i}} (I_{mkr}(x,y))} dxdy \tag{3.2}$$

where ϵ_{mkr} is the global scale to account for staining method. The cell-type, τ_i, is specified by comparing the activation of the basal and luminal markers

$$\tau_i = \begin{cases} \text{Basal} & \text{if} \quad \mathcal{I}^i_{K5} > \mathcal{I}^i_{K8}, \\ \text{Luminal} & \text{otherwise.} \end{cases} \tag{3.3}$$

To construct the cell-type dependent cell signaling graphs, which are used for cell-fate pattern analysis, we use a membrane distance threshold. The vertices v_i of the graph, $\mathcal{G}$, are given by the centroids of the segmented cell C_i. Then for all segmented cells C_i, a ball of radius d_c is centered on the boundary and is traced over the perimeter. If any other cell is located within the ball, an edge is drawn between them. As in our previous analysis of layer-dependent signal polarity, edges drawn between cells of the same type (homotypic connections) are scaled by $w_1 > 0$ and edges between cells of different types (heterotypic connections) are scaled by $w_2 > 0$. This connectivity construction process can be viewed as a boundary marching algorithm as depicted in Figure 3.3. Notably, the connectivity distance threshold, d_c, presents the characteristic length scale of the cell signalling mechanism such that $d_c \approx 3\mu$m represents juxtacrine singalling, whereas $d_c \approx 15\mu$m and $d_c \approx 30\mu$m correspond to short and long-range paracrine signalling, respectively.

3.1.4 Local tissue curvature estimation

The local curvature of the boundary of 2D cross-sections of mammary organoids is estimated through the circle fitting method, as described in [181]. Namely, the segmented cells are binarised defining a singular segmentation for the

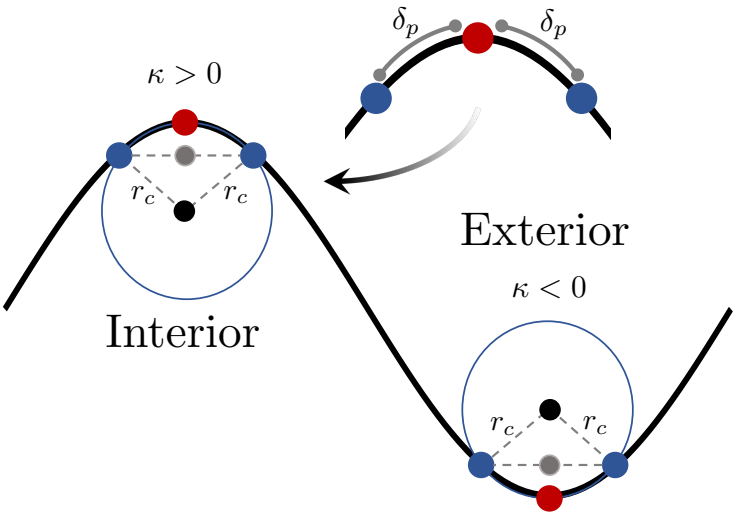

Figure 3.4: A diagram outlining local tissue boundary curvature estimation. Red points denote the positions of curvature estimation. The blue points are located at distance $\pm\delta_p$ of the red point along the boundary. A circle passing through all three boundary points is constructed with centre given by the black point, with radius r_c. The magnitude of the curvature $|\kappa|$ at the red point is given by $1/r_c$, and the sign of the curvature is dependent on whether the midpoint (grey) of the blue points is inside or outside the boundary.

complete tissue where the boundary pixels are located using the `imbinarize` and `bwboundaries` in the Image Analysis toolbox (Matlab 2021a). For each boundary pixel $x_{b,i}$, two additional boundary pixels are selected at a distance $\pm\delta_p$ pixels, $x_{b,i\pm\delta_p}$. A circle is then constructed, passing through all three points, $x_{b,i-\delta_p}, x_{b,i}$ and $x_{b,i+\delta_p}$ providing a radius, r_c. Critically, this circle is unique provided all three points are not collinear [182], if these points are collinear, then we set $\kappa = 0$ at $x_{b,i}$. The magnitude of the curvature at $x_{b,i}$ is therefore $|k| = 1/r_c$, where the sign of the curvature is determined by the position of the midpoint of $x_{b,i-\delta_p}$ and $x_{b,i+\delta_p}$ i.e., whether the midpoint lies inside, or outside the boundary. Here, we impose that midpoints within the boundary correspond to positive curvatures. A summary of the local curvature estimation procedure is provided in Figure 3.4.

To couple local tissue deformations with cell signalling connectivity, we associated the local curvature with the boundary vertices. That is, for any segmented cell that lies on the boundary of the tissue, the average curvature along the boundary cell edge is linked to the vertex representing that cell. As we only consider bilayer connectivity structures, assigning only boundary vertices with a morphological metric is sufficient to analyse how variations in tissue geometry alters connectivity topology.

3.1.5 Pipeline summary

A summary of the curvature-connectivty image analysis pipeline is provided in Figure 3.5. Namely, using a combination of deep learning, watershed, graph partition and thresholding methods, we produced a cell-type dependent weighted cell signalling graph, where local connectivity can be classified by local tissue curvature. Though we present and analyse 2D cross-sections of mammary organoids in this chapter, this pipeline is seamlessly extendable to 3D organoids provided confocal images are at a sufficiently high resolution, as demonstrated in Appendix B.

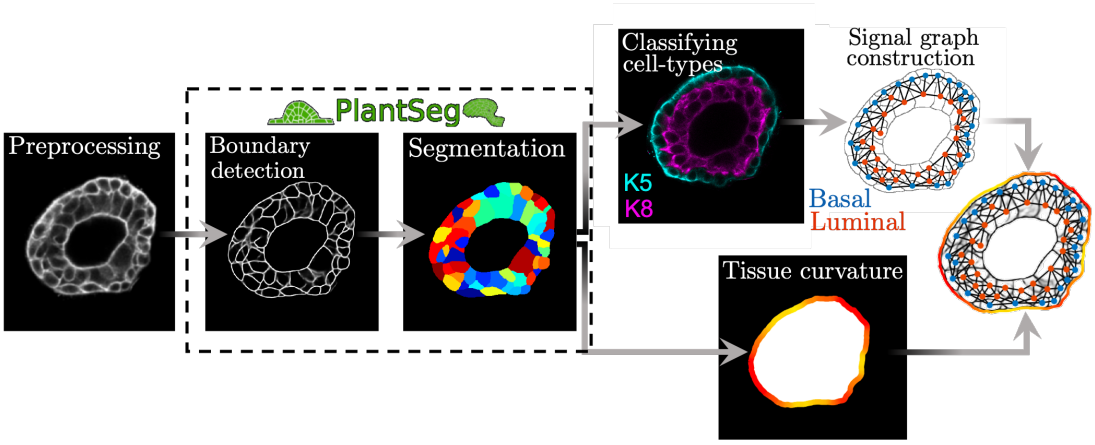

Figure 3.5: An example segmentation of a mammary organoid using the curvature-connectivity image analysis pipeline.

3.2 Initial insights into the curvature-connectivity relationship from primary image data

We apply the connectivity-curvature image analysis pipeline to 2D cross-sections of primary mammary organoids derived from transgenic mice (2-3 months) carrying the genotype for mGFP K5 activation, kindly supplied by Dr Bethan Lloyd-Lewis (University of Bristol). Organoids were additionally stained with a cytosolic K8 marker for luminal phenotype, and nucleic marker, DAPI. The confocal fluorescence images were acquired on an IX-71 inverted microscope (Olympus, Essex, UK) with an ORCA-ER camera and SimplePCI software (Hamamatsu Corporation, Hertfordshire, UK). For further details on methods and materials for organoid culture and the imaging process see [16].

Following a manual annotation of a sample image generated by an expert in organoid image analysis (Martina Bonassera, PhD candidate, ETH Zürich), validation of the pipeline for cell segmentation and cell-type classification accuracy was performed. The accuracy of the cell segmentation was measured

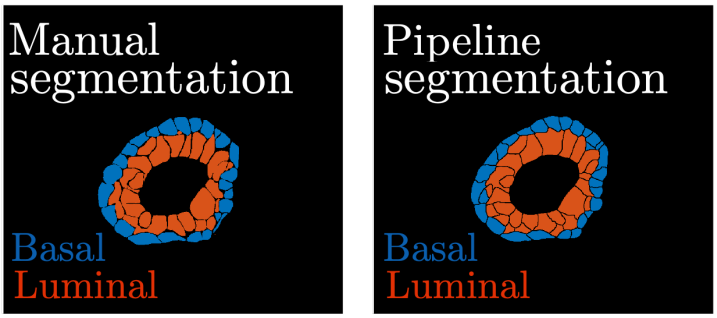

Figure 3.6: Curvature-connectivity pipeline validation of cell segmentation and cell-type classification. Basal cells (K5 active) and luminal cells (K8 active) cells are coloured blue and orange, respectively.

using the standard Jaccard index for automated S_a and manually S_m segmented pixel sets such that

$$J_{ind} = \frac{|S_a \cap S_m|}{|S_a \cup S_m|}, \tag{3.4}$$

where $J_{ind} = 1$ and $J_{ind} = 0$, represent perfect and imperfect segmentations, respectively [176]. Accuracy of the cell-type classification was conducted by manually checking the correct cell-type has been identified with reference against the K5 and K8 markers in the raw image.

Figure 3.6 shows the results of the pipeline validation for a single cross-section. Namely, the Jaccard index, $J_{ind} = 0.8672$ and the pipeline identified 95.45% cell-types correctly. The existence of artificial gaps between cell boundaries within the manual segmentation decreases the Jaccard index and therefore we propose the pipeline is adequate for preliminary investigations in the relationship between tissue shape and local cell-cell connectivity. Future use of this pipeline in more data intensive studies would required additional highly accurate annotated validation samples to ensure fit-for-purpose, however, we note that we currently have limited access to primary data.

The curvature-connectivity image analysis pipeline was then applied to five 2D cross-sections of primary mammary organoids, each increasing in size and morphological complexity, denoted A-E in Figure 3.7. As further validation of the pipeline cell-type classification, the proportion of basal and luminal cells in all images analysis is consistent with existing experimental studies. That is, luminal cells are typically the largest subpopulation, representing $50-75\%$ of the total population [183]. Additionally, we observe that the organoids with more irregular, branching morphologies have a increased luminal population, increasing the likelihood of asymmetric cell-type dependent signal connectivity structures.

To this end, we explore the connectivity of the tissue boundary cells with respect to homotypic and heterotypic neighbours, and local tissue curvature. Assuming a contact-dependence for cell-cell signalling, which is associated with

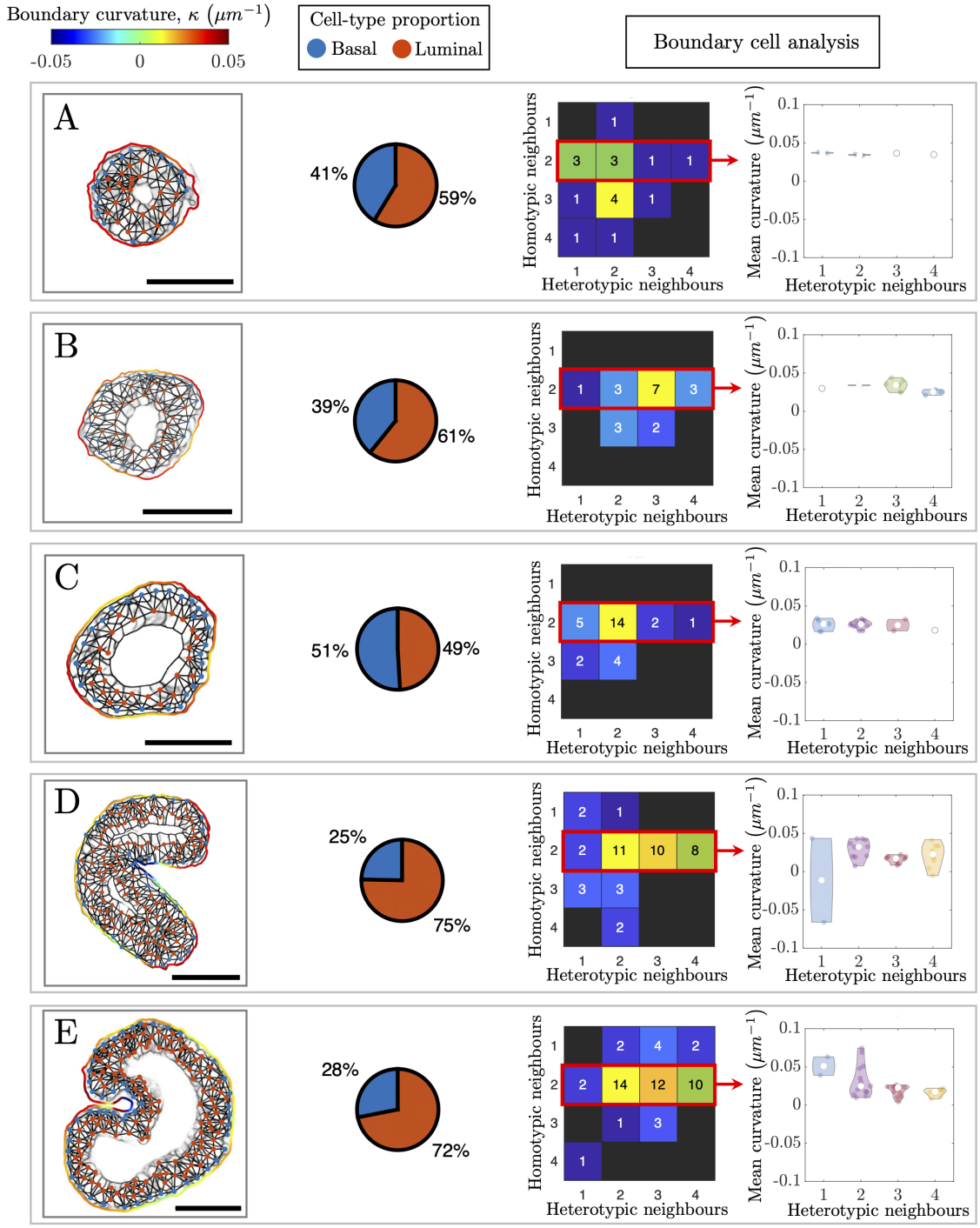

Figure 3.7: Curvature-connectivity analysis of 2D cross-sections of mammary organoids. Organoids A-E are arranged with increasing volume and variance in measured curvatures. Cell-type dependent connectivity graphs and tissue boundary curvature are superimposed over the CNN detected cell boundaries. Pie charts represent the proportions of cell-type detected. The heterotypic and homotypic connectivity counts are shown for all cells along the outer boundary of the organoid. Mean cell boundary curvature and heterotypic connectivity plots are shown for the most frequent homotypic connectivity. Scale bar $50\mu m$.

Notch-Delta interactions, we use a membrane connectivity distance of $d_c = 4\mu$m. As expected for 2D cross-sections of bilayer tissue, we found in all organoids analysed, the most frequent number of homotypic connections among the boundary cells is 2 (Figure 3.7). Subsequently, we focus on the heterotypic boundary cell connectivity for those cells with only 2 homotypic connections, indicated by the red boxes in the connectivity frequency plots in Figure 3.7.

Using local tissue curvature as a metric of morphological complexity, we observe that increased variance of observed boundary curvatures correlates with a wider range of heterotypic connectivities. Specifically, sample C presents a developed bilayer in a spheroid structure and subsequently has a consistent positive mean curvature, $\kappa_{avg} \approx 0.025 \pm 0.0062$ (SD) and 2 heterotypic neighbours in 64% of the boundary cells, with only 1 heterotypic neighbour being the second most frequent (22% of boundary cells). In contrast, organoids D and E express complex branch-like morphologies, with $\kappa_{avg} \in [-0.05, 0.05]$, we record a wider distribution of heterotypic connectivities among the boundary cells, which is skewed towards increased heterotypic with respect to homotypic connections, indicating the existence of curvature dependent cell-type dependent connectivity asymmetries. In addition, the luminal cell-type proportions in organoids D and E are only slightly larger than the smaller spheroid organoids A and B, yet the heterotypic distributions are significantly different, further supporting the theory that local tissue morphology alters cell-type neighbourhood composition in mammary organoids.

Though organoids A, B, C and E provide preliminary indication of a negative relationship between local curvature and heterotypic boundary connections, limited data prevents reliable predictions of local cell connectivity from macroscopic tissue measurements. Yet, after a transient period, it has been demonstrated that kidney epithelial cells preserve their volume after rapid changes to local boundary curvature [184], and thus variations in tissue curvature dominantly alters cell surface areas [51]. Subsequently, from a geometric and volume-preserving perspective, decreasing the local boundary curvature, bending the tissue inward should increase the basal cell contact area at the basal-luminal interface and therefore heterotypic connections with respect to the boundary cells in the mammary organoid.

3.3 *In silico* curvature-connectivity data analysis

To test the negative curvature-connectivity hypothesis in MECs, we use agent-based modelling to simulate growing mammary tissue in domains of varying morphological complexity to generate synthetic connectivity data. Employing the

Vertex Model (VM) framework for growing bilayer tissues introduced in Section 2.3.3, we mimic existing *in vitro* "stamping" experiments used to analyse the influence of constrained tissue geometry on cellular behaviour [31, 185], thereby applying the same methods of curvature-connectivity analysis as conducted on the primary images, to generate sufficient data for the examination of local connectivity prediction from tissue curvature.

3.3.1 VM calibration for curvature-connectivity data collection

To measure the effect of prescribed tissue geometry on cellular behaviour, methods of "stamping" controlled shapes into collagen gell for tissue growth domains have been designed for *in vitro* studies [185]. In particular, the same experimental design was used to demonstrate the curvature-dependent branch elongation in mammary cultures [31], where epithelial fragments were seeded within the collagen wells with prescribed geometries and grown to form tubules in the shape of the prescribed well. Therefore, we reproduce this experimental design *in silico* using the VM framework where we seed an initial small bilayer of cells and allow the tissue to grow to the geometry of a fixed boundary, representing the collagen well. Thereby, measuring local tissue curvature and cell-type dependent neighbourhood compositions along the boundary of the tissue.

We use the same VM for growing bilayer domains as described in Section 2.3.3, with the parameters values provided in Table 2.2, however, here we suppress the intercellular Notch signalling as we are interested in morphology dependent epithelial packing. The tissue domain boundaries are defined by the following parametric curve designed to mimic simple branching morphologies,

$$\begin{bmatrix} x_b(\theta) \\ y_b(\theta) \end{bmatrix} = \begin{bmatrix} (r_0 + r_b \sin(\omega\theta)) \cos(\theta) \\ (r_0 + r_b \sin(\omega\theta)) \sin(\theta) \end{bmatrix} \tag{3.5}$$

for $\theta \in (0, 2\pi]$, where r_0 represents the control spheroid geometry, and, r_b and ω determine branch amplitude and frequency. In particular, $r_b = 0$ generates a simple circle of radius r_0, in which we set $r_0 = 39.6\mu m$ similar to circular organoid C in Figure 3.7. Fixing $\omega = 4$, and increasing r_b yields a continuous transformation from spheroid to branch-like tissue boundaries. For our simulations, we consider four fixed boundaries, denoted B1-B4, corresponding to $r_b = 0, 3.96, 19.01, 26.93\mu$m, respectively, as shown in Figure 3.8. To ensure consistency between our *in vitro* and *in silico* data analysis, boundary curvatures are calculated using the same method as described in Section 3.1.4. Setting luminal area $A_0 = 1$ as in Section 2.3.3, then we have the characteristic length

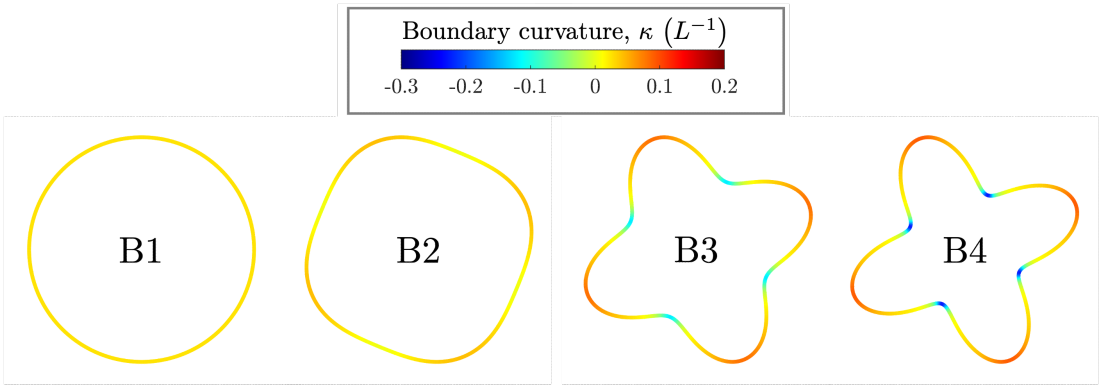

Figure 3.8: Fixed boundaries used in VM simulations for synthetic connectivity-curvature data generation.

$1L \approx 15.84\mu$m representing the cell diameter used for all VM simulation as estimated from organoid C.

Each boundary cell is associated with a mean curvature κ_{avg} which is calculated by the average curvature along the boundary edges of the cell. In the VM simulations, cells are said to be neighbours if they share a common edge, i.e., adopting the contact-based connectivity considering in our *in vitro* analysis. Simulations are initiated in a bilayer ring of boundary (basal) and non-boundary (luminal) cell-types as shown in Figure 2.12, and were run until each boundary cell was in contact with the prescribed boundary. Simulations were repeated ten times for each boundary, and local boundary curvature and connectivity data was measured at the final timestep.

3.3.2 Generating morphology and cell-type dependent connectivity regimes

Figure 3.9 provides a summary of the curvature-connectivity data produced from all fixed boundary simulations. As B1 represents our control boundary and was calibrated with the same cross-sectional area as organoid C in Figure 3.7, we see that our *in vitro* and *in silico* boundary connectivity is consistent. That is, the most frequent number non-boundary neighbours is 2, forming 66.3% of the total observations, similar to the 64% observed in organoid C. Inline with connectivity distribution observed in organoid C, we found no cells with over 3 non-boundary neighbours, further supporting the comparability of our *in vitro* and *in silico* analysis.

Increasing the tissue boundary complexity induces a wider distribution of non-boundary connections, specifically, observations of 4 non-boundary neighbours became more frequent in the branch-like geometries (B3 and B4), consistent with organoid E in Figure 3.7. However, these increased heterotypic connections are

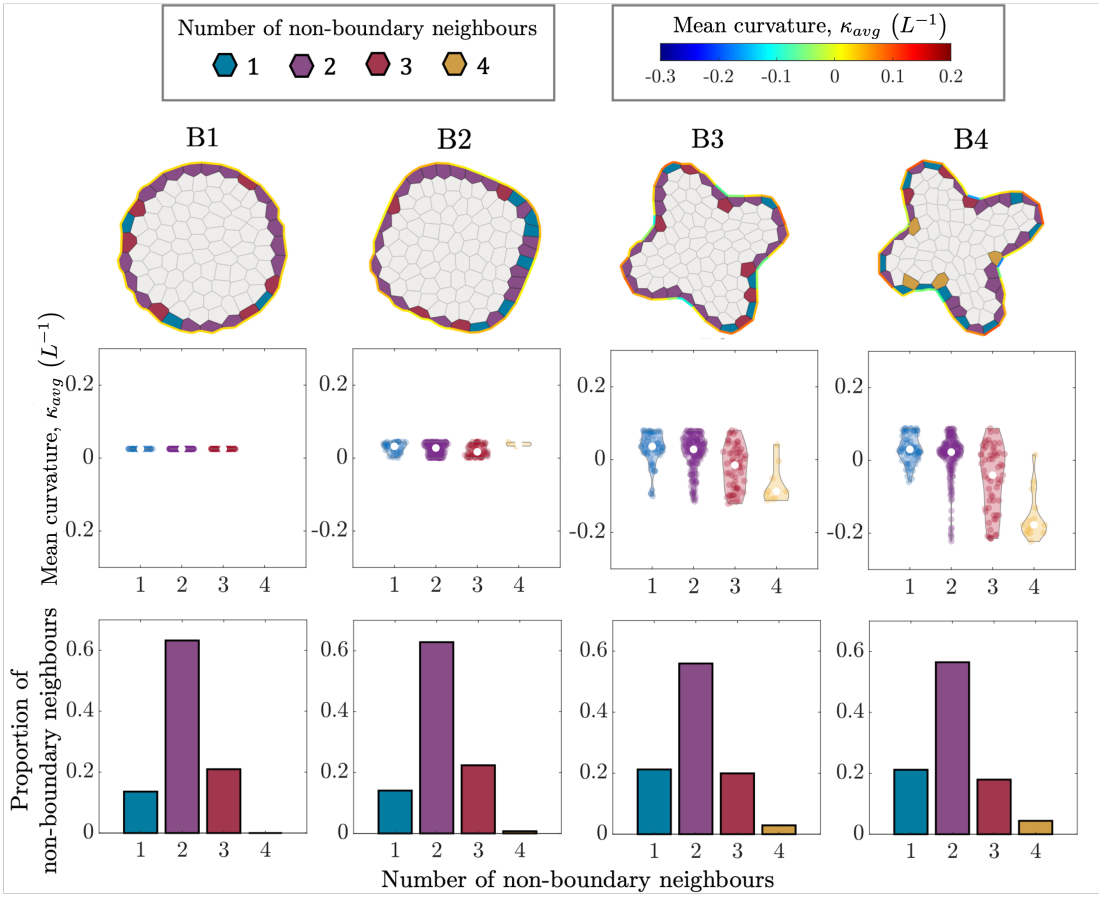

Figure 3.9: Synthetic connectivity-curvature boundary cells data. (Top) Example simulations for each fixed tissue boundary B1-B4 are shown at the final time step, where boundary cells are coloured by non-boundary neighbours. The boundary edge of the boundary cells are coloured by the mean local tissue curvature. (Middle) Violin plots showing the distributions of mean boundary curvature for each non-boundary neighbours in all simulations ($n = 10$) for each fixed boundary. (Bottom) Summary distributions of the proportion of non-boundary neighbours over all simulations in each of the tissue boundary domains.

still the least common with respect to the connectivities observed in the simple geometries (B1 and B2). In addition, the increased heterotypic connections (3 and 4 non-boundary neighbours) are correlated with negative local tissue boundary curvature, which are located at the base of the branches, providing an explanation of their infrequency.

Examining the range of boundaries, as initially proposed in our *in vitro* analysis, we find a negative relationship between local boundary curvature and non-boundary neighbours, as predicted by the volume-preservation hypothesis (Middle row of Figure 3.9). Namely, in the most varied tissue boundary we investigated (B4), at the branch tips associated with the largest positive curvature, the basal (boundary) cells have a compressed length along their apical surface, reducing their potential contact region with the luminal cells

(non-boundary). The opposite effect occurs at the base between two branches (negative curvature), where basal cells express an elongated contact surface with the luminal cells, and therefore increasing their likelihood of increased heterotypic connectivity. These observations provide further indication of the predictive power of macroscopic tissue metrics such as curvature on the microscopic connectivity features.

To further understand the relationship between local tissue geometry and cell-cell connectivity, we next examine the pair-wise connectivity within the B4 boundary simulations, i.e., the inclusion of the non-boundary cells in direct contact with the boundary in our connectivity analysis. Namely, let $n_{2,L_1}, n_{2,L_2} \in \mathbb{N}$ be the number of heterotypic connections for a boundary and non-boundary cell, respectively, in each pair-wise connection along the boundary cells. Figure 3.10a highlights that the sign of the local boundary curvature provides predictive insight into the pair-wise connectivity asymmetries between basal and luminal cells. We observe that negative curvatures are associated with basal heterotypic dominated pair-wise connectivities ($n_{2,L_1} > n_{2,L_2}$), whereas increased positive curvatures, like those observed in the tip regions have luminal heterotypic dominated pair-wise connectivities ($n_{2,L_2} > n_{2,L_1}$). In addition, we find that equal numbers of heterotypic connectivity between basal and luminal cells are located in low curvature regions of the organoid.

The delineation of the heterotypic pair-wise connectivity with respect to local boundary curvature enables the extrapolation of Figure 3.10a into characteristic connectivity regimes in different regions of mammary organoids as shown in Figure 3.10b. Critically, this allows for the approximation of local connectivity structures within different morphological regions of the organoid. Using these local structures, we can apply the cell-fate pattern analysis methods outlined in Chapter 2 to explore the role of local tissue geometry in polarity-driven cell-fate control.

3.4 Cell-fate analysis for local connectivity variations

Motivated by the variations in cell-cell connectivity for luminal and basal cells in local regions of mammary organoids, we explore the role of polarity in juxtracrine signalling-dependent bilayer cell-fate determination with respect to changes in local neighbourhood compositions. We extend the single-input-single-output (SISO) analysis conducted in Chapter 2 to include layer-wise semi-regular bilayer graph topologies in which we derive existence and stability conditions for laminar patterns for a generic lateral-inhibition model. Subsequently, we

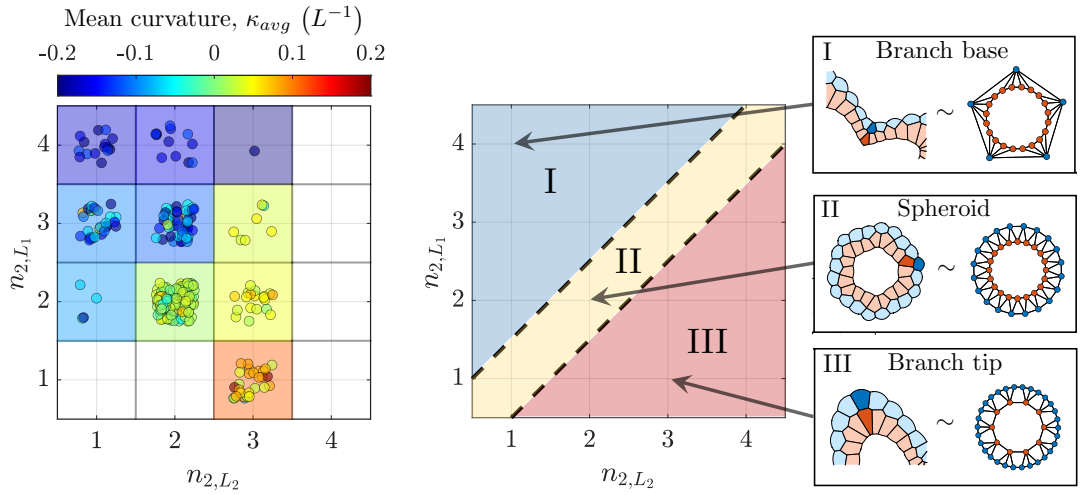

(a) Pair-wise connectivity-curvature.

(b) Characteristic connectivity regimes.

Figure 3.10: Characteristic connection regimes for different morphological regions a 2D cross-section of a mammary organoid derived from synthetic data. (a) Pair-wise cross-layer connectivities of boundary cells are extracted from the B4 VM simulations (n=247). Each connectivity pair is jittered near the true integer value to show the frequency of pair observation. Points are coloured by mean boundary tissue curvature of the boundary cell in the connected pair. The surrounding connectivity bins are coloured by the average curvature observed within the bin. (b) Approximated connectivity regimes generated from (a) and using curvature as a morphological metric for organoid region. Example bilayer graphs are given for selected cross-layer connectivities.

assess the applicability of polarity as a pattern control mechanism for various characteristic regions of mammary organoids using the classical Notch-Delta kinetics as previously studied in Section 2.3 for regular domains.

3.4.1 An interconnected dynamical system for semi-regular bilayer graphs

Consider the generic SISO interconnected dynamical system as defined in Section 2.1.4, in which we briefly reintroduce in generality to accommodate semi-regular connectivity graphs. Let $\mathcal{N} \in \mathbb{N}$ be the total number of cells in the interconnected dynamical system then denote $\boldsymbol{x}_i = [x_{i,1}, ..., x_{i,n}]^T \in X \subset \mathbb{R}^n_{\geq 0}$ the concentration of the intracellular proteins in cell i at time t, for $i \in \{1, ..., \mathcal{N}\}$. Denote the input and output signals for cell i by $u_i \in U \subset \mathbb{R}_{\geq 0}$ and $y_i \in Y \subset \mathbb{R}_{\geq 0}$. Then the interconnected SISO systems for protein evolution can be described by

$$\begin{aligned} \dot{\boldsymbol{x}}_i &= \boldsymbol{f}\left(\boldsymbol{x}_i, u_i\right), \\ y_i &= h\left(\boldsymbol{x}_i\right), \end{aligned} \tag{3.6}$$

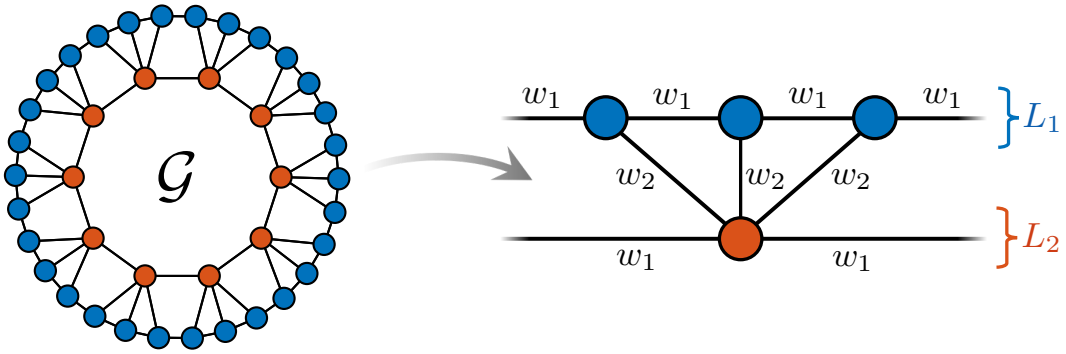

Figure 3.11: A representative layer-wise semi-regular bilayer graph, $\mathcal{G}$. Vertices are coloured by layer such that vertices in layer 1 and layer 2 are blue and orange, respectively. The layer-wise edge weight structure is shown such that adjacent vertices within the same layer and opposing layers are scaled by w_1 and w_2, respectively. All vertices within the same layer have an identical number of same layer and cross layer connections generating the semi-regular edge structure.

where $\dot{\boldsymbol{x}}_i$ is the derivative of $\boldsymbol{x}_i$ with respect to time. The function $\boldsymbol{f} : X \times U \to X$ defines the intracellular protein interactions, and $h : X \to Y$ describes the conversion from intracellular protein to output signal. We assume that both $\boldsymbol{f}(\cdot)$ and $h(\cdot)$ are $\mathcal{C}^2$ everywhere in their domains. The input-output transfer function $T : U \to Y$ describes the effect of variations to input signals on output signals, summarising the behaviour of the intracellular dynamics. As in Chapter 2, we assume that $T(\cdot)$ is bounded and sufficiently smooth, i.e. $\mathcal{C}^2$ everywhere, conforming to the properties of modelling intracellular protein dynamics [117]. Critically, for lateral-inhibition and lateral-induction cell-cell interactions, $T(\cdot)$ is characteristically decreasing and increasing, respectively.

To investigate cell-fate patterning in the mammary organoids using templating methods, we assume that each cell in the SISO system (3.6) is coupled by a bilayer layer-wise semi-regular graph, where cells are represented as vertices and an edge is drawn between two vertices if they are signalling to each other. Explicitly, each cell in the same layer has the same number of intralayer and interlayer connections, in addition to identical edge structure, as shown in Figure (3.11). Denote $\boldsymbol{W} \in \mathbb{R}_{\geq 0}^{N \times N}$ the weighted adjacency matrix associated with the semi-regular cell-cell communication graph, $\mathcal{G} = \mathcal{G}(V, E)$, for the V and E the vertex and edge sets defining the graph. Adhering to the well-mixed conditions of generic lateral-inhibition models [87, 124, 125], we assume that $\boldsymbol{W}$ is row-stochastic such that $\sum_j (\boldsymbol{W})_{ij} = 1$ for all i. We impose that the vertices of the $\mathcal{G}$ are indexed layer-wise such that $L_1 = \{v_1, ..., v_{|L_1|}\}$ and $L_2 = \{v_{|L_1+1|}, ..., v_N\}$ as depicted in Figure (3.11).

To represent signal polarity, connected vertices within the same layer ($v_i, v_j \in$

L_1 or L_2 and $v_i \sim v_j$) have edge weight $w_1 \in \mathbb{R}_{>0}$. Similarly, vertices connected from opposing layers ($v_i \in L_1$, $v_j \in L_2$ and $v_i \sim v_j$) have edge weight $w_2 \in \mathbb{R}_{>0}$. Denote the row-normalised counterparts of w_1 and w_2 by $\hat{w}_1$ and $\hat{w}_2$, respectively, then $\boldsymbol{W}$ has the block form

$$\boldsymbol{W} = \begin{bmatrix} \widehat{\boldsymbol{W}}_{1,L_1} & \widehat{\boldsymbol{W}}_{2,L_1} \\ \left(\widehat{\boldsymbol{W}}_{2,L_1}\right)^T & \widehat{\boldsymbol{W}}_{1,L_2} \end{bmatrix} \tag{3.7}$$

where $\widehat{\boldsymbol{W}}_{1,L_1}, \in \mathbb{R}_{\geq 0}^{|L_1|\times|L_1|}$ contains all intracellular connections that are scaled by $\hat{w}_1$ for the vertices in L_1. Similarly, $\widehat{\boldsymbol{W}}_{1,L_2}, \in \mathbb{R}_{\geq 0}^{|L_2|\times|L_2|}$ contains all intracellular connections that are scaled by $\hat{w}_1$ for the vertices in L_2. The matrix $\widehat{\boldsymbol{W}}_{2,L_1} \in \mathbb{R}_{\geq 0}^{|L_1|\times|L_2|}$ denotes the interlayer connections with respect to the L_1 vertices where connection is each scaled by $\hat{w}_2$. Owing to the undirected edge connections, the interlayer connections with respective to L_2 vertices can be represented as the transpose of $\widehat{\boldsymbol{W}}_{2,L_1} \in \mathbb{R}_{\geq 0}^{|L_1|\times|L_2|}$.

Following the graphical description of cell-cell signalling, the output signals, y_i, are transformed to input signals u_i by the relation,

$$\boldsymbol{u} = \boldsymbol{W}\boldsymbol{y}, \tag{3.8}$$

where $\boldsymbol{u} = [u_1, ...u_{\mathcal{N}}]^T$ and $\boldsymbol{y} = [y_1, ...y_{\mathcal{N}}]^T$. Subsequently, the semi-regular SISO system (3.6) is a closed-loop system with no interactions from external sources, i.e., extracellular matrix or surrounding organoids, discussed further in Section 3.6.

Leveraging the layer-wise semi-regular structure of the cell signalling graphs $\mathcal{G}$, we apply the laminar pattern templating methods that were introduced in Chapter 2, to derive analytic conditions on laminar pattern existence and stability with respect to signal polarity and variations in cross-layer connections. An alternative perspective of the pattern templating methods for spatial dimension reduction is the construction of equivalence classes where vertices are equivalent if they converge to the same pattern state. For laminar cell-fate patterning, vertices are said to be equivalent if they are contained within the same layer, L_1 or L_2. As we consider bilayer geometries, this produces only two equivalence classes of representative vertices from each layer, generating our spatially reduced quotient graphs as stated in Definition 2.1.1.

In the case of layer-wise semi-regular bilayers, the topological quotient graph structures are identical to those considered in Chapter 2 (Figure 2.6a), however, the respective polarity edge weights have a different form. Namely, for the layer-wise equitable partition π_2, the quotient graph, $\mathcal{G}_{\pi_2}$ has the reduced weighted adjacency matrix

$$\overline{\boldsymbol{W}} = \begin{bmatrix} a & 1-a \\ 1-b & b \end{bmatrix} \tag{3.9}$$

where

$$a = \frac{n_{1,L_1}}{n_{1,L_1}w_1 + n_{2,L_1}w_2} \quad \text{and} \quad b = \frac{n_{1,L_2}}{n_{1,L_2}w_1 + n_{2,L_1}w_2} \tag{3.10}$$

for n_{1,L_1} and n_{1,L_2} the number of same-layer connections for any given vertex in layers 1 and 2, respectively. Similarly, n_{2,L_1} and n_{2,L_2} define the number of cross-layer connections for any vertex, with respect to layers 1 and 2. For example, in Figure 3.11, $n_{1,L_1} = n_{1,L_2} = 2$, $n_{2,L_1} = 1$ and $n_{2,L_2} = 3$. This formulation allows for differing edge structures between the layers of cells, whilst preserving the row-stochasticity of the weight averaging of signals in a low-dimensional representation.

We have previously studied the cases of symmetric bilayer domains in which we concluded that signal polarisation may weaken if cross-layer connections increase to maintain laminar patterning, as demonstrated in Chapter 2. By relaxing the regularity constraints on the connectivity graphs, we further this investigation by focusing on the signal polarity required to induce laminar patterning in bilayer tissues with locally varying complex morphology, as observed in Figure 3.9.

3.4.1.1 A focus on cross-layer connectivity and polarity for laminar pattern existence with lateral-inhibition

Applying Theorem 2.2.1 for laminar pattern existence to general quotient layer-wise semi-regular graphs, $\mathcal{G}_{\pi_2}$, we generate necessary conditions for the convergence of laminar patterns in our associated large-scale SISO systems. Specifically, the following statement provides an explicit relationship between the signal graph topology and polarity weights which are required for the instability of the homogeneous steady state (HSS) generating the asymptotic convergence to contrasting states in the quotient space.

Theorem 3.4.1. *Let $\mathcal{G}$ be an undirected, layer-wise semi-regular bilayer graph and let π_2 be the equitable partition that generates the laminar pattern quotient graph, $\mathcal{G}_{\pi_2}$, composed of two representative vertices of L_1 and L_2. Denote $\overline{\boldsymbol{W}}$ the associated reduced weighted adjacency matrix (3.9) for $\mathcal{G}_{\pi_2}$. Assume that the input-output transfer function, $T : U \to Y$, is positive, bounded and decreasing, then the reduced SISO system converges to contrasting states if*

$$\frac{w_1}{w_2} < \frac{-\left(n_{1,L_1}n_{2,L_2}+n_{1,L_2}n_{2,L_2}\right)+\sqrt{\left(n_{1,L_1}n_{2,L_2}+n_{1,L_2}n_{2,L_2}\right)^2+4(|T'(u^*)|^2-1)n_{1,L_1}n_{2,L_1}n_{1,L_2}n_{2,L_2}}}{2(|T'(u^*)|+1)n_{1,L_1}n_{1,L_2}}, \tag{3.11}$$

for u^* the homogeneous input signal steady state.

Proof. As $T(\cdot)$ is sufficiently smooth ($\mathcal{C}^2$), bounded, and decreasing, then there exists a homogeneous input signal state, u^* which satisfies the homogeneous input-output relation

$$[u^*, u^*]^T = \overline{\boldsymbol{W}}[T(u^*), T(u^*)]^T, \tag{3.12}$$

by Lemma 2 in [186]. Subsequently, the application of Theorem 2.1.2 to our reduced SISO system (3.6) at the HSS generates the following inequality for the convergence of contrasting states in the quotient graph,

$$\min\left(\mathrm{Spec}\left(\overline{\boldsymbol{W}}\right)\right)|T'(u^*)| < -1. \tag{3.13}$$

By direct computation, $\mathrm{Spec}\left(\overline{\boldsymbol{W}}\right) = \{1, a+b-1\}$, and therefore as $w_1, w_2 > 0$ and $\mathcal{G}$ is a semi-regular, connected bilayer graph, we have $a, b > 0$. Consequently,

$$1 < |T'(u^*)|\,(1-a-b), \tag{3.14}$$

which we use to isolate the polarity coefficients w_1 and w_2 from the connectivity parameters of $\mathcal{G}_{\pi_2}$. Rearranging inequality (3.14) after substitution of a, b using equation (3.10), we have that

$$w_1\left(\frac{n_{1,L_1}}{n_{1,L_1}w_1 + n_{2,L_1}w_2} + \frac{n_{1,L_2}}{n_{1,L_2}w_1 + n_{2,L_2}w_2}\right) < 1 - \frac{1}{|T'(u^*)|}. \tag{3.15}$$

Establishing the positive common denominator in for the lower bound of inequality (3.15), we next collect terms of w_1

$$\begin{aligned} &w_1^2\left(2n_{1,L_1}n_{1,L_2}\right) + w_1w_2\left(n_{1,L_1}n_{2,L_2} + n_{1,L_2}n_{2,L_1}\right) \\ &\quad < \left(1 - \frac{1}{|T'(u^*)|}\right)\left(w_1^2\left(n_{1,L_1}n_{1,L_2}\right) + w_1w_2\left(n_{1,L_1}n_{2,L_2} + n_{1,L_2}n_{2,L_1}\right) + w_2^2 n_{2,L_1}n_{2,L_2}\right), \end{aligned} \tag{3.16}$$

and so we obtain a quadratic for w_2, which has the explicit form

$$\left(n_{1,L_1}n_{1,L_2}\left(|T'(u^*)|^2+1\right)\right)w_1^2 + w_2\left(n_{1,L_1}n_{2,L_2} + n_{2,L_1}n_{1,L_2}\right)w_1 + w_2^2 n_{2,L_1}n_{2,L_2}\left(1 - |T'(u^*)|\right) < 0. \tag{3.17}$$

Using inequality (3.17), we solve for the values of w_1 that satisfy the inequality. That is,

$$w_1 < \left(\frac{-\left(n_{1,L_1}n_{2,l_2}+n_{2,L_1}n_{1,L_2}\right)+\sqrt{\left(n_{1,L_1}n_{2,L_2}+n_{2,L_1}n_{1,L_2}\right)^2+4\left(|T'(u^*)|^2-1\right)n_{1,L_1}n_{2,L_1}n_{1,L_2}n_{2,L_2}}}{2\left(|T'(u^*)|+1\right)n_{1,L_1}n_{1,L_2}}\right)w_2, \tag{3.18}$$

where the positive solution is obtained as $w_1 > 0$ by definition. Dividing through by $w_2 > 0$ achieves the desired inequality (3.11). □

Remark 3.4.1. *Necessary conditions for the semi-regular pattern existence inequality (3.11) to be satisfied are:*

(i) $|T'(u^*)| > 1$;

(ii) $\min\left(\mathrm{Spec}\left(\overline{\boldsymbol{W}}\right)\right) < 0$.

The existence condition (i) corresponds to the necessary requirements of the intracellular kinetics for the instability of the HSS independent of spatial connectivity. We have shown in Section 2.3.2 that this property to be equivalent to the classical linear stability analysis conducted for Notch-Delta lateral-inhibition kinetics in [87]. Whereas (ii) implies that $a + b < 1$, which highlights that dominant cross-layer signalling is required for HSS instability with respect to laminar patterning.

Theorem 3.4.1 provides a bound on the signal polarity ratio w_1/w_2 for the existence of laminar patterning that is dependent on the signal graph connectivity and intracellular kinetics. If the upper bound of inequality (3.11) decreases, w_1/w_2 must also decrease for the HSS instability to be driven by the spatial eigenvalue associated with laminar patterning. Critically, this induces signalling anisotropy as $w_1/w_2 \to 0$ corresponds to signalling activity only at the basal-luminal interface. In sections 3.2 and 3.3 we have observed that cross-layer cell-cell connectivity regimes alter characteristically in local morphologies of the bilayer tissue of mammary organoids, as summarised in Figure 3.10b. Therefore, the following statement highlights how the polarity restrictions can be relaxed with respect to increasing cross-layer connectivity.

Corollary 3.4.1. *The upper bound of the laminar pattern existence inequality (3.11) is strictly increasing with respect to cross-layer connectivity.*

Proof. Define $E : \mathbb{N}^2 \to \mathbb{R}_{\geq 0}$ where

$$E\left(n_{2,L_1}, n_{2,L_2}\right) = \sqrt{\left(n_{1,L_1}n_{2,L_2} + n_{1,L_2}n_{2,L_2}\right)^2 + 4\left(|T'\left(u^*\right)|^2 - 1\right)n_{1,L_1}n_{2,L_1}n_{1,L_2}n_{2,L_2}} - \left(n_{1,L_1}n_{2,L_2} + n_{1,L_2}n_{2,L_2}\right) \tag{3.19}$$

is the cross-layer connectivity component of the upper bound inequality (3.11) assuming that the same-layer, n_{1,L_1} and n_{1,L_2}, connections remain constant. The monotonicity $E\left(n_{2,L_1}, n_{2,L_2}\right)$ follows directly from the computation of ∇E where

$$\frac{\partial E}{\partial n_{2,L_1}} = n_{1,L_2}\left(\frac{n_{1,L_1}n_{2,L_2}+n_{1,L_2}n_{2,L_1}+2\left(|T'(u^*)|^2-1\right)n_{1,L_1}n_{2,L_2}}{\sqrt{\left(n_{1,L_1}n_{2,L_2}+n_{1,L_2}n_{2,L_2}\right)^2+4(|T'(u^*)|^2-1)n_{1,L_1}n_{2,L_1}n_{1,L_2}n_{2,L_2}}} - 1\right), \tag{3.20}$$

and similarly,

$$\frac{\partial E}{\partial n_{2,L_2}} = n_{1,L_1}\left(\frac{n_{1,L_1}n_{2,L_2}+n_{1,L_2}n_{2,L_1}+2\left(|T'(u^*)|^2-1\right)n_{1,L_2}n_{2,L_1}}{\sqrt{\left(n_{1,L_1}n_{2,L_2}+n_{1,L_2}n_{2,L_2}\right)^2+4(|T'(u^*)|^2-1)n_{1,L_1}n_{2,L_1}n_{1,L_2}n_{2,L_2}}} - 1\right). \tag{3.21}$$

For the monotonicity of the gradient, we require that

$$\frac{n_{1,L_1}n_{2,L_2} + n_{1,L_2}n_{2,L_1} + 2\left(|T'\left(u^*\right)|^2 - 1\right)n_{1,L_1}n_{2,L_2}}{\sqrt{\left(n_{1,L_1}n_{2,L_2} + n_{1,L_2}n_{2,L_2}\right)^2 + 4\left(|T'\left(u^*\right)|^2 - 1\right)n_{1,L_1}n_{2,L_1}n_{1,L_2}n_{2,L_2}}} - 1 > 0, \tag{3.22}$$

for $\frac{\partial E}{\partial n_{2,L_1}} > 0$, and

$$\frac{n_{1,L_1}n_{2,L_2} + n_{1,L_2}n_{2,L_1} + 2\left(|T'\left(u^*\right)|^2 - 1\right)n_{1,L_2}n_{2,L_1}}{\sqrt{\left(n_{1,L_1}n_{2,L_2} + n_{1,L_2}n_{2,L_2}\right)^2 + 4\left(|T'\left(u^*\right)|^2 - 1\right)n_{1,L_1}n_{2,L_1}n_{1,L_2}n_{2,L_2}}} - 1 > 0, \tag{3.23}$$

for $\frac{\partial E}{\partial n_{2,L_2}} > 0$. Rearrangement and squaring both side of inequality (3.22) simplifies to

$$\left(2n_{1,L_1}n_{2,L_2}|T'\left(u^*\right)|\right)^2\left(|T'\left(u^*\right)|^2 - 1\right) > 0. \tag{3.24}$$

Inequality (3.24) holds as $|T'\left(u^*\right)|^2 > 1$ as required for HSS instability. Thus, $\frac{\partial E}{\partial n_{2,L_1}} > 0$.

Using the same argument for inequality (3.23), we have

$$\left(2n_{1,L_2}n_{2,L_1}|T'\left(u^*\right)|\right)^2\left(|T'\left(u^*\right)|^2 - 1\right) > 0, \tag{3.25}$$

that yields $\frac{\partial E}{\partial n_{2,L_2}} > 0$. Therefore, $\nabla E > 0$ which guarantees the monotonicity of $E\left(n_{2,L_1}, n_{2,L_2}\right)$ with respect to partial ordering in $\mathbb{N}^2$. □

For the existence of laminar patterning in the large-scale IO system (3.6), we have demonstrated that for fixed intralayer connections, increasing the cross-layer connections relaxes the constraints on the necessary amounts of signal polarity for the degradation of cell state homogeneity, in agreement the exploration investigations of regular signalling structures in Chapter 2. Critically, this relation is independent of the precise lateral-inhibition (competitive) kinetics, highlighting how local tissue and cellular morphology can influence mammary cell-fate commitment from a simple connectivity perspective.

As we have illustrated an inverse relationship between local tissue curvature and cross-layer connectivity using a combination of primary and synthetic data (Figure 3.10b), the symmetry of monotonicity following Corollary 3.4.1 with respect to n_{2,L_1} and n_{2,L_2} implies that both the mammary branch fold and branch tip regions tissue have a similar capacity to induce laminar cell-fate patterns. For example, using our synthetic 2D data, regions with the largest local boundary curvature, $n_{2,L_1} \approx 1$ and $n_{2,L_2} \approx 3$, whereas regions with negative boundary curvature, we have $n_{2,L_1} \approx 3$ and $n_{2,L_2} \approx 1$. Yet, mammary epithelial cells present different phenotypic behaviours within different regions of the mammary organoid. Specifically, cells near the tip of an elongating branch are more stem-like, with increased proliferation and migration to extend the tissue into the extracellular matrix [131]. While the cells that form ducts and the base of a branch are observed to be more committed to the functional myoepithelial and luminal phenotypes, with low migration and decreased proliferation [170].

The cell-fate pattern existence analysis using Theorem 3.4.1 is insufficient to distinguish between these regions owing to the symmetry of the undirected graphs used to describe the cell-cell signalling, and consequently provides no insight into the intercellular mechanisms that govern the distinct behaviors of the cells in these regions. Instead, we use a combination of signal stability and pattern templating methods to elucidate the potential of polarity to control cell-fate plasticity with cells expressing opposing cell-fate biomarkers, i.e. different output signal states, y_i.

3.4.2 The emergence of cell-fate conductor cells for the stability of laminar patterns

Before stating the signal stability conditions for semi-regular bilayer graphs, we first briefly review the gain of a closed and interconnected dynamical system with respect to biological tissues. The gain of a cell is the absolute ratio of input, u_i, and output, y_i biochemical signals, and provides a measure of how the intracellular kinetics effect the transformation from input to output. Employing the $\mathcal{L}_2$ norm, $||\cdot||_2$, to obtain the magnitude of both input and output signals, we acquire a $\mathcal{L}_2$-gain, γ_i, for each cell in our tissue, $i \in \{1, ..., N\}$, as defined in Definition 2.1.4. Let $\mathbf{\Gamma} = \text{diag}\,(\gamma_1, ..., \gamma_N)$ be a diagonal matrix containing the gain for each cell. Applying the quotient mapping to $\mathcal{G}$ using the laminar pattern template partition, π_2, we impose cells within the same later behave identically. Consequently, cells within the same layer will have identical $\mathcal{L}_2$-gains, $\gamma_i = \gamma_j$ for all $v_i, v_j \in L_1$ or L_2. Therefore, when investigating the stability of laminar patterning in the quotient IO system (3.6), define $\overline{\mathbf{\Gamma}} = \text{diag}\,(\overline{\gamma}_1, \overline{\gamma}_2)$, where $\overline{\gamma}_1 = \gamma_i$ for all $v_i \in L_1$ and $\overline{\gamma}_2 = \gamma_i$ for all $v_i \in L_2$. Applying the layer-wise semi-regular graph structures to the $\mathcal{L}_2$-gain stability criterion (see Theorem 2.1.3) we generate the following statement for the stability of laminar patterns.

Theorem 3.4.2. *Let $\mathcal{G}$ be an undirected, layer-wise semi-regular bilayer graph and let π_2 be the equitable partition that generates the laminar pattern quotient graph, $\mathcal{G}_{\pi_2}$, composed of two representative vertices of L_1 and L_2. Denote $\overline{\boldsymbol{W}}$ the associated reduced weighted adjacency matrix (3.9) for $\mathcal{G}_{\pi_2}$. Let $\overline{\gamma}_1$ and $\overline{\gamma}_2$ be the $\mathcal{L}_2$-gains associated with the heterogeneous input signal states, u_1^* and u_2^*, for each representative cell in $\mathcal{G}_{\pi_2}$. Then the laminar pattern state is locally asymptotically stable if*

$$\frac{w_1}{w_2} < \frac{n_{1,L_1}n_{2,L_2}\left(\overline{\gamma}_1 - 1\right) + n_{1,L_2}n_{2,L_1}\left(\overline{\gamma}_2 - 1\right)}{2n_{1,L_1}n_{1,L_2}\left(\overline{\gamma}_1 - 1\right)\left(\overline{\gamma}_2 - 1\right)} - \frac{\sqrt{\left(n_{1,L_1}n_{2,L_2}\left(\overline{\gamma}_1 - 1\right) + n_{1,L_2}n_{2,L_1}\left(\overline{\gamma}_2 - 1\right)\right)^2 + 4\left(\overline{\gamma}_1 - 1\right)\left(\overline{\gamma}_2 - 1\right)\left(\overline{\gamma}_1\overline{\gamma}_2 - 1\right)n_{1,L_1}n_{2,L_1}n_{1,L_2}n_{2,L_2}}}{2n_{1,L_1}n_{1,L_2}\left(\overline{\gamma}_1 - 1\right)\left(\overline{\gamma}_2 - 1\right)}. \tag{3.26}$$

for $\overline{\gamma}_1, \overline{\gamma}_2 \neq 1$. *However, if* $\overline{\gamma}_1 = 1$ *and* $\overline{\gamma}_2 < 1$, *or* $\overline{\gamma}_2 = 1$ *and* $\overline{\gamma}_1 < 1$, *then the laminar pattern state is locally asymptotically stable.*

Proof. Invoking Theorem 2.1.3, we have that the quotient SISO system (3.6) has locally asymptotically stable heterogeneous pattern states if

$$\rho\left(\overline{\boldsymbol{W}}\,\overline{\boldsymbol{\Gamma}}\right) < 1, \tag{3.27}$$

where $\rho\left(\cdot\right)$ denotes the spectral radius and

$$\overline{\boldsymbol{W}}\,\overline{\boldsymbol{\Gamma}} = \begin{bmatrix} a\overline{\gamma}_1 & (1-a)\,\overline{\gamma}_2 \\ (1-b)\,\overline{\gamma}_1 & b\overline{\gamma}_2 \end{bmatrix}. \tag{3.28}$$

As $\overline{\gamma}_1, \overline{\gamma}_2 \geq 0$, then $\overline{\boldsymbol{W}}\,\overline{\boldsymbol{\Gamma}}$ is a non-negative and irreducible matrix. Therefore, by Perron-Frobinius theorem for non-negative and irreducible matrices (Theorem 3.1 in [187]), we have that $\rho\left(\overline{\boldsymbol{W}}\,\overline{\boldsymbol{\Gamma}}\right) = \max\left(\mathrm{Spec}\left(\overline{\boldsymbol{W}}\,\overline{\boldsymbol{\Gamma}}\right)\right)$. Computing the eigenvalues of $\overline{\boldsymbol{W}}\,\overline{\boldsymbol{\Gamma}}$ yields

$$\rho\left(\overline{\boldsymbol{W}}\,\overline{\boldsymbol{\Gamma}}\right) = \frac{1}{2}\left(a\overline{\gamma}_1 + b\overline{\gamma}_2 + \sqrt{\left(a\overline{\gamma}_1 + b\overline{\gamma}_2\right)^2 - 4\left(a+b-1\right)\overline{\gamma}_1\overline{\gamma}_2}\right). \tag{3.29}$$

Applying the stability condition inequality (3.27), the expression can be reduced to

$$a\overline{\gamma}_1 + b\overline{\gamma}_2 - 1 < \left(a+b-1\right)\overline{\gamma}_1\overline{\gamma}_2 \tag{3.30}$$

as $\rho\left(\overline{\boldsymbol{W}}\,\overline{\boldsymbol{\Gamma}}\right)$ is a positive real eigenvalue and therefore taking roots preserves the inequality. Reintroducing the a and b into inequality (3.30) using their connectivity-polarity definition in equation (3.10) and rearranging yields the following quadratic in the polarity coefficients

$$n_{1,L_1}n_{1,L_2}\left(\overline{\gamma}_1 - 1\right)\left(1 + \overline{\gamma}_2\right)w_1^2 + w_2\left(n_{1,L_1}n_{2,L_2}\left(\overline{\gamma}_1 - 1\right) + n_{1,L_2}n_{2,L_1}\left(\overline{\gamma}_2 - 1\right)\right)w_1 + n_{2,L_1}n_{2,L_2}\overline{\gamma}_1\overline{\gamma}_2 w_2^2 < 0 \tag{3.31}$$

which can be solved for w_1. If $\left(\overline{\gamma}_1 - 1\right)\left(\overline{\gamma}_2 - 1\right) < 0$ then the lower bound of inequality (3.31) is a negative parabola with respect to w_1, and therefore the largest root to obtain inequality (3.26). Else if $\left(\overline{\gamma}_1 - 1\right)\left(\overline{\gamma}_1 - 1\right) > 0$, then inequality (3.31) is a positive parabola with respect to w_1 and therefore the smallest root is taken to obtain inequality (3.26), where both conditions conform with $\min\left(\mathrm{Spec}\left(\overline{\boldsymbol{W}}\right)\right) < 0$ which is necessary for the existence of laminar patterns. However, without loss of generality, if $\overline{\gamma}_1 = 1$. Then inequality (3.30) simplifies to $0 < n_{2,L_1}w_2\left(1 - \overline{\gamma}_2\right)$ which is only valid for $\overline{\gamma}_2 < 1$. □

Using the quotient representation of the signalling connectivity, the $\mathcal{L}_2$-gain laminar pattern stability condition given by Theorem 3.4.2 enables the assessment of the efficacy of signal polarisation for plasticity control in local regions of mammary organoids. For the general case where $\overline{\gamma}_1, \overline{\gamma}_2 \neq 0$, then inequality

(3.26) reveals the asymmetries in pattern stability with respect to changes in the cross-layer connectivities of signalling graph $\mathcal{G}$. Namely, for fixed same-layer connections, $n_{1,L1}$ and $n_{1,L2}$, then $n_{2,L1}$ scales the influence of $\overline{\gamma}_2$ and $n_{2,L2}$ scales $\overline{\gamma}_1$ for the amount of signal anisotropy that is sufficient to stabilise cell-fate determinants.

To elucidate the specific role of the cross-layer connectivities in the stability of laminar patterns, consider the function $F : \mathbb{N}^2 \to \mathbb{R}$ that defines the upper bound of the polarity-dependent stability inequality (3.26) such that

$$F\left(n_{2,L_1}, n_{2,L_2}\right) = \frac{n_{2,L_2}(\overline{\gamma}_1-1)+n_{2,L_1}(\overline{\gamma}_2-1)-\sqrt{\left(n_{2,L_2}(\overline{\gamma}_1-1)+n_{2,L_1}(\overline{\gamma}_2-1)\right)^2+4(\overline{\gamma}_1-1)(\overline{\gamma}_2-1)(\overline{\gamma}_1\overline{\gamma}_2-1)n_{2,L_1}n_{2,L_2}}}{2n_1(\overline{\gamma}_1-1)(\overline{\gamma}_2-1)} \tag{3.32}$$

in the case of identical same-layer connectivities $n_1 = n_{1,L_1} = n_{1,L_2}$. To ensure that $F\left(n_{2,L_1}, n_{2,L_2}\right) \in \mathbb{R}$ we assume that $\overline{\gamma}_1\overline{\gamma}_2 < 1$ and $\left(\overline{\gamma}_1 - 1\right)\left(\overline{\gamma}_2 - 1\right) < 0$, i.e., we assume the stability of the laminar pattern state using the Small Gain theorem (Theorem 2.1.1). Without loss of generality, $\overline{\gamma}_1 > \overline{\gamma}_2$ as the representative cells converge to contrasting states and therefore the signals emanating from vertex v_1 will have a larger effect on the system dynamics compared to v_2. Critically, we observe that the Small Gain assumptions guarantee a pattern control asymmetry with respect to the connectivity of tissue such that

$$\frac{\partial F}{\partial n_{2,L_1}} - \frac{\partial F}{\partial n_{2,L_2}} > 0, \tag{3.33}$$

as numerically verified with examples given in Figure 3.12a.

If we place further mild and sufficient restrictions on the gains of the quotient system, we guarantee inequality (3.33). From direct computation, we have that

$$\begin{aligned}\frac{\partial F}{\partial n_{2,L_1}} - \frac{\partial F}{\partial n_{2,L_2}} = &\frac{\overline{\gamma}_2 - \overline{\gamma}_1}{4\left(\overline{\gamma}_1 - 1\right)\left(\overline{\gamma}_2 - 1\right)} \\ &+ \frac{\left(n_{2,L_2}\left(\overline{\gamma}_1 - 1\right) + n_{2,L_1}\left(\overline{\gamma}_2 - 1\right)\right)\left(\overline{\gamma}_1 - \overline{\gamma}_2\right) + 2\left(\overline{\gamma}_1 - 1\right)\left(\overline{\gamma}_2 - 1\right)\left(\overline{\gamma}_1\overline{\gamma}_2 - 1\right)\left(n_{2,L_1} - n_{2,L_2}\right)}{4\left(\overline{\gamma}_1 - 1\right)\left(\overline{\gamma}_2 - 1\right)\sqrt{\left(n_{2,L_2}\left(\overline{\gamma}_1 - 1\right) + n_{2,L_1}\left(\overline{\gamma}_2 - 1\right)\right)^2 + 4\left(\overline{\gamma}_1 - 1\right)\left(\overline{\gamma}_2 - 1\right)\left(\overline{\gamma}_1\overline{\gamma}_2 - 1\right)n_{2,L_1}n_{2,L_2}}}\end{aligned} \tag{3.34}$$

Following algebraic manipulation, inequality (3.33) is satisfied if and only if

$$\begin{aligned}&\left(\overline{\gamma}_1 - 1\right)\left(\overline{\gamma}_2 - 1\right)\left(\overline{\gamma}_1\overline{\gamma}_2 - 1\right)\left(n_{2,L_1}^2 - n_{2,L_2}^2\right) \\ &+ \left(\left(\overline{\gamma}_1 - \overline{\gamma}_2\right)\left(1 + \overline{\gamma}_2 - \overline{\gamma}_1\right) - 2\left(\overline{\gamma}_1 - 1\right)\left(\overline{\gamma}_2 - 1\right)\left(\overline{\gamma}_1\overline{\gamma}_2 - 1\right)\right)n_{2,L_1}n_{2,L_2} \\ &+ \left(\overline{\gamma}_2 - 1\right)n_{2,L_1}^2 - \left(\overline{\gamma}_1 - 1\right)n_{2,L_2}^2 < 0.\end{aligned} \tag{3.35}$$

As $0 < \left(\overline{\gamma}_2 - 1\right)\left(\overline{\gamma}_1\overline{\gamma}_2 - 1\right) < 1$ from the Small Gain assumption, then we have that

$$\left(\overline{\gamma}_1 - 1\right)\left(\overline{\gamma}_2 - 1\right)\left(\overline{\gamma}_1\overline{\gamma}_2 - 1\right) < \left(\overline{\gamma}_1 - 1\right), \tag{3.36}$$

and thus the n_{2,L_2}^2 terms of inequality (3.35) are negative. In addition, by solving the quadratic polynomials of $\overline{\gamma}_2$ from the coefficients of the n_{2,L_1}^2 and $n_{2,L_1}n_{2,L_2}$

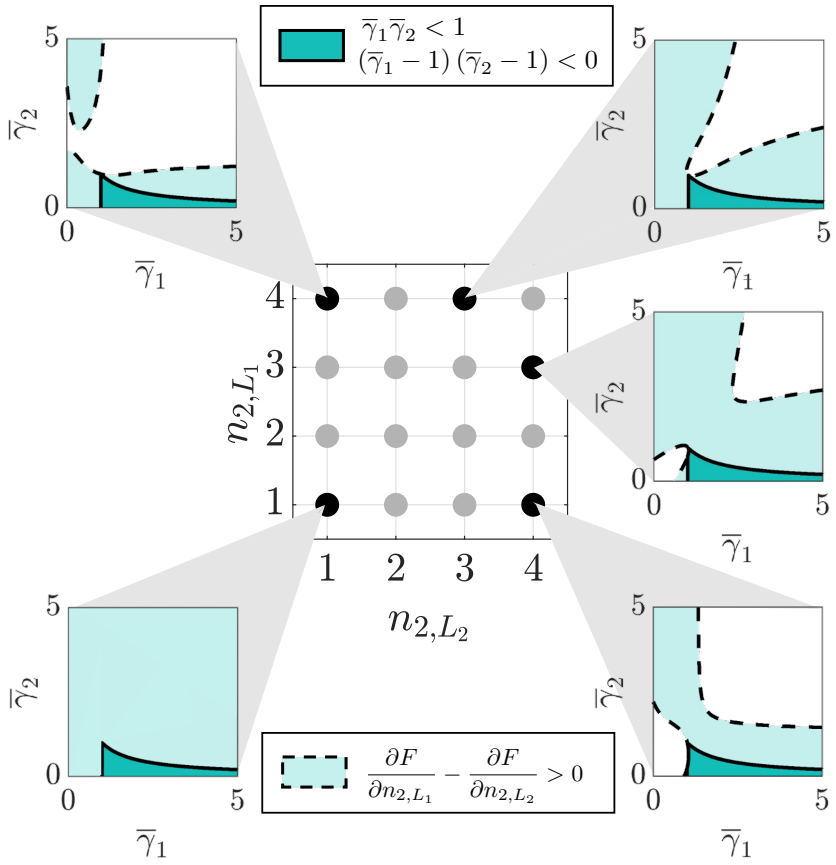

(a) Small Gains ensure asymmetry in cross-layer influence of laminar pattern stability.

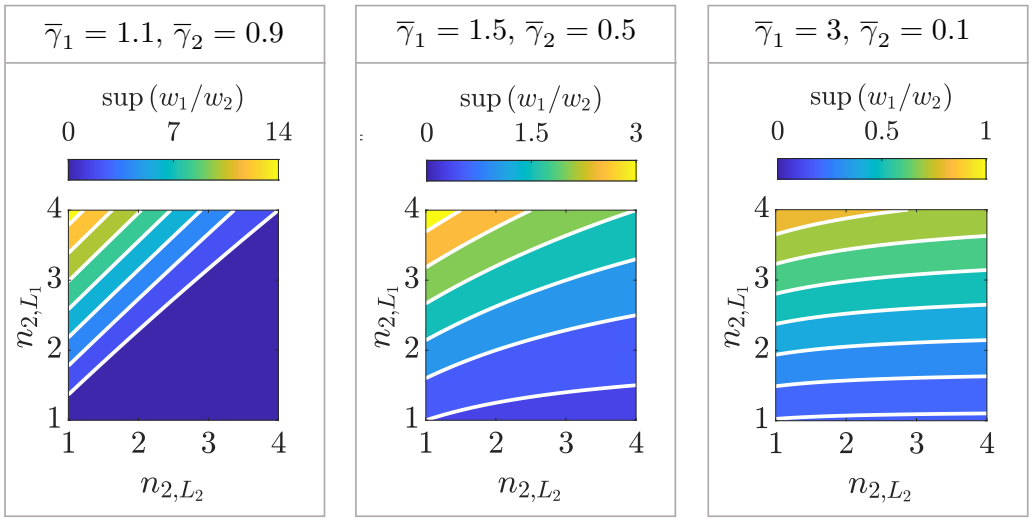

(b) Asymmetry in cross-layer influence of laminar pattern stability.

Figure 3.12: The dependence of polarity-driven laminar pattern stability on cross-layer connectivity. (a) A sample of regions of the quotient $\mathcal{L}_2$-gain space is shown for the existence of asymmetric cross-layer connectivities for laminar pattern stability such that inequality (3.33) is satisfied. The Small Gain assumptions $\overline{\gamma}_1\overline{\gamma}_2 < 1$ and $(\overline{\gamma}_1 - 1)(\overline{\gamma}_2 - 1) < 0$ are a subset of the asymmetric connectivity stability regions in all cross-layer connectivities considered. (b) Contour plots demonstrating the asymmetry in cross-layer connections in the upper bound of the polarity ratio w_1/w_2 by the stability inequality (3.26) for $\overline{\gamma}_1 > 1$, $\overline{\gamma}_2 < 1$, and $\overline{\gamma}_1\overline{\gamma}_2 < 1$. The same-layer connectivities were set to $n_{1,L_1} = n_{1,L_2} = 2$ for all plots.

terms of inequality (3.35), then if $\overline{\gamma}_2 \in \left(3-2\sqrt{2}, 1/2\right)$, we have

$$(1+\overline{\gamma}_2-\overline{\gamma}_1)<0 \quad \text{and} \quad (\overline{\gamma}_1-1)(\overline{\gamma}_2-1)(\overline{\gamma}_1\overline{\gamma}_2-1)<(\overline{\gamma}_2-1) \tag{3.37}$$

which ensures that the n_{2,L_1}^2 and $n_{2,L_1}n_{2,L_2}$ terms of (3.35) are also negative. Hence we have that the asymmetric stability inequality (3.33) is satisfied given a sufficient range of values of $\overline{\gamma}_2$.

The combination of analytic and numerical methods of examining the semi-regular polarity-dependent stability inequality (3.26) reveals that there must exist a dominant layer of cells controlling the stability of the laminar patterns. Specifically, the cross-layer connectivity of the vertex with the largest gain can have a substantially greater influence over the amount of polarity required to stablise the patterns when compared to the lower gain vertex, and critically, this discrepancy increases as the difference in gains increases, as shown in Figure 3.12b. Therefore, Theorem 3.4.2 suggests that if a lateral-inhibition mechanism governs cell-fate commitment in mammary epithelial cells, then there exists morphological regions of a branching organoid that are more susceptible to polarity-driven plasticity events, i.e. loss of laminar pattern stability, purely from the local geometry of the tissue. Specifically, this suggests the existence of a layer of cells that coordinate the cell-fate behaviour of the opposing layer, and without an audience (cross-layer connections) these cell-fate instructions are insufficient to maintain a distinct phenotypic bilayer of cells.

Throughout our analysis of the polarity-dependent stability inequality (3.26), we have assumed that the $\mathcal{L}_2$-gains of the quotient SISO system (3.6) are independent of connectivity and polarity. At steady state, the $\mathcal{L}_2$-gains of a system are equivalent to the derivative of the transfer function, $\overline{\gamma}_i = |T'(u_i^*)|$ for $i = 1, 2$, as discussion in Section 2.1.4. Therefore, in the following section we examine the inclusion of the non-monotonic $\mathcal{L}_2$-gains on the signal anisotropy required to stablise laminar patterns by introducing explicit lateral-inhibition kinetics.

3.5 Further support for polarity-dependent cell-fate control in developing mammary organoids

We revisit the lateral-inhibition dynamics of the Notch1-Dll1 kinetics for cell-fate commitment in mammary organoids [48], where we now allow for semi-regular connectivity structures to explore the impact cellular and tissue morphology, extending the regular graph pattern analysis conducted in Section 2.3.2. Firstly,

we redefine the Notch1-Dll1 IO model for cell-fate determination, then applying the existence and stability conditions derived in Section 3.4, we highlight specific morphological regions of mammary organoids that are more susceptible to plasticity event from a polarity control perspective.

Consider the Notch Delta model (NDM) derived in [87] describing core features of lateral-inhibition dynamics as previously defined in Section 2.1.1. Denote the level of active intracellular Notch1 and Dll1 in cell i by N_i and D_i, respectively. Then applying the IO representation to the NDM, let $\boldsymbol{x}_i = [N_i, D_i]^T$, such that the IO system (3.6) has the form

$$\begin{aligned} \dot{N}_i &= \frac{u_i^r}{\alpha + u_i^r} - \mu_N N_i, \\ \dot{D}_i &= \frac{1}{1 + \beta N_i^s} - \mu_D D_i, \\ y_i &= D_i, \end{aligned} \tag{3.38}$$

for $r, s \geq 1$ and $\alpha, \beta, \mu_N, \mu_D > 0$. The Delta signal outputs are transformed to input signals by the linear relation

$$\boldsymbol{u} = \boldsymbol{W}\boldsymbol{D}, \tag{3.39}$$

where $\boldsymbol{u} = [u_1, ..., u_{\mathcal{N}}]^T$, $\boldsymbol{D} = [D_1, ..., D_{\mathcal{N}}]$ and $\boldsymbol{W}$ is the weighted adjacency matrix associated with a layer-wise semi-regular graph $\mathcal{G}$ with block structure as given in equation (3.7). Applying the laminar pattern template to $\mathcal{G}$ using the equitable partition π_2, we generate the quotient NDM IO system such that we consider only two representative cells, $i \in \{1, 2\}$ ($\mathcal{N} = 2$), where intercellular interactions are now defined via the quotient weighted adjacency matrix, $\overline{\boldsymbol{W}}$, such that

$$[u_1, u_2]^T = \overline{\boldsymbol{W}}[D_1, D_2]^T, \tag{3.40}$$

where the general row-stochastic form of $\overline{\boldsymbol{W}}$ is given in equation (3.9). Inline with the connectivity regimes derived from cross-sections of primary and synthetic mammary organoids (figures 3.7 and 3.9), we will assume that same-layer connectivities are identical, $n_{1,L_1} = n_{1,L_2}$. This allows us to isolate the impact of variations in cross-layer connectivities on the laminar patterning of Notch in the mammary organoid.

To further reduce the dimensionality of the quotient IO system (3.38) and to analyse the existence and stability of laminar patterns using the methods derived in Section 3.4, we require the transfer representation of the intracellular kinetics. Namely, near steady states, we have

$$T'(u_i) = -\frac{\alpha\beta rs\mu_N^s \left(\alpha + u_i^r\right)^{s-1} u_i^{rs-1}}{\mu_D \left(\mu_N^s \left(\alpha + u_i^r\right) + \beta u_i^{rs}\right)^2} \tag{3.41}$$

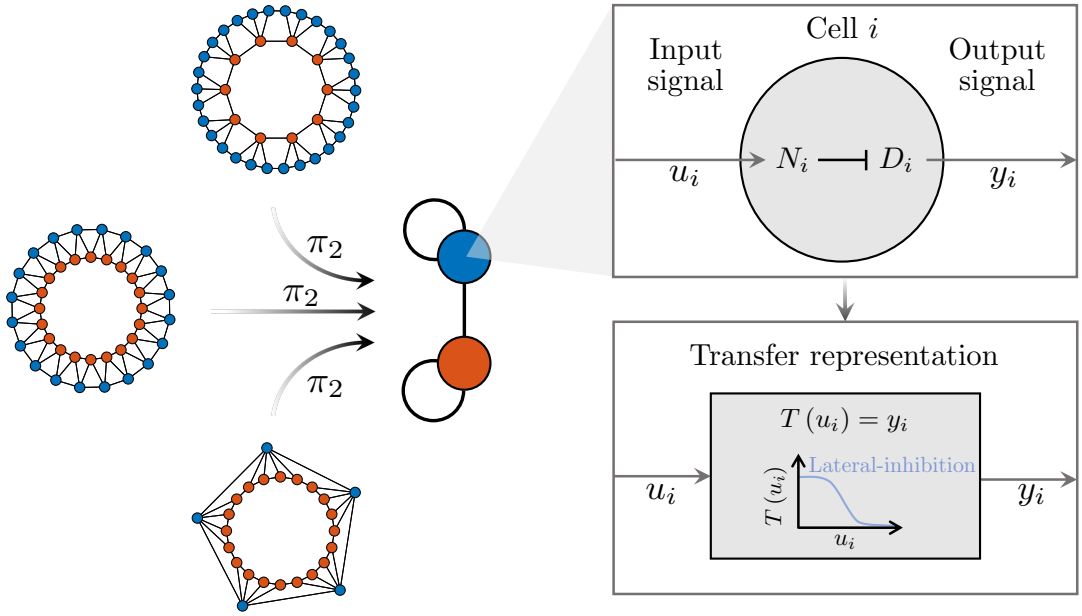

Figure 3.13: A diagram of the quotient NDM SISO system (3.38) constructed by the laminar pattern template partition, π_2, for semi-regular signal graphs. Vertices are coloured layer-wise with blue and orange vertices in L_1 and L_2, respectively. The IO flow diagram of the NDM kinetics are shown for a generic cell in the quotient graph. A reduced characteristic transfer representation of the NDM IO dynamics highlights the decreasing IO relation of lateral-inhibition.

as derived in Section 2.3.2 by linearisation of the NDM IO system (3.38), noting that $T'(u_i) \leq 0$ for all $u_i \in U$ indicating the lateral-inhibition intercellular interactions. A summary of the quotient representation of the NDM IO system (3.38) for laminar pattern analysis is given in Figure 3.13.

To apply the semi-regular laminar pattern existence condition from Theorem 3.4.1, we require the homogeneous input signal steady state, u^*. From our simple Notch-Delta formulation and previous analysis of the IO NDM (3.38), we have that $u^* = D^*$, the homogeneous steady state of Delta, where

$$\beta\mu_D (D^*)^{rs+1} + \mu_N^s (\mu_D D^* - 1)(\alpha + (D^*)^r)^s = 0. \tag{3.42}$$

To compare our semi-regular analysis to the regular connectivity analysis conducted in Chapter 2 we select the same intracellular parameter values, which are given in Table 3.1. Therefore, equation (3.42) yields a cubic polynomial in D^* which can directly solved to obtain $D^* = 0.049$. Subsequently, $|T'(u^*)| = 1.537 > 1$, satisfying our necessary requirement for instability of the homogeneous steady.

Invoking Theorem 3.4.1 for the existence of laminar pattern in the associated semi-regular large-scale IO system (3.6), we have that the quotient NDM IO system (3.38) will converge to contrasting heterogeneous states provided

Parameter	Description	Value
α	Notch activation constant	0.01
β	Delta de-activation constant	100
r	Notch activation cooperativity from input signals	2
s	Delta de-activation cooperativity from intracellular Notch	1
μ_N	Notch degradation rate	1
μ_D	Delta degradation rate	1
n_{1,L_1}	No. of same-layer connections in layer 1	2
n_{1,L_2}	No. of same-layer connections in layer 2	2

Table 3.1: Parameter values used in the analysis laminar pattern for semi-regular graphs using the NDM IO kinetics (3.38). The intracellular NDM parameters are selected from [87], as in Chapter 2. The intralayer connection parameters follow from the imposed 2D cross-sectional presentation of a mammary organoid.

inequality (3.11) holds. Figure 3.14a shows the pair-wise monotonic behaviour of the upper bound of inequality (3.11) with respect to cross-layer connectivities as predicted by Corollary 3.4.1. Namely, in agreement with our polarity-driven pattern analysis of regular connectivity networks, increasing the cross-layer connections, n_{2,L_1} and n_{2,L_2}, reduces the necessary amount of signal polarity required for HSS instability, with symmetry across $n_{2,L_1} = n_{2,L_2}$. Consequently, following our connectivity analysis conducted on cross-sections of mammary organoids, this suggests that both the branch tip and fold regions have identical Notch1 laminar pattern potential as highlighted by the characteristic cross-layer connectivity regimes superimposed over the polarity landscape.

Independent of the cross-layer connectivity symmetries, these findings suggest polarity-driven inhomogeneous Notch1 activity has a greater affinity to layer-wise semi-regular connectivity structures when compared to regular structures as we observe a maximal 1.38-fold increase in the sufficient polarity ratio w_1/w_2 for HSS instability between connectivity regimes I (or III) and II. Therefore, discrepancies in cellular shape between the layers of cells may promote the symmetry breaking of intracellular fate determinants during early organoid development. In particular, asymmetric cell division (both in size and intracellular protein distribution) of mammary stem cells has been observed to initiate morphological branching events and is promoted via Notch1 activation, suggesting a feedforward

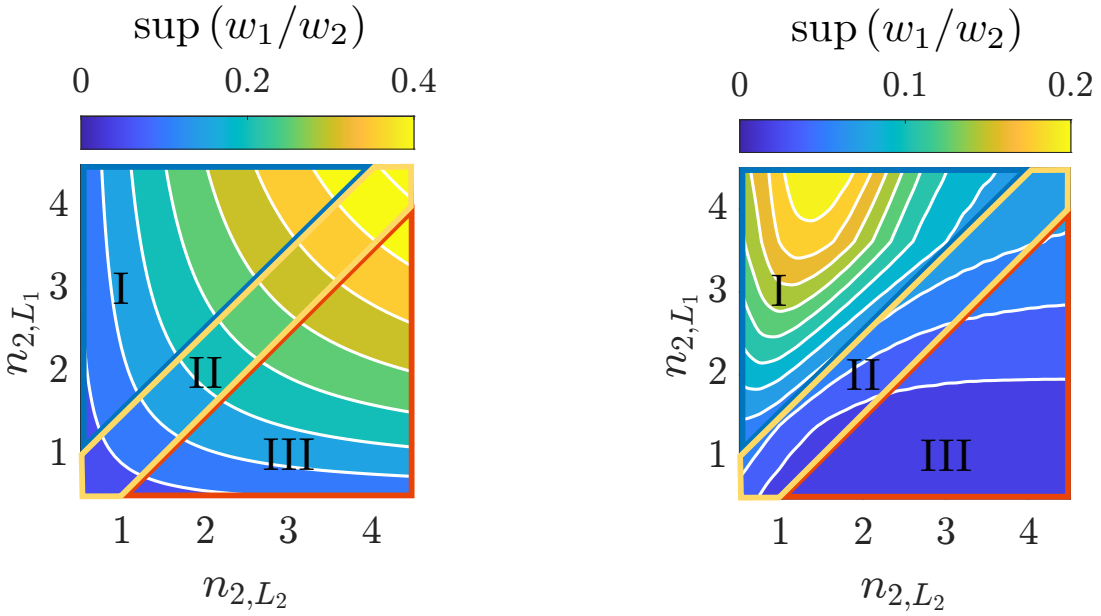

(a) Existence bound.

(b) Stability bound.

Figure 3.14: The influence of cross-layer connectivity on the Delta signal polarity for the (a) existence and (b) stability of the laminar patterns using pattern templating methods. Cross-layer connectivity regimes of developing mammary organoids identified in Section 3.3.2 are superimposed on the connectivity landscape. (a) The pair-wise monotonic behaviour of cross-layer connectivity on the upper bound of inequality (3.11) for the NDM kinetics (3.38) for pattern existence. (b) The asymmetric behaviour of cross-layer connectivity on the upper bound of inequality (3.26) for the local asymptotic stability of laminar patterns. The parameter values used to produce these plots are given in Table 3.1. Both cross-layer connectivity domains were uniformly discretised over a 50×50 grid. Polarity ratio values where linearly discretised between 0 and 0.4 with 100 values to determine $\sup(w_1/w_2)$ for each cross-layer connectivity combination, resulting in a total of 2.5×10^6 computations in (b).

mechanism of cell-fate and morphological heterogeneity for ductal development [170, 188].

To apply Theorem 3.4.2 for the stability of the laminar patterns in the quotient NDM IO system (3.38), we require the $\mathcal{L}_2$-gains associated with the heterogeneous steady input signals, $\overline{\gamma}_1$ and $\overline{\gamma}_2$. Near steady state, it can be shown that the $\mathcal{L}_2$-gains are equivalent to the singular values of the derivative of the transfer function [116], as these represent the largest local changes to the input to output dynamics. Subsequently, we have $\overline{\gamma}_i = |T'(u_i^*)|$ as $T'(u_i^*)$ is a scalar function, $i = 1, 2$ (SISO). The heterogeneous steady input states for the quotient NDM IO system (3.38) are given by

$$u_1^* = a(D_1^* - D_2^*) + D_2^* \quad \text{and} \quad u_2^* = b(D_2^* - D_1^*) + D_1^* \tag{3.43}$$

where D_1^* and D_2^* are the heterogeneous steady states Delta in each representative

cell. The parameters a and b are the quotient connectivity parameters for layers 1 and 2, respectively, as defined in equation (3.10). Without loss of generality, as the quotient NDM IO system (3.38) enters a laminar pattern state, we have $D_1^* > D_2^*$. In addition, increasing cross-layer connections, n_{2,L_1} and n_{2,L_2}, decreases the value of a and b, as these represent the same layer input signal contributions. Consequently, as $a, b \to 0$ by high signal polarity and increased cross-layer connections, then $u_1^* < u_2^*$. Figure 3.15a demonstrates that $|T'(u_i^*)|$ is decreasing for all $u_i > 0.005$, and therefore we have that $\overline{\gamma}_2 < |T'(u^*)| < \overline{\gamma}_1$. Subsequently, $\overline{\gamma}_1$ will dominate the contribution of $\overline{\gamma}_2$ for the stability of patterning due to the relatively significant increase in $\overline{\gamma}_1$ as u_1^* decreases, providing initial evidence for the predicted stability asymmetry with respect to the representative cells proposed in Section 3.4.2.

Setting the left-hand side of the quotient NDM IO system (3.38) to zero, we generate the following system of equations,

$$D_1^* = \frac{(\mu_N(\alpha + (a(D_1^* - D_2^*) + D_2^*)))^s}{(\mu_N(\alpha + (a(D_1^* - D_2^*) + D_2^*)))^s + \beta\mu_D(\alpha + (a(D_1^* - D_2^*) + D_2^*))^{rs}}, \tag{3.44}$$

$$D_2^* = \frac{(\mu_N(\alpha + (b(D_2^* - D_1^*) + D_1^*)))^s}{(\mu_N(\alpha + (b(D_2^* - D_1^*) + D_1^*)))^s + \beta\mu_D(\alpha + (b(D_2^* - D_1^*) + D_1^*))^{rs}}, \tag{3.45}$$

which we numerically solve[1] to determine the heterogeneous steady states of Delta, D_1^* and D_2^*, to obtain an upper bound on the polarity ratio w_1/w_2 for the stability of the laminar patterns.

The polarity-connectivity landscape for the stability of Notch laminar patterning determined using Theorem 3.4.2 is shown in Figure 3.14b, where we impose without loss of generality that $D_1^* > D_2^*$ and thus $\overline{\gamma}_1 > \overline{\gamma}_2$. Confirming the predicted asymmetry of the polarity-driven stability potential with respect to cross-layer connectivity, we observe the polarity required to stabilise laminar patterns is substantially less in connectivity regimes associated with branch base morphologies when compared to the ductal (spheroid) and branch tip regions. For example, the graphs with the connectivity $n_{2,L_1} = 3$ and $n_{2,L_2} = 1$ (regime I) present a 3.23-fold increase in the maximal polarity ratio w_1/w_2 when compared to graphs with $n_{2,L_1} = 2$ and $n_{2,L_2} = 2$ (regime II).

Critically, these observations suggest that polarity is a viable control mechanism for cell-fate commitment in morphological regions where myoepithelial (basal) cells have more cross-layer connections than the luminal cells, i.e., tissue regions like the base of a branch within mammary organoids where the

[1]Numerical solutions to equations (3.44-3.45) were found using the `fsolve` function in Matlab (2021a), which uses the trust-region-dogleg optimisation algorithm [151].

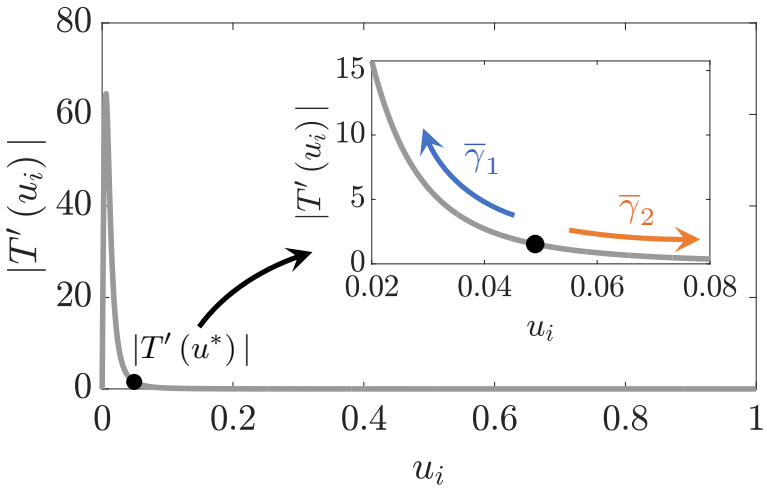

(a) Gain dynamics for the NDM kinetics.

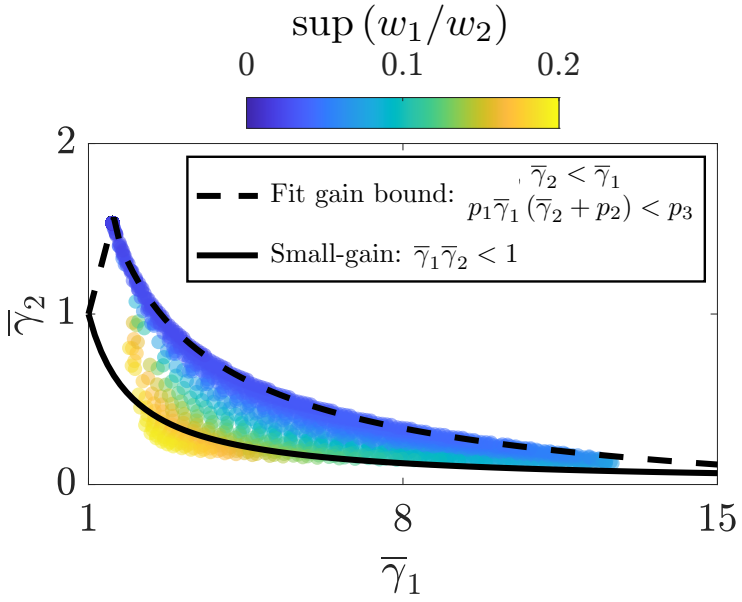

(b) Small gains are sufficient but not necessary for the stability of laminar patterns.

Figure 3.15: The $\mathcal{L}_2$-gains associated with laminar patterns in semi-regular bilayer geometries. (a) A plot of the input-output transfer function (3.41) for the NDM IO system (3.38). The homogeneous transfer state for the given homogeneous input signal, u^*, is highlighted with a solid marker. The inset provides a zoomed region about the homogeneous steady state. Gain dynamics with respect to the heterogeneous steady states are indicated with arrows such that $\overline{\gamma}_2 < \overline{\gamma}_1$. (b) The largest $\mathcal{L}_2$-gains of the quotient NDM system (3.38), $\overline{\gamma}_1$ and $\overline{\gamma}_2$, that satisfy the stability inequality (3.26) are shown for all 2500 computations used to generate the connectivity-polarity landscape in Figure 3.14*b*. Each point is coloured by the value of the upper bound of the polarity ratio for the stability of laminar patterns by inequality (3.26). The region below the solid line corresponds to the Small Gain bound $\overline{\gamma}_1\overline{\gamma}_2 < 1$ whereas the region below the dashed line represents a numerically determined bound on the $\mathcal{L}_2$-gains for the stability of laminar patterns, for all cross-layer connectivity regimes considered in Figure (3.14). The parameter values used to produce these plots are given in Table 3.1.

apical surface of the myoepithelial cells is elongated, while basal surface of the luminal cells is reduced as a consequence of tissue bending [189]. Therefore, the basal cells are positioned as the cell-fate pattern conductors of the mammary organoids due to their characteristic increase in the output signal Dll1 [49], and thus lack of contact, and subsequently, communication with basal cells may result in loss of consistent laminar patterning of cell-fate determinants. These propositions predict the existence of polarity-induced increased plastic behavior via Notch1 in MECs near the branch tip regions, while lineage commitment should be stable near branch initiation, in agreement with existing experimental observations [131, 170, 188]. Fundamentally, if cell-fate is determined via canonical Notch interactions, then these findings predict that Delta activator should be asymmetrically distributed along the basal-luminal interface of the outer basal cells.

Each pair of the $\mathcal{L}_2$-gains, $\overline{\gamma}_1$ and $\overline{\gamma}_2$, used to generate the connectivity-polarity landscape for laminar pattern stability (Figure 3.14b) is shown in Figure 3.15b. Notably, each $\overline{\gamma}_1$ and $\overline{\gamma}_2$ satisfied the asymmetric connectivity inequality (3.33) for laminar pattern stability in quotient IO systems. Only a minority of the $\overline{\gamma}_1$ and $\overline{\gamma}_2$ pairs satisfied the Small Gain bound $\overline{\gamma}_1\overline{\gamma}_2 < 1$, but these restricted gains presented the largest upper bound for the polarity ratio w_1/w_2 using inequality (3.26). That is, the Small Gain bound is a subregion of the numerically fit gain bound[2] $p_1\overline{\gamma}_1\left(\overline{\gamma}_2 + p_2\right) < p_3$ where $p_1 = 0.634$, $p_2 = 0.316$ and $p_3 = 2.417$, supporting that the Small Gain theorem (Theorem 2.1.1) is sufficient but not necessary for the stability of laminar patterns. Namely, the stability criterion for semi-regular graphs (Theorem 3.4.2) provides greater insight into the influences of connectivity and polarity on the local pattern dynamics. Yet, we observe that the $\mathcal{L}_2$-gain pairs associated with the least amount of signal polarity (highest w_1/w_2 ratios) required for pattern stability satisfy the Small Gain bound $\overline{\gamma}_1\overline{\gamma}_2 < 1$. Thus, figures 3.14b and 3.15b suggest that the Small Gain assumptions proposed in Section 3.4.2 are sufficient to guarantee the asymmetric connectivity inequality (3.33) for laminar pattern stability. However, further work is needed to verify this.

Large-scale simulations of the NDM IO system (3.38) calibrated using the quotient analysis for the stability of laminar patterns are provided in Figure 3.16. In agreement with the quotient NDM IO system (3.38) analysis, we found that the cross-layer connectivity regimes associated with the branch tip and branch base generate significantly different Notch dynamics, demonstrating the inability of polarity to control Notch dynamics in tip-like morphologies, while

[2]The coefficients of gain bound sufficient for laminar pattern stability of the quotient NDM IO system (3.38) were determined using the `lsqnonlin` function in Matlab (2019a) [151], $R^2 = 0.997$.

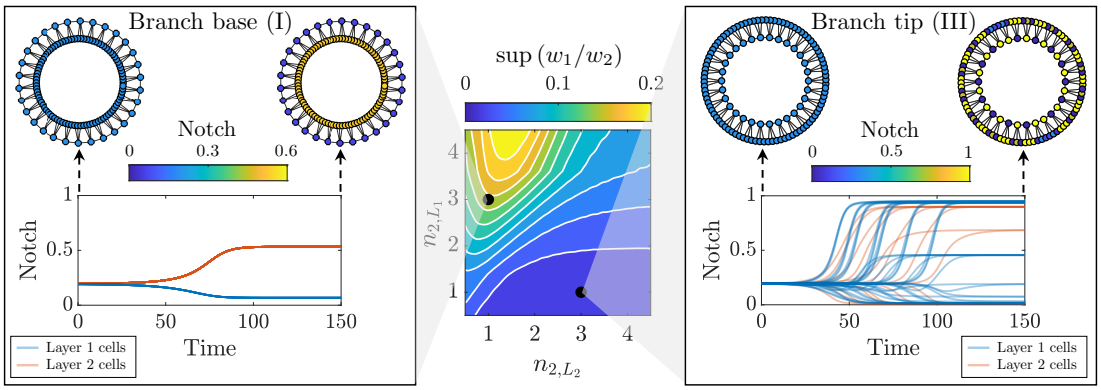

Figure 3.16: Large-scale simulations of the NDM IO system (3.38) with the characteristic branch base and branch tip connectivity graphs. Simulations are presented with $|V| = 120$ and $w_1/w_2 = 0.125$. Trajectories are numerically determined using the `ode45` function in Matlab (2021a) with initial conditions locally perturbed about the HSS $[N^*, D^*] = [0.194, 0.049]$. Cross-layer connectivity parameters are shown with respect to the polarity-connectivity landscape sufficient for laminar pattern stability in the associated quotient IO systems. Parameter values for the NDM IO system (3.38) are given in Table 3.1.

convergent laminar patterns are formed in the branch base structures. Notably, the polarity-driven HSS instability condition is identical for both large-scale dynamical systems due to the symmetry of inequality (3.11) with respect to cross-layer connectivities (Figure 3.14a), indicating a dominant role signal stability in pattern generation. Therefore, further investigation is required to understand the links between the large-scale and quotient IO systems with respect to the stability conditions sufficient to control desired patterns in systems with multiple steady states.

3.6 Discussion

In this chapter, we have used a combination of primary and synthetic data to demonstrate the predictive power of tissue curvature for estimating local cell signalling graphs in simple branching morphologies. This generated characteristic connectivity regimes for different regions of 2D cross-sections of mammary organoids, which were used to analyse the influence of local epithelial packing structure on polarity-driven cell-fate stability using IO models. Specifically, we provide evidence that convex locations of mammary organoids, like branch tips, are more susceptible to polarity-assisted plasticity events and loss of laminar patterning of Notch1 using a lateral-inhibition mechanism when compared to concave regions, like the base of a branch.

Following from the generality of our SISO analysis in Section 3.4 models, we

predict the existence of a cell-fate commitment coordinating cell type purely from the edge topology of the cell signal graph, independent of the precise lateral-inhibition kinetics and intracellular parameterisation. Critically, under the assumption that the signal gain must be larger in basal cells, as they typically have reduced Notch1 activation [21, 48], we isolate the outer basal cells as the cell-fate coordinators in developing mammary glands. Specifically, the stability of laminar patterns in bilayer tissues is significantly more sensitive to the connectivity of basal cells when compared to luminal cells. Thus, we show increasing the heterotypic connections of basal cells reduces the amount of active layer-wise signal anisotropy sufficient to stabilise cell-fate biomarkers.

These results are partially consistent with the size-dependent lateral-inhibition patterns predicted *in silico* [190] and validated *in vitro* in CHO-K1 monolayers [169]. Namely, the authors demonstrate that smaller cells are more likely to become the signal senders (high Dll1) suggesting that the outer layer of cells should converge to a low-Notch state for cell-fate stability as expected, as basal cells are approximately 20% smaller than luminal cells (confirmed using our image analysis). However, the form of their argument follows a surface-area approach such that cells with reduced cell-cell contact surface area have limited access to activator-receptor binding locations, preventing the intracellular activation of Notch. In contrast, our curvature-based approach to Notch patterning revealed that increasing the surface area of the basal cells at the basal-luminal interface increased the stability of the laminar patterns of Notch in mammary bilayers. Although, the contact area signal activation mechanism suggested in [169] may account for the cross-layer polarity ($w_1 < w_2$) necessary for laminar patterning in lateral-inhibition systems, suggesting that the total basal-basal contact area (w_1) must be significantly less than the basal-luminal contact area (w_2) for cell-fate commitment.

We predict that the differences in these conclusions may be due to the differences in tissue domain type considered in each study, i.e., we consider abstract bilayer geometries using graphs whereas the size-dependent studies focused on regular monolayers [169, 190]. Therefore, our approach provides an alternative polarity-connectivity theory for cell-fate commitment in mammary organoids, further highlighting the often under appreciated role of tissue geometry in fine-grained pattern formation. In particular, the generic perspective of signal polarity taken in this study calls for further investigations into the direct mechanisms that drive signal activator asymmetries in mammary orangoids, specifically cell shape and contact regions.

From an experimental perspective, our proposed tissue curvature-dependent cell-fate patterning is in agreement with geometry-induced branch elongation

[31] and cellular plasticity [191] studies conducted on MECs. However, explicit experimental evidence of asymmetric distributions of Delta1 on the membrane surface of MECs is yet to be found. Therefore, to verify our claims of the active role of polarity in cell-fate stability, similar collagen well "stamping" experiments for prescribed tissue geometries be applicable to observe Dll1 spatial distributions in various morphological regions of mammary organoids, specifically, comparing the concave and convex regions which should present the large discrepancies as predicted by our theoretical investigations. Furthermore, the protein Neuralized1 has been shown to actively promote Dll1 apical-basal polarity in epithelial cells [192], and is required for healthy differentiation in MECs [193]. These studies suggest that supplementation of Neuralized1 and tissue geometry may exaggerate Dll1 polarisation in mammary organoids and therefore may be exploited for experimental validation of a polarity-driven cell-fate commitment mechanism.

Organoids are fundamentally 3D tissues and therefore our approach to analyse and calibrate the IO models using data extracted from 2D cross-sections of mammary organoids is a direct limitation of this study. We note that this approach was only taken due to limited access to high-resolution primary images of mammary organoids with basal and luminal cell-type markers. Appreciating that the 2D analysis provides only a subset of the region-based connectivity information, both the image and IO analysis conducted in this study are immediately valid for 3D investigations, in preparation for future studies. Namely, the curvature-connectivity image analysis pipeline was originally designed for 3D analysis and is fully described in Appendix B. In addition, the topological description of the interconnected IO models used for cell-fate pattern analysis is independent of spatial dimension, that is, the analytic exploration in Section 3.4 revealed the monotonicity of laminar pattern existence and cross-connectivity asymmetries in pattern stability hold independent of the precise cell signalling connectivity and intracellular kinetics of the model IO system. Thus, it is anticipated that the qualitative conclusions drawn from our data analysis will be preserved when extended to a 3D context, primarily attributed to the isolated impact of tissue curvature on heterotypic connectivity. This assertion is critical to reinforce the robustness and validity of our findings on the interplay of geometry and polarity in cell-fate determination.

When performing the IO analysis in Section 3.4, pair-wise luminal and basal connectivity regimes were employed to generate local quotient cell signalling graphs facilitating low-dimensional representations of the global system. Consequently, each pair-wise quotient graph representing a distinct local region of the mammary organoid was analysed in spatial isolation, assuming global layer-wise symmetry in edge topology. Thus, how the coupling of these

local quotient connectivities to form a representative global signalling graph affects the cell-fate pattern dynamics remains to be studied. A natural extension of the semi-regular IO framework considered in this chapter to accommodate the piece-wise connections of the local quotient graphs is to adopt the *balanced systems* approach from network dynamics synchronisation which relaxes the topological symmetries to instead agree with the geometric symmetries of the tissue [194]. Specifically, using the formal construction of equivalence relations over the weighted graph to form equitable partitions for quotient representation, under the constraint of sum constant edge weightings. That is, by initially embedding weak-coupling of the laminar pattern templated quotient graphs in a multilayer representation, exploiting the structural symmetries in the coupled mutlilayer adjacency matrices may be exploited for spectral decompositions in polarity-driven pattern analysis [195], allowing for similar analytical approaches applied in this chapter but for more varied edge topologies.

The cell-fate analysis in this chapter only considered the resultant changes in local neighbourhood cell-type compositions from the variations in tissue curvature. Yet, cells have mechanosensing mechanisms for adapting to changes in tissue geometry, independent of their neighbourhood, which is particularly relevant when measured curvatures are closed to the characteristic lengths of the cells [162]. For example, deformations to the cytoskeleton induces the activation of the Hippo pathway in MECs [196]. This complex signalling cascade has been shown to play a pivotal role in mediating cell-cycle progression, and has furthermore been demonstrated to exert a significant influence on the dynamics of Notch signalling in MECs [197], evidencing a direct curvature cell-fate relationship in mammary organoids. In addition, fibroblast growth factor (FGF) signalling plays a critical role in branching morphogenesis by regulating migration and differentiation of MECs for ductal elongation [16, 198], and also is known to agonistically interact with the Notch pathway [199]. Importantly, FGF activity is also directly regulated by tissue curvature as demonstrated in lung branching and intestinal crypt formation [108, 200], providing further support for geometric dependence of MEC cell-fate control via pathway crosstalk.

Thus, to fully appreciate the multitude of factors contributing to cell-fate control in MECs during mammary organoid development, signal pathway crosstalk must be considered. Coupling inter and intracellular pathway interactions often generates multiple spatially dependent variables, which are inaccessible using our current modelling approaches. Subsequently, to comprehensively explore the role of tissue structure on intracellular patterning, a general framework for fine-grained pattern analysis should be established to account for multiple simultaneous spatially dependent signal processes.

Chapter 4

A framework for analysing polarity-driven laminar patterns with multiple cell-cell communication channels

In chapters 2 and 3, we studied cell-fate dynamics in mammary bilayers using a single signalling pathway. Yet, the cellular regulatory mechanisms that determine cell states are complex, often involving multiple inter-linked genetic regulatory networks (GRNs), commonly referred to as pathway crosstalk [201]. Consequently, pathway crosstalk may induce multiple modes of independent cell-cell communication channels, such as contact-based (juxtacrine), or short-range diffusive (paracrine) cellular interactions between local cells [16, 48]. Thus, cells potentially receive local tissue information from a range of sources to consistently select the appropriate cell type for functional ductal formation.

Due to the additional complexity involved with pathway crosstalk, from unknown intracellular kinetics to spatial cell-cell interactions, the precise role polarity has in influencing intracellular kinetics that governs cell-fate choices is widely unresolved [202]. Therefore, in this chapter, we extend the general single-input-single-output (SISO) modelling framework, initially introduced in Chapter 2, to include crosstalk kinetics in generality. This allows us to study the interplay of polarity and multiple cell-cell signalling mechanisms in generating laminar patterns of biomarkers, conforming with the process of cell-fate determination of developing bilayer tissues.

Following Turing's seminal paper in 1952 [93], the majority of theoretical results of pattern formation in developmental biology focus on diffusion-driven instabilities of reaction-diffusion (RD) systems [97, 203]. RD systems rely on the assumption that cells communicate using short-range and/or long-range paracrine signalling mechanisms, namely the local diffusion of proteins coupled

with intracellular kinetics. However, there exist many pattern-forming biological systems that rely on non-diffusive, juxtacrine communication, such as lateral-inhibition mechanisms, facilitating fine-grain pattern formation [27, 204].

The fundamental differences in paracrine and juxtacrine signalling motivate contrasting modelling approaches. The diffusion process in paracrine signalling extends to a spatial continuum limit, generating systems of partial differential equations (PDEs) allowing protein patterns to form over multiple cell lengths to represent phenomena such as morphogen gradients over the tissue [97]. In constrast, the discrete nature of juxtacrine signalling induced by membrane contact necessitates the use of spatially discrete systems of ordinary differential equations (ODEs) [138]. Subsequently, these contrasting modelling paradigms restrict the specific continuum and discrete approaches to pattern analysis in systems where both diffusive and non-diffusive mechanisms are present.

Graphs representing spatially discrete analogues of diffusive mechanisms have previously been employed to homogenise the analytical approaches to pattern formation and, further, investigate cell structure on pattern emergence [205]. That is, graph vertices depict cells and edges are drawn between cells if they are communicating via diffusive proteins. Critically, this approach preserves the concept of cell identity within diffusive models and transforms the systems of PDEs into much larger systems of ODEs, consistent with the juxtacrine model formulation. However, the central theme of pattern analysis is understanding the conditions that yield the degradation of stable homogeneity of the system and is typically conducted via linear stability analysis with coupled spatio-temporal components [87, 95, 124]. Consequently, the high dimension of these ODE descriptions and required nonlinear kinetics of multicellular domains limit analytical approaches which lead to many studies focusing on spatially reduced systems accompanied by numerical simulations for the larger cellular domains [87, 124, 138]. Critically, the analysis conducted on such spatially reduced models is insufficient for predicting the types of patterning observed numerically [124], with similar results for cell-resolution discretised diffusive systems [206].

The graphical methods of fine-grain pattern analysis using input-output (IO) systems, as initially proposed in [117] and applied in chapters 2 and 3, were later extended in [186] and [207] to include multiple channels of cell-cell communication. The authors simultaneously couple diffusive and non-diffusive signalling mechanisms within the interconnected dynamical systems framework using directed multilayer graphs, namely graphs with unidirectional edges connected to cells with multiple input and output signals. Both studies applied the pattern templating methods described in [118], which were applied to yield analytic insight into the capacity of the mixed-signalling mechanism IO systems

to generate the desired pattern. However, both studies focused on dynamical systems describing purely competitive cell-cell kinetics (e.g. lateral-inhibition) with unweighted connectivity graphs, leveraging characteristic cell properties for long-time behaviour. Namely, the influence of edge weights (polarity) and generic intracellular crosstalk kinetics on pattern existence and convergence in these multi-channel interconnected systems is yet to be investigated.

The spatial scalability of the interconnected methods of pattern analysis follows from the theory of monotone dynamical systems [115]. Provided the intracellular proteins regulated by the prescribed GRN react monotonically to intercellular stimuli, then global dynamics become predictable in a closed-loop of cells and facilitate the introduction of control theoretic tools for pattern stability [118]. Although the restriction to bipartite connectivity graphs was imposed in [117] and [207] as a sufficient measure to preserve the monotonic behaviour of lateral-inhibition models in the large-scale forms, these restrictions limit the biological applications. Such conditions can be relaxed when seeking pattern existence in quotient systems, as demonstrated in [118] but how such behaviour translates to the large-scale counterpart is not fully understood.

In chapters 2 and 3, we have analysed the role of polarity in laminar pattern formation using interconnected methods for a single juxtacrine signalling mechanism [143]. Here, we generalise and extend these results to include multiple signalling mechanisms of any type using a multilayer graph approach as defined in [207]. Namely, we explore the interplay of multilayer network topology and edge weights in laminar pattern formation in bilayer tissues using dynamical systems of generic cooperative and competitive kinetics.

Initially, we present conditions for the existence, uniqueness and instability of a homogeneous steady state for a large-scale multi-input-multi-output (MIMO) dynamical system which extends the conditions of [207] to yield analytically applicable statements for low-spatial order intracellular GRNs. Thereafter we use methods of multilayer graph partitioning to derive polarity conditions for the existence of laminar patterning in large-scale systems. Critically, we demonstrate the graph commutativity requirements imposed in [207] for simultaneous diagonalisation can be relaxed when seeking patterns of only two states, allowing a broader range of quotient connectivities to be explored.

We investigate the spectral links between quotient and large-scale dynamical systems. We prove positional changes of the eigenvalues associated with laminar patterns in the multigraphs are dependent on the amount of polarity for non-bipartite graphs. We then discuss the implications of spectral rearrangements with respect to bipartite graphs and laminar patterning. Combining our insights from the spectral rearrangements and quotient system analysis we explore the

convergence of laminar patterns in the associated large-scale dynamics systems. In the final section of this chapter, we extend the $\mathcal{L}_2$-gain interconnection stability criterion to analyse MIMO systems. Using spectral properties of the multilayer graphs, we show that assessing the stability of a MIMO system does not increase the dimensionality of the problem when compared to SISO systems, providing analytical access to generating bounds on cell signal gains for pattern stability using the polarity and topology of the MIMO system.

4.1 Existence of cellular heterogeneity

In this section, we are interested in deriving conditions for the existence and instability of a homogeneous steady state (HSS) of a large-scale dynamical system that describes intracellular kinetics within a tissue of cells. First, we define the types of interconnected dynamical systems considered in this study, namely, coupling the multiple input and output signal dynamics of individual cells using weighted connectivity graphs associated with each respective signalling mechanism. Thereafter, we exploit the repetitive structure of large-scale interconnected dynamical systems to provide analytically tractable conditions for the existence, uniqueness and stability of the HSS that is necessary for the investigation of spatially-driven cellular heterogeneity.

4.1.1 The signal polarity interconnected system for bilayer geometries with multiple signal mechanisms

Consider a large-scale interconnected dynamical system representing N spatially discrete cells, each containing n intracellular proteins. Namely, for each cell $i \in \{1, ..., N\}$, let $\boldsymbol{x}_i = [x_{i,1}, ..., x_{i,n}]^T \in X \subset \mathbb{R}^n_{\geq 0}$ be the concentration of the n intracellular proteins. The cellular signal inputs and outputs are defined by $\boldsymbol{u}_i = [u_{i,1}, ..., u_{i,r}]^T$, $\boldsymbol{y}_i = [y_{i,1}, ..., y_{i,r}]^T \in U, Y \subset \mathbb{R}^r_{\geq 0}$, respectively, for some r with $1 \leq r \leq n$. The interconnected ODE system has the form

$$\dot{\boldsymbol{x}}_i = \boldsymbol{f}\left(\boldsymbol{x}_i, \boldsymbol{u}_i\right), \tag{4.1}$$

$$\boldsymbol{y}_i = \boldsymbol{h}\left(\boldsymbol{x}_i\right), \tag{4.2}$$

where $\dot{\boldsymbol{x}}_i$ represents the derivative with respect to time. The function $\boldsymbol{f} : X \times U \to X$ defines the intracellular protein dynamics which are dependent on external stimuli, $\boldsymbol{u}_i$, produced by connected cells. We define cellular connectivity in terms of multiple signalling mechanisms later in this section. Furthermore, $\boldsymbol{h} : X \to Y$ describes the translation of intracellular dynamics to signal outputs of the cell. We assume that both functions $\boldsymbol{f}(\cdot)$ and $\boldsymbol{h}(\cdot)$ are both $\mathcal{C}^2$ over their respective

domains to ensure the continuity of the corresponding linearised system that is required for the interconnected pattern analysis in Section 4.2. The structure of the IO system (4.1) in the context of the tissue is shown in Figure 4.1. For convenience, when discussing tissue behaviour, we define the large-scale vectorised counterparts of the intracellular state variables, signal inputs and outputs by $\boldsymbol{x} = [\boldsymbol{x}_1, ..., \boldsymbol{x}_N]^T$, $\boldsymbol{u} = [\boldsymbol{u}_1, ..., \boldsymbol{u}_N]^T$ and $\boldsymbol{y} = [\boldsymbol{y}_1, ..., \boldsymbol{y}_N]^T$.

For the transition of signal outputs to inputs, we assume that each output signal is independent and defines a linear relationship between output and input signals. Let $V \coloneqq \{v_1, ..., v_N\}$, be vertices representing the cells in the tissue, then for each output signal $y_{i,j}$ there is an associated connectivity graph $\mathcal{G}_j = \mathcal{G}_j(V, E_j)$, where E_j is the set of edges for each output signal mechanism $1 \leq j \leq r$. Note that the vertex set V is identical for each connectivity graph whereas edge structure may differ between the respective graphs to allow for different signalling mechanisms within the IO system (4.1). For example, the cellular connectivity graphs of contact-dependent and long-diffusion mechanisms have potentially different edge structures as it is expected that the average degree of the contact-based graph is less than that of a diffusive mechanism due to the physical constraints of cellular junctions (Figure 4.1).

Algebraically, the cell-cell interaction graphs are represented using the weighted adjacency matrix, $\boldsymbol{W}_j \in \mathbb{R}_{\geq 0}^{N \times N}$. Let $\boldsymbol{\mathcal{W}} \coloneqq \{\boldsymbol{W}_j\}$ be the set of weighted and row-stochastic adjacency matrices, namely, for any $j \in \{1, ..., r\}$ and any row $i \in \{1, ..., n\}$ then the row-sum $\sum_k (\boldsymbol{W}_j)_{ik} = 1$ which represents the weighted average of signal transfer between connected cells. In addition, we assume that the connectivity graph $\mathcal{G}_j$ associated with $\boldsymbol{W}_j$ is undirected and connected, and thus $\boldsymbol{W}_j$ irreducible, i.e., there exists no permutation matrix that transforms $\boldsymbol{W}_j$ to upper triangular form [208].

To preserve the order of signal outputs, $y_{i,j}$, and therefore the cellular structure within the IO system (4.1), we define the global interconnection matrix, $\boldsymbol{P}$, that is constructed by interweaving each $\boldsymbol{W}_j \in \boldsymbol{\mathcal{W}}$ in order of output signal defined by $y_{i,j}$, namely,

$$\boldsymbol{P} = \sum_{j=1}^{r} \boldsymbol{W}_j \otimes \boldsymbol{D}_j, \tag{4.3}$$

where $\otimes$ is the Kronecker product and $\boldsymbol{D}_j = \operatorname{diag}(\delta_{j,1}, ..., \delta_{j,r})$ for $\delta_{i,j}$ the Kronecker delta function

$$\delta_{i,j} = \begin{cases} 1 & i = j, \\ 0 & i \neq j. \end{cases} \tag{4.4}$$

The global interconnection matrix $\boldsymbol{P} \in \mathbb{R}^{rN \times rN}$, therefore, produces a multilayer graph, $\mathcal{G}_{\boldsymbol{P}}$, that is layer-wise independent as shown in Figure 4.1.

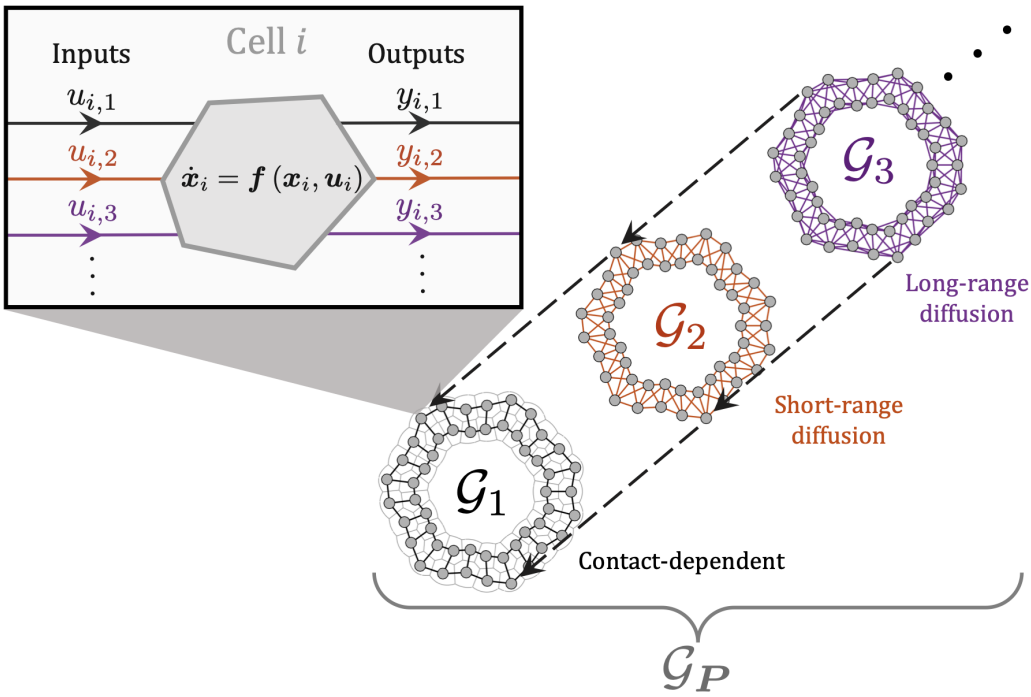

Figure 4.1: A graphical representation of the IO system (4.1) for bilayer geometries with multiple signalling mechanisms defined by the global adjacency matrix $\boldsymbol{P}$ (4.3). Example 2D bilayer graphs are shown for contact-dependent short and long-range diffusion over the same vertex set representing the cells in the tissue, which are explicitly shown with membranes in $\mathcal{G}_1$ to highlight the bilayer cellular structure. Each of the connectivity graphs is then embedded within the same vertex set as indicated by the dashed arrows. Therefore, each vertex contains the intracellular kinetics defined by the IO system (4.1), which responds to the signal outputs of adjacent cells for each signalling mechanism, which are transformed to signal inputs by $\boldsymbol{P}$, as defined in equation (4.5).

Critically, the construction of $\boldsymbol{P}$ defines the linear relationship between global signal outputs and inputs

$$\boldsymbol{u} = \boldsymbol{P}\boldsymbol{y} \tag{4.5}$$

where the cell-wise input-output structure is preserved. The fundamental cellular identity-preserving structure of $\boldsymbol{P}$ is demonstrated in the following example.

Example 4.1.1. *Consider the two general matrices*

$$\boldsymbol{W}_1 = \begin{bmatrix} a_{11} & a_{12} \\ a_{21} & a_{22} \end{bmatrix} \quad \textit{and} \quad \boldsymbol{W}_2 = \begin{bmatrix} b_{11} & b_{12} \\ b_{21} & b_{22} \end{bmatrix} \tag{4.6}$$

for the IO system (4.1) with only two cells each with two signal inputs and outputs i.e., $r = 2$. Then the global interconnection matrix, $\boldsymbol{P}$, has the form

$$\boldsymbol{P} = \begin{bmatrix} a_{11} & a_{12} \\ a_{21} & a_{22} \end{bmatrix} \otimes \begin{bmatrix} 1 & 0 \\ 0 & 0 \end{bmatrix} + \begin{bmatrix} b_{11} & b_{12} \\ b_{21} & b_{22} \end{bmatrix} \otimes \begin{bmatrix} 0 & 0 \\ 0 & 1 \end{bmatrix} = \begin{bmatrix} a_{11} & 0 & a_{12} & 0 \\ 0 & b_{11} & 0 & b_{12} \\ a_{21} & 0 & a_{22} & 0 \\ 0 & b_{21} & 0 & b_{22} \end{bmatrix}. \tag{4.7}$$

To study the role of layer-dependent signalling polarity for the generation of laminar patterns in bilayer geometries, we consider each graph to have two layers $L_1 \coloneqq \{v_1, ..., v_{|L_1|}\}$ and $L_2 \coloneqq \{v_{|L_1|+1}, ..., v_N\}$ where $|L_1| = 1, ..., N-1$, as shown in figures 4.1 and 4.2.

This layer-wise grouping of the vertices also provides a consistent structure to the weighted adjacency matrices $\boldsymbol{W}_k \in \boldsymbol{\mathcal{W}}$. As a first approach to the layer-dependent signal polarity, we consider only two values of edge weights for connected cells in the same and different layers as highlighted in Figure 4.2. Namely, consider the graph $\mathcal{G}_k$ associated with $\boldsymbol{W}_k$, then if $v_i, v_j \in L_1$ (or L_2) such that v_i and v_j are connected by an edge in $\mathcal{G}_k$ and are in the same layer, then $(\boldsymbol{W}_k)_{ij} = \hat{w}_1^{[k]}$, where $\hat{w}_1^{[k]}$ is the row-normalised intralayer edge weight. Similarly, if v_i and v_j are in different layers, $v_i \in L_1$ and $v_j \in L_2$, and are connected in $\mathcal{G}_k$ then, $(\boldsymbol{W}_k)_{ij} = \hat{w}_2^{[k]}$, where $\hat{w}_2^{[k]}$ is the row-normalised interlayer edge weight. Consequently, when vertices are indexed consecutively from L_1 then L_2, each $\boldsymbol{W}_k$ has block form

$$\boldsymbol{W}_k = \begin{bmatrix} \widehat{\boldsymbol{W}}_{1,L_1}^{[k]} & \widehat{\boldsymbol{W}}_{2,L_1}^{[k]} \\ \left(\widehat{\boldsymbol{W}}_{2,L_1}^{[k]}\right)^T & \widehat{\boldsymbol{W}}_{1,L_2}^{[k]} \end{bmatrix}, \tag{4.8}$$

where $\widehat{\boldsymbol{W}}_{1,L_1} \in \mathbb{R}_{\geq 0}^{|L_1|\times|L_1|}$ contains all intralayer connections scaled by $\hat{w}_1^{[k]}$ for all the vertices in L_1, $\widehat{\boldsymbol{W}}_{2,L_1} \in \mathbb{R}_{\geq 0}^{|L_1|\times|L_2|}$ contains all interlayer connections scaled by $\hat{w}_2^{[k]}$ for all the vertices in L_1. Similarly $\widehat{\boldsymbol{W}}_{1,L_2} \in \mathbb{R}_{\geq 0}^{|L_2|\times|L_2|}$ accounts for the intralayer connections within L_2. As each $\mathcal{G}_k$ is undirected, the interlayer connections for all vertices in L_2 are represented by $\widehat{\boldsymbol{W}}_{2,L_1}^T$, that is, $\boldsymbol{W}_k$ is symmetric when $|L_1| = |L_2|$.

Example 4.1.2. *The weighted adjacency matrix $\boldsymbol{W}_1$ associated with $\mathcal{G}_1$ in Figure 4.2 has the block matrices*

$$\widehat{\boldsymbol{W}}_{1,L_1} = \begin{bmatrix} 0 & \hat{w}_1^{[1]} & 0 & \cdots & 0 & \hat{w}_1^{[1]} \\ \hat{w}_1^{[1]} & 0 & \hat{w}_1^{[1]} & & & \\ & \ddots & \ddots & & & \\ & & & \ddots & & \\ & & & \hat{w}_1^{[1]} & 0 & \hat{w}_1^{[1]} \\ \hat{w}_1^{[1]} & 0 & \cdots & 0 & \hat{w}_1^{[1]} & 0 \end{bmatrix} \quad \textit{and} \quad \widehat{\boldsymbol{W}}_{2,L_1} = \begin{bmatrix} \hat{w}_2^{[1]} & 0 & 0 & \cdots & 0 & 0 \\ 0 & \hat{w}_2^{[1]} & 0 & & & \\ & \ddots & \ddots & & & \\ & & & \ddots & & \\ & & & 0 & \hat{w}_2^{[1]} & 0 \\ 0 & 0 & \cdots & 0 & 0 & \hat{w}_2^{[1]} \end{bmatrix}, \tag{4.9}$$

for $\hat{w}_1^{[1]} = w_1^{[1]}/|w^{[1]}|$ and $\hat{w}_2^{[1]} = w_2^{[1]}/|w^{[1]}|$ where $|w^{[1]}| = 2w_1^{[1]} + w_2^{[1]}$ is the normalising factor for all rows ensuring the row-stochastic property of $\boldsymbol{W}_1$. From the regularity of $\mathcal{G}_1$ in Figure 4.2, we have that $\widehat{\boldsymbol{W}}_{1,L_1} = \widehat{\boldsymbol{W}}_{1,L_2}$ as the connections within layers are identical for L_1 and L_2.

To summarise the internal cellular dynamics in terms of signal inputs and outputs, as proposed in [117], we introduce the transfer function $\boldsymbol{T} : U \to Y$

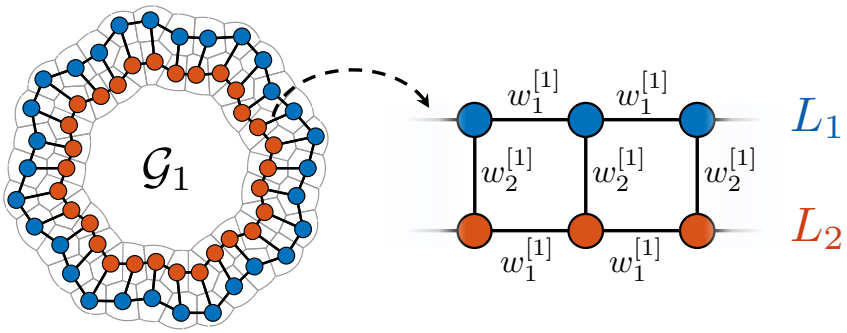

Figure 4.2: Layer-dependent edge weight structure in bilayer graphs. A 2D bilayer graph, $\mathcal{G}_1$, with contact-dependent edge connections highlight the layer vertex partitions with vertices in L_1 and L_2 coloured orange and blue, respectively. The edge weight structure within and between the layers is shown with edges between vertices in the same layer weighted by $w_1^{[1]}$ and connected vertices in different layers weighted by $w_2^{[1]}$.

that describes cellular signal output response with respect to changes to input signals determined by connected cells. It is assumed that $\boldsymbol{T}(\cdot)$ is bounded and $\mathcal{C}^2$ which conforms with the biological context of the IO system (4.1), namely, the intracellular expression must remain finite with continuous dependence on the cellular microenvironment. The introduction of $\boldsymbol{T}(\cdot)$ allows the analysis of the IO system (4.1) from an alternative macroscopic perspective, such that $\boldsymbol{T}(\cdot)$ retains the underlying features of the intracellular kinetics defined by $\boldsymbol{f}(\cdot)$ and $\boldsymbol{h}(\cdot)$ while not explicitly defining the intracellular interactions. For instance, intercellular communication of lateral-inhibition and lateral-induction pathways have a decreasing and increasing transfer function $\boldsymbol{T}(\cdot)$, respectively [117, 209]. Explicitly, the transfer function allows for the definition of the auxiliary input-to-output transition relation

$$\boldsymbol{u} = \boldsymbol{P}[\boldsymbol{T}(\boldsymbol{u}_1), ..., \boldsymbol{T}(\boldsymbol{u}_N)]^T, \tag{4.10}$$

which reduces the analytic complexity of the macroscopic analysis of spatially driven pattern formation in large-scale systems as the dependence of cellular coupling is more accessible in this form [117, 118, 207]. However, these methods require that the characteristic behaviour of the GRNs is known with respect to intercellular signals i.e., prescribing monotone properties for $\boldsymbol{T}(\boldsymbol{u}_i)$.

In the following section, we show that the zeros of the auxiliary input to output transition equation (4.10) are the steady states of the IO system (4.1), thus enabling stability analysis of the homogeneous steady states macroscopically. Subsequently, we derive conditions for the existence and uniqueness of the HSS in the large-scale system. Thus, to induce polarity-driven pattern formation

within the IO system (4.1), we seek sufficient conditions for the instability of HSS dependent on the bilayer connectivity graphs $\mathcal{G}_k$, and in particular, the polarity weights, $w_1^{[k]}$ and $w_2^{[k]}$.

4.1.2 Existence, uniqueness and stability of the homogeneous steady state in the large-scale IO systems

The majority of statements presented in this section were initially stated in [207] for MIMO IO systems. Here, we have independently proven them and partially extended them to comment on the uniqueness of the homogeneous steady state (HSS). We include all results for completeness with a focus on the application to mixed signal mechanisms in bilayer geometries. Consider the $\mathcal{C}^2$ function $\boldsymbol{S} : U \to X$ that describes the changes to the intracellular kinetics $\boldsymbol{x}_i$ by the input signals $\boldsymbol{u}_i$ emanating from connected cells. Therefore, the following statement demonstrates that the zeros of the auxiliary transfer relation (4.10) are the steady states of the IO system (4.1).

Lemma 4.1.1 ([186])**.** *Assume that for some $\boldsymbol{u}_0 \in \mathbb{R}^r$ the function $\boldsymbol{f}(\boldsymbol{x}, \boldsymbol{u}_0) = 0$ has a solution denoted by $\boldsymbol{x}_0 = \boldsymbol{S}(\boldsymbol{u}_0)$ and therefore $\boldsymbol{T}(\boldsymbol{u}_0) = \boldsymbol{h}(\boldsymbol{S}(\boldsymbol{u}_0))$. If $\boldsymbol{u}_0$ satisfies*

$$\begin{bmatrix} \boldsymbol{u}_0 \\ \vdots \\ \boldsymbol{u}_0 \end{bmatrix} = \boldsymbol{P} \begin{bmatrix} \boldsymbol{T}(\boldsymbol{u}_0) \\ \vdots \\ \boldsymbol{T}(\boldsymbol{u}_0) \end{bmatrix} \tag{4.11}$$

then $\boldsymbol{x}_0 = \boldsymbol{S}(\boldsymbol{u}_0)$ is a steady state of the IO system (4.1). Conversely, if $\boldsymbol{S}(\cdot)$ is injective and $\boldsymbol{x}_0$ is a fixed point of the IO system (4.1), then the corresponding $\boldsymbol{u}_0$ satisfies the auxiliary system (4.11).

Following from Lemma 4.1.1, we now study the transfer dynamics defined by $\boldsymbol{T}(\cdot)$ for the existence of the steady states of the IO system (4.1). Critically, as $\boldsymbol{T}(\cdot)$ represents changes in intercellular signalling, $\boldsymbol{T}(\cdot)$ is bounded. Therefore, the following statement ensures the existence and uniqueness of a homogeneous steady state of the IO system (4.1) using the boundedness of transfer dynamics.

Lemma 4.1.2. *Let $\boldsymbol{u}_0 \in \mathbb{R}^r$ such that the conditions of Lemma 4.1.1 hold and $\boldsymbol{u}^* = \mathbf{1}_N \otimes \boldsymbol{u}_0$. Then, there exists $\boldsymbol{x}_0 \in \mathbb{R}^n$ such that $\boldsymbol{x}^* = \mathbf{1}_N \otimes \boldsymbol{x}_0$ is a steady state if the IO system (4.1). Moreover, if $\partial \boldsymbol{f}(\boldsymbol{x}, \boldsymbol{u}_0)/\partial \boldsymbol{x}$ is invertible for all $\boldsymbol{x} \in X$ then $\boldsymbol{x}^*$ is unique.*

Proof. It is sufficient to show that there exists $\boldsymbol{u}_0 \in \mathbb{R}^r$ such that $\boldsymbol{u}^* = \mathbf{1}_N \otimes \boldsymbol{u}_0$ satisfies the auxiliary system (4.11) as $\boldsymbol{x}_0 = \boldsymbol{S}(\boldsymbol{u}_0)$. As each $\boldsymbol{W}_j \in \boldsymbol{\mathcal{W}}$ is row-stochastic, then the global interconnection matrix $\boldsymbol{P}$ is also row-stochastic by construction. Consequently, there exists an eigenvalue λ of $\boldsymbol{P}$ such that $\boldsymbol{P}\mathbf{1}_{rN} =$

$\lambda \mathbf{1}_{rN}$ [210], and therefore the proof follows from verifying the existence of $\boldsymbol{u}_0$ that satisfies $\boldsymbol{u}_0 = \lambda \boldsymbol{T}(\boldsymbol{u}_0)$.

By the bounded property of $\boldsymbol{T} : U \to Y$, there exists some constant $m > 0$ where $||\lambda \boldsymbol{T}(\cdot)||_2 \leq m$. Consider the function $\boldsymbol{F} : B_m \to B_m$ where $\boldsymbol{F}(\cdot) = \lambda \boldsymbol{T}(\cdot)$ and $B_m = \{\boldsymbol{v} \in \mathbb{R}^r : ||v||_2 \leq m\}$, noting that B_m is a convex set and the continuity of $\boldsymbol{F}(\cdot)$ is induced by the continuity of $\boldsymbol{T}(\cdot)$. Therefore, by the Brouwer Fixed-Point Theorem [211], there exists some $\boldsymbol{u}_0 \in B_m$ such that $\boldsymbol{u}_0 = \boldsymbol{F}(\boldsymbol{u}_0) = \lambda \boldsymbol{T}(\boldsymbol{u}_0)$.

The uniqueness of the HSS is guaranteed by the following. Assume that for any $\boldsymbol{u}_0 \in \mathbb{R}^r$ there exists $\overline{\boldsymbol{x}}_1, \overline{\boldsymbol{x}}_2 \in \mathbb{R}^n$ where both are solutions to $\boldsymbol{f}(\boldsymbol{x}, \boldsymbol{u}_0) = \boldsymbol{0}$. Specifically, $f_j(\overline{\boldsymbol{x}}_1, \boldsymbol{u}_0) = f_j(\overline{\boldsymbol{x}}_2, \boldsymbol{u}_0)$ for all $j \in [1, n]$. Therefore by the Mean Value Theorem [212], we construct the linear system

$$\begin{bmatrix} 0 \\ \vdots \\ 0 \end{bmatrix} = \begin{bmatrix} \frac{\partial f_1}{\partial x_1}(\boldsymbol{x}, \boldsymbol{u}_0) & \cdots & \frac{\partial f_1}{\partial x_n}(\boldsymbol{x}, \boldsymbol{u}_0) \\ & \vdots & \\ \frac{\partial f_n}{\partial x_1}(\boldsymbol{x}, \boldsymbol{u}_0) & \cdots & \frac{\partial f_n}{\partial x_n}(\boldsymbol{x}, \boldsymbol{u}_0) \end{bmatrix} \begin{bmatrix} \overline{\boldsymbol{x}}_{11} - \overline{\boldsymbol{x}}_{21} \\ \vdots \\ \overline{\boldsymbol{x}}_{1n} - \overline{\boldsymbol{x}}_{2n} \end{bmatrix} \tag{4.12}$$

and from the Invertible Matrix Theorem the kernel of $\partial \boldsymbol{f} / \partial \boldsymbol{x}$ contains only the null vector [213], *i.e.* $\overline{\boldsymbol{x}}_1 = \overline{\boldsymbol{x}}_2$. □

Remark 4.1.1. *If the transfer function $\boldsymbol{T} : U \to Y$ is Lipschitz continuous with Lipschitz constant $k \in (0, 1]$, namely,*

$$||\boldsymbol{T}(\boldsymbol{u}_i) - \boldsymbol{T}(\boldsymbol{u}_j)||_2 \leq k||\boldsymbol{u}_i - \boldsymbol{u}_j||_2 \tag{4.13}$$

for all $\boldsymbol{u}_i, \boldsymbol{u}_j \in U$. Then the HSS defined in Lemma 4.1.2 is unique by the Banach Fixed-Point Theorem [214], independent of the invertibility of $\boldsymbol{f}(\boldsymbol{x}, \boldsymbol{u})$.

As we seek spatially driven instabilities of the HSS, we assume the asymptotic stability of $\boldsymbol{x}^*$ in the absence of cellular connections. We say a fixed-point of a system is stable if the associated Jacobian has all eigenvalues with negative real-part. Therefore, we are assuming that $\boldsymbol{A} \coloneqq \partial \boldsymbol{f} / \partial \boldsymbol{x}_i$ evaluated at $\boldsymbol{x}_0$ is stable i.e., the intracellular kinetics are not self-exciting in the absence of interconnections.

A necessary feature for polarity-driven pattern formation in spatially discrete interconnected systems is the connectivity-induced instability of the HSS, $\boldsymbol{x}^*$, associated with the IO system (4.1), which can be approached by linearisation. The following results provide a convenient method of analysing the linear stability of homogeneous large-scale IO systems by assuming each cellular connectivity graph $\mathcal{G}_j$ commutes, thus enabling the parallel computation of eigenvalues for each adjacency matrix $\boldsymbol{W}_j \in \boldsymbol{\mathcal{W}}$, reducing the dimensionality of the linearisation. We note that assuming commutativity of all $\mathcal{G}_j$ does not restrict the study of anisotropic signalling in biological systems, which is discussed in Appendix

C, where we provide sufficient conditions for the construction of families of commutative graphs.

Lemma 4.1.3. *Let* $\boldsymbol{A} \coloneqq \partial \boldsymbol{f}/\partial \boldsymbol{x}_i$, $\boldsymbol{B} \coloneqq \partial \boldsymbol{f}/\partial \boldsymbol{u}_i$ *and* $\boldsymbol{C} \coloneqq \partial \boldsymbol{h}/\partial \boldsymbol{x}_i$, *be each evaluated at the steady state* $\boldsymbol{x}_0$ *for fixed* $\boldsymbol{u}_0$. *Let the steady state of the global IO system be* $\boldsymbol{x}^* = \boldsymbol{1}_N \otimes \boldsymbol{x}_0$. *Assume that all* $\boldsymbol{W}_j \in \boldsymbol{\mathcal{W}}$ *commute and denote* $\boldsymbol{\Lambda}_j = diag\,(\lambda_{1,j}, ..., \lambda_{r,j})$ *where* $\lambda_{i,j}$ *is the* j*th eigenvalue of* $\boldsymbol{W}_i$ *w.r.t. the common eigenbasis of all matrices in* $\boldsymbol{\mathcal{W}}$. *Then* $\boldsymbol{x}^*$ *is asymptotically stable if* $\boldsymbol{A} + \boldsymbol{B}\boldsymbol{\Lambda}_j\boldsymbol{C}$ *is stable for all* j *and unstable otherwise.*

Proof. Linearisation of the global IO system (4.1) about the fixed point $\boldsymbol{x}^* = \boldsymbol{I}_N \otimes \boldsymbol{x}_0$ yields the Jacobian

$$\begin{aligned}
\boldsymbol{J} &= \boldsymbol{I}_N \otimes \boldsymbol{A} + (\boldsymbol{I}_N \otimes \boldsymbol{B})\, \boldsymbol{P}\, (\boldsymbol{I}_N \otimes \boldsymbol{C})\,, \\
&= \boldsymbol{I}_N \otimes \boldsymbol{A} + (\boldsymbol{I}_N \otimes \boldsymbol{B}) \left(\sum_{i=1}^{r} \boldsymbol{W}_i \otimes \boldsymbol{D}_i \right) (\boldsymbol{I}_N \otimes \boldsymbol{C})\,, \\
&= \boldsymbol{I}_N \otimes \boldsymbol{A} + \sum_{i=1}^{r} \boldsymbol{W}_i \otimes \boldsymbol{B}\boldsymbol{D}_i\boldsymbol{C}, \qquad (4.14)
\end{aligned}$$

by direct substitution of the definition of $\boldsymbol{P}$ in terms of the independent signalling mechanisms and the mixed products property of Kronecker products [215]. As $\boldsymbol{W}_i\boldsymbol{W}_j = \boldsymbol{W}_j\boldsymbol{W}_i$ for all $\boldsymbol{W}_i$, $\boldsymbol{W}_j \in \boldsymbol{\mathcal{W}}$ and all matrices $\boldsymbol{W}_i$ are real and symmetric, then there exists a matrix $\boldsymbol{R}$ that simultaneously diagonalises all adjacency matrices $\boldsymbol{W}_i \in \boldsymbol{\mathcal{W}}$ [213]. Moreover, the eigenbasis defined by $\boldsymbol{R}$ fixes the order of the diagonal entries in each $\boldsymbol{Z}_i = \boldsymbol{R}^{-1}\boldsymbol{W}_i\boldsymbol{R} = \text{diag}\,(\lambda_{i,1}, ..., \lambda_{i,N})$ such that the sum of the diagonalised matrices $\boldsymbol{Z}_i$ is unique. Specifically, reordering the eigenvectors that form the eigenbasis $\boldsymbol{R}$ would only permute the sum of the diagonal values of $\boldsymbol{Z}_i$.

Consider the transformed Jacobian $\boldsymbol{H} = (\boldsymbol{R}^{-1} \otimes \boldsymbol{I}_n)\, \boldsymbol{J}\, (\boldsymbol{R} \otimes \boldsymbol{I}_n)$ then by the mixed products property of Kronecker products

$$\begin{aligned}
\boldsymbol{H} &= \left(\boldsymbol{R}^{-1} \otimes \boldsymbol{I}_n\right) (\boldsymbol{I}_N \otimes \boldsymbol{A})\, (\boldsymbol{R} \otimes \boldsymbol{I}_n) + \left(\boldsymbol{R}^{-1} \otimes \boldsymbol{I}_n\right) \left(\sum_{i=1}^{r} \boldsymbol{W}_i \otimes \boldsymbol{B}\boldsymbol{D}_i\boldsymbol{C} \right) (\boldsymbol{R} \otimes \boldsymbol{I}_n)\,, \\
&= \boldsymbol{R}^{-1}\boldsymbol{I}_N\boldsymbol{R} \otimes \boldsymbol{I}_n\boldsymbol{A}\boldsymbol{I}_n + \sum_{i=1}^{r} \boldsymbol{R}^{-1}\boldsymbol{W}_i\boldsymbol{R} \otimes \boldsymbol{I}_n\boldsymbol{B}\boldsymbol{D}_i\boldsymbol{C}\boldsymbol{I}_n, \\
&= \boldsymbol{I}_N \otimes \boldsymbol{A} + \sum_{i=1}^{r} \boldsymbol{Z}_i \otimes \boldsymbol{B}\boldsymbol{D}_i\boldsymbol{C}. \qquad (4.15)
\end{aligned}$$

By the diagonal structure of $\boldsymbol{Z}_i$ the matrix $\boldsymbol{H}$ has the block diagonal form

$$\boldsymbol{H} = \begin{bmatrix} \boldsymbol{A} + \sum_{i=1}^{r} \lambda_{i,1}\boldsymbol{B}\boldsymbol{D}_i\boldsymbol{C} & & \\ & \ddots & \\ & & \boldsymbol{A} + \sum_{i=1}^{r} \lambda_{i,n}\boldsymbol{B}\boldsymbol{D}_i\boldsymbol{C} \end{bmatrix}, \qquad (4.16)$$

and therefore, as $\sum_{i=1}^{r} \lambda_{i,j} \boldsymbol{B}\boldsymbol{D}_i\boldsymbol{C} = \boldsymbol{B}\boldsymbol{\Lambda}_j\boldsymbol{C}$ then the eigenvalues of $\boldsymbol{H}$ are those of $\boldsymbol{A} + \boldsymbol{B}\boldsymbol{\Lambda}_j\boldsymbol{C}$ for all $1 \leq j \leq N$. Consequently, if $\boldsymbol{A} + \boldsymbol{B}\boldsymbol{\Lambda}_j\boldsymbol{C}$ has eigenvalues with all negative real-part, for all $1 \leq j \leq N$, then $\boldsymbol{H}$ is stable and therefore the stability of $\boldsymbol{J}$ follows by the bijection between the linearised systems $\boldsymbol{H}$ and $\boldsymbol{J}$. □

Before discussing the behaviour of flows of the IO system (4.1) near the HSS, we first introduce a convenient condition for the instability of a matrix.

Lemma 4.1.4 ([118]). *If $\boldsymbol{M} \in \mathbb{R}^{n\times n}$ is stable then $(-1)^n \det(\boldsymbol{M}) > 0$. Conversely, if $(-1)^n \det(\boldsymbol{M}) < 0$ then $\boldsymbol{M}$ has an eigenvalue with positive real-part.*

Invoking lemmas 4.1.3 and 4.1.4 leads to the following sufficient condition for the instability of the HSS associated with an IO system (4.1) with commuting connectivity graphs $\mathcal{G}_j$.

Theorem 4.1.1. *Consider the large-scale IO system (4.1) that is spatially coupled via the global interconnection matrix $\boldsymbol{P}$ (4.3) such that each $\boldsymbol{W}_j \in \boldsymbol{\mathcal{W}}$ commute. Denote $\mathcal{D}\boldsymbol{T} \coloneqq \partial\boldsymbol{T}/\partial\boldsymbol{u}_i$ and let $\boldsymbol{\Lambda}_j = diag(\lambda_{1,j}, ..., \lambda_{r,j})$ where $\lambda_{i,j}$ is the jth eigenvalue of $\boldsymbol{W}_i$ w.r.t. the common eigenbasis of all matrices in $\boldsymbol{\mathcal{W}}$. Then the HSS $\boldsymbol{x}^* = \boldsymbol{1}_N \otimes \boldsymbol{x}_0$ is unstable if there exists a $\boldsymbol{\Lambda}_j$ such that*

$$\prod_{i=1}^{r} (1 - \mu_{i,j}) < 0, \tag{4.17}$$

where $\mu_{i,j}$ are the eigenvalues of $\boldsymbol{\Lambda}_j\mathcal{D}\boldsymbol{T}(\boldsymbol{u}_0)$ and $\boldsymbol{u}_0$ is the steady state input vector associated with $\boldsymbol{x}_0$.

Proof. By Lemma 4.1.3 we only need to show that there exists a positive eigenvalue of $\boldsymbol{A} + \boldsymbol{B}\boldsymbol{\Lambda}_j\boldsymbol{C}$ for $\boldsymbol{\Lambda}_j$ some diagonal matrix of eigenvalues of all matrices $\boldsymbol{W}_i \in \boldsymbol{\mathcal{W}}$ to demonstrate the instability of the HSS. Consider $(-1)^n \det(\boldsymbol{A} + \boldsymbol{B}\boldsymbol{\Lambda}_j\boldsymbol{C})$, then by Sylvester's Determinant Identity [216] we have that,

$$\begin{aligned}(-1)^n \det(\boldsymbol{A} + \boldsymbol{B}\boldsymbol{\Lambda}_j\boldsymbol{C}) &= (-1)^n \det(\boldsymbol{A}) \det\left(\boldsymbol{I}_r + \boldsymbol{\Lambda}_j\boldsymbol{C}\boldsymbol{A}^{-1}\boldsymbol{B}\right), \\ &= (-1)^n \det(\boldsymbol{A}) \det(\boldsymbol{I}_r - \boldsymbol{\Lambda}_j\mathcal{D}\boldsymbol{T}(\boldsymbol{u}_0)), \end{aligned} \tag{4.18}$$

where the final equality holds from $\mathcal{D}\boldsymbol{T}(\boldsymbol{u}_0) = -\boldsymbol{C}\boldsymbol{A}^{-1}\boldsymbol{B}$ as derived in [117]. As $\boldsymbol{A}$ is stable by assumption we have that $\boldsymbol{A}^{-1}$ exists and $(-1)^n \det(\boldsymbol{A}) > 0$ by Lemma 4.1.4. Therefore if $\det(\boldsymbol{1}_r - \boldsymbol{\Lambda}_j\mathcal{D}\boldsymbol{T}(\boldsymbol{u}_0)) < 0$ then $\boldsymbol{x}^* = \boldsymbol{1}_N \otimes \boldsymbol{x}_0$ is

unstable, by the converse statement of Lemma 4.1.4. Hence as the determinant of a matrix is the product of the eigenvalues [213], we have that

$$\det\left(\boldsymbol{I}_r - \boldsymbol{\Lambda}_j \mathcal{D}\boldsymbol{T}\left(\boldsymbol{u}_0\right)\right) = \prod_{i=1}^{r}\left(1-\mu_{i,j}\right) \tag{4.19}$$

for all matrices $\boldsymbol{\Lambda}_j$ $(1 \leq j \leq N)$. □

Applying the HSS instability condition derived in Theorem 4.1.1 IO systems with one, or two, spatially dependent components, i.e., SISO and double-input-double-output (DIDO) interconnected systems produces simple forms of the instability condition (4.17). Explicitly, the IO system (4.1) is SISO when $r = 1$ and DIDO when $r = 2$. Let $\mathrm{Spec}\left(\boldsymbol{M}\right)$ denote the set of eigenvalues of $\boldsymbol{M}$ then we recover the SISO instability condition Theorem 2.2.1 derived in [117], where we allow for generic intracellular kinetics here.

Corollary 4.1.1. *Consider the large-scale IO system (4.1) and denote* $\mathcal{D}\boldsymbol{T} \coloneqq \partial \boldsymbol{T}/\partial \boldsymbol{u}_i$. *We have:*

(i) If the IO system (4.1) is SISO with connectivity matrix $\boldsymbol{W}_1$ *then the HSS* $x^* = \boldsymbol{1}_N \otimes \boldsymbol{x}$ *is unstable if*

$$1 < \lambda_{1,j} T'\left(u_0\right) \tag{4.20}$$

for some $\lambda_{1,j} \in \mathrm{Spec}\left(\boldsymbol{W}_1\right)$.

(ii) If the IO system (4.1) is DIDO with global interconnection matrix $\boldsymbol{P}$ *constructed by the commutative adjacency matrices* $\boldsymbol{W}_1$ *and* $\boldsymbol{W}_2$ *then the HSS* $\boldsymbol{x}^* = \boldsymbol{1}_N \otimes \boldsymbol{x}$ *is unstable if*

$$1 < \mathrm{tr}\left(\boldsymbol{\Lambda}_j \mathcal{D}\boldsymbol{T}\left(\boldsymbol{u}_0\right)\right) - \det\left(\boldsymbol{\Lambda}_j \mathcal{D}\boldsymbol{T}\left(\boldsymbol{u}_0\right)\right) \tag{4.21}$$

for some $\boldsymbol{\Lambda}_j = \mathit{diag}\left(\lambda_{1,j}, \lambda_{2,j}\right)$, *where* $\lambda_{1,j} \in \mathrm{Spec}\left(\boldsymbol{W}_1\right)$ *and* $\lambda_{2,j} \in \mathrm{Spec}\left(\boldsymbol{W}_2\right)$ *both associated with the same eigenvector.*

Proof. In the case of a SISO system when $r = 1$, the $T : U \to V$ is a scalar function and we have that inequality (4.17) simply becomes $1 - \lambda_{1,j} T'\left(u_0\right) < 0$ yielding the SISO condition (4.20). For a DIDO system where $r = 2$, there are two potentially different adjacency matrices $\boldsymbol{W}_1$ and $\boldsymbol{W}_2$ that form $\boldsymbol{P}$. Therefore from inequality (4.17) we have that

$$\begin{aligned} 0 > \left(1-\mu_1\right)\left(1-\mu_2\right) &= 1 + \mathrm{tr}\left(-\boldsymbol{\Lambda}_j \mathcal{D}\boldsymbol{T}\left(\boldsymbol{u}_0\right)\right) + \det\left(-\boldsymbol{\Lambda}_j \mathcal{D}\boldsymbol{T}\left(\boldsymbol{u}_0\right)\right), \\ &= 1 - \mathrm{tr}\left(\boldsymbol{\Lambda}_j \mathcal{D}\boldsymbol{T}\left(\boldsymbol{u}_0\right)\right) + \left(-1\right)^r \det\left(\boldsymbol{\Lambda}_j \mathcal{D}\boldsymbol{T}\left(\boldsymbol{u}_0\right)\right), \\ &= 1 - \mathrm{tr}\left(\boldsymbol{\Lambda}_j \mathcal{D}\boldsymbol{T}\left(\boldsymbol{u}_0\right)\right) + \det\left(\boldsymbol{\Lambda}_j \mathcal{D}\boldsymbol{T}\left(\boldsymbol{u}_0\right)\right), \end{aligned} \tag{4.22}$$

using the relations between determinant, trace and the eigenvalues of a matrix [213]. Rearrangement of inequality (4.22) yields the DIDO HSS instability condition (4.21). □

The HSS instability conditions outlined in Theorem 4.1.1 allow the study of polarity regimes via graph edge weights to induce heterogeneity of cellular states within the bilayer tissues using analytic methods. Critically, the sufficient patterning conditions of Theorem 4.1.1 are independent of the precise intracellular kinetics as we do not impose any specific features on the transfer function, $\boldsymbol{T}(\cdot)$, other than the mild requirement of boundedness that follows immediately when modelling protein dynamics.

In the following section, we introduce methods of graph partitioning for templating laminar patterns in bilayer geometries that produce analytic conditions for the existence of the laminar patterns with multiple signalling mechanisms. In particular, we show that the commutative properties of the adjacency matrices $\boldsymbol{W}_j \in \boldsymbol{\mathcal{W}}$ required for the HSS instability condition in Theorem 4.1.1 can be relaxed when seeking dichotomous cell states in bilayer structures with same layer connectivity symmetries, namely semi-regular bilayer graphs. In addition, by restricting the characteristic behaviour of intracellular kinetics to competitive interactions, we ensure that the HSS instability converges to laminar patterns by applying results from monotone dynamical system theory.

4.2 Laminar pattern convergence with monotone kinetics in semi-regular bilayer graphs

The instability of the HSS of the IO system (4.1) does not imply the existence of stable heterogeneous cell states, even in systems with a unique HSS and bounded dynamics as there may exist oscillatory or chaotic solution trajectories. We leverage results from monotone dynamical systems and techniques of graph symmetry reduction to ensure the convergence to dichotomous cell states at the instance of HSS instability in the bilayer geometries. These methods of discrete pattern analysis were first introduced for SISO systems in [118] and later briefly extended to MIMO systems in [207]. Here we demonstrate the applicability of these methods to two-state pattern formation with pathway crosstalk kinetics in signal anisotropic bilayer geometries. In addition, we emphasise the link to the corresponding large-scale IO system (4.1), namely, when are the predicted patterns in the symmetry-reduced system preserved in the large-scale system.

4.2.1 Monotone kinetics for pattern convergence

Let $\boldsymbol{\phi}_t(\boldsymbol{x}_1)$ and $\boldsymbol{\phi}_t(\boldsymbol{x}_2)$ be two solutions to the IO system (4.1) where $\boldsymbol{x}_1 \leq \boldsymbol{x}_2$ are initial conditions, where we consider $<$ and $\leq$ to operate component-wise. It is said that the dynamical system (4.1) is monotone if $\boldsymbol{\phi}_t(\boldsymbol{x}_1) \leq \boldsymbol{\phi}_t(\boldsymbol{x}_2)$ for all $t \in [0, \infty)$ [187]. Furthermore, the IO system (4.1) is said to be strongly monotone if $\boldsymbol{\phi}_t(\boldsymbol{x}_1) < \boldsymbol{\phi}_t(\boldsymbol{x}_2)$ for all $t \in [0, \infty)$ [187]. Critically, the property of strong monotonicity is crucial for the asymptotic convergence of solutions $\boldsymbol{\phi}_t(\boldsymbol{x})$ on bounded domains $X \subset \mathbb{R}^n_{\geq 0}$, analogous to the Monotone Convergence Theorem for bounded sequences [217].

A dynamical system can be shown to be monotone by studying the sign structure of the associated Jacobian matrix on convex domains. The trajectory domain X is convex if for any $\boldsymbol{a}, \boldsymbol{b} \in X$ then $t\boldsymbol{a} + (1-t)\boldsymbol{b} \in X$ for all $t \in [0, 1]$, i.e., there exists a line segment between any two points in the domain that lies in the interior of X. Note that it does not restrict the solutions of the IO system (4.1) as $\mathbb{R}^n_{\geq 0}$ is a convex set and $X \subset \mathbb{R}^n_{\geq 0}$. The monotone identification via the Jacobian matrix relies on the inter-component monotonicity of vector-valued functions, initially studied by Kamke [218], leading to the classification of type K functions.

Definition 4.2.1 (Type K functions [187])**.** *A function $\boldsymbol{g}(\cdot)$ is said to be type K if for each i, $\boldsymbol{g}_i(\boldsymbol{a}) \leq \boldsymbol{g}_i(\boldsymbol{b})$ for any two points $\boldsymbol{a}, \boldsymbol{b} \in X$ satisfying $\boldsymbol{a} \leq \boldsymbol{b}$ and $\boldsymbol{a}_i = \boldsymbol{b}_i$ where X is a convex domain.*

Type K functions are a generalisation of monotone vector-valued functions (Figure 4.3) that allows for non-monotone components. This property is demonstrated in the following example.

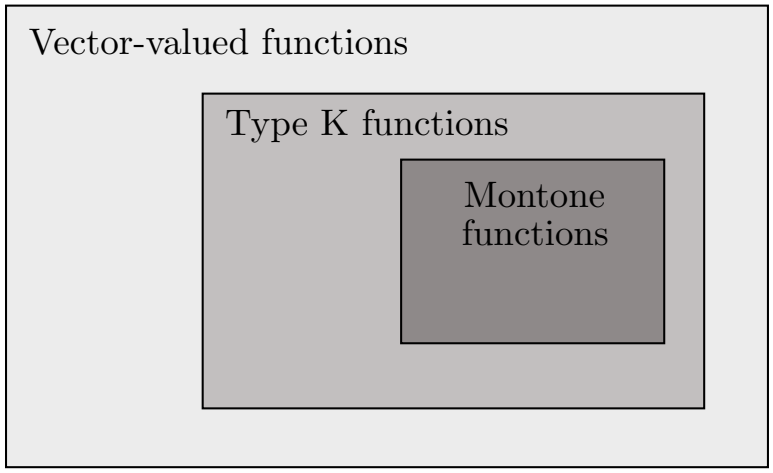

Figure 4.3: A representative diagram of the function inclusion space of vector-valued functions with respect to type K and monotone functions.

Example 4.2.1. *Consider the real-valued vector function* $\boldsymbol{g}: \mathbb{R}^2_{\geq 0} \to \mathbb{R}^2_{\geq 0}$ *defined by*

$$\boldsymbol{g}(\boldsymbol{x}) = \begin{bmatrix} x_2^3 + \cos(x_1^2) \\ x_1 + \sin(x_2) \end{bmatrix}. \tag{4.23}$$

Then define points in the domain $\boldsymbol{a} = [a_1, a_2]^T \in \mathbb{R}^2_{\geq 0}$ *and* $\boldsymbol{b} = [b_1, b_2]^T \in \mathbb{R}^2_{\geq 0}$ *where* $a_1 = b_1$ *and* $a_2 \leq b_2$. *In addition, let* $\boldsymbol{c} = [c_1, c_2]^T \in \mathbb{R}^2_{\geq 0}$ *and* $\boldsymbol{d} = [d_1, d_2]^T \in \mathbb{R}^2_{\geq 0}$ *where* $c_2 = d_2$ *and* $c_1 \leq d_1$. *Hence* $\boldsymbol{g}(\boldsymbol{x})$ *is type K as*

$$g_1(\boldsymbol{b}) - g_1(\boldsymbol{a}) = b_2^3 + \cos\left(b_1^2\right) - a_2^3 - \cos\left(a_1^2\right) = b_2^3 - a_2^3 \geq 0, \tag{4.24}$$

and similarly,

$$g_2(\boldsymbol{d}) - g_2(\boldsymbol{c}) = d_1 + \sin(d_2) - c_1 - \sin(c_2) = d_1 - c_1 \geq 0. \tag{4.25}$$

However, $\boldsymbol{g}(\boldsymbol{x})$ *is not monotone over* $\mathbb{R}^2_{\geq 0}$ *as* $\boldsymbol{g}_1((x_1, 0)) \not\leq \boldsymbol{g}_1((y_1, 0))$ *for all* $x_1, y_2 \in \mathbb{R}_{\geq 0}$.

The identification of type K functions in dynamical systems leads to the sufficient condition for monotone trajectories.

Lemma 4.2.1 (Type K monotone systems [187])**.** *Consider the general autonomous dynamical system*

$$\dot{\boldsymbol{z}} = \boldsymbol{g}(\boldsymbol{z}), \tag{4.26}$$

where $\boldsymbol{z} \in Z$ *and* $Z \subset \mathbb{R}^n$ *is convex. Then the dynamical system (4.26) is monotone if it is type K. Furthermore, by the Fundamental Theorem of Calculus, the general autonomous dynamical system (4.26) is guaranteed to be type K when the row-sums of the associated Jacobian satisfy*

$$\sum_{j \neq i} \frac{\partial \boldsymbol{g}_i}{\partial \boldsymbol{z}_j} \geq 0 \tag{4.27}$$

for all $1 \leq i \leq n$.

A direct consequence of Lemma 4.2.1 is that the IO system (4.1) is monotone provided that all off-diagonal components of the associated Jacobian are non-negative for all $\boldsymbol{x} \in X$ as previously applied in large-scale IO pattern formation studies [117, 186]. In addition, Hirsch [219] provided a sufficient condition for strong monotonicity that is dependent on the irreducibility of the Jacobian of the dynamical system. Specifically, a matrix $\boldsymbol{M}$ is said to be irreducible if there exists no permutation matrix $\boldsymbol{U}$ such that $\boldsymbol{U}^T\boldsymbol{M}\boldsymbol{U}$ is in upper block triangular form [216].

Lemma 4.2.2 ([187])**.** *Consider the dynamical system (4.26) as in Lemma 4.2.1. If the Jacobian,* $\frac{\partial \boldsymbol{g}}{\partial \boldsymbol{z}}$*, is irreducible and type K for all* $z \in Z$ *then system (4.26) is strongly monotone.*

The combination of lemmas 4.2.1 and 4.2.2 yield sufficient conditions for the identification of strongly monotone dynamical systems using standard linearisation methods, which are particularly applicable to interconnected dynamical systems. Namely, connected undirected graphs have irreducible adjacency matrices [220].

Time-dependent monotone systems are often characterised into two distinctive classes: cooperative dynamics where all solutions are monotone in forward-time ($t \to \infty$), and competitive dynamics where all solutions are monotone in backward-time ($t \to -\infty$) [187]. It has previously been demonstrated that competitive dynamics lead to pattern generation in large-scale IO systems, specifically, when studying processes of mutual cellular inhibition which are a common feature of cell-fate dynamics in developing tissues [117]. For example, the lateral-inhibition interactions of Notch1 and Delta1 are often found in tissues with a dichotomy of spatially organised cell-types and conform to the monotone competitive description [48, 87]. Extending these notions, we consider a wider range of intracellular kinetics that include purely competitive (lateral-inhibition), purely cooperative (lateral-induction), and a mix of these kinetics, which we later demonstrate can become monotone in the presence of polarity. Subsequently, these types of kinetics can be classified by the following assumption on the behaviour of the transfer function $\boldsymbol{T}(\cdot)$ to ensure the asymptotic convergence of solutions with tissue heterogeneity.

Assumption 4.2.1. *The local input linearisation of the transfer function* $\mathcal{D}\boldsymbol{T}(\boldsymbol{u}_i)$ *has one of the following sign structures:*

$$\textit{Lateral-inhibition:}\quad \mathcal{S}_0 = \begin{bmatrix} - & - & \cdots & - & - \\ - & - & \cdots & - & - \\ & & \vdots & & \\ - & - & \cdots & - & - \\ - & - & \cdots & - & - \end{bmatrix} \quad \textit{or} \quad \mathcal{S}_0' = \begin{bmatrix} - & + & \cdots & - & + \\ + & - & \cdots & + & - \\ & & \vdots & & \\ - & + & \cdots & - & + \\ + & - & \cdots & + & - \end{bmatrix}$$

$$\textit{Mixed-kinetics:}\quad \mathcal{S}_1 = \begin{bmatrix} - & - & \cdots & - & - \\ + & + & \cdots & + & + \\ & & \vdots & & \\ - & - & \cdots & - & - \\ + & + & \cdots & + & + \end{bmatrix} \quad \textit{or} \quad \mathcal{S}_1' = \begin{bmatrix} - & + & \cdots & - & + \\ - & + & \cdots & - & + \\ & & \vdots & & \\ - & + & \cdots & - & + \\ - & + & \cdots & - & + \end{bmatrix}$$

$$\textit{Mixed-kinetics:}\quad \mathcal{S}_2 = \begin{bmatrix} + & + & \cdots & + & + \\ - & - & \cdots & - & - \\ & & \vdots & & \\ + & + & \cdots & + & + \\ - & - & \cdots & - & - \end{bmatrix} \quad \textit{or} \quad \mathcal{S}_2' = \begin{bmatrix} + & - & \cdots & + & - \\ + & - & \cdots & + & - \\ & & \vdots & & \\ + & - & \cdots & + & - \\ + & - & \cdots & + & - \end{bmatrix}$$

$$\textit{Lateral-induction:}\quad \mathcal{S}_3 = \begin{bmatrix} + & + & \cdots & + & + \\ + & + & \cdots & + & + \\ & & \vdots & & \\ + & + & \cdots & + & + \\ + & + & \cdots & + & + \end{bmatrix} \quad \textit{or} \quad \mathcal{S}_3' = \begin{bmatrix} + & - & \cdots & + & - \\ - & + & \cdots & - & + \\ & & \vdots & & \\ + & - & \cdots & + & - \\ - & + & \cdots & - & + \end{bmatrix}$$

for all $\boldsymbol{u}_i \in U$ *where any sign can be replaced by zero provided* $\mathcal{D}\boldsymbol{T}(\boldsymbol{u}_i)$ *is irreducible.*

Lemma 4.2.3. *The sign structures* $\mathcal{S}_j$ *and* $\mathcal{S}_j'$ $(j \in \{0,1,2,3\})$ *are related via the following involutory linear transformation* $\boldsymbol{w}_i = \widetilde{\boldsymbol{M}}\boldsymbol{u}_i$ *for* $\widetilde{\boldsymbol{M}} \in \mathbb{R}^{r\times r}$ *of the form*

$$\widetilde{\boldsymbol{M}} = diag\left(-1, (-1)^2, ..., (-1)^{r-1}, (-1)^r\right), \tag{4.28}$$

such that if $sgn(\mathcal{D}\boldsymbol{T}(\boldsymbol{u}_i)) = \mathcal{S}_j$*, then* $sgn\left(\widetilde{\boldsymbol{M}}\mathcal{D}\boldsymbol{T}\left(\widetilde{\boldsymbol{M}}\boldsymbol{u}_i\right)\widetilde{\boldsymbol{M}}\right) = \mathcal{S}_j'$*, and vice versa.*

Proof. The statement follows by direct computation. Given $\boldsymbol{X} \in \mathbb{R}^{r\times r}_{\geq 0}$ then

$$\left(\widetilde{\boldsymbol{M}}\boldsymbol{X}\widetilde{\boldsymbol{M}}\right)_{i,j} = (-1)^{i+j}(\boldsymbol{X})_{i,j} \tag{4.29}$$

and therefore for $i+j$ odd, $(\boldsymbol{X})_{i,j}$ switches sign. □

The conditions imposed on the intracellular kinetics by Assumption 4.2.1 are applicable in the context of cellular pattern formation as activation and repression of intracellular signals are typically modelled using monotonic functions, such as Hill or logistic functions that relate to Michaelis-Menten kinetics for enzyme-catalyst reactions [221]. Furthermore, the irreducibility of $\mathcal{D}\boldsymbol{T}(\boldsymbol{u}_i)$ follows immediately if there exist no zero entries, that is, each spatially dependent component is continuously dependent on all other spatially dependent components. Moreover, the irreducibility of a matrix can be easily determined for low-order matrices by assessing the available paths in the associated directed graph (digraph) of the matrix as demonstrated in Figure 4.4. Namely, if there exists a path of edges between any two vertices then the adjacency matrix is irreducible [222].

In the following section, we will use the monotonic properties of the transfer function to predict the existence of laminar pattern formation in bilayer geometries graph partitioning. In particular, we focus on the analysis of the transfer function, as this considers only the spatially dependent components of the IO system (4.1), which potentially reduces the dimensionality of the analysis while preserving the underlying behaviour of the system.

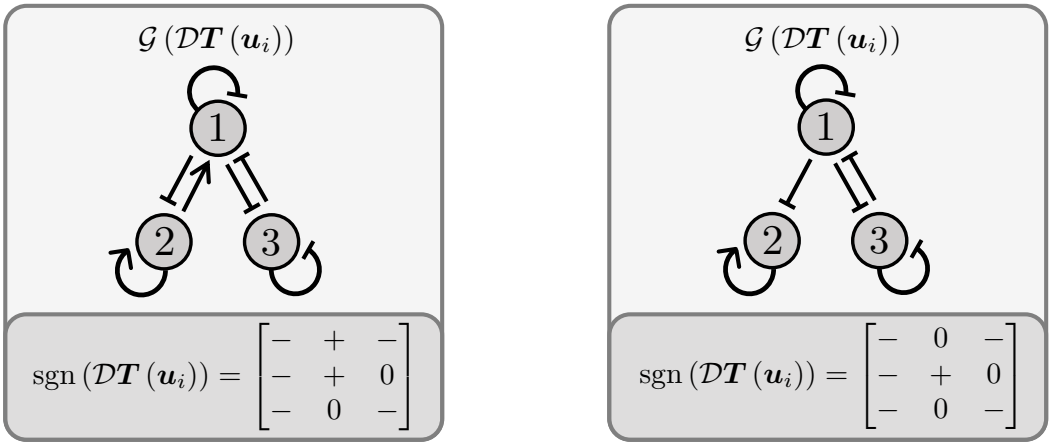

(a) An irreducible $\mathcal{DT}(\boldsymbol{u}_i)$.

(b) A reducible $\mathcal{DT}(\boldsymbol{u}_i)$.

Figure 4.4: An example of $\mathcal{DT}(\boldsymbol{u}_i)$ with sign structure $\mathcal{S}_1'$ and associated digraph topologies for (a) irreducible and (b) reducible intercellular kinetics. (a) As there exists a path of directed edges between any vertices v_i to v_j for $i, j \in \{1, 2, 3\}$ in $\mathcal{G}(\mathcal{DT}(\boldsymbol{u}_i))$ then $\mathcal{DT}(\boldsymbol{u}_i)$ is irreducible. (b) There exists no path from v_2 to v_1 or v_3 in $\mathcal{G}(\mathcal{DT}(\boldsymbol{u}_i))$ and therefore $\mathcal{DT}(\boldsymbol{u}_i)$ is reducible.

4.2.2 Dimension reduction by graph partition for polarity laminar pattern existence

We have previously used methods of graph partitioning to template desired patterns in regular and semi-regular large-scale IO systems. Here we apply these techniques to MIMO systems with semi-regular connectivity graphs as briefly considered in [186], where we highlight the applicability of these methods to constructing bespoke intracellular kinetics by exploiting the symmetries of the cellular connectivity graphs, $\mathcal{G}_k$, thereby analysing only representative vertices from each pattern partition of the large-scale graphs, vastly reducing the dimensionality associated IO systems.

Under the assumption of monotone transfer kinetics (Assumption 4.2.1), we provide sufficient conditions for the existence of polarity-driven laminar patterns in bilayer geometries with multiple spatially dependent components using graph partitioning. Critically, we demonstrate the prior requirement of commutative connectivity graphs $\mathcal{G}_j$ can be relaxed when seeking patterns with only two contrasting states, such as binary cell-fate determination.

The method of pattern templating via graph partitions seeks to group cells that are assumed to have the same steady-state solutions and therefore implies that cells within the same group behave identically. This assumption allows for the study of two representative cells from each layer in the bilayer large-scale graphs, $\mathcal{G}_k$, to predict the existence of laminar patterns as shown in Figure 4.5. As stated in Chapter 2, we are formally assuming the existence of an equitable

partition, π_2, of the vertices $v_i \in V$ into the pattern groups L_1 and L_2 of each layer for all connectivity graphs $\mathcal{G}_k$. This means that $v \in L_i$ has the same number of adjacent vertices in both L_1 and L_2, independent of the vertex, v [208]. We are imposing that cells within the same layer have the same edge connectivity structure, and therefore the connectivity graphs $\mathcal{G}_k$ must be layer-wise regular as in Figure 4.5. Algebraically, the partition π_2 is equitable if there exists some $\overline{w}_{ij}^{[k]} > 0$ such that

$$\sum_{v \in L_j} w_{uv}^{[k]} = \overline{w}_{ij}^{[k]} \quad \forall u \in L_i, \tag{4.30}$$

where $\hat{w}_{ij}^{[k]}$ are the ijth elements of the row-stochastic adjacency matrix $\boldsymbol{W}_k \in \boldsymbol{\mathcal{W}}$ [208]. In addition, we say that the laminar pattern partition, π_2, is simultaneously equitable if π_2 is equitable for all graphs $\mathcal{G}_k$.

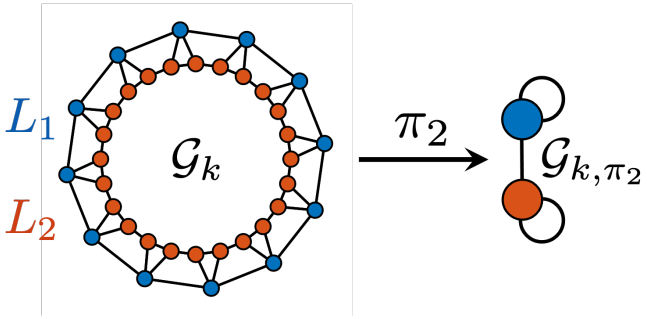

Figure 4.5: An example of templating for laminar patterns in bilayer geometries using the equitable partition π_2. The cellular connectivity graph, $\mathcal{G}_k$, is semi-regular such vertices within the same layer, L_1 or L_2, have the same number of adjacent vertices in each of the layers which induce an edge symmetry with respect to vertices in the same layer. The equitable partition, π_2, leverages the edge symmetries of $\mathcal{G}_k$ to generate a quotient graph $\mathcal{G}_{k,\pi_2}$ consisting of two representative cells, one from each layer L_1 and L_2.

Let $\overline{\boldsymbol{W}}_k \in \mathbb{R}_{\geq 0}^{2\times 2}$ be the reduced adjacency matrix for the quotient graph $\mathcal{G}_{k,\pi_2} = \mathcal{G}_k/\pi_2$ as depicted in Figure 4.5, that are element-wise composed with the constants defined by equation (4.30). Applying the IO preserving interconnection matrix definition (4.3) to the set of reduced adjacency matrices, we have the reduced interconnection matrix of the form,

$$\overline{\boldsymbol{P}} = \sum_{i=1}^{r} \overline{\boldsymbol{W}}_i \otimes \boldsymbol{D}_i, \tag{4.31}$$

noting that the row-stochastic property of each $\boldsymbol{W}_i \in \boldsymbol{\mathcal{W}}$ is preserved in the quotient mapping such that each $\overline{\boldsymbol{W}}_i$ is row-stochastic. In particular, as the

partition π_2 allocates the vertices $v \in V$ into either of the sets, L_1 or L_2, each reduced adjacency matrix is of the form,

$$\overline{\boldsymbol{W}}_k = \begin{bmatrix} a_k & 1-a_k \\ 1-b_k & b_k \end{bmatrix} \tag{4.32}$$

for all $k \in \{1, \dots, r\}r$, where $a_k, b_k \in (0,1)$ are composed of the polarity weights $w_1^{[k]}$ and $w_2^{[k]}$. Explicitly, a_k and b_k have the layer-dependent form

$$a_k = \frac{n_{1,L_1}^{[k]} w_1^{[k]}}{n_{1,L_1}^{[k]} w_1^{[k]} + n_{2,L_1}^{[k]} w_2^{[k]}} \quad \text{and} \quad b_k = \frac{n_{1,L_2}^{[k]} w_1^{[k]}}{n_{1,L_2}^{[k]} w_1^{[k]} + n_{2,L_2}^{[k]} w_2^{[k]}}, \tag{4.33}$$

where the superscripts correspond to the spatial connectivity mechanism, k, and $n_{1,L_j}^{[k]} \geq 1$ and $n_{2,L_j}^{[k]} \geq 1$ are the number of connected vertices in the same and opposing layer, respectively, from the perspective of each layer, $j = 1, 2$. For example, $n_{1,L_1}^{[k]} = n_{1,L_2}^{[k]} = 2$, $n_{2,L_1}^{[k]} = 2$ and $n_{2,L_2}^{[k]} = 1$ for $\mathcal{G}_k$ in Figure 4.5.

A key property of the equitable partition, π_2, is the preservation of eigenvalues when mapping between the large-scale and quotients graphs, that is, $\text{Spec}\left(\overline{\boldsymbol{W}}_k\right) \subset \text{Spec}\left(\boldsymbol{W}_k\right)$ [208]. Using this property, any spatially driven instability of the HSS observed in the quotient system also exists in the associated large-scale system. However, to apply the HSS instability conditions derived in Theorem 4.1.1 to large-scale connectivity graphs, we require that all $\overline{\boldsymbol{W}}_k$ must commute to generate a common eigenbasis for simultaneous diagonalisation. Commutativity is not preserved in the quotient transformation in general due to the reduced form of equation (4.32). Although, the following statement enables the use of the HSS instability conditions independent of the commutative properties of $\overline{\boldsymbol{W}}_k$ by demonstrating the existence of a common eigenbasis for all reduced adjacency matrices partitioned by π_2.

Lemma 4.2.4. *Let $\overline{\boldsymbol{P}} \in \mathbb{R}_{\geq 0}^{2r \times 2r}$ be the reduced mixed interconnection matrix (4.31) associated with the equitable partition π_2. Given any matrix $\widetilde{\boldsymbol{X}} \in \mathbb{R}^{r \times r}$ where $\boldsymbol{X} = \boldsymbol{I}_2 \otimes \widetilde{\boldsymbol{X}}$ the eigenvalues of $\overline{\boldsymbol{P}}\boldsymbol{X}$ are those of $\widetilde{\boldsymbol{X}}$ and $\overline{\boldsymbol{\Lambda}}_2\widetilde{\boldsymbol{X}}$ where $\overline{\boldsymbol{\Lambda}}_2 = diag\,(a_1 + b_1 - 1, ..., a_r + b_r - 1)$.*

Proof. By definition of the family of the reduced adjacency matrices (4.32), $\text{Spec}\left(\overline{\boldsymbol{W}}_i\right) = \{1, a_i + b_i - 1\}$, where all reduced adjacency matrices share the common eigenvector $\boldsymbol{v}_1 = \boldsymbol{1}_2$, associated with the common eigenvalue $\overline{\lambda}_{i,1} = 1$. Without loss of generality, let $\widetilde{\boldsymbol{R}}$ be the transformation matrix for $\overline{\boldsymbol{W}}_1$ such that $\widetilde{\boldsymbol{R}}^{-1}\overline{\boldsymbol{W}}_1\widetilde{\boldsymbol{R}}$ is in Jordan normal form [223]. As $\boldsymbol{v}_1$ must represent a column of $\widetilde{\boldsymbol{R}}$ as it is an eigenvector for all $\overline{\boldsymbol{W}}_i$, then let $\boldsymbol{v}_1$ form the first column of $\widetilde{\boldsymbol{R}}$ such that $\widetilde{\boldsymbol{R}}^{-1}\overline{\boldsymbol{W}}_1\widetilde{\boldsymbol{R}}$ has diagonal entries 1 and $a_1 + b_1 - 1$, respectively. Moreover, as each $\overline{\boldsymbol{W}}_i \in \mathbb{R}_{\geq 0}^{2\times 2}$, then $\widetilde{\boldsymbol{R}}^{-1}\overline{\boldsymbol{W}}_i\widetilde{\boldsymbol{R}}$ must be upper triangular form as 1 is a common

eigenvalue for all $1 \leq i \leq r$, that is, $\widetilde{\boldsymbol{R}}$ simultaneously upper triangularises the family of reduced adjacency matrices such that each $\widetilde{\boldsymbol{R}}^{-1}\overline{\boldsymbol{W}}_i\widetilde{\boldsymbol{R}}$ has diagonal entries 1 and $a_i + b_i - 1$.

Consider the invertible transformation $\boldsymbol{R} = \widetilde{\boldsymbol{R}} \otimes \boldsymbol{I}_r$. Denote the adjacency triangulation transformation of $\overline{\boldsymbol{P}}\boldsymbol{X}$ by $\boldsymbol{H} = \boldsymbol{R}^{-1}\overline{\boldsymbol{P}}\boldsymbol{X}\boldsymbol{R}$. Therefore, we have that

$$\begin{aligned}
\boldsymbol{H} &= \left(\widetilde{\boldsymbol{R}}^{-1} \otimes \boldsymbol{I}_r\right) \overline{\boldsymbol{P}}\boldsymbol{X} \left(\widetilde{\boldsymbol{R}} \otimes \boldsymbol{I}_r\right), \\
&= \left(\widetilde{\boldsymbol{R}}^{-1} \otimes \boldsymbol{I}_r\right) \left(\sum_{i=1}^{r} \overline{\boldsymbol{W}}_i \otimes \boldsymbol{D}_i\right) \left(\boldsymbol{I}_2 \otimes \widetilde{\boldsymbol{X}}\right) \left(\widetilde{\boldsymbol{R}} \otimes \boldsymbol{I}_r\right), \\
&= \sum_{i=1}^{r} \widetilde{\boldsymbol{R}}^{-1}\overline{\boldsymbol{W}}_i\widetilde{\boldsymbol{R}} \otimes \boldsymbol{D}_i\widetilde{\boldsymbol{X}}. \qquad (4.34)
\end{aligned}$$

Specifically, $\boldsymbol{H}$ is of block upper triangle form such that

$$\boldsymbol{H} = \begin{bmatrix} \boldsymbol{I}_r\widetilde{\boldsymbol{X}} & \boldsymbol{Z}\widetilde{\boldsymbol{X}} \\ \boldsymbol{0} & \overline{\boldsymbol{\Lambda}}_2\widetilde{\boldsymbol{X}}, \end{bmatrix}, \qquad (4.35)$$

where $\boldsymbol{Z}$ is some real $r \times r$ matrix constructed by interweaving the upper right entries of the transformed reduced adjacency matrices. Thus the eigenvalues of $\boldsymbol{H}$ are those of $\widetilde{\boldsymbol{X}}$ and $\overline{\boldsymbol{\Lambda}}_2\widetilde{\boldsymbol{X}}$, which are the eigenvalues of $\overline{\boldsymbol{P}}\boldsymbol{X}$ via bijective transformation defined by $\boldsymbol{R}$. □

Subsequently, by seeking the existence of laminar patterns using the partition π_2, Lemma 4.2.4 enables an analytic approach to determine the spatially driven instability of the HSS with any combination of layer-wise semi-regular bilayer graphs. Specifically, we need only determine the eigenvalues of $\mathcal{D}\boldsymbol{T}(\boldsymbol{u}^*)$ to ensure the HSS instability condition (4.17) is satisfied.

Applying the strongly monotone properties of the transfer kinetics outlined in Section 4.2.1, we seek to ensure the asymptotic convergence of heterogeneous solutions in the instance of HSS instability. However, it can be shown that the interconnection matrix, $\boldsymbol{P}$, and consequently the reduced interconnection matrix $\overline{\boldsymbol{P}}$ is reducible.

Lemma 4.2.5. *Let $\boldsymbol{P}$ be the interwoven matrix defined in equation (4.3) and let $\boldsymbol{Q}$ be the permutation matrix such that*

$$\boldsymbol{Q} = [\boldsymbol{I}_N \otimes \boldsymbol{e}_1, ..., \boldsymbol{I}_N \otimes \boldsymbol{e}_r]. \qquad (4.36)$$

where $\boldsymbol{e}_i = \left[\delta_{i,1}, \cdots, \delta_{i,r}\right]^T$. Then

$$\boldsymbol{Q}^T\boldsymbol{P}\boldsymbol{Q} = diag\left(\boldsymbol{W}_1, ..., \boldsymbol{W}_r\right). \qquad (4.37)$$

Proof. Consider the permutation map $\tau : \{1, ..., rN\} \to \{1, ..., rN\}$ such that

$$\tau(x) = ((x-1) \bmod r) N + \left\lfloor \frac{x-1}{r} \right\rfloor + 1 \tag{4.38}$$

which permutes the rows and columns of $\boldsymbol{P}$ so any row and columns $\boldsymbol{W}_i$ of $\boldsymbol{P}$ become adjacent for $1 \leq i \leq r$. In cycle notation, $\tau(x)$ defines the mapping

$$\begin{pmatrix} 1 & 2 & \cdots & r & r+1 & \cdots & rN \\ 1 & N+1 & \cdots & (r-1)N+1 & 2 & \cdots & (r-1)N+N \end{pmatrix} \tag{4.39}$$

which represents the column and row permutation of $\boldsymbol{P}$. The cycle (4.39) defined by equation (4.38) yields the following matrix representation

$$\boldsymbol{Q} = [\boldsymbol{I}_N \otimes \boldsymbol{e}_1, ..., \boldsymbol{I}_N \otimes \boldsymbol{e}_r], \tag{4.40}$$

namely, $\boldsymbol{Q}_{i,\tau(i)} = 1$ and zero entries else. Therefore applying the transformation $\boldsymbol{Q}$ to $\boldsymbol{P}$ produces the block diagonal representation where

$$\boldsymbol{Q}^T \boldsymbol{P} \boldsymbol{Q} = \operatorname{diag}(\boldsymbol{W}_1, ..., \boldsymbol{W}_r). \tag{4.41}$$

□

The existence of a block diagonal form of $\boldsymbol{P}$ (and $\overline{\boldsymbol{P}}$ by identical construction) by Lemma 4.2.5 highlights that $\boldsymbol{P}$ is a reducible matrix. However, we recover the irreducibility of $\boldsymbol{P}$ and $\overline{\boldsymbol{P}}$ by multiplication with a suitable class of matrices. To demonstrate this result we first provide a useful statement for the powers $\boldsymbol{P}$ (4.3).

Lemma 4.2.6. *Let $\boldsymbol{P}$ be the interwoven matrix defined as defined in equation (4.3). Then for all $n \in \mathbb{N}$*

$$\boldsymbol{P}^n = \sum_{i=1}^{r} \boldsymbol{W}_i^n \otimes \boldsymbol{D}_i. \tag{4.42}$$

Proof. The result follows by induction. Assume for some $k \in \mathbb{N}$ that equation (4.42) holds. Consider the case for $k+1$,

$$\begin{aligned} \left(\sum_{i=1}^{r} \boldsymbol{W}_i \otimes \boldsymbol{D}_i \right)^{k+1} &= \left(\sum_{i=1}^{r} \boldsymbol{W}_i \otimes \boldsymbol{D}_i \right) \left(\sum_{i=1}^{r} \boldsymbol{W}_i \otimes \boldsymbol{D}_i \right)^{k}, \\ &= \left(\sum_{i=1}^{r} \boldsymbol{W}_i \otimes \boldsymbol{D}_i \right) \left(\sum_{i=1}^{r} \boldsymbol{W}_i^k \otimes \boldsymbol{D}_i \right), \end{aligned} \tag{4.43}$$

where the second equality follows from the inductive hypothesis. Note that

$$\boldsymbol{D}_i \boldsymbol{D}_j = \begin{cases} \boldsymbol{D}_i & i = j, \\ \boldsymbol{0}_{r \times r} & i \neq j, \end{cases} \tag{4.44}$$

then by expanding equation (4.43) and applying the mixed-product property of the Kronecker product leads to the following cancellations,

$$\begin{aligned}\left(\sum_{i=1}^{r}\boldsymbol{W}_i\otimes\boldsymbol{D}_i\right)\left(\sum_{i=1}^{r}\boldsymbol{W}_i^k\otimes\boldsymbol{D}_i\right) &= (\boldsymbol{W}_1\otimes\boldsymbol{D}_1)\left(\sum_{i=1}^{r}\boldsymbol{W}_i^k\otimes\boldsymbol{D}_i\right)\\ &\quad+\cdots+(\boldsymbol{W}_r\otimes\boldsymbol{D}_r)\left(\sum_{i=1}^{r}\boldsymbol{W}_i^k\otimes\boldsymbol{D}_i\right),\\ &= \boldsymbol{W}_1\boldsymbol{W}_1^k\otimes\boldsymbol{D}_1+\cdots+\boldsymbol{W}_r\boldsymbol{W}_r^k\otimes\boldsymbol{D}_r,\\ &= \sum_{i=1}^{r}\boldsymbol{W}_i^{k+1}\otimes\boldsymbol{D}_i. \end{aligned}\tag{4.45}$$

That is, the inductive hypothesis is satisfied and therefore equation (4.42) holds for all $n\in\mathbb{N}$. □

Now we have an accessible method of computing the powers of $\boldsymbol{P}$ and $\overline{\boldsymbol{P}}$ using Lemma 4.2.6, we next show the irreducibility of linearised IO systems that are required to satisfy the strongly monotone condition defined in Lemma 4.2.2 can be preserved provided that the global interconnection matrix (4.3) is coupled to irreducible matrices.

Lemma 4.2.7. *Let $\boldsymbol{P}$ be the mixed interconnection matrix (4.3) and $\boldsymbol{Q}=\mathrm{diag}(\boldsymbol{Q}_1,...,\boldsymbol{Q}_N)$ such that $\boldsymbol{Q}_k\in\mathbb{R}^{r\times r}$ is irreducible for each $k\in\{1,...,N\}$. Then $\boldsymbol{PQ}$ is irreducible.*

Proof. A graph is said to be strongly connected if there exists a path between any two vertices. We aim to show that the graph defined by the weighted adjacency matrix $\boldsymbol{PQ}$ is strongly connected and therefore use the property that a graph is strongly connected if and only if the associated adjacency matrix is irreducible [222].

For an unweighted, nonnegative adjacency matrix $\boldsymbol{M}$, it can be shown that the (i,j)th element of $\boldsymbol{M}^k$ represents the number of ways to travel from vertex v_i to vertex v_j along exactly k edges. Therefore if $\boldsymbol{M}$ defines a connected graph of l vertices, then $\boldsymbol{M}^l$ contains no zero entries for all (i,j), that is, there exists a path between any two vertices in less than, or equal, to l steps, where the converse statement is also true [222]. In the case of weighted, nonnegative adjacency matrices, the elements (i,j) of $\boldsymbol{M}^k$ no longer represent the number of ways to get from vertex i to vertex j along exactly k edges, but are non-zero if there exists a path between v_i to vertex v_j along k, or less, edges.

The set of vertices has cardinality $|V_{\boldsymbol{PQ}}|=rN$ owing to the total number of interconnections within the large-scale IO system (4.1). Hence consider the

adjacency matrix $(\boldsymbol{PQ})^{rN}$. From Lemma 4.2.6 it can be shown that

$$\boldsymbol{P}^{rN} = \left(\sum_{i=1}^{r} \boldsymbol{W}_i \otimes \boldsymbol{D}_i\right)^{rN} = \sum_{i=1}^{r} \boldsymbol{W}_i^{rN} \otimes \boldsymbol{D}_i, \tag{4.46}$$

and by the above argument $\boldsymbol{W}_i^{rN}$ has no zero elements as each $\boldsymbol{W}_i$ represents a connected graph of N vertices. Therefore, $\boldsymbol{P}^{rN}$ is the interweave of r completely non-zero matrices and thus w.l.o.g. for any non-zero elements $p_{i,j}$ of $\boldsymbol{P}^{rN}$ then $p_{i\pm r,j}$ and $p_{i,j\pm r}$ are also non-zero. Specifically, there exist no two non-zero elements in $\boldsymbol{P}^{rN}$ that are more than r elements apart in each row and column, as in Example 4.1.1 where $r = 2$, $N = 2$. In addition, define $\boldsymbol{Q}_k^{rN} \coloneqq \tilde{\boldsymbol{Q}}_k$. By assumption, $\tilde{\boldsymbol{Q}}_k$ has no zero entries for all $i, j \in \{1, ..., r\}$ by irreducibility and so $\boldsymbol{Q}^{rN} = \text{diag}\left(\tilde{\boldsymbol{Q}}_1, ..., \tilde{\boldsymbol{Q}}_N\right)$. Applying the definition of the matrix product, the elements of $(\boldsymbol{PQ})^{rN}$ are given by

$$\left(\boldsymbol{P}^{rN}\boldsymbol{Q}^{rN}\right)_{ij} = \sum_{k=1}^{rN} p_{i,k}\tilde{q}_{k,j} \neq 0 \tag{4.47}$$

for all $i, j \in \{1, ..., rN\}$, as every column of $\boldsymbol{Q}^{rN}$ contains r consecutive non-zero elements. Therefore $(\boldsymbol{PQ})^{rN}$ has no zero elements, which implies that the graph of $\boldsymbol{PQ}$ is strongly connected, thus $\boldsymbol{PQ}$ is irreducible. □

The statement of Lemma 4.2.7 applies also to the reduced interconnection matrix $\overline{\boldsymbol{P}}$ as it has an identical structure to the corresponding large-scale interconnection matrix $\boldsymbol{P}$ and therefore the irreducibility of the product is preserved under the quotient mapping by π_2. Hence by ensuring the irreducibility of the Jacobian of the reduced IO system (4.1) spatially coupled by $\overline{\boldsymbol{P}}$, then by Lemma 4.2.7 and Assumption 4.2.1, the following statement provides polarity-dependent conditions that guarantee the existence of laminar patterns in semi-regular bilayer graphs by using the strongly monotone dynamics of solution trajectories.

Theorem 4.2.1 (Existence of laminar patterns in MIMO systems with semi-regular graphs)**.** *Consider the IO system (4.1) with interconnection matrix $\boldsymbol{P}$ (4.3). Let π_2 be the layer-wise simultaneously equitable partition for all bilayer connectivity graphs, $\mathcal{G}_k$, defined by $\boldsymbol{P}$ such that the associated reduced interconnection matrix $\overline{\boldsymbol{P}}$ (4.31) defines the reduced IO system of representative cells from each layer. Assuming that Assumption 4.2.1 is satisfied and there exists $\overline{\boldsymbol{\Lambda}}_2$ such that the HSS instability condition (4.17) and the monotonic conditions:*

(M1) $n_{1,L_i}^{[k]} w_1^{[k]} \leq n_{2,L_i}^{[k]} w_2^{[k]}$ *if* $sgn\left(\mathcal{D}\boldsymbol{T}\right) = \mathcal{S}_0$ *or* $\mathcal{S}_0'$,

(M2) $(-1)^{k+1} n_{1,L_i}^{[k]} w_1^{[k]} \leq (-1)^{k+1} n_{2,L_i}^{[k]} w_2^{[k]}$ *if* $sgn\left(\mathcal{D}\boldsymbol{T}\right) = \mathcal{S}_1$ *or* $\mathcal{S}_1'$,

(M3) $(-1)^k n_{1,L_i}^{[k]} w_1^{[k]} \leq (-1)^k n_{2,L_i}^{[k]} w_2^{[k]}$ *if* $sgn(\mathcal{D}\boldsymbol{T}) = \mathcal{S}_2$ *or* $\mathcal{S}_2'$,

(M4) $n_{1,L_i}^{[k]} w_1^{[k]} \geq n_{2,L_i}^{[k]} w_2^{[k]}$ *if* $sgn(\mathcal{D}\boldsymbol{T}) = \mathcal{S}_3$ *or* $\mathcal{S}_3'$,

for all $i \in \{1,2\}, k \in \{1,...,r\}$, *are satisfied, then any solutions in the neighbourhood of the HSS,* $\boldsymbol{x}^*$, *converge to laminar patterns in the reduced system.*

Proof. Following from Lemma 4.11 we consider the auxiliary dynamic system defined by the transfer kinetics for the reduced IO system

$$\begin{bmatrix} \dot{\boldsymbol{z}}_1 \\ \dot{\boldsymbol{z}}_2 \end{bmatrix} = -\begin{bmatrix} \boldsymbol{z}_1 \\ \boldsymbol{z}_2 \end{bmatrix} + \overline{\boldsymbol{P}} \begin{bmatrix} \boldsymbol{T}(\boldsymbol{z}_1) \\ \boldsymbol{T}(\boldsymbol{z}_2) \end{bmatrix} := \boldsymbol{F}(\boldsymbol{z}), \tag{4.48}$$

as this represents the behaviour of the reduced IO system using only the spatially dependent components. Note that the fixed points of the auxiliary system (4.48) are those of the IO system (4.1). Namely, the auxiliary system (4.48) has HSS $\boldsymbol{z}^* = \boldsymbol{1}_2 \otimes \boldsymbol{u}_0$ for the cell-wise input steady state $\boldsymbol{u}_0$ associated with $\boldsymbol{x}^*$. Linearising the auxiliary system about the HSS yields the following Jacobian

$$\frac{\partial \boldsymbol{F}}{\partial \boldsymbol{z}}(\boldsymbol{z}^*) = -\boldsymbol{I}_{2r} + \overline{\boldsymbol{P}}\left(\boldsymbol{I}_2 \otimes \mathcal{D}\boldsymbol{T}(\boldsymbol{z}^*)\right). \tag{4.49}$$

First, we show that sign structures, $\mathcal{S}_j$ and $\mathcal{S}_j'$ for $j \in \{1,2,3,4\}$, are equivalent up to linear transformation on the Jacobian (4.49). Following that, we then use a cooperative bijective transformation using the signal polarity parameters to show that the auxiliary system is strongly monotone. Critically, the boundedness, in combination with strongly monotone kinetics of the transfer function, ensures the convergence of heterogeneous solutions in the auxiliary system (4.48) and thus the reduced IO system by Lemma 4.11. A sketch of the following proof is given in Figure 4.6 in the case of the monotonic conditions (M1).

Denote the reflection transformation $\boldsymbol{M} = \boldsymbol{I}_2 \otimes \widetilde{\boldsymbol{M}}$ for $\widetilde{\boldsymbol{M}}$ as defined in equation (4.28) in Lemma 4.2.3. Note that $\widetilde{\boldsymbol{M}}^{-1} = \widetilde{\boldsymbol{M}}$ and therefore $\boldsymbol{M}^{-1} = \boldsymbol{M}$. Introducing the coordinate transformation $\boldsymbol{w} = \boldsymbol{M}\boldsymbol{z}$, the Jacobian (4.49) with respect to $\boldsymbol{w}$ yields

$$\begin{aligned}
\boldsymbol{M}\left(\frac{\partial \boldsymbol{F}}{\partial \boldsymbol{z}}(\boldsymbol{M}\boldsymbol{w})\right)\boldsymbol{M} &= \left(\boldsymbol{I}_2 \otimes \widetilde{\boldsymbol{M}}\right)\left(-\boldsymbol{I}_{2r} + \overline{\boldsymbol{P}}\left(\boldsymbol{I}_2 \otimes \mathcal{D}\boldsymbol{T}(\boldsymbol{M}\boldsymbol{w})\right)\right)\left(\boldsymbol{I}_2 \otimes \widetilde{\boldsymbol{M}}\right), \\
&= -\boldsymbol{I}_{2r} + \left(\boldsymbol{I}_2 \otimes \widetilde{\boldsymbol{M}}\right)\left(\sum_{k=1}^{r} \overline{\boldsymbol{W}}_k \otimes \boldsymbol{D}_k\right)\left(\boldsymbol{I}_2 \otimes \mathcal{D}\boldsymbol{T}(\boldsymbol{M}\boldsymbol{w})\right)\left(\boldsymbol{I}_2 \otimes \widetilde{\boldsymbol{M}}\right), \\
&= -\boldsymbol{I}_{2r} + \left(\sum_{k=1}^{r} \overline{\boldsymbol{W}}_k \otimes \boldsymbol{D}_k\right)\left(\boldsymbol{I}_2 \otimes \widetilde{\boldsymbol{M}}\right)\left(\boldsymbol{I}_2 \otimes \mathcal{D}\boldsymbol{T}(\boldsymbol{M}\boldsymbol{w})\right)\left(\boldsymbol{I}_2 \otimes \widetilde{\boldsymbol{M}}\right), \\
&= -\boldsymbol{I}_{2r} + \left(\sum_{k=1}^{r} \overline{\boldsymbol{W}}_k \otimes \boldsymbol{D}_k\right)\left(\boldsymbol{I}_2 \otimes \widetilde{\boldsymbol{M}}\mathcal{D}\boldsymbol{T}(\boldsymbol{M}\boldsymbol{w})\,\widetilde{\boldsymbol{M}}\right),
\end{aligned} \tag{4.50}$$

where the third and fourth equality follow from the commutativity of diagonal

matrices and the mixed multiplication property of the Kronecker product. By Lemma 4.2.3, the invertible linear transformation defined by $\boldsymbol{M}$ converts between $\mathcal{DT}$ sign structures $\mathcal{S}_j$ and $\mathcal{S}'_j$. Therefore, we continue by considering the transfer function with $\mathrm{Sgn}\left(\mathcal{DT}\left(\cdot\right)\right) = \mathcal{S}_j$ as the core kinetics of the systems.

From Lemma 4.2.4 the polarity dependent eigenvalues $\lambda_{i,2}$ of $\overline{\boldsymbol{W}}_i$ have eigenvectors, $\boldsymbol{v}_{i,2}$, with sign structure $\mathrm{sgn}\left(\boldsymbol{v}_{i,2}\right) = [-,+]^T$. Therefore, motivated by polarity-driven patterning and the requirement of the positivity of the dominant instability mode for monotone kinetics [187], we construct a transformation, $\boldsymbol{R}$, to ensure that any polarity-driven instability satisfies the monotonicity criteria, that is, monotone with respect to alternating domains. Consider the transformation $\boldsymbol{R} = \widetilde{\boldsymbol{R}} \otimes \boldsymbol{I}_r$ where $\widetilde{\boldsymbol{R}} = \mathrm{diag}\left(-1, 1\right)$. Noting again that $\boldsymbol{R}^{-1} = \boldsymbol{R}$ as $\widetilde{\boldsymbol{R}}^{-1} = \widetilde{\boldsymbol{R}}$. By similar calculations as above, it can be shown that by the coordinate transformation $\boldsymbol{w} = \boldsymbol{R}\boldsymbol{z}$ the Jacobian (4.49) has the form

$$\boldsymbol{R}\left(\frac{\partial \boldsymbol{F}}{\partial \boldsymbol{z}}\left(\boldsymbol{R}\boldsymbol{w}\right)\right)\boldsymbol{R} = -\boldsymbol{I}_{2r} + \sum_{k=1}^{r} \widetilde{\boldsymbol{R}}\overline{\boldsymbol{W}}_k\widetilde{\boldsymbol{R}} \otimes \boldsymbol{D}_k\mathcal{DT}\left(\boldsymbol{R}\boldsymbol{w}\right), \tag{4.51}$$

where the quotient adjacency matrix is transformed to the following form

$$\widetilde{\boldsymbol{R}}\overline{\boldsymbol{W}}_k\widetilde{\boldsymbol{R}} = \begin{bmatrix} a_k & -\left(1-a_k\right) \\ -\left(1-b_k\right) & b_k \end{bmatrix}. \tag{4.52}$$

Therefore, let $\tau\left(i\right) = \left(i-1\right) \bmod r + 1$ then the row-sum of the transformed auxiliary Jacobian (4.51) can be expressed as

$$\sum_{j\neq i}\left(\boldsymbol{R}\left(\tfrac{\partial \boldsymbol{F}}{\partial \boldsymbol{z}}\left(\boldsymbol{R}\boldsymbol{w}\right)\boldsymbol{R}\right)\right)_{ij} = \begin{cases} \left(2a_{\tau(i)}-1\right)\displaystyle\sum_{j=1,i\neq j}^{r}\left(\boldsymbol{D}_{\tau(i)}\mathcal{DT}\left(\boldsymbol{R}\boldsymbol{w}\right)\right)_{ij} & 1 \leq i \leq r, \\ \left(2b_{\tau(i)}-1\right)\displaystyle\sum_{j=1,i\neq j}^{r}\left(\boldsymbol{D}_{\tau(i)}\mathcal{DT}\left(\boldsymbol{R}\boldsymbol{w}\right)\right)_{ij} & r+1 \leq i \leq 2r. \end{cases} \tag{4.53}$$

For each sign structure $\mathcal{S}_j$ the monotonic conditions (i-iv) are sufficient to ensure the non-negativity of the row-sum by imposing the appropriate sign of the coefficients $\left(2a_{\tau(i)}-1\right)$ and $\left(2b_{\tau(i)}-1\right)$. Explicitly, if $sgn\left(\mathcal{DT}\right) = \mathcal{S}_0$, we require each $\left(2a_{\tau(i)}-1\right) \leq 0$ and $\left(2b_{\tau(i)}-1\right) \leq 0$ which is satisfied by (M1). For $sgn\left(\mathcal{DT}\right) = \mathcal{S}_3$, we require we require each $\left(2a_{\tau(i)}-1\right) \geq 0$ and $\left(2b_{\tau(i)}-1\right) \geq 0$ which is satisfied by (M4). For the mixed kinetics $sgn\left(\mathcal{DT}\right) = \mathcal{S}_1, \mathcal{S}_2$, we require that the coefficients $\left(2a_{\tau(i)}-1\right)$ and $\left(2b_{\tau(i)}-1\right)$ switch sign as $\tau\left(i\right)$ increases, such that $\left(2a_{\tau(i)}-1\right) \leq 0$ and $\left(2b_{\tau(i)}-1\right) \leq 0$ is associated with the negative rows and, $\left(2a_{\tau(i)}-1\right) \geq 0$ and $\left(2b_{\tau(i)}-1\right) \geq 0$ is associated with the positive rows of $\mathcal{DT}$, both satisfied by (M2) and (M3), for $sgn\left(\mathcal{DT}\right) = \mathcal{S}_1, \mathcal{S}_2$, respectively. Critically, for each sign structure $\mathcal{S}_j$ the monotonic conditions (M1-M4) guarantee

$$\sum_{j\neq i}\left(\boldsymbol{R}\left(\frac{\partial \boldsymbol{F}}{\partial \boldsymbol{z}}\left(\boldsymbol{R}\boldsymbol{w}\right)\boldsymbol{R}\right)\right)_{ij} \geq 0 \tag{4.54}$$

for all $i \in \{1, ..., 2r\}$, thus satisfying the type K condition in Lemma 4.2.1. Furthermore, by Lemma 4.2.7, the transformed auxiliary Jacobian (4.51) is irreducible and therefore the auxiliary dynamical system (4.48) is strongly monotone (cooperative) with respect to the laminar pattern transformation $\boldsymbol{R}$.

The cooperative auxiliary dynamical system (4.48) is monotone with respect to the standard domain $\mathbb{R}^{2r}_{\geq 0}$ and has a positive eigenvector $\boldsymbol{v} > 0$ associated with the polarity driven instability $\overline{\boldsymbol{\Lambda}}_2$ of the transformed HSS $\boldsymbol{Rz}^*$ by the Perron-Frobenius Theorem [141]. Consequently, for small ϵ, any solution starting at $\boldsymbol{Rz} = \boldsymbol{Rz}^* + \epsilon \boldsymbol{v}$ must have positive derivative and increase in the transformed trajectory domain $\mathbb{R}^{2r}_{\geq 0}$ [187]. Critically, if the solutions of the cooperative auxiliary dynamical system (4.48) are bounded, then the strongly monotone property ensures the convergence to another steady state, $\boldsymbol{Rz}^{**} \neq \boldsymbol{Rz}^*$.

The transfer function $\boldsymbol{T}(\cdot)$ is bounded and so there exists $b > 0$ such that

$$||\overline{\boldsymbol{P}}[\boldsymbol{T}(\boldsymbol{z}_1), \boldsymbol{T}(\boldsymbol{z}_2)]^T||_2 < b \tag{4.55}$$

for all $\boldsymbol{z}_i$. Thus, as the cooperative auxiliary dynamical system (4.48) is monotone with respect to $\mathbb{R}^{2r}_{\geq 0}$, we have that the sets centred about the HSS $\mathcal{V}_\pm = \boldsymbol{Rz}^* \pm \left(\mathbb{R}^{2r}_{\geq 0} \cap [0, b]^{2r}\right)$ are forward invariant, i.e. $\boldsymbol{\phi}_t(\boldsymbol{Rz}) \in \mathcal{V}_\pm$ for all $t \in [0, \infty)$. Therefore all solutions are bounded within a compact domain and thus converge to $\boldsymbol{Rz}^{**} \neq \boldsymbol{Rz}^*$ by the Cooperative Irreducible Convergence Theorem (Theorem 4.3.3 in [187]). Subsequently, the corresponding non-transformed system (4.48) must have each vertices with solutions in $\mathcal{V}_+$ and $\mathcal{V}_-$, respectively, ensuring contrasting cell-wise solutions. Finally, as any steady state solution to the auxiliary dynamical system (4.48) is a steady state of the associated reduced IO system (4.1), by Lemma 4.11 the reduced IO system (4.1) converges to laminar patterns. □

From Theorem 4.2.1 we can conclude that the existence of a polarity-driven instability of the HSS implies the existence of heterogeneous steady states within the quotient system. This follows as solution trajectories diverge when transforming between competitive to cooperative systems as highlighted in Figure 4.6. Moreover, as the competitive dynamics of the reduced IO system (4.1) are isomorphic to cooperative dynamics, all periodic solutions are unstable [224], implying the convergence to contrasting cell states. The following example demonstrates how Theorem 4.2.1 can be applied to prove the existence of laminar patterns in large-scale IO systems.

Example 4.2.2. *Consider the DIDO system with two spatially-dependent components describing lateral-inhibition with a diffusive crosstalk as represented in Figure 4.7,*

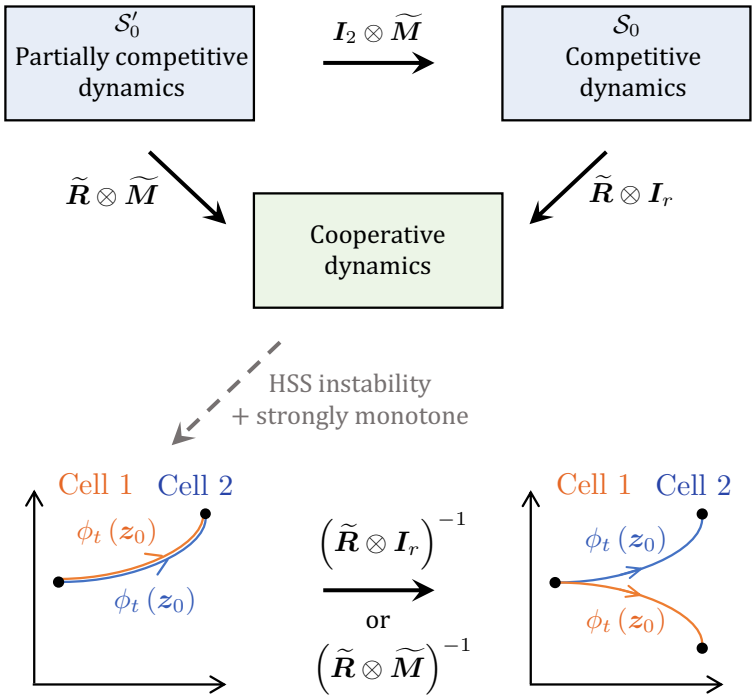

Figure 4.6: A sketch of the proof of Theorem 4.2.1 for system transformations for the monotonic case (M1) where $\boldsymbol{I}_r$ is the identity matrix, $\widetilde{\boldsymbol{M}}$ is the competitive sign structure transformation, $\widetilde{\boldsymbol{R}}$ is the competitive to cooperative transformation and $\boldsymbol{\phi}_t(\boldsymbol{z}_0)$ is a solution trajectory with initial condition $\boldsymbol{z}_0$.

$$\dot{x}_{i,1} = g_1(u_{i,1}) \cdot g_2(x_{i,2}) \cdot f_1(u_{i,2}) - x_{i,1}, \tag{4.56}$$

$$\dot{x}_{i,2} = f_2(x_{i,1}) - x_{i,2}, \tag{4.57}$$

$$\dot{x}_{i,3} = g_3(x_{i,1}) - x_{i,3}, \tag{4.58}$$

$$y_{i,1} = x_{i,2}, \tag{4.59}$$

$$y_{i,2} = x_{i,3}, \tag{4.60}$$

for each cell $1 \leq i \leq 60$. *The functions* f_j *and* g_j, $j = 1, 2, 3$, *are positive, bounded, and increasing and decreasing functions, respectively, of the form,*

$$f_j(x) = \frac{x^{k_j}}{\alpha_j + x^{k_j}} \quad \text{and} \quad g_j(x) = \frac{1}{1 + \beta_j x^{h_j}} \tag{4.61}$$

where $\alpha_j, \beta_j, k_j, h_j > 0$. *Let* $u_{i,1}$ *and* $u_{i,2}$ *be defined be short-range diffusion and contact-based bilayer connectivity graphs* $\mathcal{G}_1$ *and* $\mathcal{G}_2$, *respectively as in Figure 4.7. Explicitly, we have that outputs are converted to inputs via the global interconnection matrix such that* $\boldsymbol{u} = (\boldsymbol{W}_1 \otimes \boldsymbol{D}_1 + \boldsymbol{W}_2 \otimes \boldsymbol{D}_2)\,\boldsymbol{y}$ *for* $\boldsymbol{W}_1, \boldsymbol{W}_2 \in \boldsymbol{\mathcal{W}}$. *Here, we focus on the associated reduced IO system (4.56-4.60) which is defined by the simultaneously equitable partition* π_2. *Namely, in the reduced IO*

system, outputs are converted to inputs by $\boldsymbol{u} = \left(\overline{\boldsymbol{W}}_1 \otimes \boldsymbol{D}_1 + \overline{\boldsymbol{W}}_2 \otimes \boldsymbol{D}_2\right) \boldsymbol{y}$ *where*

$$\overline{\boldsymbol{W}}_1 = \begin{bmatrix} \frac{2w_1^{[1]}}{2w_1^{[1]}+4w_2^{[1]}} & \frac{4w_2^{[1]}}{2w_1^{[1]}+4w_2^{[1]}} \\ \frac{4w_2^{[1]}}{2w_1^{[1]}+4w_2^{[1]}} & \frac{2w_1^{[1]}}{2w_1^{[1]}+4w_2^{[1]}} \end{bmatrix} \quad \textit{and} \quad \overline{\boldsymbol{W}}_2 = \begin{bmatrix} \frac{2w_1^{[2]}}{2w_1^{[2]}+2w_2^{[2]}} & \frac{2w_2^{[2]}}{2w_1^{[1]}+2w_2^{[2]}} \\ \frac{2w_2^{[2]}}{2w_1^{[2]}+2w_2^{[2]}} & \frac{2w_1^{[2]}}{2w_1^{[2]}+2w_2^{[2]}} \end{bmatrix} \tag{4.62}$$

such that $n_{1,L_1}^{[1]} = n_{1,L_2}^{[1]} = n_{1,L_1}^{[2]} = n_{1,L_2}^{[2]} = 2$, $n_{2,L_1}^{[1]} = n_{2,L_2}^{[1]} = 4$ *and* $n_{2,L_1}^{[2]} = n_{2,L_2}^{[2]} = 2$. *We seek to show the existence of polarity-driven laminar patterns using the quotient graphs and so we first require the HSS of the IO system (4.56-4.60), then we derive the derivative of the transfer function* $\mathcal{DT}\left(\boldsymbol{u}_i\right)$, *highlighting that Assumption 4.2.1 is satisfied. Applying Theorem 4.2.1, we generate polarity regimes for the existence of patterning.*

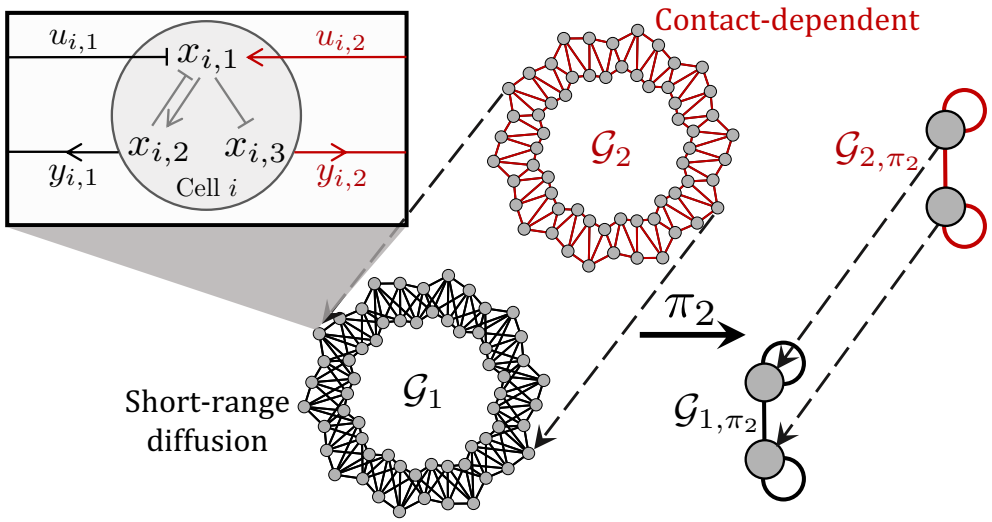

Figure 4.7: A schematic of the IO system considered in Example 4.2.2.

The HSS of the IO system (4.56 - 4.60) can be determined by solving

$$g_1\left(f_2\left(x_1^*\right)\right) \cdot g_2\left(f_2\left(x_1^*\right)\right) \cdot f_1\left(g_3\left(x_1^*\right)\right) - x_1^* = 0 \tag{4.63}$$

for x_1^* *by setting* $u_{i,1} = x_{i,2}$ *and* $u_{i,2} = x_{i,3}$, *conforming to homogeneous input and outputs of the tissue. Furthermore, the HSS defined by solving equation (4.63) is always stable in the absence of interconnections. This can be shown by considering the linearisation of the intracellular kinetics*

$$\boldsymbol{A} \coloneqq \frac{\partial \boldsymbol{f}}{\partial \boldsymbol{x}_i} = \begin{bmatrix} -1 & f_1 g_1 g_2' & 0 \\ f_2' & -1 & 0 \\ g_3' & 0 & -1 \end{bmatrix}. \tag{4.64}$$

As $\det\left(\boldsymbol{A}\right) = f_1 g_1 f_2' g_2' - 1 < 0$ *always holds by the monotonicity of the functions* f_j *and* g_j, *then the HSS defined by solving equation (4.63) is unique by Lemma 4.1.2. In addition,* $\boldsymbol{A}$ *has eigenvalues*

$$\mu_1 = -1, \quad \mu_2 = -1 + \sqrt{f_1 g_1 f_2' g_2'} \quad \textit{and} \quad \mu_3 = -1 - \sqrt{f_1 g_1 f_2' g_2'} \tag{4.65}$$

and so as $\mu_1, \Re(\mu_2), \Re(\mu_3) < 0$ *we have that* $\boldsymbol{A}$ *is stable. Thus any instability of the HSS will be induced by the interconnection of cells in the tissue.*

The derivative of the transfer function can be determined by linearisation of the IO kinetics (4.56 - 4.60) as demonstrated in [117] such that $\mathcal{D}\boldsymbol{T}(\boldsymbol{u}_i) = -\boldsymbol{C}\boldsymbol{A}^{-1}\boldsymbol{B}$ *where* $\boldsymbol{B}$ *and* $\boldsymbol{C}$ *are the linearised inputs and outputs respectively as in Lemma 4.1.3. For the IO system (4.56 - 4.60), the derivative of the transfer function has the form*

$$\begin{aligned}\mathcal{D}\boldsymbol{T}(\boldsymbol{u}_i) &= -\det(\boldsymbol{A})^{-1}\begin{bmatrix}0 & 1 & 0\\ 0 & 0 & 1\end{bmatrix}\begin{bmatrix}1 & f_1g_1g_2' & 0\\ f_2' & 1 & 0\\ g_3' & f_1g_1g_2'g_3' & 1-f_1g_1g_2'\end{bmatrix}\begin{bmatrix}f_1g_2g_1' & g_1g_2f_1'\\ 0 & 0\\ 0 & 0\end{bmatrix},\\ &= -\det(\boldsymbol{A})^{-1}\begin{bmatrix}f_1g_2f_2'g_1' & g_1g_2f_1'f_2'\\ f_1g_2g_1'g_3' & g_1g_2f_1'g_3'\end{bmatrix}, \qquad (4.66)\end{aligned}$$

where each of the functions f_j *and* g_j *are evaluated using the corresponding arguments for the given input state* $\boldsymbol{u}_i$*. The product of bounded functions are bounded [213] and subsequently* $\mathcal{D}\boldsymbol{T}(\boldsymbol{u}_i)$ *is element-wise bounded as* f_j, g_j, f_j' *and* g_j' *are bounded. In addition, from the monotonicity of* f_j *and* g_j *we have that*

$$sgn(\mathcal{D}\boldsymbol{T}(\boldsymbol{u}_i)) = \begin{bmatrix}- & +\\ + & -\end{bmatrix} = \mathcal{S}_0' \qquad (4.67)$$

and so the IO system (4.56 - 4.60) satisfies Assumption 4.2.1. Therefore by Theorem 4.2.1 we have that for the IO system (4.56 - 4.60), which spatially coupled using the quotient graphs $\mathcal{G}_{1,\pi_2}$ *and* $\mathcal{G}_{2,\pi_2}$*, then the instability of the HSS, in addition to the monotone polarity conditions* $w_1^{[1]} \leq 2w_2^{[1]}$ *and* $w_1^{[2]} \leq w_2^{[2]}$*, produce contrasting cell-wise states.*

By Corollary 4.1.1 we apply the DIDO instability inequality (4.21) to the IO system (4.56 - 4.60). As $\det(\mathcal{D}\boldsymbol{T}(\boldsymbol{u}_i)) = 0$*, the DIDO instability inequality (4.21) reduces to* $1 < \operatorname{tr}\left(\overline{\boldsymbol{\Lambda}}_2\mathcal{D}\boldsymbol{T}(\boldsymbol{u}_i)\right)$*, namely the HSS is unstable only if*

$$1 < -\det(\boldsymbol{A})^{-1}\left(\left(\frac{w_1^{[1]}-2w_2^{[1]}}{w_1^{[1]}+2w_2^{[1]}}\right)f_1g_2g_1'f_2' + \left(\frac{w_1^{[2]}-w_2^{[2]}}{w_1^{[2]}+w_2^{[2]}}\right)g_1g_2f_1'g_3'\right) \qquad (4.68)$$

for the reduced IO system (4.56 - 4.60). The monotone polarity condition (M1) $w_1^{[1]} \leq 2w_2^{[1]}$ *and* $w_1^{[2]} \leq w_2^{[2]}$ *of Theorem 4.1.1 confirm that each of the reduced connectivity matrices must have negative eigenvalues to produce the instability of the HSS as* $f_1g_2g_1'f_2' < 0$ *and* $g_1g_2f_1'g_3' < 0$ *by the monotone properties of the functions* f_j *and* g_j*. Critically, the HSS instability inequality (4.68) highlights that as the layer-wise activator/receptor polarity increases, i.e.* $w_1^{[i]} \ll w_2^{[i]}$*, the potential to induce laminar patterns also increases in the quotient system. Then by the spectral retention property of the equitable partition* π_2*, we have that laminar patterns must exist in the pattern space of the associated large-scale system.*

To illustrate the application Theorem 4.2.1 to the IO system (4.56 - 4.60) numerical verification of the polarity parameter regime for laminar pattern existence determined by inequality (4.68) is given in Figure 4.8.

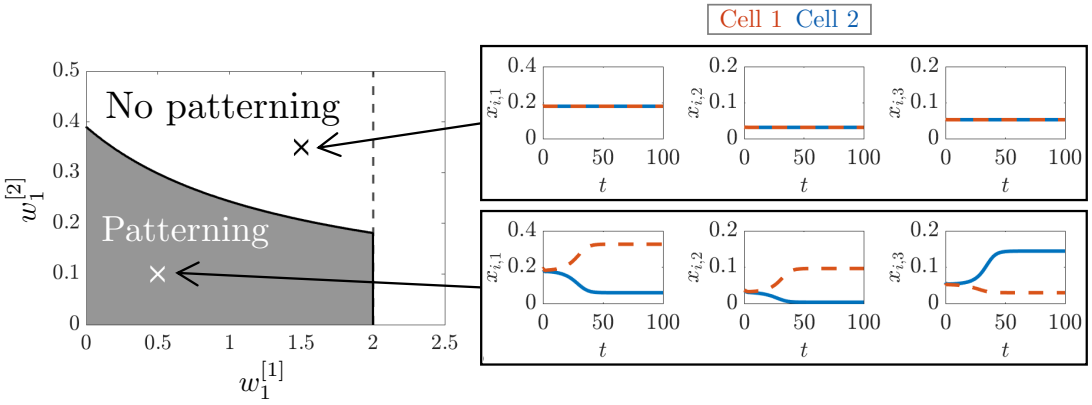

Figure 4.8: Polarity parameter regimes for the existence of laminar patterns in the IO system (4.56-4.60). For fixed $w_2^{[1]} = w_2^{[2]} = 1$, inequality (4.68) in addition to the monotone polarity conditions $w_1^{[1]} \leq w_2^{[1]}$ and $w_1^{[2]} \leq 2w_2^{[2]}$ to define a regions in $\left(w_1^{[1]}, w_1^{[2]}\right)$-space for the existence of laminar patterns. The dashed line in the $\left(w_1^{[1]}, w_1^{[2]}\right)$-space corresponds to the monotone condition (M1) $w_1^{[1]} \leq 2w_2^{[1]}$. Example simulations are given for polarity parameter values inside the pattern region, $(0.5, 0.1)$, and outside the pattern region $(1.5, 0.35)$. Initial conditions were given as small random perturbations about the HSS, $\boldsymbol{x}^* = [0.18, 0.03, 0.05]^T$. IO system (4.56-4.60) parameter values and details on simulations are given in Appendix D.

As demonstrated in Example 4.2.2, the method of pattern templating for contrasting solutions between cells in opposing layers can be used to show the existence of layer-wise differing steady states via polarity-driven instabilities. However, the associated large-scale systems may have many locally stable steady states that produce the pattern space of the IO system, which could have been lost during the dimension-reducing transformation by the partition, π_2 [118]. Therefore, in the following section, we investigate the spectral properties of the bilayer connectivity graphs to ensure that the laminar patterns produced by Theorem 4.2.1 are indeed globally dominant, namely, the behaviour observed in the quotient systems are preserved in the large-scale counterparts.

4.2.3 Spectral links between quotient and large-scale bilayer connectivity graphs

For linearised dynamical systems near steady state, the local solution trajectories are a linear combination of the associated eigenvectors scaled by the corresponding

exponent of the eigenvalues [225]. Thus, in the instance of steady-state instability, all trajectories close to the steady-state will locally tend in the direction of the eigenvector associated with the largest real-part eigenvalue. Critically, to ensure the monotone convergence of laminar patterns in the reduced IO systems in Theorem 4.2.1, we transformed the polarity-dependent eigenvector to be directed in the positive orthant, conforming to the behaviour of cooperative dynamics. Thus, motivated by this positive direction transformation, we seek to understand when the eigenvalue associated with laminar pattern formation dominates the large-scale spectra to ensure perturbed trajectories from the HSS to be preferably pointed in the direction to achieve layer-wise contrasting states in the large-scale IO systems.

Previous studies on pattern formation using IO systems have imposed the sufficient condition that the large-scale and quotient multilayer connectivity graphs $\mathcal{G}_k$ are bipartite, as this generates monotone dynamics with respect to the bipartition vector [117, 118, 186, 207]. Namely, a graph $\mathcal{G}_k$ is said to be bipartite if the vertices $v \in V$ can be partitioned into two independent sets V_1 and V_2 such that no two vertices in the same set are adjacent [220]. Example bipartite bilayer graphs are given in Figure 4.9a. However, it can be demonstrated that for bipartite bilayer graphs, the polarity-dependent eigenvalue, $\overline{\lambda}_{k,2}$, associated with laminar pattern formation cannot be minimal in the spectrum, a requirement for local laminar pattern trajectory dominance near the HSS with competitive kinetics.

Lemma 4.2.8. *Let $\mathcal{G}_k$ be a bipartite bilayer graph with weighted adjacency matrix $\boldsymbol{W}_k \in \boldsymbol{\mathcal{W}}$. Then for any $w_1^{[k]}, w_2^{[k]} > 0$ the polarity-dependent eigenvalue $\overline{\lambda}_{k,2}$ associated with the reduced adjacency matrix $\overline{\boldsymbol{W}}_k$ satisfies*

$$\overline{\lambda}_{k,2} \neq \min\left(\mathrm{Spec}\left(\boldsymbol{W}_k\right)\right). \tag{4.69}$$

Proof. Consider $\lambda_{k,j} \in \mathrm{Spec}\left(\boldsymbol{W}_k\right)$, then by the spectral symmetry of bipartite graphs about the origin we have that $-\lambda_{k,j} \in \mathrm{Spec}\left(\boldsymbol{W}_k\right)$ [220]. As $\boldsymbol{W}_k \in \boldsymbol{\mathcal{W}}$ then $\lambda_{k,1} = \max\left(\mathrm{Spec}\left(\boldsymbol{W}_k\right)\right) = 1$ by the connected and row-stochastic properties of $\boldsymbol{W}_k$ [210]. Consequently, $-\lambda_{k,1} = \min\left(\mathrm{Spec}\left(\boldsymbol{W}_k\right)\right) = -1$. However, the minimal eigenvalue of the reduced adjacency matrix $\overline{\boldsymbol{W}}_k$ defined by the laminar pattern partition, π_2, must be of the form $\overline{\lambda}_{k,2} = a_k + b_k - 1$ for $a_k, b_k \in (0,1)$ by Lemma 4.2.4. Critically, this implies that $\overline{\lambda}_{k,2} \in (-1,1)$ and therefore $\overline{\lambda}_{k,2} \neq \min\left(\mathrm{Spec}\left(\boldsymbol{W}_k\right)\right)$ for any layer-wise polarity values $w_1^{[k]}, w_2^{[k]} > 0$. □

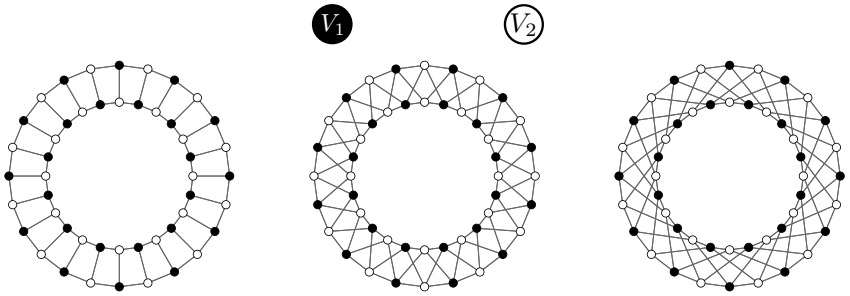

(a) Bipartite bilayer graphs.

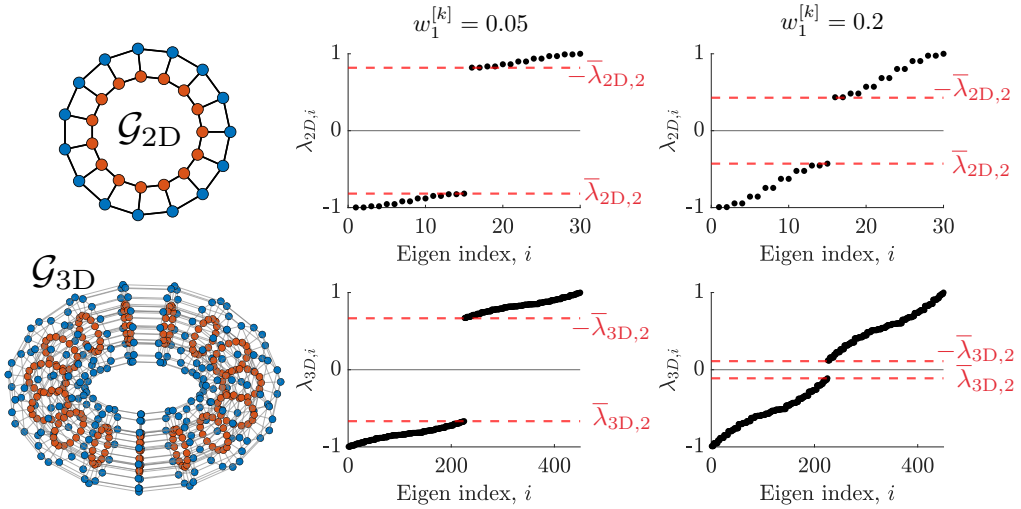

(b) Example spectra of bipartite bilayers.

Figure 4.9: Structure and spectra of bipartite bilayer connectivity graphs. (A) Example regular bipartite graphs where vertices are coloured with respect to the bipartition sets V_1 and V_2 in black and white, respectively. (B) Spectra of two bipartite graphs $\mathcal{G}_{2D}$ and $\mathcal{G}_{3D}$ is shown for $w_1^{[k]} = 0.05$ and $w_1^{[k]} = 0.2$ for fixed $w_2^{[k]} = 1$ ($k \in \{2D, 3D\}$) where the eigen index refers to the position of the eigenvalue when listed in ascending order. The dashed red lines correspond to the polarity-dependent eigenvalue $\overline{\lambda}_{k,2}$ highlighting its position with respect to the ascending spectrum of the associated large-scale graph. The vertices of the graphs are coloured layer-wise to emphasise their bilayer structure.

A direct consequence of Lemma 4.2.8 is that if the large-scale IO system (4.1) with competitive kinetics and spatially coupled by a bipartite bilayer graph $\mathcal{G}_k$, any trajectory initiated from a small perturbation of an unstable HSS will not be dominantly travelling in the direction of the eigenvector associated with laminar patterning. Critically, the eigenvector that direct solutions towards laminar patterns are the weakest component of the linear combinations of eigenvectors that approximate the trajectories near the HSS. Subsequently, it has previously been shown that the dominant patterns by the bipartition vectors, independent of graph edge weights [207] for purely competitive kinetics. Figure 4.9b demonstrates the consequences of Lemma 4.2.8, and for the given bipartite

graphs, the laminar patterning polarity-dependent eigenvalue $\overline{\lambda}_{k,2}$ defines a spectral gap about the origin which is verified in Appendix E.

Following Lemma 4.2.8, we focus our attention on the spectral investigation of non-bipartite bilayer graphs. As we are interested in the polarity-driven pattern events using a pre-defined pattern template, π_2, we seek to understand where $\overline{\lambda}_{k,2}$ is positioned in the spectrum of the associated large-scale graph $\mathcal{G}_k$.

Lemma 4.2.9. *Let $\mathcal{G}_k$ be a non-bipartite regular graph with weighted adjacency matrix $\boldsymbol{W}_k \in \boldsymbol{\mathcal{W}}$ and eigenvalues in descending order $\lambda_{k,1} \geq ... \geq \lambda_{k,N}$. Consider the following polarity regimes:*

(I) cross-layer dominated polarity regime, $w_1^{[k]} \ll w_2^{[k]}$, then $\overline{\lambda}_{k,2} = \lambda_{k,N}$,

(II) same-layer dominated polarity regime, $w_1^{[k]} \gg w_2^{[k]}$, then $\overline{\lambda}_{k,2} = \lambda_{k,2}$,

where $\overline{\lambda}_{k,2}$ is the polarity dependent eigenvalue of $\overline{\boldsymbol{W}}_k$.

Proof. As π_2 is an equitable partition of $\mathcal{G}_k$, there exists a lifting matrix $\boldsymbol{L} \in \{0,1\}^{N\times 2}$ which defines the quotient mapping algebraically

$$\boldsymbol{W}_k\boldsymbol{L} = \boldsymbol{L}\overline{\boldsymbol{W}}_k, \tag{4.70}$$

as defined in [220]. The lifting matrix is constructed by grouping vertices of $\mathcal{G}_k$ with the associated partition, for example, $\boldsymbol{L}_{ij} = 1$ if $v_i \in L_j$. By the block definition of $\boldsymbol{W}_k$, the lifting matrix for bilayer graphs has the form

$$\boldsymbol{L} = \begin{bmatrix} \mathbf{1}_{|L_1|,1} & \mathbf{0}_{|L_1|,1} \\ \mathbf{0}_{|L_2|,1} & \mathbf{1}_{|L_2|,1} \end{bmatrix}. \tag{4.71}$$

Consider polarity-dependent eigenvalue $\overline{\lambda}_{k,2} = a_k + b_k - 1$ and associated eigenvector $\overline{\boldsymbol{v}}_{k,2} = c\,(-1,1)^T$ of $\overline{\boldsymbol{W}}_k$ for any $c \in \mathbb{R}\backslash\{0\}$. Following equation (4.70), multiplication by $\overline{\boldsymbol{v}}_{k,2}$ yields

$$\boldsymbol{W}_k\boldsymbol{L}\overline{\boldsymbol{v}}_{k,2} = \boldsymbol{L}\overline{\boldsymbol{W}}_k\overline{\boldsymbol{v}}_{k,2} = \overline{\lambda}_{k,2}\boldsymbol{L}\overline{\boldsymbol{v}}_{k,2} \tag{4.72}$$

and therefore $\boldsymbol{L}\overline{\boldsymbol{v}}_{k,2}$ is an eigenvector of the large-scale graph $\mathcal{G}_k$ and has the normalised form

$$\boldsymbol{L}\overline{\boldsymbol{v}}_{k,2} = \frac{1}{\sqrt{N}}\begin{bmatrix} -\mathbf{1}_{|L_1|,1} \\ \mathbf{1}_{|L_2|,1} \end{bmatrix} \tag{4.73}$$

for the polarity-dependent eigenvalue $\overline{\lambda}_{k,2} = a_k + b_k - 1$. We focus on the position of eigenpair $\left(\overline{\lambda}_{k,2}, \boldsymbol{L}\overline{\boldsymbol{v}}_{k,2}\right)$ within Spec $(\boldsymbol{W}_k)$.

The Rayleigh quotient provides a bound on the numerical range of a matrix [220] and for $\boldsymbol{W}_k$ is defined by

$$R_{\boldsymbol{W}_k}(\boldsymbol{y}) = \frac{\boldsymbol{y}^T\boldsymbol{W}_k\boldsymbol{y}}{\boldsymbol{y}^T\boldsymbol{y}}. \tag{4.74}$$

The regularity of $\mathcal{G}_k$ implies that $\boldsymbol{W}_k$ is symmetric and therefore by the Min-Max theorem we have that $R_{\boldsymbol{W}_k}(\boldsymbol{y}) \in [\min(\mathrm{Spec}(\boldsymbol{W}_k)), \max(\mathrm{Spec}(\boldsymbol{W}_k))]$. Note that if $\boldsymbol{v}_{k,i}$ is an eigenvector of $\boldsymbol{W}_k$, then $R_{\boldsymbol{W}_k}(\boldsymbol{v}_{k,i}) = \lambda_{k,i}$.

The eigenvectors of $\boldsymbol{W}_k$ form an orthonormal basis in $\mathbb{R}^N$ as $\boldsymbol{W}_k$ is real and symmetric, and therefore $\boldsymbol{y}^T\boldsymbol{y} = 1$. By the block structure of $\boldsymbol{W}_k$ (4.8) and direct computation, the Rayleigh quotient can be expressed as follows

$$\begin{aligned} R_{\boldsymbol{W}_k}(\boldsymbol{y}) &= \boldsymbol{y}^T\boldsymbol{W}_k\boldsymbol{y}, \\ &= \sum_{i=1}^{N}\sum_{j=1}^{N}(\boldsymbol{W}_k)_{ij}\,\boldsymbol{y}_i\boldsymbol{y}_j, \\ &= \sum_{i=1}^{|L_1|}\left(\sum_{j=1}^{|L_1|}\left(\widehat{\boldsymbol{W}}_{1,L_1}^{[k]}\right)_{ij}\boldsymbol{y}_i\boldsymbol{y}_j + \sum_{j=|L_1|+1}^{N}\left(\widehat{\boldsymbol{W}}_{2,L_1}^{[k]}\right)_{ij}\boldsymbol{y}_i\boldsymbol{y}_j\right) \\ &\quad + \sum_{i=|L_1|+1}^{N}\left(\sum_{j=1}^{|L_1|}\left(\widehat{\boldsymbol{W}}_{2,L_1}^{[k]}\right)_{ji}\boldsymbol{y}_i\boldsymbol{y}_j + \sum_{j=|L_1|+1}^{N}\left(\widehat{\boldsymbol{W}}_{1,L_2}^{[k]}\right)_{ij}\boldsymbol{y}_i\boldsymbol{y}_j\right). \end{aligned} \tag{4.75}$$

In the cross-layer polarity regime (I), $w_1^{[k]} \ll w_2^{[k]}$, by definition of the weighted adjacency matrices $\boldsymbol{W}_k$ we have that $0 < \left(\widehat{\boldsymbol{W}}_{1,L_1}^{[k]}\right)_{ij}, \left(\widehat{\boldsymbol{W}}_{1,L_2}^{[k]}\right)_{ij} \ll \left(\widehat{\boldsymbol{W}}_{2,L_1}^{[k]}\right)_{ij} < 1$ and the Rayleigh quotient can be estimated by

$$R_{\boldsymbol{W}_k}(\boldsymbol{y}) \approx \sum_{i=1}^{|L_1|}\left(\sum_{j=|L_1|+1}^{N}\left(\widehat{\boldsymbol{W}}_{2,L_1}^{[k]}\right)_{ij}\boldsymbol{y}_i\boldsymbol{y}_j\right) + \sum_{i=|L_1|+1}^{N}\left(\sum_{j=1}^{|L_1|}\left(\widehat{\boldsymbol{W}}_{2,L_1}^{[k]}\right)_{ji}\boldsymbol{y}_i\boldsymbol{y}_j\right), \tag{4.76}$$

which is minimised when $\boldsymbol{y}_i\boldsymbol{y}_j < 0$ for any $i \in \{1, ..., |L_1|\}$ and $j \in \{|L_1|+1, ..., N\}$. As each eigenvector of $\boldsymbol{W}_k$ is orthonormal, $\boldsymbol{L}\overline{\boldsymbol{v}}_{k,2}$ is the only eigenvector to satisfy this minimisation property because any other eigenvector $\tilde{\boldsymbol{y}}$ has $\tilde{\boldsymbol{y}}_i\tilde{\boldsymbol{y}}_j > 0$ for some $i \in \{1, ..., |L_1|\}$ and $j \in \{|L_1|+1, ..., N\}$ by orthogonality, $\boldsymbol{y}^T\tilde{\boldsymbol{y}} = 0$. Therefore $\overline{\lambda}_{k,2} = \min(\mathrm{Spec}(\boldsymbol{W}_k))$ for $w_1^{[k]} \ll w_2^{[k]}$ by the Min-Max theorem for symmetric matrices [220].

In the same-layer polarity regime (II), $w_1^{[k]} \gg w_2^{[k]}$, we have that $0 < \left(\widehat{\boldsymbol{W}}_{2,L_1}^{[k]}\right)_{ij} \ll \left(\widehat{\boldsymbol{W}}_{1,L_1}^{[k]}\right)_{ij}, \left(\widehat{\boldsymbol{W}}_{1,L_2}^{[k]}\right)_{ij} < 1$. The maximum eigenvalue $\lambda_{k,1} = 1$ with the associated normalised positive eigenvector

$$\boldsymbol{v}_{k,1} = \frac{1}{\sqrt{N}}[1, ..., 1] \tag{4.77}$$

by the row-stochasticity of $\boldsymbol{W}_k$, and thus we seek the second largest eigenvalue. Following our previous approach, the Rayleigh quotient in the same-layer polarity

regime (II) has the approximate form

$$R_{\boldsymbol{W}_k}(\boldsymbol{y}) \approx \sum_{i=1}^{|L_1|}\left(\sum_{j=1}^{|L_1|}\left(\widehat{\boldsymbol{W}}_{1,L_1}^{[k]}\right)_{ij}\boldsymbol{y}_i\boldsymbol{y}_j\right)+\sum_{i=|L_1|+1}^{N}\left(\sum_{i=|L_1|+1}^{N}\left(\widehat{\boldsymbol{W}}_{1,L_2}^{[k]}\right)_{ij}\boldsymbol{y}_i\boldsymbol{y}_j\right), \tag{4.78}$$

which is maximised when $\boldsymbol{y}_i\boldsymbol{y}_j > 0$ for all $i,j \in \{1,...,|L_1|\}$ and $i,j \in \{|L_1|+1,...,N\}$. Critically, the only eigenvectors to satisfy this property are $\boldsymbol{v}_{k,1}$, and $\boldsymbol{L}\overline{\boldsymbol{v}}_{k,2}$ by orthogonality. Then as $\overline{\lambda}_{k,2} < \lambda_{k,1} = 1$, we have that $\overline{\lambda}_{k,2} = \lambda_{k,2}$.

□

We have demonstrated that we can control the position of the polarity-dependent eigenvalue $\overline{\lambda}_{k,2}$ in the ordered spectrum of the large-scale adjacency matrix $\boldsymbol{W}_k$ by imposing high signalling anisotropy in bilayer structures. Critically, in cross-layer polarity regimes (I), the extrema of the spectra is preserved in the quotient mapping, π_2, and therefore local behaviour about the HSS will be consistent in the reduced and associated large-scale IO system.

The block representation of the Rayleigh quotient (4.75) indicates that the number of same-layer, $n_{1,L_{1,2}}$, and cross-layer, $n_{2,L_{1,2}}$, connections for each cell dictates the amount of polarisation required to achieve the spectral positions defined Lemma 4.2.9. Namely, $n_{1,L_{1,2}}$ determines the number of $\left(\widehat{\boldsymbol{W}}_{1,L_{1,2}}^{[k]}\right)_{ij} > 0$ and n_{2,L_j} determines the number of $\left(\widehat{\boldsymbol{W}}_{2,L_{1,2}}^{[k]}\right)_{ij} > 0$ in each row sum. Consequently, achieving $\overline{\lambda}_{k,2} = \lambda_{k,N}$ requires less polarity in graphs with a large number of cross-layer connections, and conversely $\overline{\lambda}_{k,2} = \lambda_{k,2}$ requires less polarity in graphs with a large number of same-layer connections. A demonstration of this property and Lemma 4.2.9 is given in Figure 4.10.

Theorem 4.2.1 demonstrated that the existence of laminar patterns is dependent on the existence of polarity within the quotient connectivity graphs to induce both HSS instability and monotonicity of solutions. In this section, we have shown that polarity, namely the values $w_1^{[k]}$ and $w_2^{[k]}$, can be used to control the position of the eigenvalue associated with laminar patterns in the quotient graphs in the spectra of the large-scale graphs. Therefore, in the following section, we explore whether solution behaviours observed in the reduced systems are preserved in the associated large-scale systems when the quotient graphs preserve the extrema of the spectra of the large-scale graphs. Namely, we show that the analysis conducted on the reduced IO systems yields global pattern convergence in high polarity regimes.

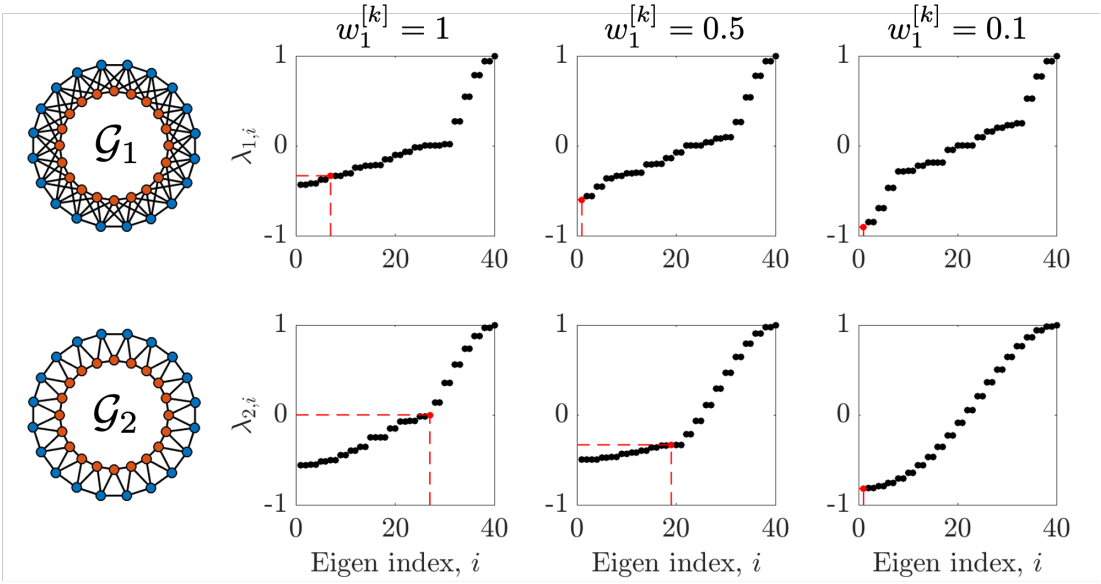

(a) Spectral shifts in a cross-layer polarity regime (I).

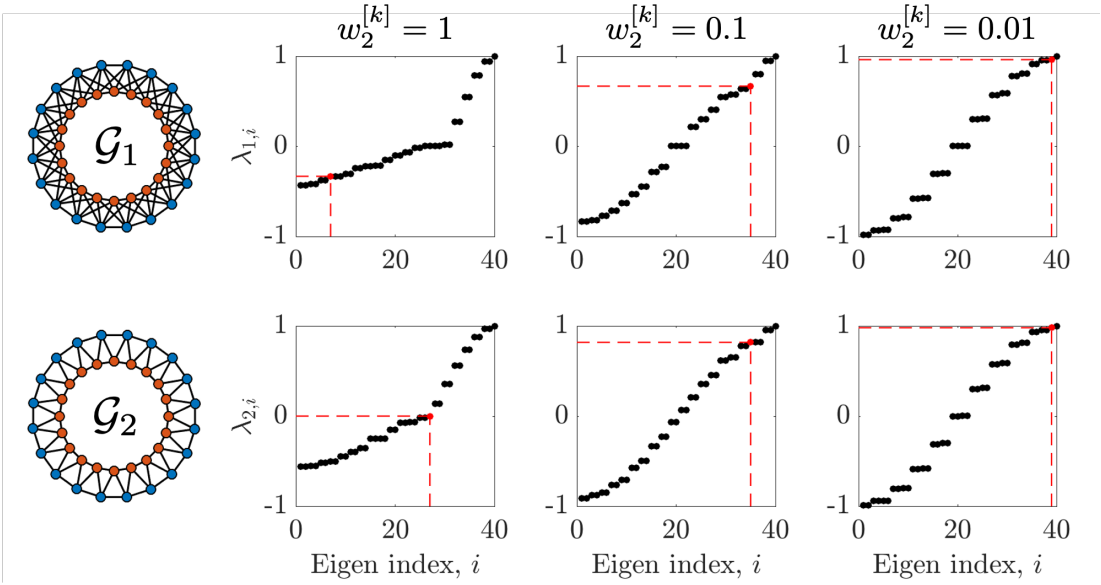

(b) Spectral shifts in a same-layer polarity regime (II).

Figure 4.10: Eigenvalues associated with laminar pattern trajectories tend to change position in the large-scale spectra in regular non-bipartite bilayer graphs with high signal anisotropy. Cell connectivity graphs $\mathcal{G}_1$ and $\mathcal{G}_2$ from Example 4.2.2 with vertices coloured layer-wise are shown on the left. The spectrum of each graph is then shown in ascending order where the eigen index corresponds to the increasing ordering of the eigenvalues. The polarity-dependent eigenvalue $\overline{\lambda}_{k,2}$ is shown in red with dashed lines to highlight the position in the large-scale spectra. (a) For fixed $w_2^{[k]} = 1$, the values of $w_1^{[2]}$ decrease from left to right to demonstrate the transition to a cross-layer polarity regime (I). (b) For fixed $w_1^{[k]} = 1$, the values of $w_2^{[k]}$ decrease from left to right to demonstrate a transition to a same-layer polarity regime (II).

4.2.4 Polarity induced laminar pattern formation derived by quotient systems for large-scale bilayer geometries

We explore the conditions in which the patterns predicted using the dimension reduction technique of quotient templating are the globally dominant patterns produced in the large-scale IO systems. We have demonstrated in Section 4.2.3 that the spectra of regular non-bipartite bilayer connectivity graphs can be bounded by the extrema of the spectra of the associated quotient graphs defined by π_2. This implies that the polarity-driven HSS instability imposed by the pattern existence condition of Theorem 4.2.1 in the quotient systems must also exist in the large-scale systems and can become dominant in high-polarity regimes. Therefore, we focus our attention on whether the large-scale IO system is monotone with respect to the eigenvector locally directing solutions to laminar patterns, thus preserving trajectory direction.

Lemma 4.2.10. *Consider the large-scale IO system (4.1) spatially coupled by the global adjacency matrix $\boldsymbol{P}$ (4.3) where $\boldsymbol{W}_k \in \boldsymbol{\mathcal{W}}$ for $k \in \{1, ..., r\}$. Let Assumption 4.2.1 be satisfied and the laminar pattern partition, π_2, be simultaneously equitable, for all regular and non-bipartite connectivity graphs $\mathcal{G}_k$. Given that the global monotonic (GM) conditions:*

(GM1) $w_1^{[k]} \ll w_2^{[k]}$ *if* $sgn\left(\mathcal{D}\boldsymbol{T}\right) = \mathcal{S}_0$ *or* $\mathcal{S}_0'$,

(GM2) $(-1)^{k+1} w_1^{[k]} \ll (-1)^{k+1} w_2^{[k]}$ *if* $sgn\left(\mathcal{D}\boldsymbol{T}\right) = \mathcal{S}_1$ *or* $\mathcal{S}_1'$,

(GM3) $(-1)^{k} w_1^{[k]} \ll (-1)^{k} w_2^{[k]}$ *if* $sgn\left(\mathcal{D}\boldsymbol{T}\right) = \mathcal{S}_2$ *or* $\mathcal{S}_2'$,

(GM4) $w_1^{[k]} \gg w_2^{[k]}$ *if* $sgn\left(\mathcal{D}\boldsymbol{T}\right) = \mathcal{S}_3$ *or* $\mathcal{S}_3'$,

are satisfied then the large-scale IO system (4.1) generates monotone solutions in the direction of laminar patterns.

Proof. Similar to Theorem 4.2.1 we consider the large-scale auxiliary system

$$\begin{bmatrix} \dot{\boldsymbol{z}}_1 \\ \vdots \\ \dot{\boldsymbol{z}}_N \end{bmatrix} = - \begin{bmatrix} \boldsymbol{z}_1 \\ \vdots \\ \boldsymbol{z}_N \end{bmatrix} + \boldsymbol{P} \begin{bmatrix} \boldsymbol{T}\left(\boldsymbol{z}_1\right) \\ \vdots \\ \boldsymbol{T}\left(\boldsymbol{z}_N\right) \end{bmatrix} \coloneqq \boldsymbol{F}\left(\boldsymbol{z}\right), \tag{4.79}$$

which has identical behaviour to the large-scale IO system (4.1) by Lemma 4.1.1. First, we will construct the sign structure of the eigenvector associated with laminar patterns in the large-scale graphs. Then, by transforming the auxiliary system (4.79) to ensure the positivity of the laminar pattern eigenvector, we demonstrate that the large-scale IO system (4.1) has the capacity to become type K in high polarity regimes in bilayers.

Linearising the auxiliary system (4.79) about a generic point $\boldsymbol{z} \in \mathbb{R}^{rN}_{\geq}$ yields

$$\frac{\partial \boldsymbol{F}}{\partial \boldsymbol{z}} = -\boldsymbol{I}_{rN} + \boldsymbol{P} \begin{bmatrix} \mathcal{D}\boldsymbol{T}(\boldsymbol{z}_1) & & \\ & \ddots & \\ & & \mathcal{D}\boldsymbol{T}(\boldsymbol{z}_N) \end{bmatrix} \tag{4.80}$$

where $\boldsymbol{T}(\cdot)$ satisfies Assumption 4.2.1. From Lemma 4.2.3 the bijective coordinate transformation $\boldsymbol{M}\boldsymbol{w} = \boldsymbol{z}$, where $\boldsymbol{M} = \boldsymbol{I}_N \otimes \widetilde{\boldsymbol{M}}$, converts between sign structures $\mathcal{S}_i$ and $\mathcal{S}'_i$ $(i \in \{0,1,2,3\})$, and therefore we continue with $sgn(\mathcal{D}\boldsymbol{T}(\cdot)) = \mathcal{S}_i$ without loss of generality.

The reduced graphs associated with the laminar pattern template $\mathcal{G}_{k,\pi_2}$ of regular graphs $\mathcal{G}_k$ has eigenvalues $\overline{\lambda}_{k,1} = 1$ and $\overline{\lambda}_{k,2} = a_k + b_k - 1$ with normalised eigenvectors

$$\overline{\boldsymbol{v}}_{k,1} = \frac{1}{\sqrt{2}} \begin{bmatrix} 1 \\ 1 \end{bmatrix} \quad \text{and} \quad \overline{\boldsymbol{v}}_{k,2} = \frac{1}{\sqrt{2}} \begin{bmatrix} -1 \\ 1 \end{bmatrix}, \tag{4.81}$$

by definition of the reduced adjacency matrix $\overline{\boldsymbol{W}}_k$ (4.32). Subsequently, the polarity dependent eigenvector has sign structure $sgn(\overline{\boldsymbol{v}}_{k,2}) = [-,+]^T$. As shown in Lemma 4.2.9 there exists a matrix $\boldsymbol{L} \in \{0,1\}^{N \times 2}$ that maps the large-scale graph into the quotient graph such that

$$\boldsymbol{L}\overline{\boldsymbol{W}}_k = \boldsymbol{W}_k \boldsymbol{L}, \tag{4.82}$$

where $\boldsymbol{L}$ allocates the vertices of the large-scale system into the reduced groups associated with the laminar pattern template [220]. From the quotient to large-scale algebraic relation (4.82), we have that $\boldsymbol{L}\overline{\boldsymbol{v}}_{k,2}$ is an eigenvector of $\boldsymbol{W}_k$ with eigenvalue $\overline{\lambda}_{k,2}$. Specifically, this implies that the eigenvector associated with laminar patterning in the large-scale graphs has the sign structure $sgn(\boldsymbol{L}\overline{\boldsymbol{v}}_{k,2}) = [-,...,-,+,...,+]^T$ which has $|L_1|$ and $|L_2|$ negative and positive entries, respectively. Hence, the matrix $\widetilde{\boldsymbol{R}} = \text{diag}(-1,...,-1,1,...,1)$ orientates the laminar patterning eigenvector $\boldsymbol{L}\overline{\boldsymbol{v}}_{k,2}$ in the positive orthant, i.e., $\widetilde{\boldsymbol{R}}\boldsymbol{L}\overline{\boldsymbol{v}}_{k,2} > 0$.

We next introduce the transformation $\boldsymbol{w} = \boldsymbol{R}\boldsymbol{z}$ where $\boldsymbol{R} = \widetilde{\boldsymbol{R}} \otimes \boldsymbol{I}_r$, noting that $\boldsymbol{R}^{-1} = \boldsymbol{R}$. Following this change of variables, let $\boldsymbol{X}_1 = \text{diag}\left(\mathcal{D}\boldsymbol{T}(\boldsymbol{z}_1), ..., \mathcal{D}\boldsymbol{T}\left(\boldsymbol{z}_{|L_1|}\right)\right)$ and $\boldsymbol{X}_2 = \text{diag}\left(\mathcal{D}\boldsymbol{T}\left(\boldsymbol{z}_{|L_1|+1}\right), ..., \mathcal{D}\boldsymbol{T}(\boldsymbol{z}_N)\right)$, then by the layer-wise block formulation of the bilayer adjacency matrices, $\boldsymbol{W}_k$ (4.8),

the linearised auxiliary system (4.80) has the form

$$\begin{aligned}
\boldsymbol{R}\frac{\partial \boldsymbol{F}}{\partial \boldsymbol{z}}\boldsymbol{R} &= -\boldsymbol{I}_{rN} + \boldsymbol{R}\boldsymbol{P}\begin{bmatrix}\boldsymbol{X}_1 & \boldsymbol{0}\\ \boldsymbol{0} & \boldsymbol{X}_2\end{bmatrix}\boldsymbol{R},\\
&= -\boldsymbol{I}_{rN} + \left(\sum_{i=1}^{r}\widetilde{\boldsymbol{R}}\boldsymbol{W}_i\otimes\boldsymbol{D}_i\right)\cdot\begin{bmatrix}\boldsymbol{X}_1 & \boldsymbol{0}\\ \boldsymbol{0} & -\boldsymbol{X}_2\end{bmatrix},\\
&= -\boldsymbol{I}_{rN} + \left(\sum_{i=1}^{r}\begin{bmatrix}\widehat{\boldsymbol{W}}^{[i]}_{1,L_1}\otimes\boldsymbol{D}_i & \widehat{\boldsymbol{W}}^{[i]}_{2,L_1}\otimes\boldsymbol{D}_i\\ -\left(\widehat{\boldsymbol{W}}^{[i]}_{2,L_1}\right)^T\otimes\boldsymbol{D}_i & -\widehat{\boldsymbol{W}}^{[i]}_{1,L_2}\otimes\boldsymbol{D}_i\end{bmatrix}\right)\cdot\begin{bmatrix}\boldsymbol{X}_1 & \boldsymbol{0}\\ \boldsymbol{0} & -\boldsymbol{X}_2\end{bmatrix},\\
&= -\boldsymbol{I}_{rN} + \sum_{i=1}^{r}\begin{bmatrix}\left(\widehat{\boldsymbol{W}}^{[i]}_{1,L_1}\otimes\boldsymbol{D}_i\right)\boldsymbol{X}_1 & -\left(\widehat{\boldsymbol{W}}^{[i]}_{2,L_1}\otimes\boldsymbol{D}_i\right)\boldsymbol{X}_2\\ -\left(\left(\widehat{\boldsymbol{W}}^{[i]}_{2,L_1}\right)^T\otimes\boldsymbol{D}_i\right)\boldsymbol{X}_1 & \left(\widehat{\boldsymbol{W}}^{[i]}_{1,L_2}\otimes\boldsymbol{D}_i\right)\boldsymbol{X}_2\end{bmatrix},
\end{aligned} \tag{4.83}$$

by the mixed-product and block-product properties of the Kronecker, product [226]. The transformed auxiliary system (4.83) is monotone if the off-diagonal row-sum is non-negative by Lemma 4.2.1. Namely, if $\tau(i) = (i-1) \bmod r + 1$ then

$$\sum_{j\neq i}\left(\boldsymbol{R}\frac{\partial \boldsymbol{F}}{\partial \boldsymbol{z}}\boldsymbol{R}\right)_{ij} = \begin{cases}\hat{w}_1^{[\tau(i)]}\displaystyle\sum_{j=1,j\neq i}^{r|L_1|}(\boldsymbol{X}_1)_{ij} - \hat{w}_2^{[\tau(i)]}\sum_{j=1,j\neq i}^{r|L_2|}(\boldsymbol{X}_2)_{ij} & 1\leq i\leq r|L_1|,\\ -\hat{w}_2^{[\tau(i)]}\displaystyle\sum_{j=1,j\neq i}^{r|L_1|}(\boldsymbol{X}_1)_{ij} + \hat{w}_1^{[\tau(i)]}\sum_{j=1,j\neq i}^{r|L_2|}(\boldsymbol{X}_2)_{ij} & r|L_1|+1\leq i\leq rN.\end{cases} \tag{4.84}$$

Note that $\hat{w}_i^{[k]}$ are the row-normalised components of $w_i^{[k]}$, then if $sgn(\mathcal{D}\boldsymbol{T}) = \mathcal{S}_0$, then $\boldsymbol{X}_1$ and $\boldsymbol{X}_2$ are non-positive matrices and thus resultant row-sums are positive if condition (GM1) is satisfied. Conversely, if $sgn(\mathcal{D}\boldsymbol{T}) = \mathcal{S}_3$, then $\boldsymbol{X}_1$ and $\boldsymbol{X}_2$ are non-negative matrices and so the positivity of the row sum is guaranteed if condition (GM4) holds. For $sgn(\mathcal{D}\boldsymbol{T}) = \mathcal{S}_1, \mathcal{S}_2$, then $\boldsymbol{X}_1$ and $\boldsymbol{X}_2$ have alternating positive and negative row entries, and thus conditions (GM2) and (GM3) ensure row-sum positivity, respectively.

Critically, from the GM conditions we have that,

$$\sum_{j\neq i}\left(\boldsymbol{R}\frac{\partial \boldsymbol{F}}{\partial \boldsymbol{z}}\boldsymbol{R}\right)_{ij} \geq 0 \tag{4.85}$$

for all $1 \leq i \leq rN$. Therefore the auxiliary system (4.79) is type K by Lemma 4.2.1 and so is monotone in the direction for solutions associated with laminar patterning in high polarity regimes. □

Applying the cooperative transformation in high-polarity regimes to an IO system (4.1) where the extrema of the spectra are preserved in the quotient mapping guarantees the global convergence of laminar patterns in the large-scale

systems. Critically, this extends the existence statement of Theorem 4.2.1 to sufficient conditions for large-scale laminar patterning.

Theorem 4.2.2 (Global convergence of laminar patterns in highly-polarised regimes)**.** *Consider the highly polarised IO system as defined in Lemma 4.2.10. If the laminar pattern existence criterion, Theorem 4.2.1, is satisfied, then laminar patterns are globally convergent in the large-scale IO system (4.1).*

Proof. Following Theorem 4.2.1, by analysing the quotient graphs there exists $\overline{\boldsymbol{\Lambda}}_2$ such that the HSS instability condition (4.17) is satisfied. In addition, Lemma 4.2.10 guarantees that the IO system (4.1) generates monotone solutions in the direction of laminar patterns, such that the eigenvector associated with $\overline{\lambda}_{k,2}$ is directed in the positive orthant, $\widetilde{\boldsymbol{R}}\boldsymbol{L}\overline{\boldsymbol{v}}_{k,2} > 0$. Furthermore, Lemma 4.2.7 ensures that the linearised IO system is irreducible and thus the IO system (4.1) is strongly monotone by Lemma 4.2.2.

By the identical arguments of Theorem 4.2.1, the corresponding large-scale auxiliary system (4.80) has bounded solutions, which induces the convergence of solutions to steady-state $\boldsymbol{R}\boldsymbol{z}^{**} \neq \boldsymbol{R}\boldsymbol{z}^{*}$ by the Cooperative Irreducible Convergence Theorem (Theorem 4.3.3 in [187]). Critically, mapping back to the original coordinating system guarantees that vertices in different layers have contrasting solutions. □

The sufficient conditions for large-scale laminar patterning outlined in Theorem 4.2.2 ensure that the behaviour observed in the quotient systems is preserved in the corresponding large-scale systems in highly polarised parameter regimes. Subsequently, this enables an analytic approach to pattern prediction as we can fully determine the spectra of the quotient graphs $\mathcal{G}_{k,\pi_2}$ independently and without imposing commutativity conditions on the reduced adjacency matrices. The following example demonstrates the accessibility of the analysis for large-scale IO systems with spatially coupled multilayer connectivity graphs.

Example 4.2.3. *We revisit Example 4.2.2 to seek a polarity regime that guarantees the global convergence of laminar patterns using analysis conducted in the quotient systems when templating the large-scale system using the equitable partition, π_2. Namely, in conjunction with the results of applying Theorem 4.2.1 to the DIDO system (4.56-4.60) as in Example 4.2.2, we also invoke Theorem 4.2.2 to isolate regions of polarity parameter values for $w_1^{[1]}$ and $w_1^{[2]}$ that ensure global monotonicity of solutions with respect to laminar pattern trajectories. Namely, as the DIDO system (4.56-4.60) has $sgn\,(\mathcal{D}\boldsymbol{T}) = \mathcal{S}_0'$, then we seek to satisfy condition (GM1) such that the extrema of the quotient graph spectra are the extrema of the large-scale graphs.*

As the large-scale and quotient graphs are row-stochastic, we always have

$$\max\left(\mathrm{Spec}\left(\overline{\boldsymbol{W}}_k\right)\right) = \max\left(\mathrm{Spec}\left(\boldsymbol{W}_k\right)\right) = 1, \tag{4.86}$$

therefore, the quotient graphs retain the maximum eigenvalues, and so now we focus on the preservation of the minimal eigenvalues.

In Figure 4.10a we have demonstrated that for $w_1^{[k]} < 0.5$ *and* $w_2^{[k]} = 1$*, the quotient connectivity graphs for short-range diffusion and contact-dependent signalling mechanism,* $\mathcal{G}_{1,\pi_2}$ *and* $\mathcal{G}_{2,\pi_2}$ *have the capacity to bound the spectra of the large-scale graphs* $\mathcal{G}_1$ *and* $\mathcal{G}_2$ *from below. Critically, this implies that for any* $w_1^{[k]} \leq 0.5$ *with fixed* $w_2^{[k]} = 1$*, that induced HSS instability, the solutions of the DIDO system (4.56-4.60) will be locally directed towards laminar patterning and so following from Theorem 4.2.2, for sufficiently small* $w_1^{[k]} < 0.5$*, the large-scale DIDO system (4.56-4.60) will converge to laminar patterns.*

To highlight the results of applying both theorems 4.2.1 and 4.2.2 to the example DIDO system (4.56-4.60), regions of pattern convergence were found numerically in Figure 4.11 which includes examples of large-scale simulations for which laminar patterns are and are not dominant. It is worth noting that the magnitude of the difference between $w_1^{[k]}$ *and* $w_2^{[k]}$ *is dependent on the magnitude of the entries of* $\mathcal{D}\boldsymbol{T}\left(\boldsymbol{u}_i\right)$ *and thus assuming that* $w_1^{[k]} \ll w_2^{[k]}$ *is sufficient for the monotonicity of the large-scale system but is not necessary to satisfy the type K criteria (Lemma 4.2.1). Subsequently, selecting polarity parameters in which both the HSS instability condition for the reduced system (4.68) and*

$$\min\left(\mathrm{Spec}\left(\overline{\boldsymbol{W}}_k\right)\right) = \min\left(\mathrm{Spec}\left(\boldsymbol{W}_k\right)\right) \tag{4.87}$$

are satisfied resulting in the large-scale system converging to laminar patterns without requiring significant cross-layer polarity.

As highlighted in Example 4.2.3, theorems 4.2.1 and 4.2.2 facilitate the analytic study of laminar pattern formation in large-scale interconnected dynamical systems, independent of the number of cells in the system or physical dimension owing to the topological definition of the connectivity graphs. Hence the pattern analysis conducted on the quotient systems can evolve from explorative (in which geometries enable laminar patterning), to constructive (how much edge weight manipulation is required to robustly generate laminar patterns).

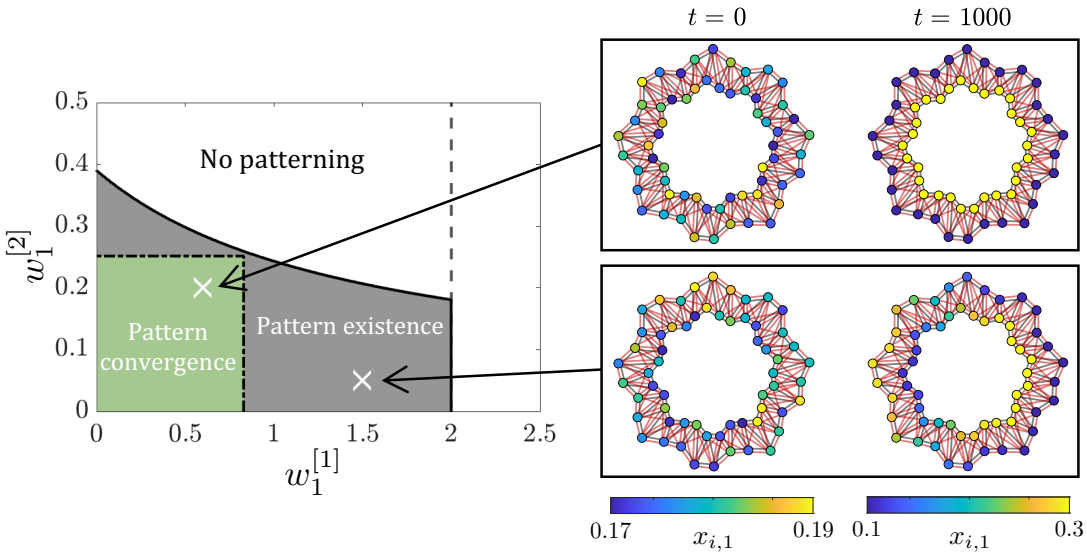

Figure 4.11: Polarity parameter regimes for the existence and convergence of laminar pattern in the large-scale IO system (4.56-4.60). The grey existence region is determined using the quotient system analysis and is defined by polarity-driven HSS instability inequality (4.68) for fixed $w_2^{[1]} = w_2^{[2]} = 1$. The green convergence region highlights the subset of the grey region in $\left(w_1^{[1]}, w_1^{[2]}\right)$-space in which $\min\left(\mathrm{Spec}\left(\overline{\boldsymbol{W}}_k\right)\right) = \min\left(\mathrm{Spec}\left(\boldsymbol{W}_k\right)\right)$. Example large-simulations are shown for polarity parameters inside the convergence region, (0.6,0.2), and inside the existence region (1.5,0.05). Large-scale bilayer graphs are shown with both $\mathcal{G}_1$ and $\mathcal{G}_2$ embedded in the same vertex set with edges in black and red, respectively. Vertex colour corresponds to the values of $x_{i,1}$ in each v_i. Simulations were initiated from small random perturbations about the HSS of the IO system (4.56-4.60) and first and final states are shown following trajectory convergence. IO system (4.56-4.60) parameter values and details on simulations are given in Appendix D.

4.3 Extending the small-gain criterion for quotient stability in MIMO systems

We have demonstrated quotient IO systems can be used to determine the trajectory behaviour of the associated large-scale IO systems by controlling the relative amount of signalling polarity between cells, such that solutions must converge to laminar patterns. However, patterns need to be robust to both spatial and temporal perturbations to be able to describe cell-fate determination in a developing biological system. Therefore, to determine the stability of laminar patterns with a focus on the interconnection strength between cells, we extend the small-gain criterion for pattern stability (Theorem 2.2.2) to include multiple inputs and outputs. Critically, this provides a sufficient low-dimensional and semi-analytic method to assess the robustness of the laminar patterns found using

our analytic approaches.

The gain of a cell is simply the magnitude of the ratio of input signals to output signals [227]. Moreover, the $\mathcal{L}_2$-gain, γ_i, of a cell i is the ratio where the $\mathcal{L}_2$ norm, $||\cdot||_2$, is applied to obtain the input and output signals as defined previously (Definition 2.1.4). Subsequently, γ_i remains a scalar for MIMO systems and provides a measure of the signal sensitivity of cells.

Let $\boldsymbol{\Gamma} = \text{diag}\,(\gamma_1, ..., \gamma_N)$ be the diagonal matrix of $\mathcal{L}_2$-gains of the IO system (4.1). By definition, cells with identical behaviour i.e. the same input signals $\boldsymbol{u}_i$ and output signals, $\boldsymbol{y}_i$, will have identical $\mathcal{L}_2$-gains. Hence, $\gamma_i = \gamma_j \quad \forall v_i, v_j \in L_k$ $(k = 1, 2)$ as imposed by the laminar pattern partition π_2. Therefore, when seeking laminar patterns, we have that $\boldsymbol{\Gamma} = \text{diag}\left(\overline{\gamma}_1 \boldsymbol{I}_{|L_1|}, \overline{\gamma}_2 \boldsymbol{I}_{|L_2|}\right)$, where $\overline{\gamma}_i$ are the $\mathcal{L}_2$-gains of the two representative cells in the reduced IO system (4.1). When analysing the stability of quotient systems, define $\overline{\boldsymbol{\Gamma}} = \text{diag}\,(\overline{\gamma}_1, \overline{\gamma}_2)$ as the reduced $\mathcal{L}_2$-gain matrix. Before stating the MIMO small-gain stability criterion, we first provide the following statements for spectral decoupling of the global interconnection matrix of a MIMO system.

Lemma 4.3.1. *Let $\boldsymbol{P}$ be the interconnection matrix as defined in equation (4.3). Then $\boldsymbol{P}$ has the following properties:*

(i)

$$\text{Spec}\,(\boldsymbol{P}) = \bigcup_{k=1}^{r} \text{Spec}\,(\boldsymbol{W}_k) \tag{4.88}$$

including multiplicities;

(ii) if $\boldsymbol{W}_k$ is invertible for all $k \in \{1, \ldots, r\}$, then the inverse of the interconnection matrix $\boldsymbol{P}$ is the interweave of the inverse of the adjacency matrices. That is,

$$\boldsymbol{P}^{-1} = \sum_{k=1}^{r} \boldsymbol{W}_k^{-1} \otimes \boldsymbol{D}_k, \tag{4.89}$$

(iii) the trace of the interconnection matrix is the sum of the traces of the adjacency matrices

$$\text{tr}\,(\boldsymbol{P}) = \sum_{k=1}^{r} \text{tr}\,(\boldsymbol{W}_k)\,, \tag{4.90}$$

(iv) the determinant of the interconnection matrix is the product of the determinant of the adjacency matrices

$$\det\,(\boldsymbol{P}) = \prod_{k=1}^{r} \det\,(\boldsymbol{W}_k)\,. \tag{4.91}$$

Proof. Let $\lambda_{k,j} \in \operatorname{Spec}(\boldsymbol{W}_k)$ with its associated eigenvector $\boldsymbol{v}_{k,j}$. Define the interweave extension of $\boldsymbol{v}_{k,j}$ by

$$\tilde{\boldsymbol{v}}_{k,j} = \boldsymbol{v}_{k,j} \otimes \begin{bmatrix} \delta_{k,1} \\ \vdots \\ \delta_{k,r} \end{bmatrix}. \tag{4.92}$$

Applying the definition of an eigenvector to $\boldsymbol{P}$ yields

$$\begin{aligned} \boldsymbol{P}\tilde{\boldsymbol{v}}_{k,j} &= \left(\sum_{i=1}^{r} \boldsymbol{W}_i \otimes \boldsymbol{D}_i \right) \tilde{\boldsymbol{v}}_{k,j}, \\ &= \left(\sum_{i=1}^{r} \boldsymbol{W}_i \otimes \boldsymbol{D}_i \right) \left(\boldsymbol{v}_{k,j} \otimes \left[\delta_{k,1}, \cdots, \delta_{k,r} \right]^T \right), \\ &= \left(\sum_{i=1}^{r} \boldsymbol{W}_i \boldsymbol{v}_{k,j} \otimes \boldsymbol{D}_i \left[\delta_{k,1}, \cdots, \delta_{k,r} \right]^T \right), \\ &= \boldsymbol{W}_k \boldsymbol{v}_{k,j} \otimes \left[\delta_{k,1}, \cdots, \delta_{k,r} \right]^T, \end{aligned} \tag{4.93}$$

where the last two equalities follow from the mixed product property of the Kronecker product and that direct multiplication of the Kronecker matrix and vector is non-zero only if $i = j$. Therefore we have that

$$\boldsymbol{P}\tilde{\boldsymbol{v}}_{k,j} = \boldsymbol{W}_k \boldsymbol{v}_{k,j} \otimes \left[\delta_{k,1}, \cdots, \delta_{k,r} \right]^T = \lambda_{k,j} \boldsymbol{v}_{k,j} \otimes \left[\delta_{k,1}, \cdots, \delta_{k,r} \right]^T = \lambda_{k,j} \tilde{\boldsymbol{v}}_{k,j}, \tag{4.94}$$

thus $\lambda_{k,j}$ is an eigenvalue of $\boldsymbol{P}$ with associated eigenvector $\tilde{\boldsymbol{v}}_{k,j}$.

Next, assume there exists $\boldsymbol{W}_k^{-1}$ for all $1 \leq k \leq r$. Consider the following matrix $\boldsymbol{R}$ defined by the multiplication

$$\begin{aligned} \boldsymbol{R} &= \left(\sum_{k=1}^{r} \boldsymbol{W}_k \otimes \boldsymbol{D}_k \right) \left(\sum_{k=1}^{r} \boldsymbol{W}_k^{-1} \otimes \boldsymbol{D}_k \right), \\ &= (\boldsymbol{W}_1 \otimes \boldsymbol{D}_1) \left(\sum_{k=1}^{r} \boldsymbol{W}_k^{-1} \otimes \boldsymbol{D}_k \right) + \ldots + (\boldsymbol{W}_r \otimes \boldsymbol{D}_r) \left(\sum_{k=1}^{r} \boldsymbol{W}_k^{-1} \otimes \boldsymbol{D}_k \right). \end{aligned} \tag{4.95}$$

From the mixed-product property of the Kronecker product and equation (4.44), we have that equation (4.95) reduces to

$$\begin{aligned} \boldsymbol{R} &= \boldsymbol{W}_1 \boldsymbol{W}_1^{-1} \otimes \boldsymbol{D}_1 + \ldots + \boldsymbol{W}_r \boldsymbol{W}_r^{-1} \otimes \boldsymbol{D}_r, \\ &= \sum_{k=1}^{r} \boldsymbol{I}_n \otimes \boldsymbol{D}_k = \boldsymbol{I}_{rN}, \end{aligned} \tag{4.96}$$

hence the inverse of $\boldsymbol{P}$ is given by $\boldsymbol{P}^{-1} = \sum_{k=1}^{r} \boldsymbol{W}_k^{-1} \otimes \boldsymbol{D}_k$ as required for (ii).

The trace of a Kronecker product is the product of the trace of each matrix independently [215] such that $\operatorname{tr}(\boldsymbol{W}_k \otimes \boldsymbol{D}_i) = \operatorname{tr}(\boldsymbol{W}_k)\operatorname{tr}(\boldsymbol{D}_k)$. Therefore applying the trace to the definition of $\boldsymbol{P}$ (4.3) yields

$$\operatorname{tr}(\boldsymbol{P}) = \operatorname{tr}\left(\sum_{k=1}^{r} \boldsymbol{W}_k \otimes \boldsymbol{D}_k\right) = \sum_{k=1}^{r} \operatorname{tr}(\boldsymbol{W}_k \otimes \boldsymbol{D}_k) = \sum_{k=1}^{r} \operatorname{tr}(\boldsymbol{W}_k)\operatorname{tr}(\boldsymbol{D}_k) = \sum_{k=1}^{r} \operatorname{tr}(\boldsymbol{W}_k), \tag{4.97}$$

where the second equality holds by the trace of the sum of matrices [215] and the fourth holds by $\operatorname{tr}(\boldsymbol{D}_k) = 1$ for all $1 \leq k \leq r$.

Property (iv) follows immediately from (i) by expressing the determinant of a matrix as the product of the eigenvalues including multiplicities [215]. From (i) we have that $\operatorname{Spec}(\boldsymbol{P}) = \operatorname{Spec}(\boldsymbol{W}_1) \cup ... \cup \operatorname{Spec}(\boldsymbol{W}_r)$ including multiplicities and so we know the eigenvalues of $\boldsymbol{P}$ are all the eigenvalues of each $\boldsymbol{W}_k$. Subsequently, the determinant of $\boldsymbol{P}$ must be the product of all these eigenvalues which leads to the required representation

$$\det(\boldsymbol{P}) = \left(\prod_{j=1}^{N} \lambda_{1,j}\right) ... \left(\prod_{j=1}^{N} \lambda_{r,j}\right) = \det(\boldsymbol{W}_1) ... \det(\boldsymbol{W}_r) = \prod_{k=1}^{r} \det(\boldsymbol{W}_k). \tag{4.98}$$

□

A direct consequence of Lemma 4.3.1 is that as $\boldsymbol{W}_k \in \boldsymbol{\mathcal{W}}$ (and therefore $\overline{\boldsymbol{W}}_k$) are nonnegative and irreducible, then the spectral radius, ρ, of the interwoven matrix $\boldsymbol{P}$ is a real eigenvalue and is defined by

$$\rho(\boldsymbol{P}) = \max_k(\rho(\boldsymbol{W}_k)) = \max\left(\bigcup_{k=1}^{r} \operatorname{Spec}(\boldsymbol{W}_k)\right), \tag{4.99}$$

by the Perron-Frobenius theorem [187].

Note that Lemma 4.3.1 also applies to $\overline{\boldsymbol{P}}$ as they are constructed identically. Using the spectral decoupling properties of Lemma 4.3.1, we next provide an extension to the small-gain condition for SISO systems derived by [118] to MIMO systems for laminar patterns.

Theorem 4.3.1 (Laminar pattern stability criterion for MIMO systems)**.** *Consider the IO system (4.1) spatially coupled by the interconnection matrix $\boldsymbol{P}$ (4.3). Let π_2 be the layer-wise simultaneous equitable partition for all semi-regular bilayer connectivity graphs $\mathcal{G}_k$ defined by $\boldsymbol{P}$, such that the associated reduced interconnection matrix $\overline{\boldsymbol{P}}$ (4.32) defines the reduced IO system of representative cells from each layer. Let $\overline{\gamma}_1$ and $\overline{\gamma}_2$ be the $\mathcal{L}_2$-gains associated with the*

heterogeneous input steady states $\boldsymbol{u}_1^*$ *and* $\boldsymbol{u}_2^*$ *for each representative cell. Then the laminar pattern state is locally asymptotically stable if*

$$\max_{k\in\{1,\ldots,r\}} \left(\rho\left(\overline{\boldsymbol{W}}_k\overline{\boldsymbol{\Gamma}}\right)\right) < 1 \tag{4.100}$$

where $\overline{\boldsymbol{\Gamma}} = diag\left(\gamma_1, \gamma_2\right)$.

Proof. Consider the coordinate transformation $\boldsymbol{z}_i = \boldsymbol{x}_i - \boldsymbol{x}_i^*$ where $\boldsymbol{x}_i^* = \boldsymbol{S}\left(\boldsymbol{u}_i^*\right)$, and so the laminar pattern state is located at the origin. From Assumption 4.2.1 we have that the transfer dynamics are nonnegative and bounded, which implies that the IO systems (4.1) have finite $\mathcal{L}_2$-gain, γ_i, for each cell $i \in \{1, ..., N\}$. Therefore, by the Bounded Real Lemma [228], there exists a positive definite matrix $\boldsymbol{Q}_i$ such that for any $V_i\left(\boldsymbol{z}_i\left(t\right)\right) = \boldsymbol{z}_i^T\boldsymbol{Q}_i\boldsymbol{z}_i$ we have that $\dot{V}\left(\boldsymbol{z}_i\left(t\right)\right) \leq \gamma_i^2\boldsymbol{u}_i^T\boldsymbol{u}_i - \boldsymbol{y}_i^T\boldsymbol{y}_i$. Let $d_i > 0$ and define $\boldsymbol{D} = \text{diag}\left(d_1, ..., d_N\right)$ to form the global energy function

$$\begin{aligned}
\dot{\boldsymbol{V}}\left(\boldsymbol{z}\right) &= \sum_{i=1}^{N} d_i\dot{V}_i\left(\boldsymbol{z}_i\right), \\
&\leq \sum_{i=1}^{N} d_i\gamma_i^2\boldsymbol{u}_i^T\boldsymbol{u}_i - d_i\boldsymbol{y}_i^T\boldsymbol{y}_i, \\
&= \sum_{i=1}^{N} \boldsymbol{u}_i^T\left(d_i\gamma_i^2\boldsymbol{I}_r\right)\boldsymbol{u}_i - \boldsymbol{y}_i^T\left(d_i\boldsymbol{I}_r\right)\boldsymbol{y}_i, \\
&= \boldsymbol{u}^T\left(\boldsymbol{D}\boldsymbol{\Gamma}^2 \otimes \boldsymbol{I}_r\right)\boldsymbol{u} - \boldsymbol{y}^T\left(\boldsymbol{D}\otimes\boldsymbol{I}_r\right)\boldsymbol{y}.
\end{aligned} \tag{4.101}$$

Applying the IO relation $\boldsymbol{u} = \boldsymbol{P}\boldsymbol{y}$, inequality (4.101) becomes,

$$\begin{aligned}
\dot{V}\left(\boldsymbol{z}\right) &\leq \boldsymbol{y}^T\left(\boldsymbol{P}^T\left(\boldsymbol{D}\boldsymbol{\Gamma}^2\otimes\boldsymbol{I}_r\right)\boldsymbol{P} - \boldsymbol{D}\otimes\boldsymbol{I}_r\right)\boldsymbol{y}, \\
&= \boldsymbol{y}^T\left(\left(\left(\boldsymbol{\Gamma}\otimes\boldsymbol{I}_r\right)\boldsymbol{P}\right)^T\left(\boldsymbol{D}\otimes\boldsymbol{I}_r\right)\left(\boldsymbol{\Gamma}\otimes\boldsymbol{I}_r\right)\boldsymbol{P} - \left(\boldsymbol{D}\otimes\boldsymbol{I}_r\right)\right)\boldsymbol{y}
\end{aligned} \tag{4.102}$$

where equality (4.102) follows from the commutativity of diagonal matrices.

By Lyapunov's second method for stability [142], the heterogeneous steady states $\boldsymbol{u}_1^*$ and $\boldsymbol{u}_2^*$ are locally asymptotically stable if there exists a matrix $\boldsymbol{D}$ such that

$$\left(\left(\boldsymbol{\Gamma}\otimes\boldsymbol{I}_r\right)\boldsymbol{P}\right)^T\left(\boldsymbol{D}\otimes\boldsymbol{I}_r\right)\left(\boldsymbol{\Gamma}\otimes\boldsymbol{I}_r\right)\boldsymbol{P} - \left(\boldsymbol{D}\otimes\boldsymbol{I}_r\right) \tag{4.103}$$

is negative definite. From Theorem 4 in [229] we have that the matrix (4.103) is negative definite if

$$\boldsymbol{I}_{rN} - \left(\boldsymbol{\Gamma}\otimes\boldsymbol{I}_r\right)\boldsymbol{P} \tag{4.104}$$

has eigenvalues with nonnegative real-parts [229]. As $\left(\boldsymbol{\Gamma}\otimes\boldsymbol{I}_r\right)\boldsymbol{P}$ is nonnegative then by Lemma 4.3.1 and the Perron-Frobenius theorem [141], the matrix (4.104)

has real and positive eigenvalues if $\rho\left(\left(\boldsymbol{\Gamma}\otimes\boldsymbol{I}_r\right)\boldsymbol{P}\right)<1$ in the large-scale IO system (4.1).

Conforming the laminar pattern template defined by π_2, cells within the same layer will have identical solutions and therefore identical $\mathcal{L}_2$-gains. Therefore in the reduced IO system, from Lemma 8 in [118], it can be shown that $\rho\left(\left(\boldsymbol{\Gamma}\otimes\boldsymbol{I}_r\right)\boldsymbol{P}\right)=\rho\left(\left(\overline{\boldsymbol{\Gamma}}\otimes\boldsymbol{I}_r\right)\overline{\boldsymbol{P}}\right)$ for π_2 an equitable partition. By definition of $\overline{\boldsymbol{P}}$ (4.32) and mixed-product property of the Kronecker product, we have that

$$\left(\overline{\boldsymbol{\Gamma}}\otimes\boldsymbol{I}_r\right)\overline{\boldsymbol{P}}=\sum_{k=1}^{r}\overline{\boldsymbol{\Gamma}}\,\overline{\boldsymbol{W}}_k\otimes\boldsymbol{D}_i. \tag{4.105}$$

Applying Lemma 4.3.1 to the matrix (4.105) we have that

$$\rho\left(\left(\overline{\boldsymbol{\Gamma}}\otimes\boldsymbol{I}_r\right)\overline{\boldsymbol{P}}\right)=\max_{k\in\{1,\dots,r\}}\left(\rho\left(\overline{\boldsymbol{\Gamma}}\,\overline{\boldsymbol{W}}_k\right)\right)=\max_{k\in\{1,\dots,r\}}\left(\rho\left(\overline{\boldsymbol{W}}_k\overline{\boldsymbol{\Gamma}}\right)\right), \tag{4.106}$$

and therefore assumption (4.100) guarantees the local asymptotic stability of the heterogeneous states $\boldsymbol{u}_1^*$ and $\boldsymbol{u}_2^*$ such that $\boldsymbol{z}_i$ converges to the origin. □

Remark 4.3.1. *For monotone systems the $\mathcal{L}_2$-gains γ_i represents the largest local changes to outputs $\boldsymbol{y}_i$ for perturbations to the input $\boldsymbol{u}_i$, i.e. the maximal gradient of the transfer function $\boldsymbol{T}(\cdot)$ [116]. Namely, if $\sigma(\boldsymbol{M})$ is the set of singular values of matrix $\boldsymbol{M}\in\mathbb{R}^{n\times m}$, then $\gamma_i=\max\left(\sigma\left(\mathcal{D}\boldsymbol{T}\left(\boldsymbol{u}_i^*\right)\right)\right)$.*

Corollary 4.3.1. *If $\overline{\boldsymbol{W}}_k$ is a nonnegative and irreducible matrix, then $\overline{\boldsymbol{W}}_k\overline{\boldsymbol{\Gamma}}$ is also nonnegative and irreducible as $\overline{\boldsymbol{\Gamma}}$ is a positive diagonal matrix. Consequently,*

$$\rho\left(\overline{\boldsymbol{W}}_k\overline{\boldsymbol{\Gamma}}\right)=\max\left(\mathrm{Spec}\left(\overline{\boldsymbol{W}}_k\overline{\boldsymbol{\Gamma}}\right)\right). \tag{4.107}$$

Proof. The statement follows directly by the Perron-Frobenius theorem for nonnegative and irreducible matrices [187]. □

Corollary 4.3.2. *If*

$$\lim_{p\to\infty}\left(\overline{\boldsymbol{W}}_k\overline{\boldsymbol{\Gamma}}\right)^p=\boldsymbol{0} \tag{4.108}$$

for all $k\in\{1,\dots,r\}$, then the laminar pattern state is locally asymptotically stable.

Proof. The power convergence theorem of matrices [216] which states that the limit (4.108) holds if and only if $\rho\left(\overline{\boldsymbol{W}}_k\overline{\boldsymbol{\Gamma}}\right)<1$. Therefore, the laminar patterns are asymptotically stable by Theorem 4.3.1. □

Following the spectral decoupling property of $\boldsymbol{P}$ and $\overline{\boldsymbol{P}}$ in Lemma 4.3.1, we have demonstrated that assessing the stability of laminar patterns in a MIMO system requires no additional computational complexity when compared to a SISO system as each spectral radius can be computed independently. Critically,

for MIMO systems with less than five inputs and outputs ($r \leq 4$), the laminar pattern stability criterion (4.100) is analytically accessible as requires evaluating singular values of the linearised transfer function. However, this is not a completely analytic solution as we require the heterogeneous steady states of the quotient nonlinear IO system (4.1). We illustrate an application of the laminar pattern stability criterion for MIMO systems (4.100) in the following example.

Example 4.3.1. *Building upon our previous analysis in examples 4.2.2 and 4.2.3, we consider the DIDO system (4.56-4.60) to determine polarity regimes that ensure the stability of the laminar patterns previously found. To determine the $\mathcal{L}_2$-gains of the reduced IO system, we first require heterogeneous steady states of the system which can be found by solving*

$$\begin{aligned} x_{1,1}^* &= g_1\left(a_1 f_2\left(x_{1,1}^*\right) + (1-a_1)\, f_2\left(x_{2,1}^*\right)\right) \cdot g_2\left(f_2\left(x_{1,1}^*\right)\right) \cdot f_1\left(a_2 g_3\left(x_{1,1}^*\right) + (1-a_2)\, g_3\left(x_{2,1}^*\right)\right) \\ x_{2,1}^* &= g_1\left(b_1 f_2\left(x_{2,1}^*\right) + (1-b_1)\, f_2\left(x_{1,1}^*\right)\right) \cdot g_2\left(f_2\left(x_{2,1}^*\right)\right) \cdot f_1\left(b_2 g_3\left(x_{2,1}^*\right) + (1-b_2)\, g_3\left(x_{1,1}^*\right)\right) \end{aligned} \tag{4.109}$$

for $x_{1,1}^*$ and $x_{2,1}^*$ derived by setting the derivatives of the reduced IO system (4.56-4.60) to zero, and a_k, b_k are the diagonal entries of $\overline{\boldsymbol{W}}_k$ defined in Example 4.2.2. Subsequently, the heterogeneous steady input states of the DIDO system (4.56-4.60) are given by

$$\boldsymbol{u}_1^* = \begin{bmatrix} a_1 f_2\left(x_{1,1}^*\right) + (1-a_1)\, f_2\left(x_{2,1}^*\right) \\ b_1 f_2\left(x_{2,1}^*\right) + (1-b_1)\, f_2\left(x_{1,1}^*\right) \end{bmatrix} \text{ and } \boldsymbol{u}_2^* = \begin{bmatrix} a_2 g_3\left(x_{1,1}^*\right) + (1-a_2)\, g_3\left(x_{2,1}^*\right) \\ b_2 g_3\left(x_{2,1}^*\right) + (1-b_2)\, g_3\left(x_{1,1}^*\right) \end{bmatrix} \tag{4.110}$$

from the IO relation (4.5). Therefore, the $\mathcal{L}_2$-gains of the representative cells are obtained by

$$\overline{\gamma}_1 = \max\left(\operatorname{Spec}\left(\mathcal{D}\boldsymbol{T}\left(\boldsymbol{u}_1^*\right)^T \mathcal{D}\boldsymbol{T}\left(\boldsymbol{u}_1^*\right)\right)\right) \text{ and } \overline{\gamma}_2 = \max\left(\operatorname{Spec}\left(\mathcal{D}\boldsymbol{T}\left(\boldsymbol{u}_2^*\right)^T \mathcal{D}\boldsymbol{T}\left(\boldsymbol{u}_2^*\right)\right)\right), \tag{4.111}$$

that is, the singular values of the linearised transfer function at the pattern states, and so we define $\overline{\boldsymbol{\Gamma}} = \operatorname{diag}\left(\overline{\gamma}_1, \overline{\gamma}_2\right)$. Finally, we compute the eigenvalues of $\overline{\boldsymbol{W}}_k \overline{\boldsymbol{\Gamma}}$ for $k = 1, 2$, taking the largest to determine the stability by applying inequality (4.100).

Repeating this process over the $\left(w_1^{[1]}, w_1^{[2]}\right)$-space as explored in examples 4.2.2 and 4.2.3 defines a region within the convergence space that guarantees the local stability of laminar patterns (Figure 4.12). The stability region lies about the origin, skewed in the direction of the $w_1^{[1]}$, consistent with previous analysis in examples 4.2.2 and 4.2.3. Therefore, the combination of our analytic and numerical investigation highlights that the contact-based signalling, $\mathcal{G}_2$, is the dominant mechanism in forming stable laminar patterns for the DIDO system (4.56-4.60), as it requires the most cross-layer polarity $\left(w_1^{[2]} \ll w_2^{[2]}\right)$.

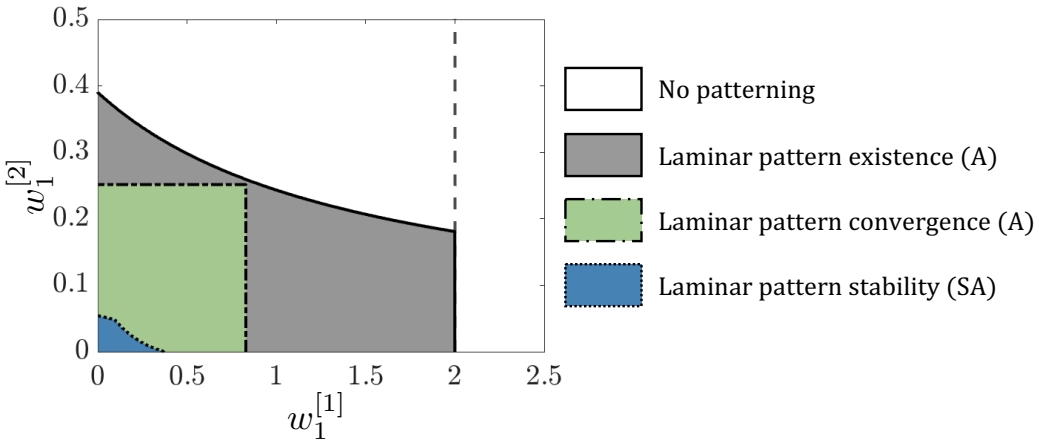

Figure 4.12: Polarity parameter regimes for the existence, convergence and stability of laminar patterns in the IO system (4.56-4.60) for fixed $w_2^{[1]} = w_2^{[2]} = 1$, extending the laminar pattern regimes presented in Figure 4.11. Regions shaded in blue satisfy the MIMO laminar pattern stability criterion (4.100). (A) and (SA) in the legend refer to analytic and semi-analytic methods of laminar pattern analysis, respectively. The IO system (4.56-4.60) parameter values and details on simulations are given in Appendix D.

4.4 Discussion

In this chapter, we have developed analytic methods for exploring the interplay of cellular polarity and multiple signalling mechanisms in the emergence of laminar patterns in bilayer tissues independent of the precise intracellular kinetics. To facilitate such analysis we focused on methods of dimension reduction of large interconnected dynamical systems that preserve fundamental cellular behaviour. Specifically, we demonstrate that cell signalling transfer dynamics can be treated as a proxy for intracellular components, reducing the dimensionality of the spatially discrete ODE systems by analysing only the spatially dependent intracellular components, which enabled us to provide sufficient conditions for the existence and uniqueness of the homogeneous steady state.

In addition, we use the properties of commuting graphs to decompose large MIMO systems into lower-order interconnected systems, decoupling the spatial and temporal components. This not only has advantages in reducing the computational cost associated with large-scale eigenvalue problems but also enables the direct analysis of the influence each signalling mechanism has on driving spatial instabilities of the homogeneous steady state. From a practical standpoint, the requirement of commuting graphs of cell signalling currently limits the applications of the large-scale HSS instability results in general pattern formation problems, as discussed previously [207], and therefore we

provide analytic methods of constructing families of commutative weighted graphs in Appendix C. However, our current methods are dependent on underlying regularity in local connectivities to simultaneously diagonalise each signalling graph and so to broaden the scope of the large-scale pattern analysis to cell-cell signal graphs that more accurately describe developing bilayer tissues with local connectivity irregularities, we required more general conditions for commutativity of their associated weighted adjacency matrices. One potential and possibly most general methods of conforming to the commutativity condition is the construction of cell-cell signal graphs directly from a prescribed eigenbasis (co-spectral methods) [230]. Namely, for a given row-stochastic and connected graph, its eigenvectors form the eigenbasis of the space of commuting graphs. Therefore, commuting adjacency matrices can be constructed by selecting different sets of eigenvalues subject to structural constraints. A subset of this commutative space would be defined by the commutative families defined in Appendix C.

By combining methods of multilayer graph partitions with monotone dynamical systems theory, we demonstrate the existence of laminar pattern formation with competitive kinetics relies on the amount of signalling polarisation present within each graph. Critically, the application of equitable partitions to the connectivity structures where layer-wise symmetries are present enables drastic dimensionality reductions of the global dynamical system when seeking contrasting steady-states between the bilayer of cells. Thereby exploiting the eigenvalue structure of the quotient graphs we demonstrate the instability conditions derived for large-scale interconnected dynamical systems that can be applied to the reduced system, independent of the commutativity of the quotient graphs. This facilitates the investigation of whether the pre-defined contrasting states are achievable with the given kinetics. The symmetry requirements of the equitable partitions need not be restricted to globally regular cell-cell interaction graphs. We only require regularity within each partition which therefore permits the application of semi-regular graphs for dimension reduction. Such graphs can then capture the characteristic traits of the biological system such as subpopulation phenotypes and tissue curvature, and their influence on intracellular behaviour as highlighted in Chapter 3.

The partitioning methods of prescribing patterns allude to studying the inverse problem, specifically, starting with the desired pattern of the tissue and then defining constraints for the intracellular kinetics that have the potential to induce such instabilities, as previously demonstrated in spatially continuous Turing systems [231]. Namely, we have demonstrated that if the spatial network has the capacity to induce monotone dynamics, then potential patterns of the system are determined by the sign structure of the network eigenvectors as

highlighted in Lemma 4.2.10. Hence, prescribing networks with the desired eigenvector sign structure, and kinetics can be designed to induce monotonicity and HSS instability. Furthermore, as the full and quotient system analysis depends only on the topology of the connectivity networks, the results from this study are immediately applicable to more biologically relevant 3D morphologies. Classically, introducing 3D structures drastically increases the computational complexity in pattern formation analysis [203, 232, 233], yet the topological approach allows for the transition between physical dimension with no additional requirements as discussed in [143] and Chapter 2.

Investigating the link between the reduced and large-scale dynamical systems when seeking laminar patterns, we demonstrate the statements of laminar existence derived using pattern-templating can be globally convergent in the corresponding large-scale interconnected system in high polarity regimes. To show the existence of a monotone transformation we imposed weak but sufficient conditions that in general $w_1^{[k]} \ll w_2^{[k]}$, or $w_1^{[k]} \gg w_2^{[k]}$, depending on intracellular dynamics, highlighting the requirement of edge weight anisotropy for laminar pattern formation. We suspect that this condition can be significantly refined by illustrating a dependence on the magnitude of entries of $\mathcal{DT}(\boldsymbol{u}_i)$ when applying the type K criterion for monotone solution behaviour, namely, having *a priori* estimations of the size of the cellular output signals for given input signal regimes.

As discussed in the previous interconnected monotone systems studies of pattern formation [117, 186, 207], the most limiting assumption in large-scale systems analysis is the existence of competitive to cooperative monotone kinetics transformation, which previously relied on the sufficient requirement of the connectivity graphs being bipartite. However, in Section 4.2.4 we not only demonstrate that laminar patterns are not the dominant pattern of bipartite bilayer graphs but also manipulating graph edge weights of non-bipartite graphs enables competitive to cooperative kinetics transformations for laminar pattern formation. Critically, this allowed us to extend the MIMO modelling framework introduced in [207] to include kinetics with both cooperative (inductive) and competitive (inhibitory) features, broadening the scope of applications to developmental systems with signal crosstalk, which is fundamental in the investigation of cell-fate dynamics in mammary organoids [16, 234]. The key feature of cooperative dynamics used in these pattern formation studies is the guarantee of non-periodic solutions when considering bounded kinetics [187]. Therefore another promising direction to ensure such solution behaviour is the study of variational families associated with the interconnected systems [235], that is, applying Lyapunov methods for non-oscillatory dynamics to

enable the investigation of intracellular crosstalk inference in biologically relevant morphologies.

Extending the $\mathcal{L}_2$-gain interconnection signal stability criteria to include multiple spatially dependent intracellular components provides a semi-analytic method of assessing the stability of laminar patterns by bounding the spectra of the gain matrix. We have demonstrated that the spectral radius of the interconnected gains can be computed independently for each connectivity mechanism, which vastly reduces the dimensionality of stability analysis when compared to the standard linearisation approach on the quotient system. As demonstrated in chapters 2 and 3, the $\mathcal{L}_2$-gain conditions can be used to investigate the influence of polarisation and local cell-cell connections on the stability of cell-fate patterning and is now accessible for MIMO systems whilst preserving the dimensionality of the SISO systems.

Throughout this chapter, we have reserved precise definitions of intracellular kinetics and associated signalling mechanisms to consider general MIMO dynamics. Subsequently, the generality of results presented here enables the investigation of crosstalk of key molecular pathways with multiple spatially dependent intracellular signalling components, such as the well-established Wnt-Notch interactions that have been observed in both intestinal and mammary epithelia [64]. Both the Wnt and Notch pathways are involved in cell-fate determination and have been observed to have active polarity mechanisms during tissue development [133, 236]. However, analysis conducted on existing models have previously been limited to one, or two cells [89, 237], the methods we provide here allow us to study how the geometry of the tissue influences such cell-fate choices, specifically within the bilayer structures commonly found in mammary glands.

Chapter 5

Discussion

Understanding the factors mediating plasticity events during mammary morphogenesis is of critical importance for mammary organoid culture innovation [20]. Though organoid culture technologies are rapidly developing [15], the media conditions, and the consequential epithelial processes, that support the self-organisation required for robust long-term mammary organoid expansion require further investigation [16]. Subsequently, in this thesis, we examined how two characteristic features of mammary glands; bilayer tissue architecture and epithelial polarity, regulate cell-fate determination and commitment in mammary epithelial cells (MECs).

We have used a variety of tools from monotone dynamical systems, graph and control theory to examine how the cell-cell connectivity graph structure (local geometry) and edge weights (signalling polarity) influence intracellular dynamics of cell-fate determinants. That is, applying and extending the fine-grained pattern templating methods for interconnected input-output (IO) dynamical systems from [117, 118] to polarised mammary bilayer morphologies such that each chapter in this thesis builds upon the spatial complexity of the tissue structures observed within mammary organoids.

From symmetric to multilayer semi-symmetric bilayer geometries, our low-dimensional representations of the collective intracellular dynamics enable the isolation of particular cell-fate patterns. Thereby, providing alternative methods from the standard techniques of classical linear analysis [87, 125] to derive tissue scale pattern convergence and stability polarity conditions, independent of the number of cells and the physical dimension of the modelled tissue due to the graphical representation of cells. This approach allowed us to seamlessly compare local tissue structures with respect to sufficient polarity conditions for stable laminar pattern formation of cell-fate determinants, presenting a significant advantage over fixed lattice approaches [99, 100, 138] when modelling spatially dynamic biological systems.

In Chapter 2, we introduced regular weighted bilayer graph structures to the pattern templating methods developed in [118] for single input single output (SISO) interconnected systems. This produced analytically approachable conditions for the existence and stability of cell-fate determinants in developing mammary organoids. Using our layer-wise orthogonal representation of cell signalling polarity that represents both apical-basal and planar polarity, our analysis highlighted that significant cross-layer signalling is required for laminar patterning of cell-fate determinants with lateral-inhibition in physiologically relevant spatial domains. Critically, these results are independent of the precise intracellular kinetics, evidencing the requirement of sustained polarity during cell-fate decisions and commitment.

Furthermore, both existence and stability conditions show that increasing the number of connections between the layers of cells reduces the amount of signal polarity required, which is further explored in Chapter 3 with respect to local tissue geometries. Motivated by the dichotomous Notch1-Delta1 gene and protein expression observed in MECs [21, 49], we confirmed these general connectivity-dependent polarity predictions using the Collier Notch-Delta intercellular model [87] over a wide variety of static spatial domains.

Developing a cell-based model for growing bilayer domains using the vertex modelling framework in Chaste [119, 145], we extended our polarity-driven pattern analysis to dynamic spatial domains. We show that calibrating the cell signalling polarity using our agglomerative static domain analysis of the Collier Notch-Delta model is sufficient to initiate and sustain laminar patterns of Notch during tissue growth. Furthermore, we demonstrate that cells using quorum-sensing polarity mechanisms in cell-signalling present greater consistency in cell-fate patterns, supporting an additive cell-fate commitment control mechanism in developing biological systems.

We extended our analysis on polarity-driven cell-fate patterning in Chapter 3 to focus on the effects of local tissue geometry. We introduced an image analysis pipeline designed to extract and couple local boundary curvatures, cell types and cell-cell signalling graphs from confocal images of cell-type stained mammary organoids. Using this pipeline on datasets provided by the Lloyd-Lewis lab (University of Bristol), in addition to representative synthetic data from cell-based models, we generate characteristic signal connectivity regimes for local morphologies in mammary organoids. Namely, we suggest there exists an inverse relationship between local boundary curvature and cross-layer connections with respect to basal cells, facilitating the connectivity inference from macroscopic imaging.

In Chapter 3 we extend our pattern analysis conducted in Chapter 2, to derive conditions for the existence and stability of laminar patterns of cell-fate determinants in layer-wise semi-regular spatial domains. Critically, we highlight the existence of a connectivity-driven asymmetry in controlling cell-fates between basal and luminal cells using generic lateral-inhibition kinetics. Namely, the connectivity of the cells with the largest signal gain dictates the capacity of polarity to sustain laminar patterns. Revisiting the Collier Notch-Delta model in combination with the characteristic connectivity regimes with mammary organoid morphologies, we isolate the basal cells as the cell-fate coordinators, consistent with existing volume-dependent studies of sender-receiver specification [50]. Furthermore, the analysis supports that polarity has a greater efficacy in concave tissue regions (branch bases) when compared to more convex regions (branch tips). These results are in agreement with existing evidence of phenotypic switching during branch elongation [131].

In Chapter 4, we generalise our existing SISO systems methods for pattern analysis to develop a framework for analysing polarity-driven laminar patterns of cell-fate determinants with multiple spatially dependent components, multiple input multiple output (MIMO) systems. Using multilayer semi-regular bilayer graphs to represent spatial connectivity, we extend existing multilayer IO descriptions [207] to include cell signalling polarity. For general kinetics of inhibition, induction and a mix of the two, we present novel analytically tractable conditions for the existence and convergence of laminar patterns in large-scale IO systems using component-wise independent polarity parameters. We show that cell signalling using both inhibition and inductive kinetics must be orthogonally polarised to ensure the convergence of laminar patterns.

We provided sufficient conditions on graph structure and signalling polarity for the coherent links between the quotient and large-scale IO dynamics, highlighting that previously used bipartite properties cannot be applied to systems with laminar patterns [117, 186, 207]. Finally, we extend the pattern stability conditions derived in [118] to MIMO systems. By exploiting the structure of the multilayer cell signalling graphs, we show that analysing the stability of MIMO systems requires no additional computational complexity when compared to SISO systems. Furthermore, our MIMO stability conditions predict the existence of a dominant cell signalling graph for laminar pattern stability within the multilayer structure, controlled by polarity and edge structure. Critically, our MIMO framework laminar pattern analysis framework enables us to examine the additional influence of pathway crosstalk in cell-fate commitment during mammary morphogenesis.

5.1 Mammary organoid culture technologies

As an overarching summary, this study provides additional support for the critical role of signalling polarity as a homeostatic control mechanism during organogenesis. We have shown how epithelial polarity can extend the fine-grained patterning potential of simple lateral-inhibition kinetics to form bespoke tissue-dependent intracellular dynamics, independent of the physical tissue geometry. Critically, this implies that different organs can employ the same core intercellular motifs (such as lateral inhibition or induction) and polarity induced from extracellular cues can fine-tune these behaviours for precise organ development.

Specifically, this study suggests that the establishment and preservation of apical-basal polarity is fundamental to the stabilisation of cell-type stratified bilayers in developing mammary organoids, independent of deformations to local tissue morphology. That is, in chapters 2, 3 and 4, we consistently demonstrate that if the Notch1-Delta1 lateral-inhibition kinetics are a feature driving differentiation in MECs, then substantial localisation of the activator Delta1 at the luminal-basal interface (cross-layer signalling) is sufficient for the existence and conservation of layer-wise laminar patterns of Notch1, preventing plasticity events. However, the local geometry of mammary organoids, namely, local cellular neighbourhood compositions, mediates the efficacy of polarity for Notch1 laminar patterning.

To our knowledge, direct evidence of spatial localisation of Delta1-ligand or Notch1-receptor is yet to be observed on the surface or within MECs. Namely, there is a lack of literature concerned with the spatial distribution of Notch1 and its downstream counterparts at the single-cell resolution in the mammary gland which is required to address the biological predictions produced in this study. However, both Notch and Delta (homologues alike) have been shown to exhibit polarity effects in various developmental contexts. Namely, Notch and Delta have been found to localised at the apical and subapical compartment during *Drosophila* wing disc development, respectively [67]. Similarly, in neuroepithelial cells, Notch activity was preferentially located at the apical surface, forming an intracellular Notch gradient [69]. Moreover, basally localised Notch receptors have been associated with intra-lineage fate decisions in *Drosophila* sensory organ precursor cells [68]. Taken together, these studies provide sufficient evidence for the viability of polarity-regulated Notch-Delta interactions within MECs during the initial stages of organoid development. However, further experimental work should be undertaken to confirm this hythopesis.

Following the verification of polarity-guided cell-fate decisions in MECs, a promising direction for mammary organoid culture innovation could be

the control of epithelial polarity through appropriate media supplementation, specifically for the industrialisation of mammary organoid production where batch homogeneity is critical for reliability and reproducibility for consumers. Control of polarity within organoid cultures has previously been considered in intestinal organoids [238, 239]. These studies demonstrate how altering the media conditions can reverse apical-basal polarity, which has specific applications to nutrient/drug up-take interactions, as access to the apical cellular surface is available. However, polarity mediation for homeostasis through media conditions is currently not considered in mammary organoids expansion [20]. Neuralized1 is a protein that simultaneously promotes apical-basal polarity of Notch1 by facilitating activated Notch release into the cytosol within localised regions [240, 241]. Subsequently, investigations into the regulated activation of Neuralized1 in mammary organoid cultures for Notch polarity mediation may provide preliminary insights for culture innovation.

5.1.1 A summary of testable biological propositions derived from theoretical cell-fate pattern analysis

The cell-fate pattern analysis conducted in chapters 2, 3 and 4 produced a range of biologically tractable hypotheses relating to the stability of bilayer phenotypic structure in mammary organoids. Each has been discussed in the respective chapter and here we provide a brief overview of these predictions.

5.1.1.1 Delta1-Notch1 localisation at the basal-luminal interface

A consistent result of this study is that if the canonical Notch1-Delta1 kinetics govern cell-fate decisions in MECs then external inventions are required to produce the laminar patterns of Notch1 expression as experimentally observed [48, 49, 56]. Following our interconnected IO modelling analysis, we show polarised signalling of Delta1 is sufficient to form such patterns, independent of precise tissue structure. Subsequently, our analysis predicts that Notch1-Delta1 interactions occur along the apical-basal axis, specifically at the membrane interface between the luminal and basal layers of cells.

5.1.1.2 Spatial exclusion of Delta1 and Ecad in luminal subpopulations promote polarisation

In Section 2.4, we propose a mechanism simple exclusion-based mechanism that may promote the polarisation of Notch1-Delta1 interactions in MECs. Following recent experimental findings that suggest the existence of agonistic Delta1-Ecad1 interactions and spatial exclusion on the cellular membrane [160, 161], in addition

to the expression of Ecad in the luminal subpopulations [157, 158], we suggest that the polarisation mechanism driving the laminar patterns of Notch1 is supported by the instigation of differential adhesion that is required for the initial stages of lumen formation in mammary organoids [131].

5.1.1.3 Tissue curvature mediated plasticity events in mammary organoids

A core result from Chapter 3 is the existence of an asymmetry in Notch1-dependent phenotypic stability with respect to local tissue geometry. Specifically, we use a combination of curvature-connectivity analysis on primary and synthetic data to guide our pattern stability analysis on competitive IO systems to demonstrate that MEC plasticity events are more likely in regions of high positive curvature, like a branch-tip. In these regions, our analysis suggests that polarisation of Notch1-Delta1 signalling is insufficient to control and generate laminar patterns of Notch1. Similar geometry-dependent MEC behaviours have previously been obsevred in the context of disease progression [31] however have yet to be experimentally studied in terms of Notch dynamics. We discuss the experimental implications of this study further in Section 3.6.

5.2 Polarity and fine-grained pattern analysis

The control of fine-grained patterns using cellular polarity has been studied for over two decades, with the majority of applications dedicated to the influence of planar cell polarity in hair follicle formation in the *Drosophila* wing, as reviewed in [242]. For example, directed intracellular diffusive ligand-receptor induction kinetics coupled to intercellular lateral-inhibition kinetics was shown to be sufficient to generate follicle-like cell clusters given sufficient polarity strength, even with irregular cellular domains [126]. Although planar cell and apical-basal polarity are intimately linked [243, 244], the influence of apical-basal polarity in tissue cell-fate regulation is often overlooked. The modelling techniques presented in this study simultaneously encapsulate both planar and apical-basal polarity in cell singalling from a multiscale perspective, enabling the comparisons and requirements of each polarity process for homeostatic intracellular dynamics.

The central theme of our analysis is using quotient presentations of the spatial structures to isolate cell-fate patterns within the tissues. Such methods were initially introduced by Steward, Golubitsky and co-authors in the early 2000s [112, 113], focusing on graph structure influence dynamical synchrony within subgroups of cells, classifying dynamics motifs from edge structure maps. Later, Rufino and Arcak extended the quotient transformations by the introduction

IO system representations, allowing for qualitative analysis of intracellular cellular dynamics using only characteristic information [118]. These quotient IO representations have later been used to predict the existence of lateral-inhibition kinetics underlying spontaneous gene expression in *E. coli* cell lines [245]. In this thesis, we have extended these quotient IO methods to consider polarity, i.e., anisotropic cell signalling through edge-weighted graphs. This has allowed us to relax the bipartite tissue structure constraints and types of intracellular kinetics considered in [117, 118] for pattern convergence and stability, improving the applicability of this analytical framework to a wider range of problems in developmental biology.

Though we have focused on cell-fate dynamics within mammary organoids, our bilayer representations are immediately applicable analysing intracellular behaviours to other polarised tissues with ductal structures such as salivary [246] and sweat glands [247]. Furthermore, as we exploited symmetries within the weighted graphs to generate low-dimensional quotient representations for pattern templates, such methods can be naturally extended to any tissue with distinct and regular structural features where spatial symmetries can be approximated. For example, the crypt and villi structure of the intestine [248] or the cell-type patterns in branched morphologies in the lung [249].

A direct application of the IO modelling framework developed in this thesis is to modelling fibroblast-epithelial cell-fate dynamics at various cross-sections of the intestinal crypt. The existence of a BMP-Wnt-Notch exchange between fibroblasts and epithelial cells forms competitive cell-cell interactions that dictate both fibroblast and epithelial phenotypes [250]. The fibroblast-epithelial cellular architecture is similar to the mammary duct, forming a bilayer with an outer layer of elongated fibroblasts and an inner layer of cuboidal epithelial cells [251]. Subsequently, it would interesting to study the existence of phenotypic patterning in the context of a Wnt gradient as cross-sections are taken moving up the cyrpt from the perspective of disease initiation.

The IO patterning methods developed in this thesis can also be naturally extended to analyse cellular systems with multiple layers of cell and well-defined phenotypic patterning. An example of a multilayer system with distinct phenotypic compartments is the epidermis, dermis and hypodermis layers of human skin [252]. However, applying templating methods to complex structures may still produce large quotient representations. That is, the more features preserved within the tissue under a partition mapping, the larger the dimension resultant quotient IO system. Consequently, such analytic approaches to fine-grained pattern analysis may still be limited in systems with complex spatial geometries.

Although quotient representations of weighted graphs were yet to be considered in the context of polarity-guided cell-fate patterning, they have been used to isolate components within large intracellular genetic regulatory networks [253]. Using gene interaction graph structure coupled to transcription dynamics, genetic synchrony spaces can be formed from weighted interactions by seeking equitable partitions. Such methods can be used to highlight genetic redundancy and demonstrate dynamic equivalences between genetic networks within various healthy and disease contexts. It would be interesting to combine these spatial perspectives of weighted quotient representations to examine tissue-scale implications from the dynamics of large intracellular genetic regulatory networks. For example, exploring the vast genetic networks associated breast cancer metastasis constructed from a ground-up approach [254], specifically in the context of loss of polarity.

5.3 Future directions

An immediate direction for further work is the application of the multichannel results outlined in Chapter 4 to explore the inclusion of the feedforward Notch1-Jagged1 interactions in MEC cell-fate commitment. In addition to the contrasting expression of Notch1 and Delta1 between basal and luminal cells, Jagged1 is preferentially expressed in luminal cells [21, 49]. These observations are in agreement with the inductive kinetics of Notch1-Jagged1. That is, Jagged1 is transmembrane Notch1 receptor activator, requiring cell-cell contact for Notch1-Jagged1 binding. However, intracellular activation of Notch1 leads to the upregulation of Jagged1 in the same cell [255]. Our analysis from Chapter 4 predicts that orthogonal signalling polarity between Jagged1 and Delta1 communication is required for laminar patterns of Notch. Using existing intracellular models of Notch-Jagg-Delta kinetics [256, 257], it would be interesting to investigate if the additional feedforward mechanism plays a role in stabilising Notch1 patterning, relaxing our current substantial polarity constraints.

In addition, the laminar pattern analysis framework presented in Chapter 4 enables the investigations of crosstalk intracellular kinetics with different signalling mechanisms. Thus, a promising direction for future work is the analysis of Wnt-Notch cell-fate regulation, as discussed in Section 4.4. By applying existing intracellular Wnt-Notch crosstalk models [89, 237], we are able to explore how the differences in signalling mechanisms can influence cell fate decisions within local morphologies of the mammary organoid. However,

further work would be required to ensure the transfer monotonicity of the Wnt-Notch crosstalk interactions, specifically the Wnt kinetics in isolation are non-monotone (based on preliminary unshown analysis). There exist methods to recover transfer monotonicity through monotone dynamics decomposition for near monotone systems [258], which can be employed by weakly coupling non-monotone components.

In Chapter 4, we show that with monotone transfer kinetics, the sign structure of the eigenvectors of the connectivity graphs dictates the patterns produced by the global dynamics (see proof of Lemma 4.2.10). Specifically, we demonstrated how edge weights can be manipulated to ensure that desired patterns generated from templating methods are globally convergent in the context of bilayer geometries with simple weight structures. These observations suggest that the spectral composition of weighted connectivity graphs can be used for intracellular kinetics inference. That is, suppose we are provided with a specific dichotomous pattern within a tissue, then by embedding edge weight structures, we seek the eigenvector sign structure that is aligned with the cell states of the observed pattern. From the structure of the edge weight, classifications of intracellular kinetics may be inferred using monotone transfer presentations. The design of systematic algorithms for graph-guided intracellular kinetics inference in polarised tissues may be used to accelerate the intracellular kinetics model design process in biological systems with limited access to temporal intracellular data, such as the subcellular dynamics of the mammary organoid as presented in this study. An example application of such as methodology is the exploration of mechanically-dependent intracellular kinetics that relate cell-fate decisions in mammary organoids. In a proposed future study in collaboration with Dr Bethan Lloyd-Lewis, we suggest these methods to accelerate the experimental design process to identify the core coupling interactions between the Wnt, Notch and Hippo pathways under mechanical perturbations. Namely, identifying compatible intracellular models of these pathways under varying cell-cell signalling networks as mechanical stress is induced over the tissue.

A significant limitation of the IO methods of cell-fate pattern analysis applied in this study is the restriction to static spatial domains, which is inherently a poor assumption when modelling developing biological systems. Subsequently, introducing temporally evolving graphs into our interconnected IO pattern analysis framework will facilitate the examination of the influence of transient and long-term edge structure rearrangements in polarity-driven pattern control. Namely, the analytic consideration of cell birth, death and migration using the graph edge topologies. Persistence and loss of pattern subspaces have previously been studied under elementary graph operations such as vertex addition, removal,

and rewiring in unweighted graphs [259]. By extending these methods to consider weighted vertex interactions and IO representations of intracellular dynamics, we facilitate analytical links between the fine-grained pattern analysis conducted using IO methods and the cell-based models, which may provide novel insights into the viability of polarity control plasticity events during morphogenesis.

5.4 Concluding remarks

We have studied the interplay of local tissue geometry and cell signalling polarity and their effect on cell-fate determination and commitment in mammary organoids. Fundamentally, we demonstrate that if lateral-inhibition kinetics are a component of the processes driving the cell-type stratified bilayer structures, then cell signalling polarity is required to initiate cell-fate specification and to prevent plasticity events, independent of the local tissue geometry. However, we show that local geometry can influence the amount of signal anisotropy required for cell-type stability. Critically, this work proposes that epithelial polarity is a dominant factor in cell-fate symmetry breaking and plasticity prevention, and hence the manipulation of these mechanisms through organoid culture technologies holds potential for enhancing phenotypic and genetic stability during the extended expansion of mammary organoids.

This work highlights the importance of tissue geometry and signal polarity for healthy mammary morphogenesis. However, these two features of the mammary gland are only a portion of the components within the complex machinery controlling homeostasis. Including additional homeostatic control mechanisms from mechanical-biochemical interactions, intracellular crosstalk and extracellular conditions should be considered to develop a comprehensive understanding of cell-fate dynamics in mammary organoids. However, we have demonstrated that by combining techniques from image analysis, interconnected dynamical systems, control theory, graph theory and cell-based modelling, we can gain a deeper understanding of the underlying processes that govern mammary development than applying any one of these fields alone, even when analysing relatively simple intercellular interactions.

Appendix A

Limitations of polarity for laminar pattern preservation in stochastic spatial domains

In Section 2.3.3, we demonstrate that polarity is able to generate and sustain laminar patterns of Notch in growing bilayer domains. To ensure consistency between our analytic and VM simulations, we imposed the preservation of bilayer morphologies. However, these cell-type delineated bilayer architectures are only an approximation of the tissue observed experimentally, specifically during early stages of lumen formation where the loss of basal contact is a common feature for initiating apoptosis and the core of the epithelial fragment [105, 160]. Subsequently, we briefly study the influence of stochastic connectivity in polarity-driven laminar pattern existence and stability. We use cell-based models in 2D and 3D in bilayer configurations with stochastic movements to explore if fixed and adaptive variations of the polarity conditions derived for static domains in Section 2.3.2 preserve patterns.

A.1 Methods for lattice free simulations using a cell-based model

Cell-based simulations were carried out using Chaste v2019.1 (Cancer, Heart and Soft Tissue Environment) [119], where the Overlapping Spheres (OS) framework was used to enable seamless transition between 2D and 3D geometries. In addition, it has been previously demonstrated that OS models are highly applicable to study short ranged signal-reaction networks in cellular systems due to the mechanical methods used to define cellular contact [102].

In this modelling framework, cells are connected by a mechanical force which is proportional to the region of overlap of spheres defined around each cellular node, as shown in Figure A.1. Here, we used the OS force model as defined in

[260], where the displacement of two nodes representing cell centres is represented by the vector $\boldsymbol{r}_{ij} = \boldsymbol{r}_i - \boldsymbol{r}_j$ and the force between the cells is defined by,

$$\boldsymbol{F}_{ij}(t) = \begin{cases} \eta_{ij} s_{ij}(t) \hat{\boldsymbol{r}}_{ij}(t) \log\left(1 + \frac{||\boldsymbol{r}_{ij}(t)|| - s_{ij}(t)}{s_{ij}(t)}\right), & \text{for} \quad ||\boldsymbol{r}_{ij}(t)|| < s_{ij}(t), \\ \eta_{ij} \left(||\boldsymbol{r}_{ij}(t)|| - s_{ij}(t)\right) \hat{\boldsymbol{r}}_{ij}(t) \exp\left(-k_c \frac{||\boldsymbol{r}_{ij}(t)|| - s_{ij}(t)}{s_{ij}(t)}\right), & \text{for} \quad s_{ij}(t) \leq ||\boldsymbol{r}_{ij}(t)|| < r_{\max}, \\ 0, & \text{for} \quad ||\boldsymbol{r}_{ij}(t)|| > r_{\max}, \end{cases} \tag{A.1}$$

where $\eta_{ij}, s_{ij}(t) > 0$ are the spring constant and rest length between cells i and j. $\hat{\boldsymbol{r}}_{ij}(t)$ corresponds to the unit vector of $\boldsymbol{r}_{ij}(t)$ and k_c defines the decay of force between the cells. Upon cellular division, the rest length $s_{ij}(t)$ of both parent and daughter cells are set to $s_{ij}^{\text{div}} = s_{ij}(t)/2$ and will tend back to $s_{ij}(t)$ in finite time as the cell grows. In all simulations, a random motion was introduced to each cell to stimulate a dynamic cellular domain. The random motion was implemented by an additional force acting on each cell node at each timestep,

$$\boldsymbol{F}^{\text{rand}} = \sqrt{\frac{2\xi}{\Delta t}} \boldsymbol{\nu}, \tag{A.2}$$

where ξ is a constant defining the size of random perturbation, $\boldsymbol{\nu}$ is a vector of samples from a standard multivariate normal distribution and Δt the timestep of the simulation, as previously defined [102]. The resultant force acting on cell i is defined by,

$$\boldsymbol{F}_i^{\text{res}}(t) = \boldsymbol{F}_i^{\text{rand}} + \sum_j^{\mathcal{N}_i} \boldsymbol{F}_{ij}(t), \tag{A.3}$$

for $\mathcal{N}_i$ is the number of cells within the cut-off distance, $r_{\max}$. Using this resultant force acting upon each cell, we relate this to cellular movement using the assumption that the inertia terms are small in comparison to the dissipative terms acting upon the cell. This is because both *in vivo* and *in vitro* cells move in dissipative environments with small Reynolds number [261], thus the position of each cell is governed in the Aristotelian regime, such that the velocity of a cell is proportional to the force acting on it. Namely, the spatial dynamics of each cell are determined by,

$$\nu \frac{d\boldsymbol{r}_i}{dt} = \boldsymbol{F}_i^{\text{res}}(t), \tag{A.4}$$

where $\nu > 0$ denotes the damping constant of the spring force. Equation (A.4) is solved using the simple forward Euler method to determine the location of each cell at each timestep, Δt, as given in Table A.1 [151].

Simulations were initialised with a bilayer structure, as in Figure A.1b. Basal and luminal cell types were considered to be mechanically identical to isolate the effects of neighbourhood cell-type composition on Delta patterning. Cells were assumed to not proliferate in both 2D and 3D simulations, this was done to control the spatial organisation of cell types in each layer.

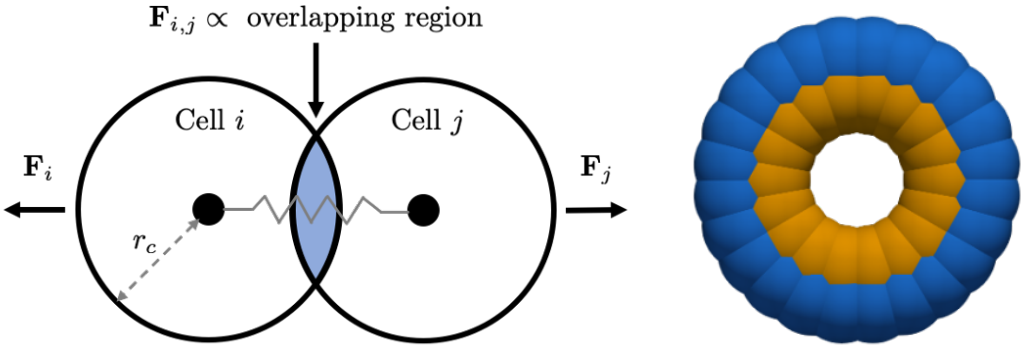

(a) Force diagram of OS model. (b) Initial bilayer structure.

Figure A.1: The cell-based model using the Overlapping Spheres framework. (a) A schematic of the mechanical dynamics that determines the motion of a cell using the Overlapping Spheres framework. The mechanical force acting on each cell is proportional to the region of overlapped space between any two nodes which are the centre of spheres with radius r_c. The mechanical force between cells i and j can be interpreted as a spring force and due to the relevantly low viscosity of the medium, it is assumed that the motion of each cell is governed in an Aristotelian regime, that is, the force is directly proportional to the velocity of the cell. (b) An example of the 2D initial spatial conditions when simulating the bilayer spheroid. The colours of the cells denote cell types, where the blue and orange cells are the basal and luminal cells respectively. The present example has a spheroid radius of 3 cell diameters (CD).

The NDM (2.1-2.2) kinetics were integrated into each cell in the population and was solved using the explicit Runge-Kutta45 method [151], which is built into the Chaste software. At every timestep, each cell would sweep through the population to determine the connectivity neighbourhood, which is defined by all nodes within a radius of ρ_c, as in the fixed geometry simulations. In the simulations presented in this section, we assume the connectivity radius, ρ_c, is equal to the mechanical cut-off length, $r_{\max}$. Once a cellular neighbourhood has been determined for each cell, the average Delta is calculated using equation (2.7), and then updated in the state variables to be used to solve the next timestep of the NDM (2.1-2.2). In all dynamic lattice simulations in this section, we choose $\alpha = 0.01$, $\beta = 100$, $\mu_N = \mu_D = 1$, $s = 1$ and $r = 2$ as parameter values for the NDM (2.1-2.2).

The seeds used to initialise the generation of the pseudo-random numbers were fixed for all simulations to compare signal strength parameters on dynamic domains. In addition, $w_2 = 1$ was fixed for each comparison simulation. Parameter values used in all cell-based simulations can be found in Table A.1.

Parameter	Description	Value	Units	Reference
t_{tot}	Total simulation time	100	h	[102]
Δt	Simulation timestep	0.01	h	[102]
η_{ij}	Spring constant	25^*	NCD^{-1}	[102]
s_{ij}	Spring rest length	1	CD	[102]
$r_{\max}$	Force cut-off length	$3/2^*$	CD	[102]
k_c	Decay of force	5	*Dim'less*	[260]
ξ	Random motion perturbation	0.0025^*	*Dim'less*	[102]
ν	Damping constant	1	NhCD^{-1}	[262]

Table A.1: Table of parameters used in each cell-based simulation. The unit of length CD refers to the fixed cell diameter used in simulations. The asterisks * indicate parameter values tuned for bilayer structure maintenance.

A.2 The degradation of laminar patterns upon bilayer disconnect

We simulate dynamic cellular domains using cell-based modelling such that each cell is represented as a point in space equipped with a connectivity radius that corresponds to the cell membrane. We say that cells are connected if their connectivity regions overlap in space, which generates a connectivity graph as described in Section 2.1.2. By embedding small amounts of stochastic motion in addition to spring-like mechanical properties to a bilayer of cells, we generate a time-dependent stochastic connectivity network that artificially approximates junction transitions in developing tissues. Furthermore, each node is designated a cell type which allows for the study of cell-type dependent signal edges for stochastic networks when coupled with the NDM intracellular kinetics (2.1-2.2) as in Section 2.3.3.

When transitioning to dynamic domains, we cannot always satisfy the equitable property of the cell-type partitions P_1 and P_2 in the bilayer connectivity graph due to the absence of regularity. Consequently, the analytical conditions derived in Section 2.2 cannot be applied at each timestep of the simulations, instead, we use the static domain inequalities (2.48-2.49) to gain an intuition for ligand activator polarisation conditions in dynamic geometries to generate and maintain laminar patterns. Similarly to Section 2.3.3, we explore fixed and adaptive polarity mechanisms which agree with the connectivity-polarity inequalities derived for static regular domains. Specifically, we determine the efficacy of both pattern control mechanisms by the mean difference in Notch

activation between each cell-type, ΔN, and is defined as

$$\Delta N = \frac{1}{\mathcal{N}_L}\sum_{i}^{\mathcal{N}}(1-\delta_{\tau(i),\tau(B)})N_i - \frac{1}{\mathcal{N}_B}\sum_{i}^{\mathcal{N}}\delta_{\tau(i),\tau(B)}N_i, \tag{A.5}$$

where $\mathcal{N}$ is the total number of cells, $\mathcal{N}_L$ is the number of luminal cells and $\mathcal{N}_B$ is the number of basal cells. The function $\delta_{\tau(i),\tau(B)}$ is the cell-type Kronecker delta function,

$$\delta_{\tau(i),\tau(B)} = \begin{cases} 1 & \text{if cell } i \text{ is a basal cell,} \\ 0 & \text{if cell } i \text{ is a luminal cell.} \end{cases} \tag{A.6}$$

Specifically, $\Delta N \approx 1$ implies complete laminar patterns of Notch activation, whereas $\Delta N \approx 0$ is considered as no consistent laminar patterns between the layers of cells.

In this stochastic connectivity investigation, we consider two globally fixed polarity parameters values to agree with the static stability bound (2.48) and the static observed bound (2.49), which is denoted by 'Fixed p_{stab}' (Fp_{stab}) and 'Fixed p_{obs}' (Fp_{obs}), respectively. Namely, the values of w_1 and w_2 are fixed for all cells at simulation initialisation to agree with either bound using the initial connectivity structure of the bilayer system (Figure A.1b). As previously considered in Section 2.3.3, we also consider the quorum sensing methods of adaptive polarity, such that cells sense their cell-type neighbourhood composition and adjust signal polarity levels accordingly. Namely, during the adaptive polarity simulation, each cell ensures that the observed static polarity bound for laminar patterning formation (2.49) is satisfied, denoted by 'Adaptive p_{obs}' (Ap_{obs}).

Simulating each signal strength mechanism, Fp_{stab}, Fp_{stab}, Ap_{obs} for 100 time units highlighted that conditions defining laminar pattern regions in static geometrics, inequalities (2.48) and (2.49), allow for the emergence of laminar patterns in stochastic edge graphs up to small spatial perturbations, Figure A.2a. That is, each mechanism initially ($t < 50h$) produced concentric contrasting layers of Notch expression, however, as the bilayer geometry became deformed due to the random perturbations of each cell, the definition between layers was lost by 100 hours (figures A.2a-A.2c). Thus, information about layer-wise signal polarisation is preserved when partitions of the connected graph are no longer equitable, however, the retained information is insufficient for the long-term stability of the Notch states.

In terms of pattern intensity and retention, using the Fixed p_{stab} polarisation mechanism performed the best (Figure A.2a). Though due to the high contrast between layers, the variance in Notch expression quickly becomes very large once consistent patterning is lost, figures A.2a-A.2c. The region of (w_1, w_2)-space, defined by inequality (2.48), which is sufficient for the stability of heterogeneous

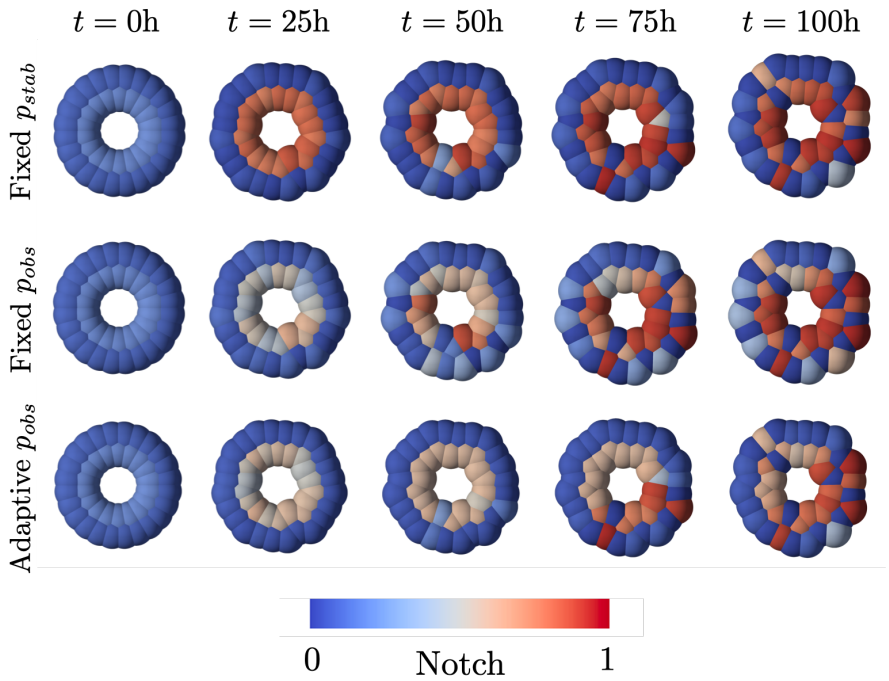

(a) 2D stochastic OS simulations.

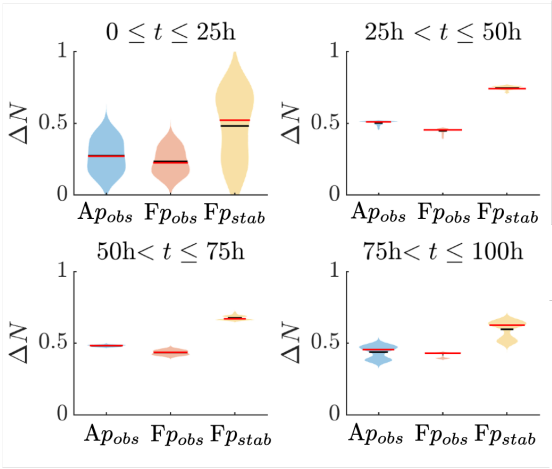

(b) Notch difference distributions.

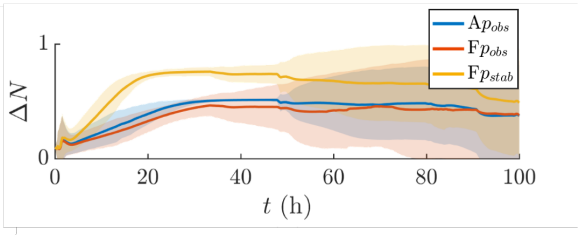

(c) Laminar patterns over time.

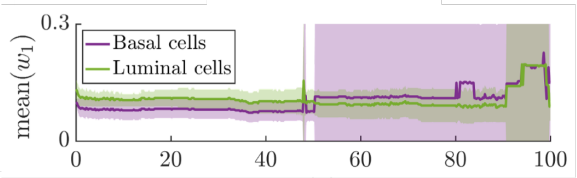

(d) Layer-wise polarity over time.

Figure A.2: 2D dynamic cellular domain simulation results of fixed and adaptive signal strength polarisation with each simulation using a globally fixed value of $w_2 = 1$. (a) Cell-based simulations of a cross-section of a bilayer spheroid. The simulations were run for 100 hours, initialised with cell-type stratification, and ODE initial conditions $\boldsymbol{x}_B(0) = [0.1, 0.2]^T$ and $\boldsymbol{x}_L(0) = [0.2, 0.1]^T$ for basal and luminal cells, respectively. The colour of each sphere represents the intracellular level of Notch. No noise was introduced to the ODE systems for Notch and Delta dynamics, the variability in these values presented is induced by the small spatial perturbations on each cell. (b) Violin plots summarising the Notch values in (a) over four 25h periods. Shaded regions denote the probability density of the ΔN values over each period. The black and red lines are the means and medians of the ΔN values, respectively. (c) A plot of the ΔN value for each signal polarity mechanism over time. Shaded regions represent standard deviations from the mean Notch expression of each cell type. (Continued on the following page.)

Figure A.2: (Continued.) (d) An additional output plot for the adaptive signalling mechanism demonstrating the disparity of w_1 values for basal and luminal cells over time. Shaded regions represent standard deviations from the mean w_1 of each cell type.

states between layers of static bilayers is highly restrictive, such that $w_1 \approx 0$ for all 2D and 3D geometries. In the context of the mammary bilayer, the simulation using Fixed p_{stab} accounts for the situation of almost no Delta ligands located on the luminal-luminal and basal-basal interface, supporting the existence of a Delta inhibition mechanism at these membranes.

The Fixed p_{obs} signalling mechanism produced the least contrast of Notch expression between layers initially and was quick to lose the consistency of expression, therefore performing the worst out of the signal strength mechanisms with respect to pattern retention (figures A.2a-A.2c). However, the Adaptive p_{obs} signal strength mechanism yielded the greatest pattern retention over the total time, highlighted by the lowest variance from ΔN values, see figures A.2a-A.2c. As Adaptive p_{obs} allows for $w_1 \approx w_2$ under highly heterotypic neighbourhood compositions (Figure A.2d), this highlights that homotypic signalling may be observed provided the adjacent cells are highly polarised. Subsequently, this supports the observation of the cell-wise heterogeneous membrane distribution of Notch within the luminal compartment whilst maintaining the concentric patterning given that the Delta activators are primarily located on the basal-luminal interface.

Furthermore, using the Adaptive p_{obs} signal strength mechanism revealed that there are stricter polarisation conditions in the basal cells than luminal cells while laminar patterning is maintained, for $t < 50$h (Figure A.2c). Subsequently, by the inverse relationship between the cell-type connectivity and lateral-inhibition model (Theorem 2.2.1), the restricted cellular signalling imposed on the basal cells may induce laminar pattern formation within the luminal cells, whilst allowing for greater luminal-luminal cell communication (Figure A.2d). Critically, at $t \approx 50$h, a basal cell was disconnected from the luminal layer, producing a transient irregularity for w_1 values (bounded above by inequality (2.46)), and therefore initiating the deterioration of laminar patterning.

The analysis conducted on static geometries suggested that the signal strength conditions on w_1 are independent of the physical dimension. We show in Figure A.3 that simulations of 3D spheroids are in agreement with 2D cross-sections. Namely, both the fixed and adaptive signalling mechanisms are capable of generating laminar patterning but are unable to retain the definition of the layers for long periods with stochastic edge cellular connectivity. Due to the increase

of cells in the 3D simulations, the variance of local connectivities is greater as random motion applied was to each cell at every timestep. Consequently, the time at which consistent laminar patterning is lost much earlier at $t \approx 20$h when using the same parameter values as in the 2D simulations.

In summary, these results indicate that our current methods of static laminar pattern analysis are insufficient for providing insight into systems with stochastic edge connectivity where we allow for loss of bilayer connectivity. We have demonstrated in Section 2.3.3 that polarity is a feasible mechanism controlling lateral-inhibition laminar cell-fate determination in growing bilayers, dynamic spatial domains where neighbourhood exchanges are common. However, the underlying formation of the VM cell-based description allows for a consistent bilayer structure throughout the simulation, even with stochastic vertex movement, satisfying our fundamental assumption of bilayer graph connectivity used to derive our analytic polarity-dependent patterning conditions for static domains. This assumption is violated in these OS simulations, as we allow for bilayer disconnection which ultimately led to the deterioration of laminar patterns. Therefore, a potential remedy for these misalignments between the VM and OS cell-based model results could be found in applying mean-field descriptions [263] of bilayer connectivities in an attempt to relax the consistent bilayer connectivity assumptions used in the analytic investigations in Chapter 2.

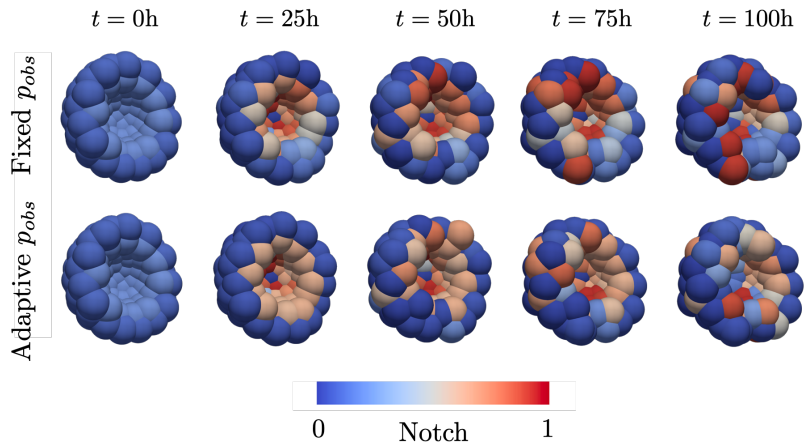

(a) 2D stochastic OS simulations.

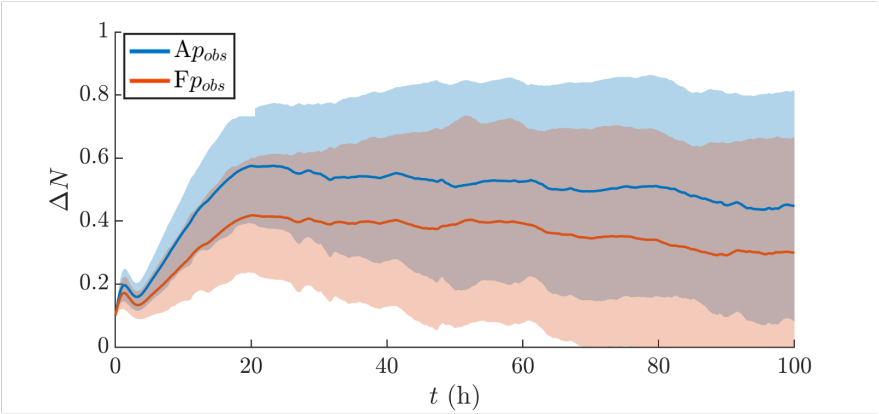

(b) Cell-type differences in Notch activation over time.

Figure A.3: 3D cell-based simulation of a bilayer spheroid representing a developing mammary organoid using examples of the adaptive and fixed signal strength mechanisms. (a) The simulations were run for 100 hours, initialised with cell-type stratification and ODE initial conditions $\boldsymbol{x}_B(0) = [0.1, 0.2]^T$ and $\boldsymbol{x}_L(0) = [0.2, 0.1]^T$. The colour of each sphere represents the intracellular level of Notch. A slice through the midpoint of the spheroid is presented to visualise the internal cell dynamics. (b) A plot of the ΔN value for both Fixed p_{obs} and Adaptive p_{obs} signal polarity mechanisms over time for the 3D simulations. Shaded regions represent standard deviations from the mean difference Notch expressions of each cell-type.

Appendix B

Extending the curvature-connectivity image analysis pipeline to 3D

In preparation for future data-driven studies, we describe a natural extension of the image analysis pipeline designed in Section 3.1 for 2D cross-sections to reconstruct the 3D structures from the confocal image stacks of mammary organoids. To do this, we apply the 2D pipeline to each image within a z-stack, constructing a cell-type dependent signalling graph for each slice, then clustering vertices in the z-axis we generate a 3D graphical representation of the mammary organoid. Geometric surface features such as curvature are also extended to their 3D analogues. An overview of the pipeline is given in Figure B.1 and an example of the 3D construction is shown in Figure B.2. We note that these 3D methods were not applied in this study due to limited access to high-resolution 3D images of mammary organoids that were stained for cell-type markers.

B.1 Constructing 3D graphs from 2D slices

For each slice in the stack, we apply the 2D curvature-connectivity pipeline described in Section 3.1 to generate a cell-type dependent signal connectivity graph, where the vertices represent the centroids of the segmented cells. To bind these graphs representing the 2D cross-sections into one single graph, we use a distance-based vertex clustering method. Specifically, we consider the vertices associated with each cell-type separately to ensure that only cells of the same type are clustered. Vertices in each layer are then stacked with a separation distance consistent with the z-resolution prescribed from the confocal imaging. Applying a weighted distance 2-norm $||\cdot||_{\varphi,2}$, defined by

$$||\boldsymbol{x}||_{\varphi,2} = \sqrt{\sum_{i=1}^{n} \varphi_i |x_i|^2} \tag{B.1}$$

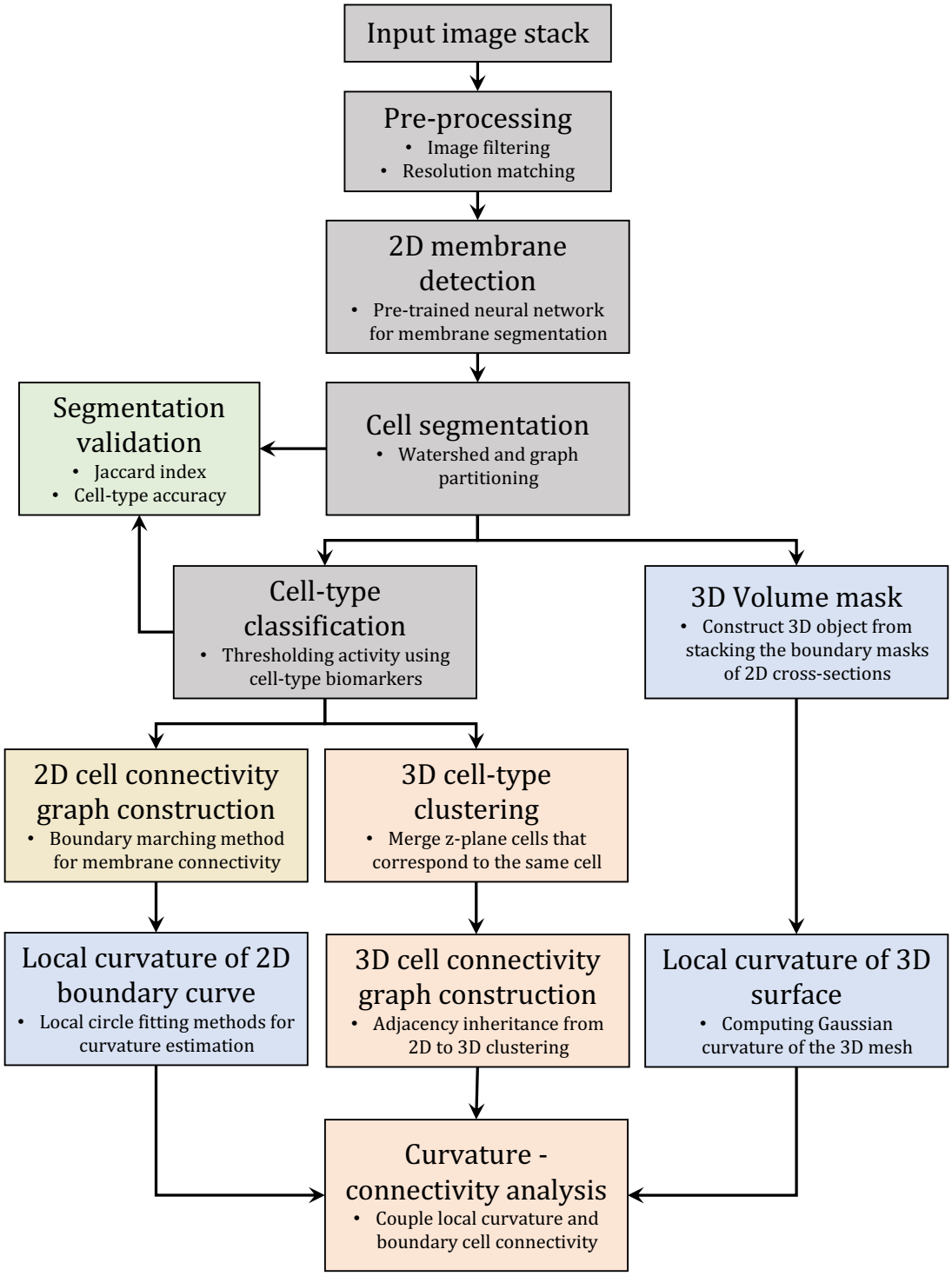

Figure B.1: A diagram of the 2D and 3D extension of the image analysis pipeline for cell-type dependent signal graph construction and boundary surface curvature estimation.

for some $\boldsymbol{x} = [x_1, ..., x_n] \in \mathbb{R}^n$ and $\varphi_i > 0$. Fixing $n = 3$ for points $\boldsymbol{x}$ in 3D space, we bias the norm for z-stack inclusion by setting $\varphi_1 = \varphi_2 = 1$ and $\varphi_3 > 1$, as these scale the x, y and z component magnitudes, respectively. Namely, this z-bias norm generates an ellipsoid vertex clustering region for each cell, such that vertices v_i and v_j, with position vectors $\boldsymbol{x}_i$ and $\boldsymbol{x}_j$, are in the cluster set $\mathcal{S}_k$ if $||\boldsymbol{x}_i - \boldsymbol{x}_j||_{\varphi,2} < \delta_z$ for some threshold $\delta_z > 0$. A new cluster vertex v_k representing the cluster of vertices in $\mathcal{S}_k$ is then generated, where v_k has position

$$\boldsymbol{x}_k = \frac{1}{|\mathcal{S}_k|} \sum_{i:v_i \in \mathcal{S}_k} \boldsymbol{x}_i, \tag{B.2}$$

i.e., the arithmetic mean of the vertex positions with the cluster $\mathcal{S}_k$.

To construct the edges of the 3D graph, we use a method of connectivity inheritance for the new cluster vertices. Let v_k and v_l be the cluster vertices for the cluster sets $\mathcal{S}_k$ and $\mathcal{S}_l$, then if $v_i \in \mathcal{S}_k$ and $v_j \in \mathcal{S}_l$ and $v_i \sim v_j$ in a 2D graph cell-type dependent signalling graph, then $v_k \sim v_l$. That is, clusters are connected if vertices between the clusters are connected. Note that the clusters are cell-type dependent as the vertex clustering was conducted separately for the basal and luminal vertices, and therefore the type-dependent weighted edge structure is preserved in the 3D graph. An example of the 3D z-stack clustering is given in Figure B.2.

B.2 Curvature in higher dimensions

A natural extension of the curvature of a boundary in 2D is the Gaussian curvature of a surface. As a generalisation of 2D curvature, Gaussian curvature measures how much a surface deviates from being flat at a given point and is defined as the product of the principal curvatures at that point on the surface. The principal curvatures are the maximum, κ_{max}, and minimum, κ_{min}, curvatures of the surface at that point, and are determined by the shape of the surface in two perpendicular directions [162]. Therefore, we have $\kappa = \kappa_{max}\kappa_{min}$ for the Gaussian curvature.

To calculate the Gaussian curvature on the surface of an organoid, we stack the filled boundary mask from each 2D segmented slice, creating a solid volume in 3D. The size of the voxels in the 3D space is aligned to the image resolution to ensure no artificial elongation or compression in the z-axis of the solid volume. The boundary surface is then transformed into a triangulated mesh where we then apply the discrete surface curvature estimation algorithm presented in [264].

B.3 Example, limitations and code availability

An example of the 3D curvature-connectivity pipeline is provided in Figure B.2, using organoid C from our primary 2D image analysis in Figure 3.7. We note that PlantSeg [173], which is used to segment cell membranes in Section 3.2, allows for direct 3D segmentation. However, we observed poor accuracy with a very high computational demand when attempting to generate direct 3D segmentations, even after parameter tuning. We suspect this is due to noise and heterogeneity of light intensity induced by confocal imaging because the boundary detection CNNs were trained on high-contrast membrane images of Arabidopsis cells.

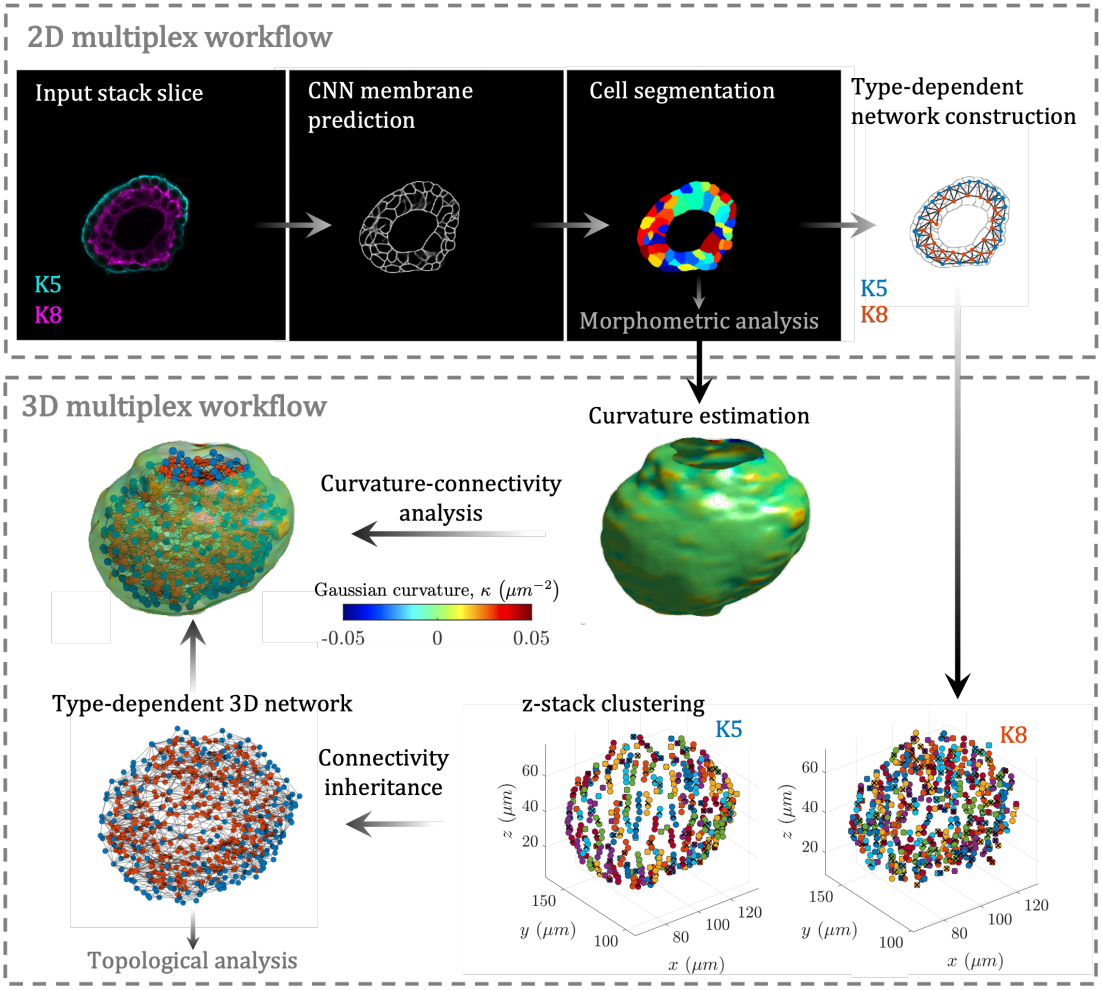

Figure B.2: An example of the outputs of the 3D curvature-connectivity image analysis pipeline at each stage for a spherical mammary organoid with basal and luminal cell-type markers.

Subsequently, we found improved accuracy from segmenting each 2D cross-section individual, allowing for fine parameter tuning at each z-depth. Yet, this pseudo-3D method for curvature-connectivity analysis is time-consuming and still requires high-resolution imaging in each x-y plane. Provided we obtain sufficient

quality and quantity of imaging data in the future, we suggest re-training the existing CNNs in PlantSeg for 3D mammary organoid segmentation, which has been shown to drastically improve segmentation accuracy in intestine, hepatic, and neuroectoderm organoids with as little as 10 stacks using the same U-net architecture [177].

The source code for the 2D and 3D curvature-connectivity image analysis pipeline can be found at `https://github.com/joshwillmoore1/Mammary_image_analysis`.

Appendix C

Conditions for commutative undirected weighted graphs in biological systems

Section 4.1 focuses on the application of graphs to represent cell-cell interactions with various signalling mechanisms over a fixed tissue domain. Here, we show that graphs describing these interaction mechanisms with different signal ranges commute underlying cellular domain is assumed to be regular, namely, the same edge structure for all vertices. Critically, we extend conditions for commutative graphs produced previously in [265] to derive convenient conditions for generating sets of commuting graphs with the inclusion of cell signalling polarity, modelled by anisotropic edge weights.

An example of the regular tissue structure can be seen in Figure C.1, where we highlight the differences in edge connectivity for characteristic short-range and long-range diffusive cell-cell signalling, with respect to the central cell. Assuming that diffusion is isotropic in direction but not in terms of signal strength (as this is controlled by the polarity edge weights), we see that the short-range diffusion is a subgraph of long-range diffusion in terms of edge connectivity due to the regular structure of the hexagonal lattice of cells. Subsequently, the assumption of regular morphological structure of the cells within a tissue generates identical edge structure in the connectivity graphs of cell-cell interactions for all cells, as shown for short-range and long-range diffusive cell-cell signalling in Figure C.1.

In general, let $V = \{v_1, ..., v_N\}$ be the set of vertices representing each cell in the tissue. Define the connectivity template $\mathcal{T}_1$ to be the edge and weight structure of all vertices $v_i \in V$ that is used to construct a simple, undirected and d_1-regular graph $\mathcal{G}_1$, such that the $\mathcal{T}_1$ has d_1 weighted edges and no self-loops as shown in Figure C.2. Namely, the template $\mathcal{T}_1$ is applied to every vertex ensuring that edge weight values agree.

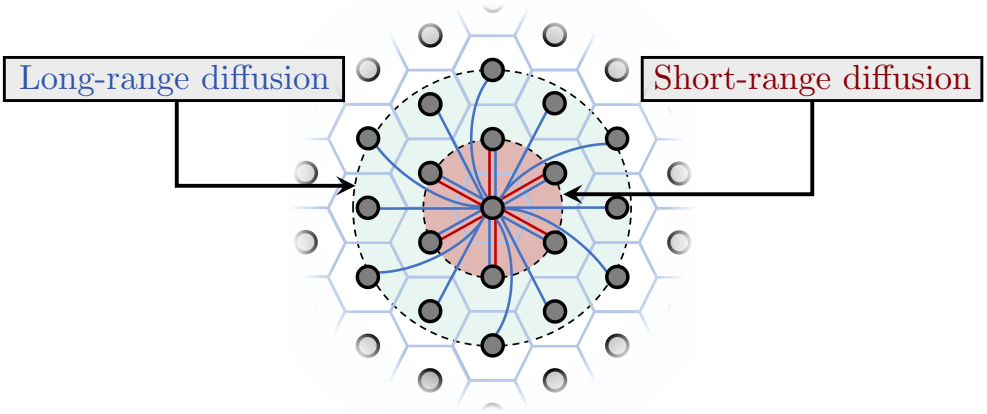

Figure C.1: A representative edge connectivity template for cell signalling with long and short range diffusion on a regular lattice of hexagonal cells. Edges emanate from the representative central vertex which defines a connectivity template for each cell in the tissue. A radius of cell-cell interaction is drawn for each diffusive mechanism with edges coloured in blue and red for short and long-range mechanisms, respectively.

Let $\mathcal{G}_2$ be a subgraph of $\mathcal{G}_1$ constructed by removing an edge from the connectivity template $\mathcal{T}_1$ which is denoted by $\mathcal{T}_2$ and thus $\mathcal{G}_2$ is constructed similarly, see Figure C.2. Following this construction of the subgraph, $\mathcal{G}_2$ will inherit the structure of the weighted connectivity template defined for $\mathcal{G}_1$, however, we allow the edge values on the connectivity template to differ between $\mathcal{G}_1$ and $\mathcal{G}_2$.

The graphs $\mathcal{G}_1$ and $\mathcal{G}_2$ have weighted adjacency matrices $\boldsymbol{W}_1$ and $\boldsymbol{W}_2$, respectively. Critically, we say that $\mathcal{G}_1$ and $\mathcal{G}_2$ commute when their associated adjacency matrices commute. To measure the commutativity of the two matrices, we define the commutator as follows

$$[\boldsymbol{A}, \boldsymbol{B}] = \boldsymbol{A}\boldsymbol{B} - \boldsymbol{B}\boldsymbol{A}. \tag{C.1}$$

Specifically, matrices $\boldsymbol{A}$ and $\boldsymbol{B}$ commute if $[\boldsymbol{A}, \boldsymbol{B}] = 0$.

To explore how regular edge structure influences the commutativity of $\mathcal{G}_1$ and $\mathcal{G}_2$, we modify our current representation of adjacency matrices. Let $\boldsymbol{E}_{ij}$ be the $N \times N$ matrix with 1 at the (i, j)-th entry and 0 else. We can represent any $N \times N$ matrix $\boldsymbol{M}$ in terms of matrices $\boldsymbol{E}_{ij}$ by the following

$$\boldsymbol{M} = \sum_{i=1}^{N} \sum_{j=1}^{N} m_{ij} \boldsymbol{E}_{ij}. \tag{C.2}$$

As $\mathcal{G}_1$ and consequently $\mathcal{G}_2$ are undirected graphs, their adjacency matrices are symmetric. Denote $\boldsymbol{E}_{\{i,j\}} = \boldsymbol{E}_{ij} + \boldsymbol{E}_{ji}$ and thus we represent any adjacency matrix

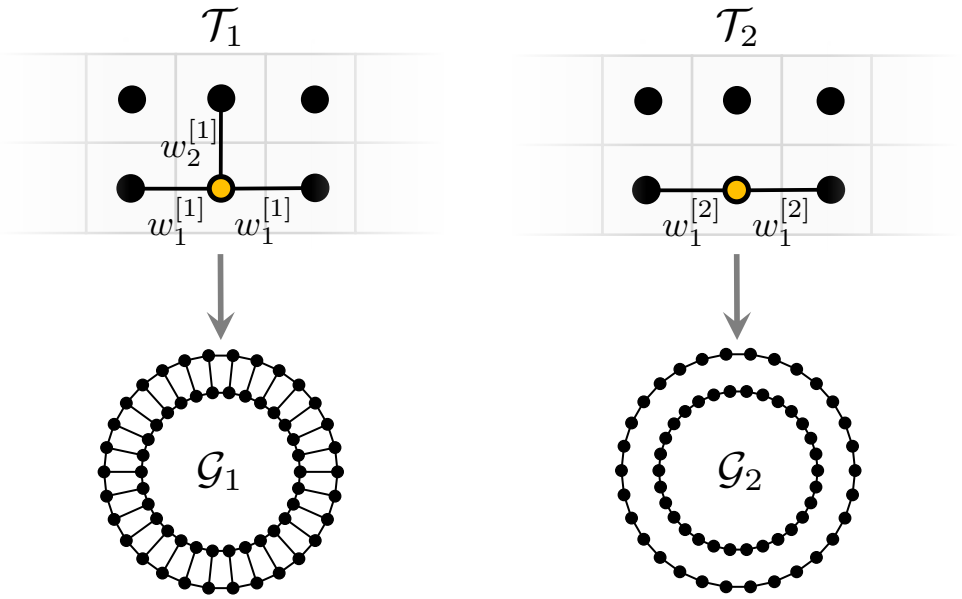

Figure C.2: An example of constructing a graph and a subgraph using connectivity templates. Using an orthogonal bilayer lattice of vertices, the connectivity template $\mathcal{T}_1$ defines two same-layer connections and one cross-layer connection weighted by $w_1^{[1]}$ and $w_2^{[1]}$, respectively. Applying the template to every vertex in the lattice generates the 3-regular graph $\mathcal{G}_1$. The connectivity template $\mathcal{T}_2$ is derived by removing the cross-later edge from $\mathcal{T}_1$, constructing a 2-regular graph $\mathcal{G}_2$ where we allow $w_1^{[1]} \neq w_1^{[2]}$.

associated with an undirected weighted graph by

$$\boldsymbol{W}_p = \sum_{i=1}^{N} \sum_{j=i}^{N} w_{ij}^{[p]} \boldsymbol{E}_{\{i,j\}} \tag{C.3}$$

where $(\boldsymbol{W}_p)_{ij} = w_{ij}^{[p]}$. As demonstrated in [265], the commutativity of graphs can be characterised by the commutativity of the matrices $\boldsymbol{E}_{\{i,j\}}$, particularly the commutator of any two adjacency matrices has the form

$$[\boldsymbol{W}_p, \boldsymbol{W}_q] = \sum_{i=1}^{N} \sum_{j=i}^{N} \sum_{k=1}^{N} \sum_{l=k}^{N} w_{ij}^{[p]} w_{kl}^{[q]} \left[\boldsymbol{E}_{\{i,j\}}, \boldsymbol{E}_{\{k,l\}}\right]. \tag{C.4}$$

The commutator within the summand of equation (C.4) can significantly reduce the number of terms of the sum as demonstrated in the following statement.

Lemma C.0.1 ([265]). *Let $\boldsymbol{E}_{ij}$ be the $N \times N$ matrix with 1 at the (i,j)-th entry and 0 else. Denote $\boldsymbol{E}_{\{i,j\}} = \boldsymbol{E}_{ij} + \boldsymbol{E}_{ji}$ then*

$$\left[\boldsymbol{E}_{\{i,j\}}, \boldsymbol{E}_{\{k,l\}}\right] = \delta_{jk}\left(\boldsymbol{E}_{il} - \boldsymbol{E}_{li}\right) + \delta_{jl}\left(\boldsymbol{E}_{ik} - \boldsymbol{E}_{ki}\right) + \delta_{ik}\left(\boldsymbol{E}_{jl} - \boldsymbol{E}_{lj}\right) + \delta_{il}\left(\boldsymbol{E}_{jk} - \boldsymbol{E}_{kj}\right). \tag{C.5}$$

Moreover, at most one of the terms of equation (C.5) is nonzero. The commutator is nonzero if and only if $|\{v_i, v_j, v_k, v_l, \}| \neq 3$. *Thus an unweighted edge commutes with another unless (and only unless) they share a single vertex.*

Lemma C.0.1 yields two conditions for graph commutativity: (1) identical edges in $\mathcal{G}_1$ and $\mathcal{G}_2$ commute and (2) edges in $\mathcal{G}_1$ and $\mathcal{G}_2$ with no common vertex commute. Subsequently, to analyse graphs where these two conditions are more common, we introduce the difference graph $\mathcal{H}$ with adjacency matrix $\boldsymbol{W}_3 = \boldsymbol{W}_1 - \boldsymbol{W}_2$. In particular, $\mathcal{H}$ is regular with degree d_3 with $d_3 \leq d_1$. The construction of $\mathcal{H}$ leads to our first condition for the commutativity of $\mathcal{G}_1$ and $\mathcal{G}_2$ which allows for the use of $\mathcal{H}$ which may reduce the number of cases required to check for vertex sharing edges, i.e. reducing the number of non-zero terms in equation (C.4).

Lemma C.0.2. *Let* $\mathcal{G}_1$ *be a weighted, regular and undirected graph constructed using a connectivity template* $\mathcal{T}_1$ *and* $\mathcal{G}_2$ *be a regular subgraph of* $\mathcal{G}_1$ *constructed by edge removal from* $\mathcal{T}_1$. *If* $\mathcal{H}$ *is the difference graph of* $\mathcal{G}_1$ *and* $\mathcal{G}_2$ *then* $\mathcal{G}_1$ *and* $\mathcal{G}_2$ *commute if and only if* $\mathcal{H}$ *and* $\mathcal{G}_2$ *commute.*

Proof. The result follows from the definition of the difference graph and direct calculation. Assuming $\mathcal{G}_1$ and $\mathcal{G}_2$ commute, consider the product

$$\boldsymbol{W}_2\boldsymbol{W}_3 = \boldsymbol{W}_2(\boldsymbol{W}_1 - \boldsymbol{W}_2) = \boldsymbol{W}_2\boldsymbol{W}_1 - \boldsymbol{W}_2^2 = \boldsymbol{W}_1\boldsymbol{W}_2 - \boldsymbol{W}_2^2 = (\boldsymbol{W}_1 - \boldsymbol{W}_2)\boldsymbol{W}_2 = \boldsymbol{W}_3\boldsymbol{W}_2 \tag{C.6}$$

implying that $\mathcal{H}$ and $\mathcal{G}_2$ commute. Similarly, assume that $\mathcal{H}$ and $\mathcal{G}_2$ commute,

$$\boldsymbol{W}_1\boldsymbol{W}_2 = (\boldsymbol{W}_2 + \boldsymbol{W}_3)\boldsymbol{W}_2 = \boldsymbol{W}_2^2 + \boldsymbol{W}_3\boldsymbol{W}_2 = \boldsymbol{W}_2^2 + \boldsymbol{W}_2\boldsymbol{W}_3 = \boldsymbol{W}_2(\boldsymbol{W}_2 + \boldsymbol{W}_3) = \boldsymbol{W}_2\boldsymbol{W}_1, \tag{C.7}$$

and therefore $\mathcal{G}_1$ and $\mathcal{G}_2$ commute. □

From Lemma C.0.2, we now seek conditions in which $[\boldsymbol{W}_2, \boldsymbol{W}_3] = 0$ for graph commutativity. Before stating the commutativity conditions for $\mathcal{G}_1$ and $\mathcal{G}_2$ in the cases of differing or identical edge weights, we first need to define two vertex connectivity properties.

Definition C.0.1 (x-step path and circuits [208])**.** *Let* $\mathcal{G}$ *be a graph with vertices* $v \in V$. *An* x*-step path is a sequence of* $x+1$ *vertices denoted by the tuple* $(v_i, ..., v_j)$ *such that consecutive vertices are connected by an edge. A path is closed if it starts and ends at the same vertex i.e.* $(v_i, ..., v_i)$. *Furthermore, a circuit of length* x *is a closed* x*-step path of distinct vertices.*

Using vertex paths in graphs, we can quantify the minimal number of paths and circuits emanating from a single vertex that is required to ensure that $\mathcal{H}$ and $\mathcal{G}_2$ commute. We are specifically interested in counting 2-paths, an example of

this is given in Figure C.3. We demonstrate that we can bound the number of 2-paths by knowing the number of unique edge weights defined in the connectivity template. Namely, denote n_p the number of 2-paths with alternating edges from $\mathcal{H}$ and $\mathcal{G}_2$ such that the product of these edges weights are unique.

Let e_2 and e_3 be the number of unique edge weights emanating from vertex v_i in $\mathcal{H}$ and $\mathcal{G}_2$, respectively. As $\mathcal{H}$ and $\mathcal{G}_2$ are regular and undirected then $n_p = e_2 e_3$. Moreover, $0 \leq n_p \leq d_1 d_2$, where the upper bound of n_p is achieved when all edges emanating for any vertex have different edge weights in both $\mathcal{H}$ and $\mathcal{G}_2$, and, $\mathcal{G}_1$ and $\mathcal{G}_2$ share no common edge weights. Both results follow directly from the connectivity template construction of $\mathcal{G}_1$ and $\mathcal{G}_2$.

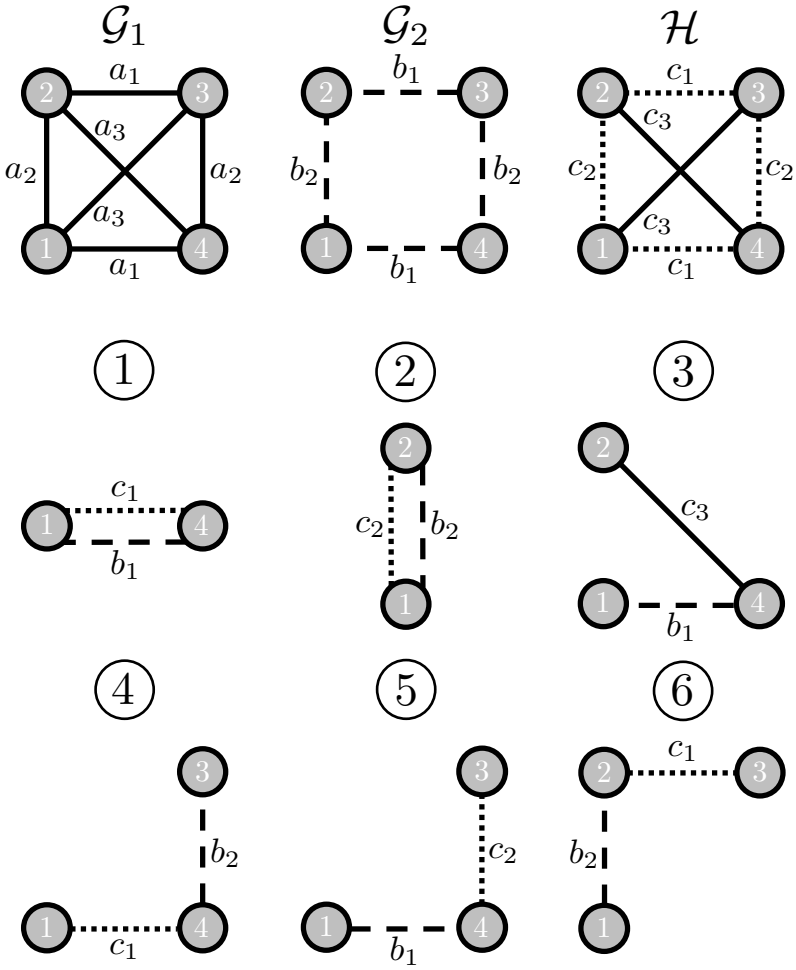

Figure C.3: Unique alternating 2-path weight products from a representative vertex. $\mathcal{G}_1$ is the complete graph K_4 with each edge stemming from a vertex having a different weight a_i. The subgraph $\mathcal{G}_2$ is 2-regular with edge weights b_i. The difference graph $\mathcal{H}$ corresponds to the edge difference between $\mathcal{G}_1$ and $\mathcal{G}_2$ such that $c_i = a_i - b_i$. As each node has 2 and 3 distinct edges in $\mathcal{G}_2$ and $\mathcal{H}$, representatively, there are $n_p = 6$ unique 2-path edge products emanating from any given vertex. All 2-paths with respect to vertex v_1 are shown.

C.1 Commutativity conditions for graphs and subgraphs with identical edge weights

In the case $\mathcal{G}_2$ is constructed by only removing edges from the connectivity template $\mathcal{T}_1$ of $\mathcal{G}_1$, preserving the original edge weights, then $(\boldsymbol{W}_2)_{ij} \leq (\boldsymbol{W}_1)_{ij}$. The difference graph $\mathcal{H}$ is then constructed from those edges contained in $\mathcal{G}_1$ but not in $\mathcal{G}_2$, i.e. $\mathcal{H}$ and $\mathcal{G}_2$ have disjoint edge sets. Consequently, we need only to consider the case of a single shared vertex between edges in $\mathcal{H}$ and $\mathcal{G}_2$ to guarantee their commutativity by Lemma C.0.1. Specifically, the following statement yields a necessary and sufficient condition for $\mathcal{G}_2$ and $\mathcal{H}$ commutativity which is dependent on the existence of circuits with edges alternating in $\mathcal{G}_2$ and $\mathcal{H}$. An example of alternating edge circuits is given in Figure C.4.

Lemma C.1.1. *Let $\mathcal{G}_1$ be a weighted, regular and undirected graph constructed using a connectivity template $\mathcal{T}_1$ and $\mathcal{G}_2$ be a regular subgraph of $\mathcal{G}_1$ constructed by regular edge removal where $\mathcal{G}_1$ and $\mathcal{G}_2$ have identical weights on common edges. $\mathcal{G}_1$ and $\mathcal{G}_2$ commute if for any vertex $v_i \in V$ there exists n_p distinct 4-vertex circuits consisting of alternating edges from $\mathcal{G}_2$ and $\mathcal{H}$ where the product of the edge weights first two edge weights are equal to the product of the final two edge weights in the circuit.*

Proof. If $n_p = 0$ then there exists no alternating 2-paths from vertex v_i with edges from $\mathcal{G}_2$ and $\mathcal{H}$. This case follows directly from Lemma C.0.1 since $\left[\boldsymbol{E}_{\{i,j\}}, \boldsymbol{E}_{\{k,j\}}\right] = 0$ for all vertex indices $(i, j, k, l \in \{1, ..., N\})$ as no two edges of $\mathcal{H}$ and $\mathcal{G}_2$ share a common vertex. Consequently, $[\boldsymbol{W}_2, \boldsymbol{W}_3] = 0$ which implies $[\boldsymbol{W}_1, \boldsymbol{W}_2] = 0$ by Lemma C.0.2.

If $n_p \neq 0$ there exists a common vertex between two edges from $\mathcal{H}$ and $\mathcal{G}_2$. Due to the regularity of $\mathcal{G}_1$, $\mathcal{G}_2$ and consequently $\mathcal{H}$, the symmetry of the structures allows for the investigation of commuting edges emanating from a single vertex. Consider the vertices v_i, v_k and v_j such that there exists a 2-path connecting v_i and v_j through v_k on alternating edges from $\mathcal{H}$ and $\mathcal{G}_2$, starting with $\mathcal{G}_2$, without loss of generality. As v_i and v_j share the common connected vertex v_k, Lemma C.0.1 yields $\left[\boldsymbol{E}_{\{i,k\}}, \boldsymbol{E}_{\{k,j\}}\right] \neq 0$.

Reversing the order of the commutator with a common connected vertex has the following property

$$\left[\boldsymbol{E}_{\{j,k\}}, \boldsymbol{E}_{\{k,i\}}\right] = -\left(\boldsymbol{E}_{ij} - \boldsymbol{E}_{ji}\right) = -\left[\boldsymbol{E}_{\{i,k\}}, \boldsymbol{E}_{\{k,j\}}\right] \tag{C.8}$$

following from Lemma C.0.1. Namely, reversing the path order changes the sign of the commutator. As $\mathcal{H}$ and $\mathcal{G}_2$ have a disjoint edge set, there exists no such reverse direction 2-path from v_j and v_i passing over v_k starting with an edge in

$\mathcal{H}$. However, from the constructive symmetry of the connectivity induced by the connectivity template, there exists some vertex $v_{k'} \neq v_k$ where there exists a 2-path from v_j to v_i over $v_{k'}$ starting with an edge from $\mathcal{H}$, forming an alternating edge 4-circuit from v_i to itself. By equation (C.8), the commutator of this 4-circuit becomes

$$\left[\boldsymbol{E}_{\{j,k'\}}, \boldsymbol{E}_{\{k',i\}}\right] = \boldsymbol{E}_{ji} - \boldsymbol{E}_{ij} = -\left(\boldsymbol{E}_{ij} - \boldsymbol{E}_{ji}\right) = -\left[\boldsymbol{E}_{\{i,k\}}, \boldsymbol{E}_{\{k,j\}}\right]. \tag{C.9}$$

Critically, the existence of $v_{k'}$ implies that $w_{ik}^{[2]} w_{kj}^{[3]}$ and $-w_{jk'}^{[2]} w_{k'i}^{[3]}$ are within the summand of equation (C.4). Hence if $w_{ik}^{[2]} w_{kj}^{[3]} = w_{jk'}^{[2]} w_{k'i}^{[3]}$ then these non-zero terms in equation (C.4) cancel. This process can be repeated over all alternating 4-circuits emanating from v_i, cancelling all terms associated with v_i in equation (C.4).

By the regularity of the graphs and therefore the symmetries of the edge structures in $\mathcal{G}_2$ and $\mathcal{H}$, there are only n_p unique alternating edge 4-circuits with the graphs and thus there exists an automorphism that assigns any identical alternating 2-path connected vertices to v_i and v_j. Subsequently, all non-zero terms of equation (C.4) cancel, yielding $[\boldsymbol{W}_3, \boldsymbol{W}_2] = 0$ and therefore $\mathcal{G}_1$ and $\mathcal{G}_2$ commute by Lemma C.0.2. □

Corollary C.1.1. *Let $\mathcal{G}_1$ be a regular undirected unweighted graph and $\mathcal{G}_2$ be a regular subgraph of graph of $\mathcal{G}_1$ constructed by regular edge removal. If there exists an alternating edge 4-circuit in $\mathcal{G}_2$ and $\mathcal{H}$ then $\mathcal{G}_1$ and $\mathcal{G}_2$ commute.*

Proof. $\mathcal{G}_1$ undirected implies that $w_{ij}^{[1]} = 1$ if v_i is adjacent to v_j and $w_{ij}^{[1]} = 0$ else. $\mathcal{G}_2$ inherits the undirected property from $\mathcal{G}_1$ by construction. Therefore, for the existence of a 4-circuit of alternating edges in $\mathcal{G}_2$ and $\mathcal{H}$, it is guaranteed that $w_{ik}^{[2]} w_{kj}^{[3]} = w_{jk'}^{[2]} w_{k'i}^{[3]} = 1$. Following from the edge structure symmetry induced by regularity in $\mathcal{G}_2$ and $\mathcal{H}$, there exists an automorphism that relabels the vertices of $\mathcal{G}_2$ and $\mathcal{H}$ which reconstructs all possible 4-circuit of alternating edges emanating from v_i. □

These graphical methods of demonstrating commutativity of subgraphs by exploiting the symmetries induced by a connectivity template are computationally efficient as the number of cases that we are required to check only depends on the degree of the vertices and are critically independent if the number of vertices in the graph. We demonstrate this feature in Figure C.4 where we highlight that when $w_1^{[1]} = w_1^{[2]}$ the graphs $\mathcal{G}_1$ and $\mathcal{G}_2$ from C.2 commute by Lemma C.1.1 and the existence of a single alternating edge 4-vertex circuit.

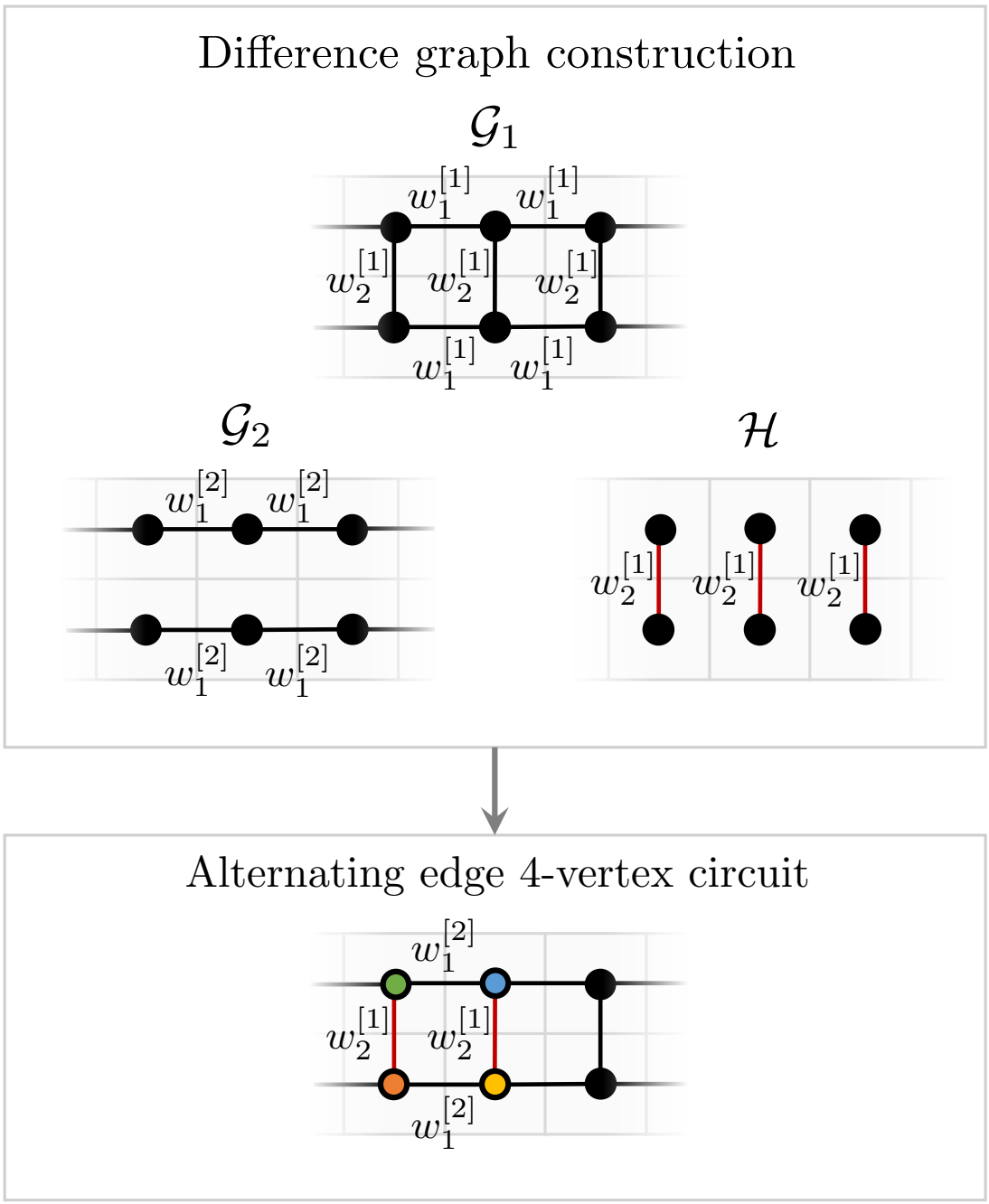

Figure C.4: Commutativity of a simple periodic bilayer graph and a subgraph constructed from edge removal. The graphs $\mathcal{G}_1$ and $\mathcal{G}_2$ from Figure C.2 are shown with the difference graph $\mathcal{H}$ for the case $w_1^{[1]} = w_1^{[2]}$. The single unique alternating edge 4-vertex circuit for $\mathcal{G}_2$ and $\mathcal{H}$ is given below starting at the yellow vertex and passing through the blue, green and orange vertices, respectively.

C.2 Constructing families of commuting undirected regular weighted graphs

Next, we consider the case when edge weight values are not preserved when removing edges from the connectivity template $\mathcal{T}_1$ to construct subgraphs. For

this case, $\mathcal{H}$ and $\mathcal{G}_2$ may have commonly connected vertices with different weights, i.e. in Figure C.3, v_1 and v_2 are connected by weighted edges b_2 and c_2 in $\mathcal{G}_2$ and $\mathcal{H}$, respectively, where $b_2 \neq c_2$. Therefore we cannot exclude the existence of 2-paths that return to the starting vertex in our analysis. Hence the following statement includes such common edge structure. Specifically, including such edge structures increases the number of cases that we are required to validate.

Lemma C.2.1. *Let $\mathcal{G}_1$ be a weighted, regular and undirected graph constructed using a connectivity template $\mathcal{T}_1$ and $\mathcal{G}_2$ be a regular subgraph of $\mathcal{G}_1$ constructed by regular edge removal with differing edge weights. $\mathcal{G}_1$ and $\mathcal{G}_2$ commute if for any v_i there exists n_p distinct closed 4-step paths consisting of alternating edges from $\mathcal{G}_2$ and $\mathcal{H}$ such that the product of the edge weights first two edge weights are equal to the product of the final two edge weights in the closed 4-step paths.*

Proof. The result follows almost identically as the proof of Theorem C.1.1. However, in the case of common vertices between edges ($n_p \neq 0$) then the required existence of $v_{k'}$ need not be different from v_k and therefore the adjacent vertices defining the closed four-step may not be unique. Moreover, the regularity of $\mathcal{G}_1$, $\mathcal{G}_2$ and $\mathcal{H}$ induce symmetries within the graphs as in Theorem C.1.1 and thus there are only n_p unique closed 4-step paths of alternating edges up to vertex relabelling via a common automorphism on $\mathcal{G}_2$ and $\mathcal{H}$. □

We now seek to reduce the number of computations required to generate a family of commuting graphs by exploiting the symmetry of the structures defined by the connectivity templates. Namely, if $\mathcal{G}_1$ commutes with itself up to differing edge weight values we show that any subgraphs $\mathcal{G}_i$ and $\mathcal{G}_j$ of $\mathcal{G}_1$ must commute with $\mathcal{G}_1$ and each other. Critically, this construction allows us to generate a family of commuting subgraphs derived from $\mathcal{G}_1$.

Theorem C.2.1 (Regular subgraphs commute)**.** *Let $\mathcal{G}_1$ and $\hat{\mathcal{G}}_1$ be two regular, undirected and weighted graphs constructed from the same connectivity template $\mathcal{T}_1$ where edge values are allowed to differ. If $\mathcal{G}_1$ and $\hat{\mathcal{G}}_1$ commute then any subgraph $\mathcal{G}_i$ constructed by regular edge removal commutes with $\mathcal{G}_1$. Moreover, if $\mathcal{G}_j$ is another subgraph of $\mathcal{G}_1$ constructed by regular edge removal, then $\mathcal{G}_i$ and $\mathcal{G}_j$ commute.*

Proof. For any $v_i \in V$, the number of edges with a unique weight value emanating from v_i is given by e_1. Following from the commutativity of $\mathcal{G}_1$ and $\hat{\mathcal{G}}_1$ and Lemma C.2.1, there exists e_1^2 unique closed 4-step paths consisting of alternating edges from $\mathcal{G}_1$ and $\hat{\mathcal{G}}_1$. Critically, any subgraph $\mathcal{G}_j$ of $\mathcal{G}_1$ must commute by Lemma C.2.1 as it is constructed by regularly removing edges from $\mathcal{G}_1$, and all of the unique

alternating 4-steps paths in $\mathcal{G}_j$ and $\mathcal{G}_1$ already exist in the unique alternating 4-steps paths of $\mathcal{G}_1$ and $\hat{\mathcal{G}}_1$. The argument follows similarly for the commutativity of any two subgraphs $\mathcal{G}_i$ and $\mathcal{G}_j$ of $\mathcal{G}_1$, as the unique alternating 4-step paths in $\mathcal{G}_i$ and $\mathcal{G}_j$ already exist due to the preservation of the edge weight structure via the connectivity template construction. □

Critically, checking the commutativity of only one graph with itself ensures the commutativity of all regular subgraphs and therefore, Theorem C.2.1 provides a convenient method of constructing larger families of commuting graphs which has applications to polarity-dependent cell signalling mechanisms that operate over different ranges. In the context of pattern formation in developmental systems, families of commuting graphs can be constructed by the following steps:

1. Define a regular and periodic lattice representing a cellular domain.
2. Define a connectivity template, $\mathcal{T}_1$, on the lattice that represents the most connected cell-cell signalling mechanism (largest degree).
3. Let $\hat{\mathcal{T}}_1$ be the connectivity template with the same structure as $\mathcal{T}_1$ where edge weights may differ.
4. Construct the graphs $\mathcal{G}_1$ and $\hat{\mathcal{G}}_1$ from the templates $\mathcal{T}_1$ and $\hat{\mathcal{T}}_1$, respectively.
5. Choose some vertex $v_i \in V$ and show the existence of e_1^2 alternating closed 4-paths emanating from v_i of edges in $\mathcal{G}_1$ and $\hat{\mathcal{G}}_1$.
6. Construct a commuting subgraph of $\mathcal{G}_1$ by removing edges from $\mathcal{T}_1$ to represent another cell-cell signalling mechanism.

The following example provides a demonstration of these steps and the resultant family of commuting subgraphs that are inherited from the commutativity of $\mathcal{G}_1$.

Example C.2.1. *Consider the fixed and regular bilayer hexagonal lattice as in Figure C.5. Let $\mathcal{T}_1$ be the graph template describing long-range diffusion of signalling ligands between cells that has a characteristic length scale of two cells, namely, each cell is signalling to their closest 6 neighbours with associated weights dependent on distance from the diffusing cell as given in Figure C.5. Applying $\mathcal{T}_1$ to each cell in the hexagonal lattice whilst imposing that edges are undirected produces the cell-cell connectivity graph $\mathcal{G}_1$.*

The connectivity template $\hat{\mathcal{T}}_1$ is formed by taking the same edge structure as $\mathcal{T}_1$ but allowing the edge weights to differ such that $w_i^{[1]} \neq \hat{w}_i^{[1]}$ as in C.5. We construct the associated graph $\hat{\mathcal{G}}_1$ from $\hat{\mathcal{T}}_1$ using the same method as $\mathcal{G}_1$. We

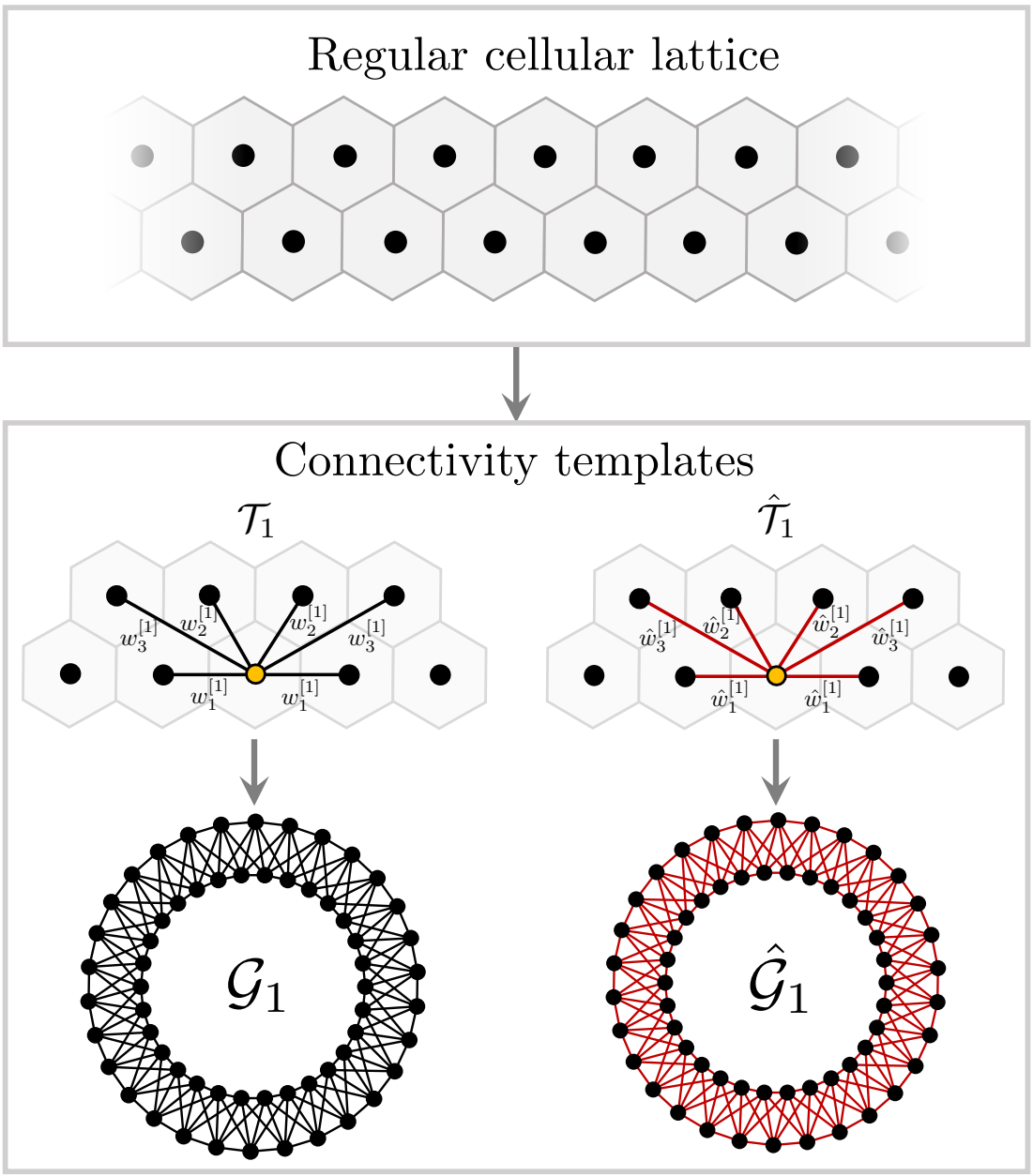

Figure C.5: Periodic bilayer graphs constructed from a hexagonal lattice and a connectivity template. Connectivity templates $\mathcal{T}_1$ and $\hat{\mathcal{T}}_1$ are shown on a portion of the hexagonal lattice with respect to a fixed vertex highlighted in yellow. We allow the edge weights in $\mathcal{T}_1$ and $\hat{\mathcal{T}}_1$ to differ such that $w_i^{[1]} \neq \hat{w}_i^{[1]}$. Example graphs $\mathcal{G}_1$ and $\hat{\mathcal{G}}_1$ constructed by $\mathcal{T}_1$ and $\hat{\mathcal{T}}_1$ are shown for $|V| = 60$.

are left to show that $\mathcal{G}_1$ and $\hat{\mathcal{G}}_1$ commute to generate a family of commutative subgraphs from $\mathcal{G}_1$ by Theorem C.2.1.

Each connectivity template $\mathcal{T}_1$ and $\hat{\mathcal{T}}_1$ has 3 distinct weighted edges emanating from any given vertex, denoted by $e_1 = \hat{e}_1 = 3$. Therefore by Lemma C.2.1, if there exists 9 distinct closed 4-step paths of alternating edges from $\mathcal{G}_1$ and $\hat{\mathcal{G}}_1$ where the product of the first two edge weights are equal to the final two edge

weights, then $\mathcal{G}_1$ and $\hat{\mathcal{G}}_1$ commute. These paths can be formed by applying the appropriate connectivity template to each vertex in the sequence of the path, to return to the initial vertex in four steps, as shown in Figure C.6 for the alternating closed 4-path (2). This process is repeated for all edge weight combinations in $\mathcal{T}_1$ and $\hat{\mathcal{T}}_1$. All nine resulting alternating closed 4-paths are given in Figure C.6 and consequently we have that $\mathcal{G}_1$ and $\hat{\mathcal{G}}_1$ commute. Note that due to the symmetry of the templates, we only needed to check the existence of the alternating closed 4-paths of (2), (3) and (6) however all nine are shown for completeness.

Following from Theorem C.2.1, any subgraph of $\mathcal{G}_1$ generated by removing edges from the connectivity template $\mathcal{T}_1$ commutes with $\mathcal{G}_1$ and any other subgraph produced similarly. Figure C.7 highlights a systematic approach to generating a family of commuting graphs, each inherited from the connectivity template $\mathcal{T}_1$. Subsequently, we produced seven different commuting graphs, each with differing edge weights by only examining the commutativity of the largest connectivity template. Note that the characteristic representations of long-range and short-range diffusion cell-cell signalling templates in Figure C.1 are given by $\mathcal{G}_1$ and $\mathcal{G}_2$ in Figure C.7 for the bilayer lattice. These graphs are later used in large-scale laminar pattern analysis in Chapter 4.

The prescribed lattice geometry and connectivity template induces regularity in the graphs we consider in this section, which represent cell-cell commutation. Cellular structure regularity is not a feature observed in biological tissue due to the intrinsic complexity and stochasticity involved in developing biological systems [48]. However, the methods described here allow us to conveniently construct commutative graphs, independent of the number of vertices and numerical computation, which enables the study of large-scale tissues in cell-fate pattern analysis (Chapter 4).

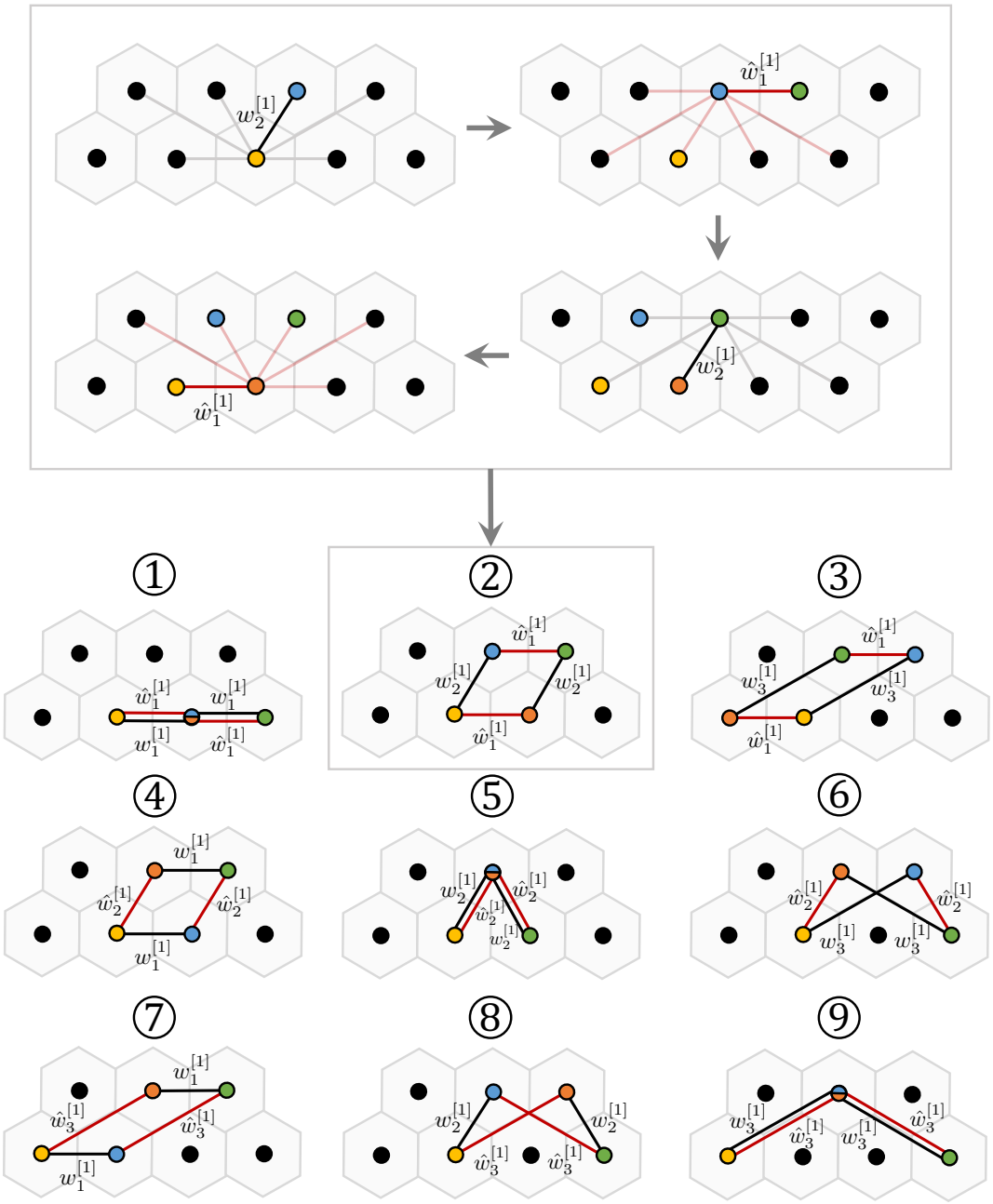

Figure C.6: All possible closed alternating 4-paths of edges in $\mathcal{G}_1$ and $\hat{\mathcal{G}}_1$ emanating from a fixed vertex highlighted in yellow and pass through the blue, green and orange vertices, respectively. The construction of the second closed alternating 4-path using the connectivity templates $\mathcal{T}_1$ and $\hat{\mathcal{T}}_1$ is shown above.

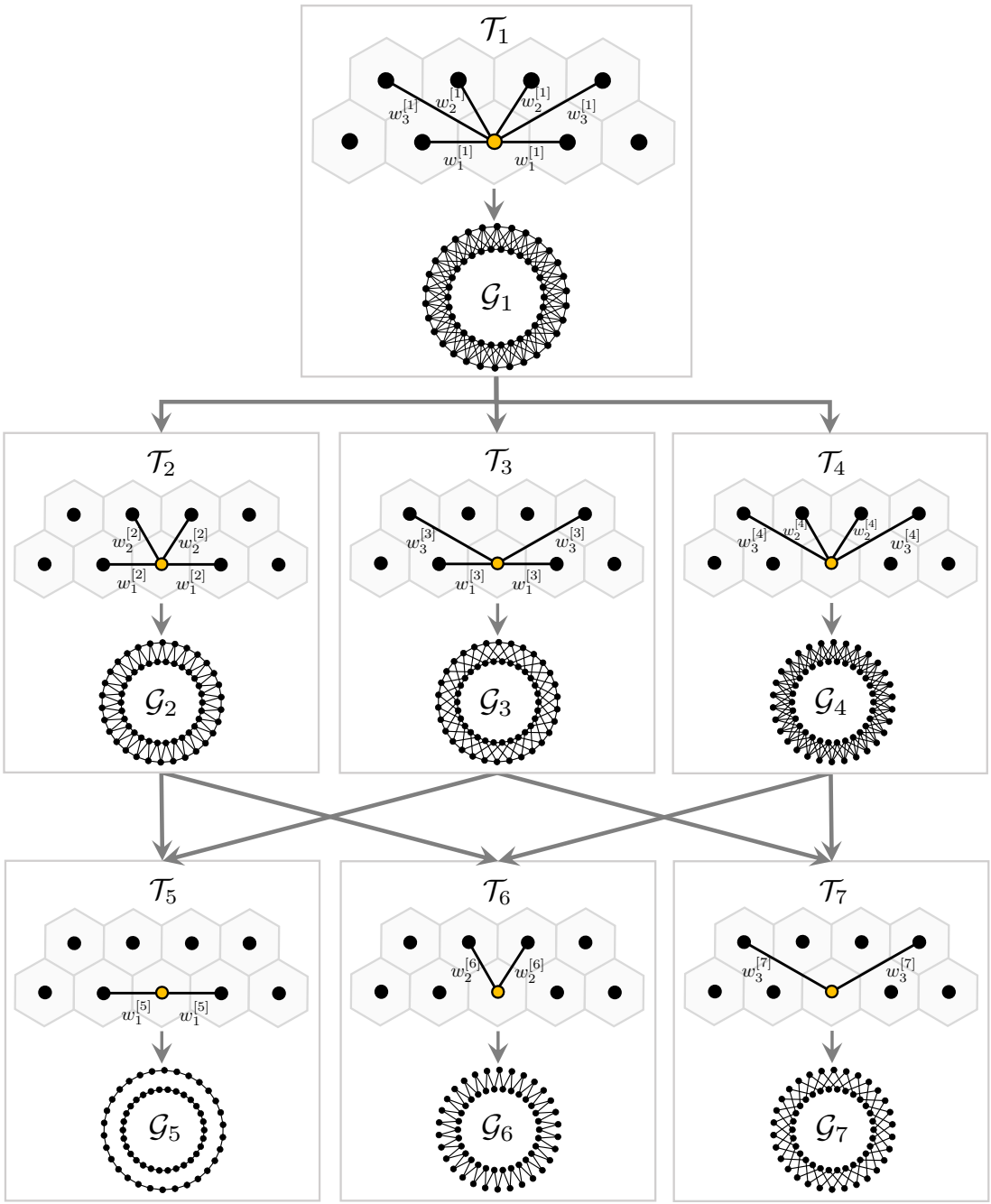

Figure C.7: A family of commuting weighted graphs constructed by subgraphs of $\mathcal{G}_1$. Connectivity templates with associated graphs are shown with arrows directing the subgraph inheritance.

Appendix D

Computational methods for MIMO simulations

The ODE systems in this study were solved numerically using the `ODE15s` solver in Matlab (R2021a). Simulations were performed over a total of 10000 time units in addition to a stopping event applied to the ODE solver to check for solution convergence. Namely, if all trajectories varied less than 1×10^{-4} over four consecutive iterations, then we assume that the system has converged to a steady state. We note that all simulations presented in this study satisfied the convergence criteria.

Random initial conditions were sampled from a uniform distribution using the `rand` function. The homogeneous steady state of the system was calculated using the `fsolve` function that implements the trust-region-dogleg minimisation algorithm [151]. Eigenvalues of the adjacency matrices were calculated using the `eig` function from the Linear Algebra toolbox in Matlab (R2021a). To visualise the approximate cell membranes in the large-scale simulation Voronoi diagrams were drawn around graph vertices using the `delaunayTriangulation` and `voronoi` functions within the Computational Geometry toolbox in Matlab (R2021a). Ghost vertices were introduced to ensure that each graph vertex has a closed boundary. The source code for the simulations presented in Chapter 4 can be found at `https://github.com/joshwillmoore1/Mixed_Signal_mechanisms`.

The intracellular kinetics parameter values of the IO system (4.56-4.60) used in all simulations are given in Table D.1 below.

Parameter	α_1	α_2	β_1	β_2	β_3	k_1	k_2	h_1	h_2	h_3
Value	0.01	1	100	10	100	2	2	2	2	1

Table D.1: Parameter values used in the simulations of the IO system (4.56-4.60).

Appendix E

Proof of π_2-dependent spectral gap for $\mathcal{G}_{\mathbf{2D}}$ and $\mathcal{G}_{\mathbf{3D}}$ from Figure 4.9B

The existence of a block off-diagonal canonical form of the adjacency matrix of a bipartite graph is often exploited in spectral investigations [266]. For any bipartite graph $\mathcal{G}_k$ with adjacency matrix $\boldsymbol{W}_k$ there exists a permutation matrix $\boldsymbol{U}$ that re-indexes the vertices with respect to the independent sets V_1 and V_2 such that

$$\boldsymbol{U}^T \boldsymbol{W}_k \boldsymbol{U} = \begin{bmatrix} \mathbf{0} & \boldsymbol{X}_k \\ \boldsymbol{X}_k^T & \mathbf{0} \end{bmatrix}, \tag{E.1}$$

where $\boldsymbol{X}_k$ is the biadjacency matrix [220]. Subsequently, the spectra of the bipartite graphs have a distinct structure such that there is a symmetry of eigenvalues respective to the biadjacency matrices, i.e., $\mathrm{Spec}\left(\boldsymbol{W}_k\right) = \mathrm{Spec}\left(\boldsymbol{X}_k\right) \cup \mathrm{Spec}\left(-\boldsymbol{X}_k\right)$. Leveraging the spectral symmetry of bipartite graphs and the spectral retention of equitable partitions, we demonstrate that for the bipartite bilayer graphs $\mathcal{G}_{2\mathrm{D}}$ and $\mathcal{G}_{3\mathrm{D}}$ in Figure 4.9, the smallest eigenvalue of $\boldsymbol{X}_k$ is $-\overline{\lambda}_{k,2}$, the polarity driven eigenvalue associated with laminar pattern template π_2.

Lemma E.0.1. *Let $\mathcal{G}_k$ be a regular bipartite bilayer graphs as shown in Figure 4.9 ($k = 2D, 3D$) with associated weighted adjacency matrix $\boldsymbol{W}_k$. Consider the equitable partition π_2 such that the quotient graph, $\mathcal{G}_{k,\pi_2}$, consists of only two representative vertices in each layer of $\mathcal{G}_k$ and has the reduced adjacency matrix $\overline{\boldsymbol{W}}_k$ (4.32). Then biadjacency matrix $\boldsymbol{X}_k$ associated with $\boldsymbol{W}_k$ satisfies*

$$-\overline{\lambda}_{k,2} = \min\left(\mu_{k,j} : \mu_{k,j} \in \mathrm{Spec}\left(\boldsymbol{X}_k\right)\right), \tag{E.2}$$

where $\overline{\lambda}_{k,2}$ is the smallest eigenvalue of $\overline{\boldsymbol{W}}_k$ with associated eigenvector $\overline{\boldsymbol{v}}_{k,2}$.

Proof. We present the proof for $\mathcal{G}_{2\mathrm{D}}$ as the following argument holds immediately for $\mathcal{G}_{3\mathrm{D}}$ also. As we make use of the biadjacency form of $\boldsymbol{W}_{2\mathrm{D}}$, we first construct the biadjacency transformation $\boldsymbol{U}$. The bipartite bilayer graph $\mathcal{G}_{2\mathrm{D}}$ has vertex

indices in layer-wise order as defined in Section 4.1.1 with block adjacency matrices given in equation (4.9). To reorder the vertices of $\mathcal{G}_{2\mathrm{D}}$ such that vertex groups V_1 and V_2 are ordered consecutively, we define the permutation matrix

$$\boldsymbol{U} = \begin{bmatrix} \boldsymbol{I}_{|L_1|/2} \otimes \boldsymbol{D}_1 & \boldsymbol{I}_{|L_1|/2} \otimes \boldsymbol{D}_2 \\ \boldsymbol{I}_{|L_2|/2} \otimes \boldsymbol{D}_2 & \boldsymbol{I}_{|L_2|/2} \otimes \boldsymbol{D}_1 \end{bmatrix}, \tag{E.3}$$

where $|L_1| = |L_2|$ as each layer has the same number of vertices. In particular, we have the biadjacency form

$$\begin{aligned} \boldsymbol{U}^T \boldsymbol{W}_{2\mathrm{D}} \boldsymbol{U} &= \begin{bmatrix} \boldsymbol{I}_{|L_1|/2} \otimes \boldsymbol{D}_1 & \boldsymbol{I}_{|L_1|/2} \otimes \boldsymbol{D}_2 \\ \boldsymbol{I}_{|L_2|/2} \otimes \boldsymbol{D}_2 & \boldsymbol{I}_{|L_2|/2} \otimes \boldsymbol{D}_1 \end{bmatrix} \begin{bmatrix} \widehat{\boldsymbol{W}}_{1,L_1} & \widehat{\boldsymbol{W}}_{2,L_1} \\ \widehat{\boldsymbol{W}}_{2,L_1}^T & \widehat{\boldsymbol{W}}_{1,L_2} \end{bmatrix} \begin{bmatrix} \boldsymbol{I}_{|L_1|/2} \otimes \boldsymbol{D}_1 & \boldsymbol{I}_{|L_1|/2} \otimes \boldsymbol{D}_2 \\ \boldsymbol{I}_{|L_2|/2} \otimes \boldsymbol{D}_2 & \boldsymbol{I}_{|L_2|/2} \otimes \boldsymbol{D}_1 \end{bmatrix}, \\ &= \begin{bmatrix} 0 & \boldsymbol{X}_{2\mathrm{D}} \\ \boldsymbol{X}_{2\mathrm{D}} & 0 \end{bmatrix}, \end{aligned} \tag{E.4}$$

for $\boldsymbol{X}_{2\mathrm{D}}$ in periodic tridiagonal form

$$\boldsymbol{X}_{2\mathrm{D}} = \begin{bmatrix} \hat{w}_2^{[2\mathrm{D}]} & \hat{w}_1^{[2\mathrm{D}]} & 0 & \cdots & 0 & \hat{w}_1^{[2\mathrm{D}]} \\ \hat{w}_1^{[2\mathrm{D}]} & \hat{w}_2^{[2\mathrm{D}]} & \hat{w}_1^{[2\mathrm{D}]} & & & \\ & & \ddots & & & \\ & & & \ddots & & \\ & & & \hat{w}_1^{[2\mathrm{D}]} & \hat{w}_2^{[2\mathrm{D}]} & \hat{w}_1^{[2\mathrm{D}]} \\ \hat{w}_1^{[2\mathrm{D}]} & 0 & \cdots & 0 & \hat{w}_1^{[2\mathrm{D}]} & \hat{w}_2^{[2\mathrm{D}]} \end{bmatrix}, \tag{E.5}$$

noting that $\boldsymbol{X}_{2\mathrm{D}}^T = \boldsymbol{X}_{2\mathrm{D}}$ by the regularity of $\mathcal{G}_{2\mathrm{D}}$ and therefore $\boldsymbol{U}^T \boldsymbol{W}_{2\mathrm{D}} \boldsymbol{U}$ is symmetric.

As the laminar pattern template partition π_2 is equitable there exists a lifting matrix $\boldsymbol{L} \in \{0,1\}^{N \times 2}$ that maps the large-scale adjacency matrix $\boldsymbol{W}_{2\mathrm{D}}$ into its reduced form $\overline{\boldsymbol{W}}_{2\mathrm{D}}$ such that

$$\boldsymbol{W}_{2\mathrm{D}} \boldsymbol{L} = \boldsymbol{L} \overline{\boldsymbol{W}}_{2\mathrm{D}}, \tag{E.6}$$

as demonstrated in [137]. The lifting transformation is constructed by grouping vertices associated with the partition π_2 on $\boldsymbol{W}_{2\mathrm{D}}$ for example $\boldsymbol{L}_{ij} = 1$ if $v_i \in L_j$. Owing to the block structure of $\boldsymbol{W}_{2\mathrm{D}}$ (4.8) which follows from the layer-wise vertex indexing, we have that

$$\boldsymbol{L} = \begin{bmatrix} \mathbf{1}_{|L_1|,1} & \mathbf{0}_{|L_1|,1} \\ \mathbf{0}_{|L_2|,1} & \mathbf{1}_{|L_2|,1} \end{bmatrix}. \tag{E.7}$$

Critically, the lifting matrix $\boldsymbol{L}$ provides the algebraic link between the quotient and large-scale graphs.

Following from the regular structure of $\mathcal{G}_{2\mathrm{D}}$ and direct computation, the eigenvector associated with $\overline{\lambda}_{2\mathrm{D},2}$ has the form $\overline{\boldsymbol{v}}_{2\mathrm{D},2} = [1,-1]^T$. The spectral retention property of the equitable partition, π_2, guarantees that $\overline{\lambda}_{2\mathrm{D},2} \in \mathrm{Spec}\,(\boldsymbol{W}_{2\mathrm{D}})$ where $\boldsymbol{L}\overline{\boldsymbol{v}}_{2\mathrm{D},2}$ is the corresponding eigenvector for the large-scale

graph $\mathcal{G}_{2\mathrm{D}}$ (by Theorem 9.3.3 in [220]). Explicitly, we have that the lifted eigenvector is of the form

$$\boldsymbol{L}\overline{\boldsymbol{v}}_{2\mathrm{D},2} = \begin{bmatrix} \mathbf{1}_{|L_1|,1} \\ -\mathbf{1}_{|L_2|,1} \end{bmatrix}, \tag{E.8}$$

with associated eigenvalue $\overline{\lambda}_{2\mathrm{D},2}$. In the biadjacency matrix form (E.4), the corresponding eigenvector has the transformed representation

$$\boldsymbol{\nu} \coloneqq \boldsymbol{U}^T\boldsymbol{L}\overline{\boldsymbol{v}}_{2\mathrm{D},2} = \big[\underbrace{1 \quad -1 \quad \cdots \quad 1 \quad -1}_{|L_1|} \quad \underbrace{1 \quad -1 \quad \cdots \quad 1 \quad -1}_{|L_2|}\big]^T. \tag{E.9}$$

The spectral symmetry of bipartite graphs ensures that if there exists an eigenpair $\left(\overline{\lambda}_{2\mathrm{D},2}, \boldsymbol{\nu} = [\boldsymbol{x}, \boldsymbol{y}^T]\right)$ then there must also exist the eigenpair $\left(-\overline{\lambda}_{2\mathrm{D},2}, \tilde{\boldsymbol{\nu}} = [\boldsymbol{x}, -\boldsymbol{y}^T]\right)$ [220]. Therefore the eigenvector associated with $-\lambda_{2\mathrm{D},2}$ has biadjacency form

$$\tilde{\boldsymbol{\nu}} = \big[\underbrace{1 \quad -1 \quad \cdots \quad 1 \quad -1}_{|L_1|} \quad \underbrace{-1 \quad 1 \quad \cdots \quad -1 \quad 1}_{|L_2|}\big]^T. \tag{E.10}$$

which negates the signs of those entries associated with the latter half of the vertices in $\mathcal{G}_{2\mathrm{D}}$. Subsequently, the first $|L_1|$ entries of $\tilde{\boldsymbol{\nu}}$ are an eigenvector of $\boldsymbol{X}_{2\mathrm{D}}$ with eigenvalue $-\overline{\lambda}_{2\mathrm{D},2}$ following from the canonical bidjacency representation of $\boldsymbol{W}_{2\mathrm{D}}$ (E.4). We denote this reduced eigenvector in normalised form

$$\tilde{\boldsymbol{\nu}}_1 = \frac{1}{\sqrt{|L_1|}}\big[\underbrace{1 \quad -1 \quad \cdots \quad 1 \quad -1}_{|L_1|}\big]^T, \tag{E.11}$$

and therefore it remains to show that the eigenpair $\left(-\overline{\lambda}_{2\mathrm{D},2}, \tilde{\boldsymbol{\nu}}_1\right)$ is minimal in the spectrum of $\boldsymbol{X}_{2\mathrm{D}}$.

The Rayleigh quotient for $\boldsymbol{X}_{2\mathrm{D}}$ is defined by

$$R_{\boldsymbol{X}_{2\mathrm{D}}}(\boldsymbol{y}) = \frac{\boldsymbol{y}^T\boldsymbol{X}_{2\mathrm{D}}\boldsymbol{y}}{\boldsymbol{y}^T\boldsymbol{y}} \tag{E.12}$$

and as $\boldsymbol{X}_{2\mathrm{D}}$ is real and symmetric by the Min-Max theorem the Rayleigh quotient is bounded by the maximal and minimal eigenvalues of the matrix, $R_{\boldsymbol{X}_{2\mathrm{D}}}(\boldsymbol{y}) \in [\lambda_{\min}, \lambda_{\max}]$ [220]. In particular, $R_{\boldsymbol{X}_{2\mathrm{D}}}(\boldsymbol{y})$ generates the eigenvalues of $\boldsymbol{X}_{2\mathrm{D}}$ when $\boldsymbol{y}$ is the respective eigenvector. Hence we show that $\tilde{\boldsymbol{\nu}}_1$ minimises $R_{\boldsymbol{X}_{2\mathrm{D}}}(\boldsymbol{y})$, namely

$$\underset{\substack{\boldsymbol{y}\in\mathbb{R}^{|L_1|} \\ ||\boldsymbol{y}||=1}}{\arg\min}\left(R_{\boldsymbol{X}_{2\mathrm{D}}}(\boldsymbol{y})\right) = \tilde{\boldsymbol{\nu}}_1. \tag{E.13}$$

where the normality constraint follows from $\boldsymbol{X}_{2\mathrm{D}}$ being real and symmetric and so the eigenvectors of $\boldsymbol{X}_{2\mathrm{D}}$ are orthonormal with real eigenvalues.

The normalised form of $\tilde{\boldsymbol{\nu}}_1$ yields $\tilde{\boldsymbol{\nu}}_1^T\tilde{\boldsymbol{\nu}}_1 = 1$ and therefore the Rayleigh quotient evaluated at $\tilde{\boldsymbol{\nu}}_1$ simplifies to $R_{\boldsymbol{X}_{2\mathrm{D}}}(\tilde{\boldsymbol{\nu}}_1) = \tilde{\boldsymbol{\nu}}_1^T\boldsymbol{W}_{2\mathrm{D}}\tilde{\boldsymbol{\nu}}_1$. By direct computation, we have that

$$\begin{aligned}
\tilde{\boldsymbol{\nu}}_1^T\boldsymbol{X}_{2\mathrm{D}}\tilde{\boldsymbol{\nu}}_1 &= \sum_{k=1}^{|L_1|}\sum_{j=1}^{|L_1|}(\boldsymbol{X}_{2\mathrm{D}})_{k,j}(\tilde{\boldsymbol{\nu}}_1)_k(\tilde{\boldsymbol{\nu}}_1)_j, \\
&= \sum_{i=1}^{|L_1|}(\boldsymbol{X}_{2\mathrm{D}})_{ii}(\tilde{\boldsymbol{\nu}}_1)_i^2 + \sum_{i=2}^{|L_1|-1}(\tilde{\boldsymbol{\nu}}_1)_i\Big((\boldsymbol{X}_{2\mathrm{D}})_{i,i-1}(\tilde{\boldsymbol{\nu}}_1)_{i-1} + (\boldsymbol{X}_{2\mathrm{D}})_{i,i+1}(\tilde{\boldsymbol{\nu}}_1)_{i+1}\Big) \\
&+ (\tilde{\boldsymbol{\nu}}_1)_1\Big((\boldsymbol{X}_{2\mathrm{D}})_{1,2}(\tilde{\boldsymbol{\nu}}_1)_2 + (\boldsymbol{X}_{2\mathrm{D}})_{1,|L_1|}(\tilde{\boldsymbol{\nu}}_1)_{|L_1|}\Big) \\
&+ (\tilde{\boldsymbol{\nu}}_1)_{|L_1|}\Big((\boldsymbol{X}_{2\mathrm{D}})_{|L_1|,1}(\tilde{\boldsymbol{\nu}}_1)_1 + (\boldsymbol{X}_{2\mathrm{D}})_{|L_1|,|L_1|-1}(\tilde{\boldsymbol{\nu}}_1)_{|L_1|-1}\Big) \qquad \text{(E.14)}
\end{aligned}$$

by the cyclic tridiagonal form of $\boldsymbol{X}_{2\mathrm{D}}$ (E.5). Critically as $(\boldsymbol{X}_{2\mathrm{D}})_{i,j} \geq 0$ for all i, j, then $\tilde{\boldsymbol{\nu}}_1^T\boldsymbol{X}_{2\mathrm{D}}\tilde{\boldsymbol{\nu}}_1$ is minimised when $sgn((\tilde{\boldsymbol{\nu}}_1)_k) \neq sgn\left((\tilde{\boldsymbol{\nu}}_1)_{k+1}\right)$ for all $k \in \{1, ..., |L_1| - 1\}$, which is satisfied by definition of $\tilde{\boldsymbol{\nu}}_1$. Furthermore, the orthonormal property of the eigenbasis of $\boldsymbol{X}_{2\mathrm{D}}$ ensures that no other eigenvector has this alternating sign structure which implies that $-\overline{\lambda}_{2\mathrm{D},2}$ is the smallest eigenvalue of $\boldsymbol{X}_{2\mathrm{D}}$. □

A consequence of Lemma E.0.1 is the existence of a spectral gap about the origin for $\mathcal{G}_{2\mathrm{D}}$ and $\mathcal{G}_{3\mathrm{D}}$.

Theorem E.0.1. *Let $\mathcal{G}_k$ and $\mathcal{G}_{k,\pi_2}$ be defined as in Lemma E.0.1 and let $\lambda_{k,j} \in \mathrm{Spec}(\boldsymbol{W}_k)$. If $\overline{\lambda}_{k,2} < 0$ then $\lambda_{k,j} \notin \left(\overline{\lambda}_{k,2}, -\overline{\lambda}_{k,2}\right)$.*

Proof. From Lemma E.0.1 we have that $-\overline{\lambda}_{k,2} = \min(\mu_{k,j} : \mu_{k,j} \in \mathrm{Spec}(\boldsymbol{X}_k))$ and thus $-\overline{\lambda}_{k,2} > 0$. From the symmetry of the spectrum of bipartite graphs, we have that $\overline{\lambda}_{k,2} < 0$ is the maximum of the negative eigenvalues of $\boldsymbol{W}_k$, therefore, defining a region about the origin bounded by $\overline{\lambda}_{k,2}$ and $-\overline{\lambda}_{k,2}$ that contains no eigenvalues. □

References

[1] Sara McNally and Torsten Stein. *Overview of mammary gland development: a comparison of mouse and human*, pages 1–17. Springer, USA, 2017.

[2] Gat Rauner and Charlotte Kuperwasser. Microenvironmental control of cell fate decisions in mammary gland development and cancer. *Developmental Cell*, 56:1875–1883, 2021.

[3] Xiaofeng Dai, Liangjian Xiang, Ting Li, and Zhonghu Bai. Cancer hallmarks, biomarkers and breast cancer molecular subtypes. *Journal of Cancer*, 7:1281, 2016.

[4] Cancer Research UK. Breast cancer statistics, 2020.

[5] Pengfei Lu, Tao Zhou, Chongshen Xu, and Yunzhe Lu. Mammary stem cells, where art thou? *Wiley Interdisciplinary Reviews: Developmental Biology*, 8:e357, 2019.

[6] Agla J.R. Fridriksdottir, Ole W. Petersen, and Lone Rønnov-Jessen. Mammary gland stem cells: current status and future challenges. *International Journal of Developmental Biology*, 55:719–729, 2011.

[7] William R. Crowley and William E. Armstrong. Neurochemical regulation of oxytocin secretion in lactation. *Endocrine Reviews*, 13:33–65, 1992.

[8] Jane E. Visvader and John Stingl. Mammary stem cells and the differentiation hierarchy: current status and perspectives. *Genes & Development*, 28:1143–1158, 2014.

[9] Kara L. Britt, Howard Kendrick, Joseph L. Regan, Gemma Molyneux, Fiona-Ann Magnay, Alan Ashworth, and Matthew J. Smalley. Pregnancy in the mature adult mouse does not alter the proportion of mammary epithelial stem/progenitor cells. *Breast Cancer Research*, 11:1–15, 2009.

[10] Larissa Mourao, Amber L. Zeeman, Katrin E. Wiese, Anika Bongaarts, Lieve L. Oudejans, Isabel Mora Martinez, Yorick BC van de Grift, Jos

Jonkers, and Renée van Amerongen. Hyperactive wnt/ctnnb1 signaling induces a competing cell proliferation and epidermal differentiation response in the mouse mammary epithelium. *bioRxiv*, 2021.

[11] Bryony S. Wiseman and Zena Werb. Stromal effects on mammary gland development and breast cancer. *Science*, 296:1046–1049, 2002.

[12] John Muschler and Charles H. Streuli. Cell–matrix interactions in mammary gland development and breast cancer. *Cold Spring Harbor perspectives in biology*, 2:a003202, 2010.

[13] Charis-P Segeritz and Ludovic Vallier. *Cell Culture: Growing Cells as Model Systems In Vitro*, chapter 9, pages 151–172. Academic Press, 2017.

[14] Jihoon Kim, Bon-Kyoung Koo, and Juergen A Knoblich. Human organoids: model systems for human biology and medicine. *Nature Reviews Molecular Cell Biology*, 21:571–584, 2020.

[15] Claudia Corro, Laura Novellasdemunt, and Vivian S.W. Li. A brief history of organoids. *American Journal of Physiology-Cell Physiology*, 319:C151–C165, 2020.

[16] Thierry Jardé, Bethan Lloyd-Lewis, Mairian Thomas, Howard Kendrick, Lorenzo Melchor, Lauriane Bougaret, Peter D. Watson, Kenneth Ewan, Matthew J. Smalley, and Trevor C. Dale. Wnt and neuregulin1/erbb signalling extends 3d culture of hormone responsive mammary organoids. *Nature communications*, 7:1–14, 2016.

[17] Elsa Charifou, Jakub Sumbal, Zuzana Koledova, Han Li, and Aurélie Chiche. A robust mammary organoid system to model lactation and involution-like processes. *Bio-protocol*, 11:e3996–e3996, 2021.

[18] Walburga Dieterich, Markus F Neurath, and Yurdagül Zopf. Intestinal ex vivo organoid culture reveals altered programmed crypt stem cells in patients with celiac disease. *Scientific Reports*, 10:3535–3545, 2020.

[19] Toshiro Sato, Daniel E. Stange, Marc Ferrante, Robert G.J. Vries, Johan H. Van Es, Stieneke Van Den Brink, Winan J. Van Houdt, Apollo Pronk, Joost Van Gorp, and Peter D. Siersema. Long-term expansion of epithelial organoids from human colon, adenoma, adenocarcinoma, and barrett's epithelium. *Gastroenterology*, 141:1762–1772, 2011.

[20] Mairian Thomas. Developing and utlilising a mouse mammary organoid model. *ORCA*, 2016.

[21] Anna M. Lilja, Veronica Rodilla, Mathilde Huyghe, Edouard Hannezo, Camille Landragin, Olivier Renaud, Olivier Leroy, Steffen Rulands, Benjamin D. Simons, and Silvia Fre. Clonal analysis of notch1-expressing cells reveals the existence of unipotent stem cells that retain long-term plasticity in the embryonic mammary gland. *Nature Cell Biology*, 20:677–687, 2018.

[22] Marika Caruso, Sjanie Huang, Larissa Mourao, and Colinda L.G.J. Scheele. A mammary organoid model to study branching morphogenesis. *Frontiers in Physiology*, 13:269, 2022.

[23] Jakub Sumbal, Aurelie Chiche, Elsa Charifou, Zuzana Koledova, and Han Li. Primary mammary organoid model of lactation and involution. *Frontiers in Cell and Developmental Biology*, 8:68, 2020.

[24] Soojung Lee, Marco Mele, Pernille Vahl, Peer M. Christiansen, Vibeke E.D. Jensen, and Ebbe Boedtkjer. Na+, hco 3–cotransport is functionally upregulated during human breast carcinogenesis and required for the inverted ph gradient across the plasma membrane. *Pflügers Archiv-European Journal of Physiology*, 467:367–377, 2015.

[25] Jakub Sumbal, Zuzana Budkova, Gunnhildur Ásta Traustadóttir, and Zuzana Koledova. Mammary organoids and 3d cell cultures: old dogs with new tricks. *Journal of Mammary Gland Biology and Neoplasia*, 25:273–288, 2020.

[26] Srivarshini Cherukupalli Mohan, Tian-Yu Lee, Armando E. Giuliano, and Xiaojiang Cui. Current status of breast organoid models. *Frontiers in Bioengineering and Biotechnology*, 9:745943, 2021.

[27] Scott F. Gilbert. *Developmental Biology*, chapter 1. Sinauer Associates Inc., USA, 2016.

[28] Sergio Casas-Tintó and Marta Portela. Cytonemes, their formation, regulation, and roles in signaling and communication in tumorigenesis. *International Journal of Molecular Sciences*, 20:5641, 2019.

[29] Jean-Paul Vincent and Laurence Dubois. Morphogen transport along epithelia, an integrated trafficking problem. *Developmental Cell*, 3:615–623, 2002.

[30] Karl Francis and Bernhard O. Palsson. Effective intercellular communication distances are determined by the relative time constants for cyto/chemokine secretion and diffusion. *Proceedings of the National Academy of Sciences*, 94:12258–12262, 1997.

[31] Celeste M. Nelson, Martijn M. VanDuijn, Jamie L. Inman, Daniel A. Fletcher, and Mina J. Bissell. Tissue geometry determines sites of mammary branching morphogenesis in organotypic cultures. *Science*, 314:298–300, 2006.

[32] Alexis Matamoro-Vidal and Romain Levayer. Multiple influences of mechanical forces on cell competition. *Current Biology*, 29:R762–R774, 2019.

[33] Clare E. Buckley and Daniel St Johnston. Apical–basal polarity and the control of epithelial form and function. *Nature Reviews Molecular Cell Biology*, 23:1–19, 2022.

[34] Fernando Martin-Belmonte and Mirna Perez-Moreno. Epithelial cell polarity, stem cells and cancer. *Nature Reviews Cancer*, 12:23–38, 2012.

[35] Masuko Katoh and Masaru Katoh. Wnt signaling pathway and stem cell signaling network. *Clinical Cancer Research*, 13:4042–4045, 2007.

[36] Fumio Motegi, Nicolas Plachta, and Virgile Viasnoff. Novel approaches to link apicobasal polarity to cell fate specification. *Current Opinion in Cell Biology*, 62:78–85, 2020.

[37] Sudipa June Chatterjee and Luke McCaffrey. Emerging role of cell polarity proteins in breast cancer progression and metastasis. *Breast Cancer: Targets and Therapy*, 6:15–27, 2014.

[38] Kentaro Nagaoka, Tsuyoshi Udagawa, and Joel D. Richter. Cpeb-mediated zo-1 mrna localization is required for epithelial tight-junction assembly and cell polarity. *Nature communications*, 3:675, 2012.

[39] Mina J. Bissell and David Bilder. Polarity determination in breast tissue: desmosomal adhesion, myoepithelial cells, and laminin 1. *Breast cancer research*, 5:1–3, 2003.

[40] Alejandra Guzmán-Herrera and Yanlan Mao. Polarity during tissue repair, a multiscale problem. *Current Opinion in Cell Biology*, 62:31–36, 2020.

[41] Beenu Moza Jalali, Karolina Lukasik, Krzysztof Witek, Agnieszka Baclawska, and Dariusz J. Skarzynski. Changes in the expression and distribution of junction and polarity proteins in the porcine endometrium during early pregnancy period. *Theriogenology*, 142:196–206, 2020.

[42] Maria E. Piroli, James O. Blanchette, and Ehsan Jabbarzadeh. Polarity as a physiological modulator of cell function. *Frontiers in bioscience (Landmark edition)*, 24:451, 2019.

[43] Hae-Yun Jung, Laurent Fattet, Jeff H. Tsai, Taketoshi Kajimoto, Qiang Chang, Alexandra C. Newton, and Jing Yang. Apical–basal polarity inhibits epithelial–mesenchymal transition and tumour metastasis by par-complex-mediated snai1 degradation. *Nature Cell Biology*, 21:359–371, 2019.

[44] Joëlle Roche. The epithelial-to-mesenchymal transition in cancer. *Cancers*, 10:52, 2018.

[45] Lixing Zhan, Avi Rosenberg, Kenneth C. Bergami, Min Yu, Zhenyu Xuan, Aron B. Jaffe, Craig Allred, and Senthil K. Muthuswamy. Deregulation of scribble promotes mammary tumorigenesis and reveals a role for cell polarity in carcinoma. *Cell*, 135:865–878, 2008.

[46] Anne C. Rios, Nai Yang Fu, Geoffrey J. Lindeman, and Jane E. Visvader. In situ identification of bipotent stem cells in the mammary gland. *Nature*, 506:322–327, 2014.

[47] Chunhui Wang, John R. Christin, Maja H. Oktay, and Wenjun Guo. Lineage-biased stem cells maintain estrogen-receptor-positive and-negative mouse mammary luminal lineages. *Cell reports*, 18:2825–2835, 2017.

[48] Bethan Lloyd-Lewis, Philippos Mourikis, and Silvia Fre. Notch signalling: sensor and instructor of the microenvironment to coordinate cell fate and organ morphogenesis. *Current Opinion in Cell Biology*, 61:16–23, 2019.

[49] Toula Bouras, Bhupinder Pal, François Vaillant, Gwyndolen Harburg, Marie Liesse Asselin-Labat, Samantha R. Oakes, Geoffrey J. Lindeman, and Jane E. Visvader. Notch signaling regulates mammary stem cell function and luminal cell-fate commitment. *Cell Stem Cell*, 3:429–441, 2008.

[50] Sungrim Seirin Lee. Lateral inhibition-induced pattern formation controlled by the size and geometry of the cell. *Journal of Theoretical Biology*, 404:51–65, 2016.

[51] Sandra B. Lemke and Celeste M. Nelson. Dynamic changes in epithelial cell packing during tissue morphogenesis. *Current Biology*, 31:R1098–R1110, 2021.

[52] Amalia Capilla, Ruth Johnson, Maki Daniels, María Benavente, Sarah J. Bray, and Máximo Ibo Galindo. Planar cell polarity controls directional notch signaling in the drosophila leg. *Development*, 139:2584–2593, 2012.

[53] Mette C. Jørgensen, Kristian H. de Lichtenberg, Caitlin A. Collin, Rasmus Klinck, Jeppe H. Ekberg, Maja S. Engelstoft, Heiko Lickert, and Palle Serup. Neurog3-dependent pancreas dysgenesis causes ectopic pancreas in hes1 mutant mice. *Development (Cambridge)*, 145:1–11, 2018.

[54] Silvia Fre, Mathilde Huyghe, Philippos Mourikis, Sylvie Robine, Daniel Louvard, and Spyros Artavanis-Tsakonas. Notch signals control the fate of immature progenitor cells in the intestine. *Nature*, 435:964–968, 2005.

[55] Daniel Lafkas, Amy Shelton, Cecilia Chiu, Gladys De Leon Boenig, Yongmei Chen, Scott S. Stawicki, Christian Siltanen, Mike Reichelt, Meijuan Zhou, Xiumin Wu, Jeffrey Eastham-Anderson, Heather , Meron Roose-Girma, Yvonne Chinn, Julie Q. Hang, Søren Warming, Jackson Egen, Wyne P. Lee, Cary Austin, Yan Wu, Jian Payandeh, John B. Lowe, and Christian W. Siebel. Therapeutic antibodies reveal notch control of transdifferentiation in the adult lung. *Nature*, 528:127–131, 2015.

[56] Sarah J. Bray. Notch signalling: A simple pathway becomes complex. *Nature Reviews Molecular Cell Biology*, 7:678–689, 2006.

[57] Teneale A. Stewart and Felicity M. Davis. A primary cell and organoid platform for evaluating pharmacological responses in mammary epithelial cells. *ACS Pharmacology & Translational Science*, 3:63–75, 2020.

[58] Philip Bland and Beatrice A. Howard. Mammary lineage restriction in development. *Nature Cell Biology*, 20:637–639, 2018.

[59] Aline Wuidart, Alejandro Sifrim, Marco Fioramonti, Shigeru Matsumura, Audrey Brisebarre, Daniel Brown, Alessia Centonze, Anne Dannau, Christine Dubois, and Alexandra Van Keymeulen. Early lineage segregation of multipotent embryonic mammary gland progenitors. *Nature Cell Biology*, 20:666–676, 2018.

[60] Claudio Ballabio, Matteo Gianesello, Chiara Lago, Konstantin Okonechnikov, Marica Anderle, Giuseppe Aiello, Francesco Antonica, Tingting Zhang, Francesca Gianno, Felice Giangaspero, et al. Notch1 switches progenitor competence in inducing medulloblastoma. *Science advances*, 7:eabd2781, 2021.

[61] Jinwook Choi, Yu Jin Jang, Catherine Dabrowska, Elhadi Iich, Kelly V. Evans, Helen Hall, Sam M. Janes, Benjamin D. Simons, Bon-Kyoung Koo, and Jonghwan Kim. Release of notch activity coordinated by il-1β signalling confers differentiation plasticity of airway progenitors via fosl2 during alveolar regeneration. *Nature Cell Biology*, 23:953–966, 2021.

[62] Sylvestre Chea, Thibaut Perchet, Maxime Petit, Thomas Verrier, Delphine Guy-Grand, Elena-Gaia Banchi, Christian A.J. Vosshenrich, James P. Di Santo, Ana Cumano, and Rachel Golub. Notch signaling in group 3 innate lymphoid cells modulates their plasticity. *Science signaling*, 9:ra45–ra45, 2016.

[63] Bethan Lloyd-Lewis, Alexander G. Fletcher, Trevor C. Dale, and Helen M. Byrne. Toward a quantitative understanding of the wnt/β-catenin pathway through simulation and experiment. *Wiley Interdisciplinary Reviews: Systems Biology and Medicine*, 5:391–407, 2013.

[64] Giovanna M. Collu, Ana Hidalgo-Sastre, and Keith Brennan. Wnt–notch signalling crosstalk in development and disease. *Cellular and Molecular Life Sciences*, 71:3553–3567, 2014.

[65] Jakub Sumbal and Zuzana Koledova. Fgf signaling in mammary gland fibroblasts regulates multiple fibroblast functions and mammary epithelial morphogenesis. *Development*, 146:dev185306, 2019.

[66] Jacqueline Whyte, Orla Bergin, Alessandro Bianchi, Sara McNally, and Finian Martin. Key signalling nodes in mammary gland development and cancer. mitogen-activated protein kinase signalling in experimental models of breast cancer progression and in mammary gland development. *Breast Cancer Research*, 11:1–14, 2009.

[67] Nobuo Sasaki, Takeshi Sasamura, Hiroyuki O. Ishikawa, Maiko Kanai, Ryu Ueda, Kaoru Saigo, and Kenji Matsuno. Polarized exocytosis and transcytosis of notch during its apical localization in drosophila epithelial cells. *Genes to Cells*, 12:89–103, 2007.

[68] Mateusz Trylinski, Khalil Mazouni, and François Schweisguth. Intra-lineage fate decisions involve activation of notch receptors basal to the midbody in drosophila sensory organ precursor cells. *Current Biology*, 27:2239–2247, 2017.

[69] Filippo Del Bene, Ann M. Wehman, Brian A. Link, and Herwig Baier. Regulation of neurogenesis by interkinetic nuclear migration through an apical-basal notch gradient. *Cell*, 134:1055–1065, 2008.

[70] James D. Murray. *Mathematical biology: I. An introduction*, chapter 6. Springer, 2002.

[71] Meritxell Sáez, James Briscoe, and David Rand. Dynamical landscapes of cell fate decisions. *Interface Focus*, 12, 2022.

[72] Conrad Hal Waddington. The strategy of the genes. 1957.

[73] William J.R. Longabaugh, Eric H. Davidson, and Hamid Bolouri. Visualization, documentation, analysis, and communication of large-scale gene regulatory networks. *Biochimica et Biophysica Acta (BBA)-Gene Regulatory Mechanisms*, 1789:363–374, 2009.

[74] Roberto Barbuti, Roberta Gori, Paolo Milazzo, and Lucia Nasti. A survey of gene regulatory networks modelling methods: from differential equations, to boolean and qualitative bioinspired models. *Journal of Membrane Computing*, 2:207–226, 2020.

[75] Oleg U. Kirnasovsky, Yuri Kogan, and Zvia Agur. Analysis of a mathematical model for the molecular mechanism of fate decision in mammary stem cells. *Mathematical Modelling of Natural Phenomena*, 3:78–89, 2008.

[76] Khuloud Jaqaman and Gaudenz Danuser. Linking data to models: data regression. *Nature Reviews Molecular Cell Biology*, 7:813–819, 2006.

[77] Christopher V. Rao, Denise M. Wolf, and Adam P. Arkin. Control, exploitation and tolerance of intracellular noise. *Nature*, 420:231–237, 2002.

[78] Amani A. Alahmadi, Jennifer A. Flegg, Davis G. Cochrane, Christopher C. Drovandi, and Jonathan M. Keith. A comparison of approximate versus exact techniques for bayesian parameter inference in nonlinear ordinary differential equation models. *Royal Society open science*, 7:191315, 2020.

[79] Alexandru Mizeranschi, Paul Thompson, Huiru Zheng, and Werner Dubitzky. A multi-model reverse-engineering algorithm for large gene regulation networks. In *2014 IEEE International Conference on Bioinformatics and Biomedicine (BIBM)*, pages 510–514. IEEE, 2014.

[80] Kamil Erguler and Michael P.H. Stumpf. Practical limits for reverse engineering of dynamical systems: a statistical analysis of sensitivity and parameter inferability in systems biology models. *Molecular BioSystems*, 7:1593–1602, 2011.

[81] Johan Paulsson. Models of stochastic gene expression. *Physics of life reviews*, 2:157–175, 2005.

[82] Daniel T. Gillespie. Exact stochastic simulation of coupled chemical reactions. *The Journal of Physical Chemistry*, 81:2340–2361, 1977.

[83] Roland Somogyi and Carol Anne Sniegoski. Modeling the complexity of genetic networks: understanding multigenic and pleiotropic regulation. *Complexity*, 1:45–63, 1996.

[84] Jae Il Joo, Joseph X. Zhou, Sui Huang, and Kwang-Hyun Cho. Determining relative dynamic stability of cell states using boolean network model. *Scientific Reports*, 8:1–14, 2018.

[85] Osama Shiraz Shah, Muhammad Faizyab Ali Chaudhary, Hira Anees Awan, Fizza Fatima, Zainab Arshad, Bibi Amina, Maria Ahmed, Hadia Hameed, Muhammad Furqan, Shareef Khalid, et al. Atlantis-attractor landscape analysis toolbox for cell fate discovery and reprogramming. *Scientific Reports*, 8:3554, 2018.

[86] John W. Pinney, David R. Westhead, and Glenn A. McConkey. Petri net representations in systems biology. *Biochemical Society Transactions*, 31:1513–1515, 2003.

[87] Joanne R. Collier, Nicholas A.M. Monk, Philip K. Maini, and Julian H. Lewis. Pattern formation by lateral inhibition with feedback: A mathematical model of delta-notch intercellular signalling. *Journal of Theoretical Biology*, 183:429 –446, 1996.

[88] Udi Binshtok and David Sprinzak. Modeling the notch response. *Molecular Mechanisms of Notch Signaling*, 1066:79–98, 2018.

[89] Sophie K. Kay, Heather A. Harrington, Sarah Shepherd, Keith Brennan, Trevor C. Dale, James M. Osborne, David J. Gavaghan, and Helen M. Byrne. The role of the hes1 crosstalk hub in notch-wnt interactions of the intestinal crypt. *PLoS Computational Biology*, 13:e1005400, 2017.

[90] Nele Moelans, Bart Blanpain, and Patrick Wollants. An introduction to phase-field modeling of microstructure evolution. *Calphad*, 32:268–294, 2008.

[91] Nara Guisoni, Rosa Martinez-Corral, Jordi Garcia-Ojalvo, and Joaquín de Navascués. Diversity of fate outcomes in cell pairs under lateral inhibition. *Development*, 144:1177–1186, 2017.

[92] Thomas Carraro, Elfriede Friedmann, and Daniel Gerecht. Coupling vs decoupling approaches for pde/ode systems modeling intercellular signaling. *Journal of Computational Physics*, 314:522–537, 2016.

[93] Alan M. Turing. The chemical basis of morphogenesis. *Philosophical Transactions of the Royal Society of London. Series B, Biological Sciences*, 237:37–72, 1952.

[94] B.N. Nagorcka and J.R. Mooney. The role of a reaction-diffusion system in the initiation of primary hair follicles. *Journal of Theoretical Biology*, 114:243–272, 1985.

[95] James D. Murray. *Mathematical Biology: II Spatial models and biomedical applications*. Springer, Germany, 2003.

[96] Jonathan B.L. Bard. A model for generating aspects of zebra and other mammalian coat patterns. *Journal of Theoretical Biology*, 93:363–385, 1981.

[97] Thomas E. Woolley, Ruth E. Baker, and Philip K. Maini. Turing's theory of morphogenesis: where we started, where we are and where we want to go. In *The Incomputable*, pages 219–235. Springer, USA, 2017.

[98] Mukul Tewary, Joel Ostblom, Laura Prochazka, Teresa Zulueta-Coarasa, Nika Shakiba, Rodrigo Fernandez-Gonzalez, and Peter W. Zandstra. A stepwise model of reaction-diffusion and positional information governs self-organized human peri-gastrulation-like patterning. *Development*, 144:4298–4312, 2017.

[99] Reuben D. O'Dea and John R. King. Continuum limits of pattern formation in hexagonal-cell monolayers. *Journal of Mathematical Biology*, 64:579–610, 2012.

[100] Reuben D. O'Dea and John R. King. Multiscale analysis of pattern formation via intercellular signalling. *Mathematical Biosciences*, 231:172–185, 2011.

[101] Shin-Ichiro Ei, Hiroshi Ishii, Makoto Sato, Yoshitaro Tanaka, Miaoxing Wang, and Tetsuo Yasugi. A continuation method for spatially discretized models with nonlocal interactions conserving size and shape of cells and lattices. *Journal of Mathematical Biology*, 81:981–1028, 2020.

[102] James M. Osborne, Alexander G. Fletcher, Joe M. Pitt-Francis, Philip K. Maini, and David J. Gavaghan. Comparing individual-based approaches to modelling the self-organization of multicellular tissues. *PLOS Computational Biology*, 13:e1005387, 2017.

[103] Chad M. Glen, Melissa L. Kemp, and Eberhard O. Voit. Agent-based modeling of morphogenetic systems: Advantages and challenges. *PLoS Computational Biology*, 15:e1006577, 2019.

[104] Kerri-Ann Norton, Travis Wallace, Niranjan B Pandey, and Aleksander S Popel. An agent-based model of triple-negative breast cancer: the interplay between chemokine receptor ccr5 expression, cancer stem cells, and hypoxia. *BMC Systems Biology*, 11:1–15, 2017.

[105] Jonathan Tang, Heiko Enderling, Sabine Becker-Weimann, Christopher Pham, Aris Polyzos, Chen-Yi Chen, and Sylvain V. Costes. Phenotypic transition maps of 3d breast acini obtained by imaging-guided agent-based modeling. *Integrative Biology*, 3:408–421, 2011.

[106] Joseph D. Butner, Yao-Li Chuang, Eman Simbawa, A.S. Al-Fhaid, S.R. Mahmoud, Vittorio Cristini, and Zhihui Wang. A hybrid agent-based model of the developing mammary terminal end bud. *Journal of Theoretical Biology*, 407:259–270, 2016.

[107] Tim Liebisch, Armin Drusko, Biena Mathew, Ernst HK Stelzer, Sabine C Fischer, and Franziska Matthäus. Cell fate clusters in icm organoids arise from cell fate heredity and division: a modelling approach. *Scientific Reports*, 10:22405, 2020.

[108] Torsten Thalheim, Marianne Quaas, Maria Herberg, Ulf-Dietrich Braumann, Christiane Kerner, Markus Loeffler, Gabriela Aust, and Joerg Galle. Linking stem cell function and growth pattern of intestinal organoids. *Developmental Biology*, 433:254–261, 2018.

[109] Mozhgan Kabiri Chimeh, Peter Heywood, Marzio Pennisi, Francesco Pappalardo, and Paul Richmond. Parallelisation strategies for agent based simulation of immune systems. *BMC Bioinformatics*, 20:1–14, 2019.

[110] Matt Stack, Paul Macklin, Robert Searles, and Sunita Chandrasekaran. Openacc acceleration of an agent-based biological simulation framework. *Computing in Science & Engineering*, 24:53–63, 2022.

[111] Mason A. Porter and James P. Gleeson. Dynamical systems on networks. *Frontiers in Applied Dynamical Systems: Reviews and Tutorials*, 4, 2016.

[112] Ian Stewart, Martin Golubitsky, and Marcus Pivato. Symmetry groupoids and patterns of synchrony in coupled cell networks. *SIAM Journal on Applied Dynamical Systems*, 2:609–646, 2003.

[113] Martin Golubitsky, Ian Stewart, and Andrei Török. Patterns of synchrony in coupled cell networks with multiple arrows. *SIAM Journal on Applied Dynamical Systems*, 4:78–100, 2005.

[114] Martin Golubitsky and Ian Stewart. Nonlinear dynamics of networks: the groupoid formalism. *Bulletin of the American Mathematical Society*, 43:305–364, 2006.

[115] David Angeli and Eduardo D. Sontag. Monotone control systems. *IEEE Transactions on Automatic Control*, 48:1684–1698, 2003.

[116] David Angeli and Eduardo Sontag. Interconnections of monotone systems with steady-state characteristics. In *Optimal control, stabilization and nonsmooth analysis*, pages 135–154. Springer, 2004.

[117] Murat Arcak. Pattern formation by lateral inhibition in large-scale networks of cells. *IEEE Transactions on Automatic Control*, 58:1250–1262, 2013.

[118] Ana S. Rufino Ferreira and Murat Arcak. Graph partitioning approach to predicting patterns in lateral inhibition systems. *SIAM Journal on Applied Dynamical Systems*, 12:2012–2031, 2013.

[119] Gary R. Mirams, Christopher J. Arthurs, Miguel O. Bernabeu, Rafel Bordas, Jonathan Cooper, Alberto Corrias, Yohan Davit, Sara Jane Dunn, Alexander G. Fletcher, Daniel G. Harvey, Megan E. Marsh, James M. Osborne, Pras Pathmanathan, Joe Pitt-Francis, James Southern, Nejib Zemzemi, and David J. Gavaghan. Chaste: An open source c++ library for computational physiology and biology. *PLoS Computational Biology*, 9:e1002970, 2013.

[120] Ross Cagan. Principles of drosophila eye differentiation. *Current Topics in Developmental Biology*, 89:115–135, 2009.

[121] Hideru Togashi, Kanoko Kominami, Masazumi Waseda, Hitomi Komura, Jun Miyoshi, Masatoshi Takeichi, and Yoshimi Takai. Nectins establish a checkerboard-like cellular pattern in the auditory epithelium. *Science*, 333:1144–1147, 2011.

[122] Hyojin Kim, Lan Huang, Paul J. Critser, Zhenyun Yang, Rebecca J. Chan, Lin Wang, Sherry L Voytik-Harbin, Irwin D. Bernstein, and Mervin C. Yoder. Notch ligand delta-like 1 promotes in vivo vasculogenesis in human cord blood–derived endothelial colony forming cells. *Cytotherapy*, 17:579–592, 2015.

[123] Zena Hadjivasiliou, Ginger L. Hunter, and Buzz Baum. A new mechanism for spatial pattern formation via lateral and protrusionmediated lateral signalling. *Journal of the Royal Society Interface*, 13, 2016.

[124] Helen J. Wearing and Jonathan A. Sherratt. Nonlinear analysis of juxtacrine patterns. *SIAM Journal on Applied Mathematics*, 62:283–309, 2001.

[125] Steven D. Webb and Markus R. Owen. Oscillations and patterns in spatially discrete models for developmental intercellular signalling. *Journal of Mathematical Biology*, 48:444–476, 2004.

[126] Steven D. Webb and Markus R. Owen. Intra-membrane ligand diffusion and cell shape modulate juxtacrine patterning. *Journal of Theoretical Biology*, 230:99–117, 2004.

[127] Pau Formosa-Jordan and Marta Ibañes. Competition in notch signaling with cis enriches cell fate decisions. *PLoS ONE*, 9:e95744, 2014.

[128] Hiroki Hamada, Masakatsu Watanabe, Hiu Eunice Lau, Tomoki Nishida, Toshiaki Hasegawa, David M. Parichy, and Shigeru Kondo. Involvement of delta/notch signaling in zebrafish adult pigment stripe patterning. *Development*, 141:318–324, 2014.

[129] Fengming Liu, Andrew Pawliwec, Zhenqian Feng, Zivart Yasruel, Jean-Jacques Lebrun, and Suhad Ali. Prolactin/jak2 directs apical/basal polarization and luminal linage maturation of mammary epithelial cells through regulation of the erk1/2 pathway. *Stem cell research*, 15:376–383, 2015.

[130] Atlantis Russ, Jeanne M.V. Louderbough, Daniela Zarnescu, and Joyce A. Schroeder. Hugl1 and hugl2 in mammary epithelial cells: Polarity, proliferation, and differentiation. *PLoS One*, 7, 2012.

[131] Andrew J. Ewald, Audrey Brenot, Myhanh Duong, Bianca S. Chan, and Zena Werb. Collective epithelial migration and cell rearrangements drive mammary branching morphogenesis. *Developmental Cell*, 14:570–581, 2008.

[132] Daniel Lafkas, Veronica Rodilla, Mathilde Huyghe, Larissa Mourao, Hippokratis Kiaris, and Silvia Fre. Notch3 marks clonogenic mammary luminal progenitor cells in vivo. *Journal of Cell Biology*, 203:47–56, 2013.

[133] Marika Sjöqvist and Emma R. Andersson. Do as i say, not (ch) as i do: Lateral control of cell fate. *Developmental biology*, 447:58–70, 2019.

[134] Wim Hordjik. An overview of computation in cellular automata. *Phys Comp*, 96:1–10, 1996.

[135] Tommaso Toffoli and Norman Margolus. *Cellular automata machines: a new environment for modeling*, chapter 5, pages 60–65. MIT press, USA, 1987.

[136] Béla Bollobás. *Modern graph theory*, volume 184, chapter 1. Springer, USA, 2013.

[137] Chris D. Godsil. Compact graphs and equitable partitions. *Linear Algebra and Its Applications*, 255:259–266, 1997.

[138] Helen J. Wearing, Markus R. Owen, and Jonathan A. Sherratt. Mathematical modelling of juxtacrine patterning. *Bulletin of Mathematical Biology*, 62:293–320, 2000.

[139] Arjan J. van der Schaft. $\mathcal{L}_2$ *Gain and Passivity Techniques in Nonlinear Control*, chapter 1. Springer Cham, 1996.

[140] David Angeli and Eduardo D. Sontag. Multi-stability in monotone input/output systems. *Systems & Control Letters*, 51:185–202, 2004.

[141] K. Ching Chang, Kelly Pearson, and Tan Zhang. Perron-frobenius theorem for nonnegative tensors. *Communications in Mathematical Sciences*, 6:507–520, 2008.

[142] Wassim M. Haddad and VijaySekhar Chellaboina. *Nonlinear dynamical systems and control: a Lyapunov-based approach*. Princeton University Press, USA, 2011.

[143] Joshua W. Moore, Trevor C. Dale, and Thomas E. Woolley. Polarity-driven laminar pattern formation by lateral-inhibition in 2d and 3d bilayer geometries. *IMA Journal of Applied Mathematics*, 87:568–606, 2022.

[144] Zvia Agur, Yuri Kogan, Liora Levi, Hannah Harrison, Rebecca Lamb, Oleg U. Kirnasovsky, and Robert B. Clarke. Disruption of a quorum sensing mechanism triggers tumorigenesis: a simple discrete model corroborated by experiments in mammary cancer stem cells. *Biology Direct*, 5:1–11, 2010.

[145] Alexander G. Fletcher, James M. Osborne, Philip K. Maini, and David J. Gavaghan. Implementing vertex dynamics models of cell populations in biology within a consistent computational framework. *Progress in Biophysics and Molecular Biology*, 113:299–326, 2013.

[146] Tatsuzo Nagai and Hisao Honda. A dynamic cell model for the formation of epithelial tissues. *Philosophical Magazine B*, 81:699–719, 2001.

[147] Nebojsa Murisic, Vincent Hakim, Ioannis G Kevrekidis, Stanislav Y Shvartsman, and Basile Audoly. From discrete to continuum models of three-dimensional deformations in epithelial sheets. *Biophysical Journal*, 109(1):154–163, 2015.

[148] Maria Fankhaenel, Farahnaz Sadat Golestan Hashemi, Larissa Mourao, Emily Lucas, Manal Mosa Hosawi, Paul Skipp, Xavier Morin, Colinda L.G.J. Scheele, and Salah Elias. Annexin a1 is a polarity cue that directs planar mitotic spindle orientation during mammalian epithelial morphogenesis. *bioRxiv*, 2022.

[149] Guocheng Fang, Hongxu Lu, Laura Rodriguez de la Fuente, Andrew M.K. Law, Gungun Lin, Dayong Jin, and David Gallego-Ortega. Mammary tumor organoid culture in non-adhesive alginate for luminal mechanics and high-throughput drug screening. *Advanced Science*, 8:2102418, 2021.

[150] Chii J. Chan and Takashi Hiiragi. Integration of luminal pressure and signalling in tissue self-organization. *Development*, 147:dev181297, 2020.

[151] Steven C. Chapra. *Applied numerical methods with MATLAB for engineers and scientists*, chapter 23, pages 555–572. New York: McGraw-Hill, 2012.

[152] Arnaud A. Mailleux, Michael Overholtzer, and Joan S. Brugge. Lumen formation during mammary epithelial morphogenesis: insights from in vitro and in vivo models. *Cell Cycle*, 7:57–62, 2008.

[153] Mona Shehata, Paul D. Waterhouse, Alison E. Casey, Hui Fang, Lee Hazelwood, and Rama Khokha. Proliferative heterogeneity of murine epithelial cells in the adult mammary gland. *Communications Biology*, 1:1–10, 2018.

[154] Joseph L. Regan, Tony Sourisseau, Kelly Soady, Howard Kendrick, Afshan McCarthy, Chan Tang, Keith Brennan, Spiros Linardopoulos, Donald E. White, and Matthew J. Smalley. Aurora a kinase regulates mammary epithelial cell fate by determining mitotic spindle orientation in a notch-dependent manner. *Cell Reports*, 4:110–123, 2013.

[155] Heather L. Machado, Frances S. Kittrell, David Edwards, Amanda N. White, Rachel L. Atkinson, Jeffrey M. Rosen, Daniel Medina, and Michael T. Lewis. Separation by cell size enriches for mammary stem cell repopulation activity. *Stem Cells Translational Medicine*, 2:199–203, 2013.

[156] Karen A. Knudsen and Margaret J. Wheelock. Cadherins and the mammary gland. *Journal of Cellular Biochemistry*, 95:488–496, 2005.

[157] Paulo S. Pereira, Alexandra Teixeira, Sofia Pinho, Paulo Ferreira, Joana Fernandes, Carla Oliveira, Raquel Seruca, Gianpaolo Suriano, and Fernando Casares. E-cadherin missense mutations, associated with hereditary diffuse gastric cancer (hdgc) syndrome, display distinct invasive behaviors and genetic interactions with the wnt and notch pathways in drosophila epithelia. *Human Molecular Genetics*, 15:1704–1712, 2006.

[158] Kevin G. Leong, Kyle Niessen, Iva Kulic, Afshin Raouf, Connie Eaves, Ingrid Pollet, and Aly Karsan. Jagged1-mediated notch activation induces epithelial-to-mesenchymal transition through slug-induced repression of e-cadherin. *Journal of Experimental Medicine*, 204:2935–2948, 2007.

[159] Jing Chen, Naoko Imanaka, and James D. Griffin. Hypoxia potentiates notch signaling in breast cancer leading to decreased e-cadherin expression and increased cell migration and invasion. *British Journal of Cancer*, 102:351–360, 2010.

[160] Eliah R. Shamir, Elisa Pappalardo, Danielle M. Jorgens, Kester Coutinho, Wen Ting Tsai, Khaled Aziz, Manfred Auer, Phuoc T. Tran, Joel S. Bader, and Andrew J. Ewald. Twist1-induced dissemination preserves epithelial identity and requires e-cadherin. *Journal of Cell Biology*, 204:839–856, 2014.

[161] Minsuk Kwak, Kaden M Southard, Woon Ryoung Kim, Annie Lin, Nam Hyeong Kim, Ramu Gopalappa, Hyun Jung Lee, Minji An, Seo Hyun Choi, Yunmin Jung, et al. Adherens junctions organize size-selective proteolytic hotspots critical for notch signalling. *Nature Cell Biology*, 24:1–15, 2022.

[162] Sebastien J.P. Callens, Rafael J.C. Uyttendaele, Lidy E. Fratila-Apachitei, and Amir A. Zadpoor. Substrate curvature as a cue to guide spatiotemporal cell and tissue organization. *Biomaterials*, 232:119739, 2020.

[163] Wen Yih Aw, Bryan W. Heck, Bradley Joyce, and Danelle Devenport. Transient tissue-scale deformation coordinates alignment of planar cell polarity junctions in the mammalian skin. *Current Biology*, 26:2090–2100, 2016.

[164] Thomas E. Woolley, Ruth E. Baker, Eamonn A. Gaffney, and Philip K. Maini. Stochastic reaction and diffusion on growing domains: understanding the breakdown of robust pattern formation. *Physical Review E*, 84:046216, 2011.

[165] Christopher Konow, Noah H. Somberg, Jocelyne Chavez, Irving R. Epstein, and Milos Dolnik. Turing patterns on radially growing domains: experiments and simulations. *Physical Chemistry Chemical Physics*, 21:6718–6724, 2019.

[166] Andrew L. Krause, Václav Klika, Philip K. Maini, Denis Headon, and Eamonn A. Gaffney. Isolating patterns in open reaction–diffusion systems. *Bulletin of Mathematical Biology*, 83:82, 2021.

[167] Ewa Paluch and Carl-Philipp Heisenberg. Biology and physics of cell shape changes in development. *Current Biology*, 19:790–799, 2009.

[168] Tommaso Ristori, Oscar M.J.A. Stassen, Cecilia M. Sahlgren, and Sandra Loerakker. Lateral induction limits the impact of cell connectivity on notch signaling in arterial walls. *International Journal for Numerical Methods in Biomedical Engineering*, 36:e3323, 2020.

[169] Oren Shaya, Udi Binshtok, Micha Hersch, Dmitri Rivkin, Sheila Weinreb, Liat Amir-Zilberstein, Bassma Khamaisi, Olya Oppenheim, Ravi A. Desai, Richard J. Goodyear, et al. Cell-cell contact area affects notch signaling and notch-dependent patterning. *Developmental Cell*, 40:505–511, 2017.

[170] Shaan N. Chhabra and Brian W. Booth. Asymmetric cell division of mammary stem cells. *Cell Division*, 16:1–15, 2021.

[171] Vasudha Srivastava, Tyler R. Huycke, Kiet T. Phong, and Zev J. Gartner. Organoid models for mammary gland dynamics and breast cancer. *Current Opinion in Cell Biology*, 66:51–58, 2020.

[172] Candice A.M. Sauder, Jillian E. Koziel, MiRan Choi, Melanie J. Fox, Brenda R. Grimes, Sunil Badve, Rachel J. Blosser, Milan Radovich, Christina C. Lam, and Melville B. Vaughan. Phenotypic plasticity in normal breast derived epithelial cells. *BMC Cell Biology*, 15:1–15, 2014.

[173] Adrian Wolny, Lorenzo Cerrone, Athul Vijayan, Rachele Tofanelli, Amaya Vilches Barro, Marion Louveaux, Christian Wenzl, Sören Strauss, David Wilson-Sánchez, Rena Lymbouridou, et al. Accurate and versatile 3d segmentation of plant tissues at cellular resolution. *Elife*, 9:e57613, 2020.

[174] Jonathan Long, Evan Shelhamer, and Trevor Darrell. Fully convolutional networks for semantic segmentation. In *Proceedings of the IEEE conference on computer vision and pattern recognition*, pages 3431–3440, 2015.

[175] Olaf Ronneberger, Philipp Fischer, and Thomas Brox. U-net: Convolutional networks for biomedical image segmentation. In *Medical Image Computing and Computer-Assisted Intervention–MICCAI 2015: 18th International Conference, Munich, Germany, October 5-9, 2015, Proceedings, Part III 18*, pages 234–241, 2015.

[176] Jonathan M. Matthews, Brooke Schuster, Sara Saheb Kashaf, Ping Liu, Rakefet Ben-Yishay, Dana Ishay-Ronen, Evgeny Izumchenko, Le Shen, Christopher R. Weber, Margaret Bielski, et al. Organoid: A versatile deep learning platform for tracking and analysis of single-organoid dynamics. *PLOS Computational Biology*, 18:e1010584, 2022.

[177] Anne Beghin, Gianluca Grenci, Geetika Sahni, Su Guo, Harini Rajendiran, Tom Delaire, Saburnisha Binte Mohamad Raffi, Damien Blanc, Richard de Mets, Hui Ting Ong, et al. Automated high-speed 3d imaging of organoid cultures with multi-scale phenotypic quantification. *Nature Methods*, 19:881–892, 2022.

[178] Anuradha Kar, Manuel Petit, Yassin Refahi, Guillaume Cerutti, Christophe Godin, and Jan Traas. Benchmarking of deep learning algorithms for 3d instance segmentation of confocal image datasets. *PLoS Computational Biology*, 18:e1009879, 2022.

[179] Jos B.T.M. Roerdink and Arnold Meijster. The watershed transform: Definitions, algorithms and parallelization strategies. *Fundamenta Informaticae*, 41:187–228, 2000.

[180] Alberto Bailoni, Constantin Pape, Nathan Hütsch, Steffen Wolf, Thorsten Beier, Anna Kreshuk, and Fred A Hamprecht. Gasp, a generalized framework for agglomerative clustering of signed graphs and its application to instance segmentation. In *Proceedings of the IEEE/CVF Conference on Computer Vision and Pattern Recognition*, pages 11645–11655, 2022.

[181] Meghan K. Driscoll, Colin McCann, Rael Kopace, Tess Homan, John T. Fourkas, Carole Parent, and Wolfgang Losert. Cell shape dynamics: from waves to migration. *PLoS Computational Biology*, 8:e1002392, 2012.

[182] Michael Corral. *Elementary Trigonometry*, chapter Chapter 2, pages 58–69. OER LibreTexts Project, 2009.

[183] Mona Shehata, Paul D. Waterhouse, Alison E. Casey, Hui Fang, Lee Hazelwood, and Rama Khokha. Proliferative heterogeneity of murine epithelial cells in the adult mammary gland. *Communications Biology*, 1:1–10, 2018.

[184] Caterina Tomba, Valeriy Luchnikov, Luca Barberi, Carles Blanch-Mercader, and Aurélien Roux. Epithelial cells adapt to curvature induction via transient active osmotic swelling. *Developmental cell*, 57:1257–1270, 2022.

[185] Nikolche Gjorevski, Mikhail Nikolaev, Tobin Brown, Olga Mitrofanova, Nathalie Brandenberg, Frank W. DelRio, Francis Yavitt, Prisca Liberali, Kristi Anseth, and Matthias Lutolf. Tissue geometry drives deterministic organoid patterning. *Science*, 375:eaaw9021, 2022.

[186] Andras Gyorgy and Murat Arcak. Pattern formation in large-scale networks with asymmetric connections. *IFAC-PapersOnLine*, 50:10944–10949, 2017.

[187] Hal L. Smith. *Monotone dynamical systems: an introduction to the theory of competitive and cooperative systems: an introduction to the theory of competitive and cooperative systems*. American Mathematical Soc., USA, 2008.

[188] Robert J. Huebner, Terry Lechler, and Andrew J. Ewald. Developmental stratification of the mammary epithelium occurs through symmetry-breaking vertical divisions of apically positioned luminal cells. *Development*, 141:1085–1094, 2014.

[189] Harold Fernando Gomez, Mathilde Sabine Dumond, Leonie Hodel, Roman Vetter, and Dagmar Iber. 3d cell neighbour dynamics in growing pseudostratified epithelia. *Elife*, 10:e68135, 2021.

[190] Supriya Bajpai, Raghunath Chelakkot, Ranganathan Prabhakar, and Mandar M Inamdar. Role of delta-notch signalling molecules on cell–cell adhesion in determining heterogeneous chemical and cell morphological patterning. *Soft Matter*, 18:3505–3520, 2022.

[191] Junmin Lee, Amr A. Abdeen, Kathryn L. Wycislo, Timothy M. Fan, and Kristopher A. Kilian. Interfacial geometry dictates cancer cell tumorigenicity. *Nature Materials*, 15:856–862, 2016.

[192] Najate Benhra, Françoise Vignaux, Aurore Dussert, François Schweisguth, and Roland Le Borgne. Neuralized promotes basal to apical transcytosis of delta in epithelial cells. *Molecular Biology of the Cell*, 21:2078–2086, 2010.

[193] Benedikt Vollrath, Jeffrey Pudney, Sylvia Asa, Philip Leder, and Kevin Fitzgerald. Isolation of a murine homologue of the drosophila neuralized gene, a gene required for axonemal integrity in spermatozoa and terminal maturation of the mammary gland. *Molecular and Cellular Biology*, 21:7481–7494, 2001.

[194] Manuela AD Aguiar and Ana Paula S Dias. Synchronization and equitable partitions in weighted networks. *Chaos: An Interdisciplinary Journal of Nonlinear Science*, 28:073105, 2018.

[195] Rubén J Sánchez-García, Emanuele Cozzo, and Yamir Moreno. Dimensionality reduction and spectral properties of multilayer networks. *Physical Review E*, 89:052815, 2014.

[196] Yu-Chiuan Chang, Jhen-Wei Wu, Chueh-Wen Wang, and Anna C-C Jang. Hippo signaling-mediated mechanotransduction in cell movement and cancer metastasis. *Frontiers in molecular biosciences*, 6:157, 2020.

[197] Antonio Totaro, Martina Castellan, Daniele Di Biagio, and Stefano Piccolo. Crosstalk between yap/taz and notch signaling. *Trends in Cell Biology*, 28:560–573, 2018.

[198] Sounak Sahu, Mary E. Albaugh, Betty K. Martin, Nimit L. Patel, Lisa Riffle, Susan Mackem, Joseph D. Kalen, and Shyam K. Sharan. Growth factor dependency in mammary organoids regulates ductal morphogenesis during organ regeneration. *Scientific Reports*, 12:7200, 2022.

[199] Andrew T. Baker, Andrei Zlobin, and Clodia Osipo. Notch-egfr/her2 bidirectional crosstalk in breast cancer. *Frontiers in Oncology*, 4:360, 2014.

[200] Tsuyoshi Hirashima and Michiyuki Matsuda. Erk-mediated curvature feedback regulates branching morphogenesis in lung epithelial tissue. *bioRxiv*, pages 2021–07, 2021.

[201] Lucia Jimenez-Rojo, Zoraide Granchi, Daniel Graf, and Thimios A. Mitsiadis. Stem cell fate determination during development and regeneration of ectodermal organs. *Frontiers in physiology*, 3:107, 2012.

[202] Susanne Vorhagen and Carien M. Niessen. Mammalian apkc/par polarity complex mediated regulation of epithelial division orientation and cell fate. *Experimental cell research*, 328:296–302, 2014.

[203] Andrew L. Krause, Eamonn A. Gaffney, Philip K. Maini, and Václav Klika. Introduction to 'recent progress and open frontiers in turing's theory of morphogenesis'. *Philosophical Transactions of the Royal Society A*, 379:20200280, 2021.

[204] David Sprinzak, Amit Lakhanpal, Lauren LeBon, Leah A. Santat, Michelle E. Fontes, Graham A. Anderson, Jordi Garcia-Ojalvo, and Michael B. Elowitz. Cis-interactions between notch and delta generate mutually exclusive signalling states. *Nature*, 465:86–90, 2010.

[205] Werner Horsthemke, Kwan Lam, and Peter K. Moore. Network topology and turing instabilities in small arrays of diffusively coupled reactors. *Physics Letters A*, 328:444–451, 2004.

[206] Peter K. Moore and Werner Horsthemke. Localized patterns in homogeneous networks of diffusively coupled reactors. *Physica D: Nonlinear Phenomena*, 206:121–144, 2005.

[207] Andras Gyorgy and Murat Arcak. Pattern formation over multigraphs. *IEEE transactions on network science and engineering*, 5:55–64, 2017.

[208] Chris Godsil and Gordon F. Royle. *Algebraic graph theory*, volume 207. Springer Science & Business Media, 2001.

[209] Lewis Wolpert, Cheryll Tickle, and Alfonso Martinez Arias. *Principles of Development*, chapter 1, pages 29–35. Oxford University Press, USA, 2015.

[210] Charles R. Johnson. Row stochastic matrices similar to doubly stochastic matrices. *Linear and Multilinear Algebra*, 10:113–130, 1981.

[211] Giovanni Leoni. *A first course in Sobolev spaces*. American Mathematical Soc., USA, 2017.

[212] Devendra Kumar. *Advanced calculus of several variables*. Alpha Science International Limited, UK, 2014.

[213] Liesen Jorg and Mehrmann Volker. *Linear algebra*. Springer,Switzerland, 2015.

[214] Praveen Agarwal, Mohamed Jleli, and Bessem Samet. Banach contraction principle and applications. In *Fixed Point Theory in Metric Spaces*, pages 1–23. Springer, Singapore, 2018.

[215] Yorick Hardy and Willi-Hans Steeb. *Matrix Calculus, Kronecker Product and Tensor Product: A Practical Approach to Linear Algebra, Multilinear Algebra and Tensor Calculus with Software Implementations*. World Scientific, Singapore, 2019.

[216] Fuzhen Zhang. *Matrix theory: basic results and techniques*. Springer, USA, 2011.

[217] John M Howie. *Real analysis*. Springer, UK, 2006.

[218] Erich Kamke. Zur theorie der systeme gewöhnlicher differentialgleichungen. ii. *Acta Mathematica*, 58:57–85, 1932.

[219] Morris W. Hirsch. Differential equations and convergence almost everywhere in strongly monotone semiflows. *Contemporary Mathematics*, 17:267–285, 1983.

[220] Chris Godsil and Gordon F. Royle. *Algebraic graph theory*. Springer New York, USA, 2001.

[221] Edda Klipp and Wolfram Liebermeister. Mathematical modeling of intracellular signaling pathways. *BMC neuroscience*, 7:1–16, 2006.

[222] Richard A Brualdi and Herbert J Ryser. *Combinatorial matrix theory*. Cambridge University Press, UK, 1991.

[223] Jorg Liesen Jorg Liesen and Volker Mehrmann Volker Mehrmann. *Linear algebra*. Springer, 2015.

[224] Hal L. Smith. Periodic solutions of periodic competitive and cooperative systems. *SIAM Journal on Mathematical Analysis*, 17:1289–1318, 1986.

[225] James D. Murray. *Mathematical Biology I. An Introduction.* Springer, Germany, 2002.

[226] Alexander Graham. *Kronecker products and matrix calculus with applications.* Courier Dover Publications, UK, 2018.

[227] John C. Doyle, Bruce A. Francis, and Allen R. Tannenbaum. *Feedback control theory.* Courier Corporation, USA, 2013.

[228] Kumpati S. Narendra and Anuradha M Annaswamy. *Stable adaptive systems.* Dover Publications Inc., UK, 2012.

[229] Mituhiko Araki. Application of m-matrices to the stability problems of composite dynamical systems. *Journal of Mathematical Analysis and Applications*, 52:309–321, 1975.

[230] Leiba Rodman, Hakan Seyalioglu, and Ilya M. Spitkovsky. On common invariant cones for families of matrices. *Linear Algebra and its Applications*, 432:911–926, 2010.

[231] Thomas E. Woolley, Andrew L. Krause, and Eamonn A. Gaffney. Bespoke turing systems. *Bulletin of Mathematical Biology*, 83:1–32, 2021.

[232] Javier Arpòn, Kaori Sakai, Valérie Gaudin, and Philippe Andrey. Spatial modeling of biological patterns shows multiscale organization of arabidopsis thaliana heterochromatin. *Scientific reports*, 11:1–17, 2021.

[233] Satoru Okuda, Takashi Miura, Yasuhiro Inoue, Taiji Adachi, and Mototsugu Eiraku. Combining turing and 3d vertex models reproduces autonomous multicellular morphogenesis with undulation, tubulation, and branching. *Scientific Reports*, 8:1–15, 2018.

[234] Satu-Marja Myllymäki and Marja L. Mikkola. Inductive signals in branching morphogenesis–lessons from mammary and salivary glands. *Current Opinion in Cell Biology*, 61:72–78, 2019.

[235] David Angeli, Muhammad Ali Al-Radhawi, and Eduardo D. Sontag. A robust lyapunov criterion for nonoscillatory behaviors in biological interaction networks. *IEEE Transactions on Automatic Control*, 67:3305–3320, 2022.

[236] Vincent Bertrand. β-catenin-driven binary cell fate decisions in animal development. *Wiley Interdisciplinary Reviews: Developmental Biology*, 5:377–388, 2016.

[237] Zvia Agur, Oleg U. Kirnasovsky, Genadiy Vasserman, Lilach Tencer-Hershkowicz, Yuri Kogan, Hannah Harrison, Rebecca Lamb, and Robert B. Clarke. Dickkopf1 regulates fate decision and drives breast cancer stem cells to differentiation: an experimentally supported mathematical model. *PLoS One*, 6:e24225, 2011.

[238] Julia Y. Co, Mar Margalef-Català, Denise M. Monack, and Manuel R. Amieva. Controlling the polarity of human gastrointestinal organoids to investigate epithelial biology and infectious diseases. *Nature protocols*, 16:5171–5192, 2021.

[239] Panagiota Kakni, Carmen López-Iglesias, Roman Truckenmüller, Pamela Habibović, and Stefan Giselbrecht. Reversing epithelial polarity in pluripotent stem cell-derived intestinal organoids. *Frontiers in Bioengineering and Biotechnology*, 10:669, 2022.

[240] Kati Taal, Jürgen Tuvikene, Grete Rullinkov, Marko Piirsoo, Mari Sepp, Toomas Neuman, Richard Tamme, and Tõnis Timmusk. Neuralized family member neurl1 is a ubiquitin ligase for the cgmp-specific phosphodiesterase 9a. *Scientific Reports*, 9:7104, 2019.

[241] Gantas Perez-Mockus and Francois Schweisguth. Cell polarity and notch signaling: Linked by the e3 ubiquitin ligase neuralized? *BioEssays*, 39:1700128, 2017.

[242] Jeffrey D. Axelrod and Claire J. Tomlin. Modeling the control of planar cell polarity. *Wiley Interdisciplinary Reviews: Systems Biology and Medicine*, 3:588–605, 2011.

[243] Jennifer J. Banerjee, Birgit L. Aerne, Maxine V. Holder, Simon Hauri, Matthias Gstaiger, and Nicolas Tapon. Meru couples planar cell polarity with apical-basal polarity during asymmetric cell division. *Elife*, 6:e25014, 2017.

[244] Qian Gao, Junfeng Zhang, Xiumei Wang, Ying Liu, Rongqiao He, Xingfeng Liu, Fei Wang, Jing Feng, Dongling Yang, Zhaoqing Wang, et al. The signalling receptor mcam coordinates apical-basal polarity and planar cell polarity during morphogenesis. *Nature Communications*, 8:15279, 2017.

[245] Melinda Liu Perkins, Dirk Benzinger, Murat Arcak, and Mustafa Khammash. Cell-in-the-loop pattern formation with optogenetically emulated cell-to-cell signaling. *Nature Communications*, 11:1355, 2020.

[246] Fernanda de Paula, Tathyane Harumi Nakajima Teshima, Ricardo Hsieh, Milena Monteiro Souza, Marcello Menta Simonsen Nico, and Silvia Vanessa Lourenco. Overview of human salivary glands: highlights of morphology and developing processes. *The Anatomical Record*, 300:1180–1188, 2017.

[247] Kenji Saga. Structure and function of human sweat glands studied with histochemistry and cytochemistry. *Progress in histochemistry and cytochemistry*, 37:323–386, 2002.

[248] James M. Wells and Jason R. Spence. How to make an intestine. *Development*, 141:752–760, 2014.

[249] Margherita Paschini and Carla F. Kim. An airway organoid is forever. *The EMBO Journal*, 38:e101526, 2019.

[250] Michael David Brügger and Konrad Basler. The diverse nature of intestinal fibroblasts in development, homeostasis, and disease. *Trends in Cell Biology*, 2023.

[251] Niki Chalkidi, Christina Paraskeva, and Vasiliki Koliaraki. Fibroblasts in intestinal homeostasis, damage, and repair. *Frontiers in Immunology*, 13:924866, 2022.

[252] David Sachs, Adam Wahlsten, Sebastian Kozerke, Gaetana Restivo, and Edoardo Mazza. A biphasic multilayer computational model of human skin. *Biomechanics and Modeling in Mechanobiology*, 20:969–982, 2021.

[253] Manuela A.D. Aguiar, Ana P.S. Dias, and Haibo Ruan. Synchrony patterns in gene regulatory networks. *Physica D: Nonlinear Phenomena*, 429:133065, 2022.

[254] Yifan Wang and Binhua P. Zhou. Epithelial-mesenchymal transition in breast cancer progression and metastasis. *Chinese Journal of Cancer*, 30:603, 2011.

[255] Matthieu R. Zeronian, Oleg Klykov, Júlia Portell i de Montserrat, Maria J. Konijnenberg, Anamika Gaur, Richard A. Scheltema, and Bert J.C. Janssen. Notch–jagged signaling complex defined by an interaction mosaic. *Proceedings of the National Academy of Sciences*, 118:e2102502118, 2021.

[256] Marcelo Boareto, Mohit Kumar Jolly, Mingyang Lu, José N Onuchic, Cecilia Clementi, and Eshel Ben-Jacob. Jagged–delta asymmetry in notch signaling can give rise to a sender/receiver hybrid phenotype. *Proceedings of the National Academy of Sciences*, 112:E402–E409, 2015.

[257] Daipeng Chen, Zary Forghany, Xinxin Liu, Haijiang Wang, Roeland MH Merks, and David A. Baker. A new model of notch signalling: Control of notch receptor cis-inhibition via notch ligand dimers. *PLOS Computational Biology*, 19:e1010169, 2023.

[258] Eduardo D. Sontag. Monotone and near-monotone biochemical networks. *Systems and synthetic biology*, 1:59–87, 2007.

[259] Manuela A.D. Aguiar, Ana Paula S. Dias, and H. Ruan. Synchrony and elementary operations on coupled cell networks. *SIAM Journal on Applied Dynamical Systems*, 15:322–337, 2016.

[260] Kathryn Atwell, Zhao Qin, David Gavaghan, Hillel Kugler, E. Jane Albert Hubbard, and James M. Osborne. Mechano-logical model of c. elegans germ line suggests feedback on the cell cycle. *Development (Cambridge)*, 142:3902–3911, 2015.

[261] Edward M. Purcell. Life at low reynolds number. *American journal of physics*, 45:3–11, 1977.

[262] Pras Pathmanathan, J. Cooper, Alexander G. Fletcher, Gary R. Mirams, Philip K. Murray, James M. Osborne, Joe Pitt-Francis, and Jon S. Walter, Alex .and Chapman. A computational study of discrete mechanical tissue models. *Physical Biology*, 6:036001, 2009.

[263] Albert-László Barabási, Réka Albert, and Hawoong Jeong. Mean-field theory for scale-free random networks. *Physica A: Statistical Mechanics and its Applications*, 272:173–187, 1999.

[264] Szymon Rusinkiewicz. Estimating curvatures and their derivatives on triangle meshes. In *Proceedings. 2nd International Symposium on 3D Data Processing, Visualization and Transmission, 2004. 3DPVT 2004.*, pages 486–493. IEEE, 2004.

[265] Paolo Dini and Chrystopher L Nehaniv. Diamond condition for commuting adjacency matrices of directed and undirected graphs. 2013.

[266] Jérôme Kunegis. Exploiting the structure of bipartite graphs for algebraic and spectral graph theory applications. *Internet Mathematics*, 11:201–321, 2015.